Theoretical Studies of Intramolecular Rearrangements of Siloxycarbenes

Paul G. Loncke

A Thesis

in

The Department

of

Chemistry and Biochemistry

Presented in Partial Fulfillment of the Requirements
for the Degree of Doctor of Philosophy at
Concordia University
Montreal, Quebec, Canada

November 2003

Your file Votre référence
ISBN: 0-612-90394-X
Our file Notre référence
ISBN: 0-612-90394-X

CONCORDIA UNIVERSITY
SCHOOL OF GRADUATE STUDIES

This is to certify that the thesis prepared

By: **Paul Loncke**

Entitled: **Theoretical Studies of Intramolecular Rearrangements of Siloxycarbenes**

and submitted in partial fulfillment of the requirements for the degree of

DOCTOR OF PHILOSOPHY (Chemistry)

complies with the regulations of the University and meets the accepted standards with respect to originality and quality.

Signed by the final examining committee:

Dr. B. Mangat ____ Chair

Dr. R.J. Boyd ____ External Examiner

Dr. W. Zerges ____ External to Program

Dr. H. Muchall ____ Examiner

Dr. O.S. Tee ____ Examiner

Dr. G. Peslherbe ____ Thesis Supervisor

Approved by ____
Chair of Department or Graduate Program Director

Jan 16 2004

____
Dean of Faculty

Abstract

Theoretical Studies of Intramolecular Rearrangements of Siloxycarbenes

Paul G. Loncke, Ph.D.
Concordia University, 2003

This thesis describes a thorough theoretical investigation of the mechanisms of intramolecular rearrangements of siloxycarbenes by means of contemporary ab initio molecular orbital theory and density-functional theory calculations combined with the quantum theory of atoms in molecules (AIM), the electron localization function (ELF) and natural bond orbital (NBO) analysis. New approaches for probing the mechanisms of organic reactions using these well-established electronic-structure methods are described. The thesis is divided into five chapters. Chapter 1 addresses the importance of understanding siloxycarbene reactivity, and provides a concise description of the electronic structure of carbenes, a brief review of singlet carbene rearrangements and an outline of the main objectives of this work. Chapter 2 describes an investigation of the mechanisms of intramolecular rearrangements of methoxy(siloxy)carbene, with emphasis on 1,2-silyl migration and decarbonylation. It is shown that 1,2-silyl migration and decarbonylation are concerted rearrangements involving intramolecular front-side nucleophilic attack by the carbene lone pair at silicon and by the methoxy oxygen at silicon, respectively. It is worthy to note that both of these rearrangement mechanisms are symmetry-forbidden according to Woodward-Hoffmann rules and similar rearrangements involving intramolecular front-side nucleophilic substitution are quite rare. Also noteworthy is the finding based on AIM analysis that the changes in molecular structure associated with 1,2-silyl migration occur via a bifurcation mechanism, while those associated with 1,2-methyl migration, which involves an anion-like shift to the "vacant"

carbene *p* orbital, occur via a conflict mechanism. Chapter 3 deals with the effects of substituents and the role of hyperconjugation in siloxycarbene rearrangements. It is found that electron-withdrawing substituents in methoxy(substituted-siloxy)carbenes generally lower the barriers for 1,2-silyl migration and decarbonylation, consistent with the mechanisms proposed in Chapter 2. The ease of intramolecular rearrangements of siloxycarbenes is also shown to be related to the extent of the pertinent hyperconjugative interactions in the parent carbene conformers. Chapter 4 describes a study of the mechanisms of intramolecular rearrangements of 3-sila-2-oxacyclohexylidene, a cyclic siloxycarbene. Among the most significant findings is the fact that ring contraction occurs via a symmetry-forbidden concerted rearrangement involving intramolecular front-side nucleophilic attack by the carbene lone pair at silicon. AIM analysis suggests that the changes in molecular structure accompanying ring contraction occur via a bifurcation mechanism, while those associated with 1,2-H migration, which involves a hydride-like shift to the "vacant" carbene *p* orbital, occur via a conflict mechanism. Chapter 5 summarizes the key findings of this work and provides some perspective on these findings. It also provides insight into how the approaches described in this work may be extended to other systems.

Acknowledgments

First and foremost, I wish to thank my supervisor Prof. Gilles H. Peslherbe for his guidance and support throughout my doctoral studies, and for giving me a number of opportunities to present our research findings at international renowned conferences in Canada and the United States. I also wish to thank my former supervisor Dr. Timothy A. Gadosy for initial guidance and introduction to Computational Chemistry.

Professors Heidi M. Muchall and Oswald S. Tee, as well as members of my group, Qadir, Jeff, Sean, Céline, Nhan, Cyril, Lei, Denise, Mouna, Yin, Pascal, and David (a.k.a. Sunshine), also deserve my gratitude (Of course, Qadir prefers Vodka) for the useful advice they provided during committee meetings, group meetings and coffee breaks. I am also very thankful for the constant encouragement and support of my parents (Marva and John), my aunts (Yve, Joy and Claire), my uncles (Bobby, Ham and Rudy), and my cousins (Marva, Kevin, Alicia and Desmond). Lastly, I wish to thank the faculty, graduate and undergraduate students of the department for making my stay at Concordia enjoyable.

Dedicated to the memory of my grandmother
the late Doris Ashford

Table of Contents

List of Figures

List of Schemes

List of Tables

List of Symbols

AIM	atoms in molecules
B3LYP	Becke-style three-parameter hybrid exchange/Lee-Yang-Parr correlation functional
BCP	bond critical point
BS-UDFT	broken-symmetry unrestricted density-functional theory
DFT	density-functional theory
ε	bond ellipticity; orbital energy
ELF	electron-localization function
eq	equation
Et	ethyl
FMO	frontier molecular orbital
HF	Hartree-Fock
HMPA	hexamethylphosphoric triamide
HOMO	highest occupied molecular orbital
IRC	intrinsic reaction coordinate
LDA	lithium diisopropylamide; local density approximation
LUMO	lowest unoccupied molecular orbital
$\lambda(\Omega_i)$	relative fluctuation of basin population
Me	methyl
MO	molecular orbital
MP2	second-order Møller-Plesset
NBO	natural bond orbital
NPA	natural population analysis
$N(\Omega_i)$	average basin population
PBE1PBE	Perdew-Burke-Ernzerhof one-parameter hybrid exchange-correlation functional
RCP	ring critical point
ρ	Hammett reaction constant
$\rho(\mathrm{r})$	electronic density
$\rho_b(\mathrm{r})$	bond critical point electronic density
$\nabla^2\rho(\mathrm{r})$	Laplacian of the electronic density
$\nabla^2\rho_b(\mathrm{r})$	Laplacian of the electronic density at a bond critical point
SCF	self-consistent field
$\langle S^2 \rangle$	expectation value of the spin operator
σ	Hammett substituent constant
σ_I	Swain-Lupton modified Hammett substituent constant
TBS	*t*-butyldimethylsilyl
TS	transition state
VSCC	valence-shell charge concentration
WFT	wave-function theory

Chapter 1
General Introduction

1.1 Significance of Siloxycarbene Rearrangements

The use of acylsilanes ($RCOSiR'_3$) in organic synthesis has increased considerably in recent years due to the discovery of new reactions and to the development of efficient methods for acylsilane synthesis.[1,2] Facile reactions such as conversion to aldehydes,[1-4] oxidation to carboxylic acids,[1-3,5] and the unique Brook rearrangement,[1,2,6] make these compounds useful as versatile synthons in organic synthesis. In addition, acylsilanes with bulky trialkylsilyl groups are often used to control the stereochemistry of organic reactions.[2,3,5,7,8] Below are a few examples of how some of the above mentioned properties of acylsilanes have been exploited in organic synthesis.

Aldehydes **1** were found to react with 3-methylpentadienyl lithium affording a mixture of regioisomers **2** and **3** (cf. Scheme 1.1).[3] However, only the conjugated regioisomers **2** were obtained when these aldehydes were replaced by acylsilanes **4**. The observed regiospecificity likely arises from the presence of the bulky trimethylsilyl group which hinders attack of the acyl carbon by the intermediate tertiary pentadienyl anion.

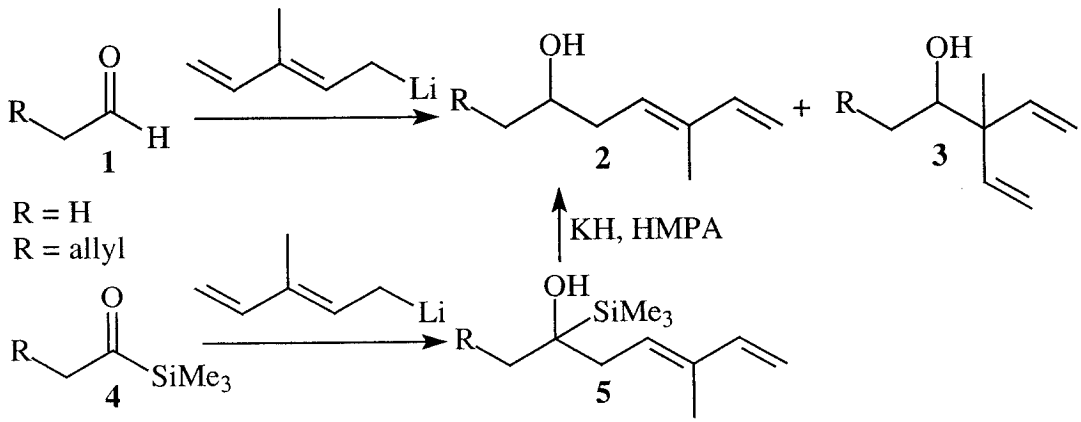

Scheme 1.1

Lithium enolates of acylsilanes **6** have been reported to undergo aldol condensation reactions with a variety of aldehydes affording primarily *syn*-β-hydroxyacylsilanes **7**, which were subsequently oxidized to *syn*-β-hydroxy acids **8** (cf. Scheme 1.2).[5] The diastereoselectivity observed is apparently due to formation of chair-like transition states between the aldehydes and the more stable *E*-isomers of the preformed lithium enolates (cf. Scheme 1.2). In the transition states **TS(syn)** leading to *syn*-β-hydroxyacylsilanes, the bulky groups R' and SiR_3 are farther apart than in the transition states **TS(anti)** for formation of the *anti*-β-hydroxyacylsilanes. As a consequence, there is less steric interaction in **TS(syn)** than in **TS(anti)**, which results in **TS(syn)** being more stable than **TS(anti)**.

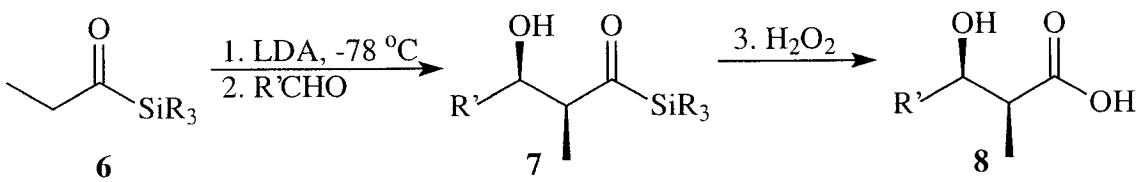

6 **7** **8**

R = *t*-$BuMe_2$, Et, n-Pr
R' = Ph, *i*-Pr

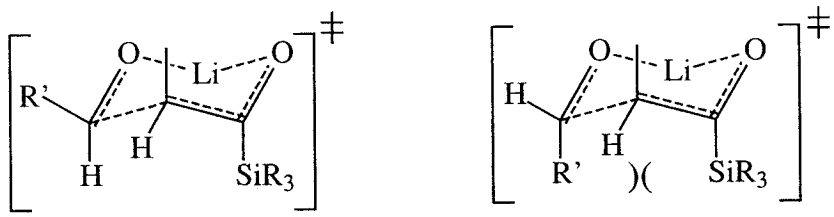

TS(syn) **TS(anti)**

Scheme 1.2

Recently, a new synthetic procedure for the enantioselective total synthesis of the natural product (+)-α-onocerin (**12**) was described, in which the unusual reactivity of acylsilanes was exploited (cf. Scheme 1.3).[7] One of the key steps in this procedure is the stereoselective synthesis of diepoxide **11**, which involves coupling of the chelated

Z-allylic lithium reagent **10** that results from nucleophilic addition of vinyl lithium to acylsilane **9,** followed by a Brook rearrangement (i.e. migration of TBS from C to O).

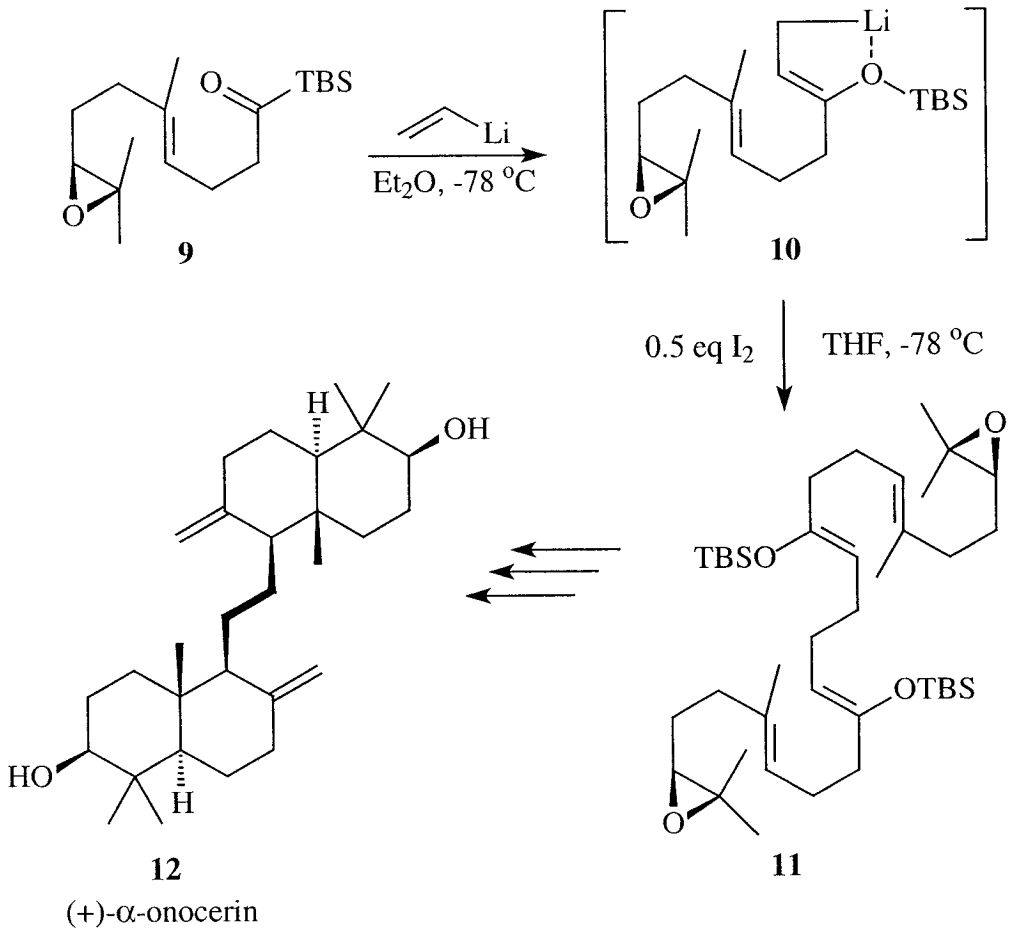

Scheme 1.3

One of the important properties of acylsilanes is that they can be converted to siloxycarbenes upon thermal or photochemical activation.[9-16] For example, Brook *et al.* have reported that photolysis of 2,2-dimethyl-2-silacyclohexanone (**13**) leads to formation of 3,3-dimethyl-3-sila-2-oxacycloheptylidene (**14**), which was trapped with acetaldehyde as oxirane **16** and as the ring-opened hydrolysis product **17** (cf. Scheme 1.4).[10] Duff and Brook were also able to generate a series of siloxycarbenes **19** by

photochemical activation of acylsilanes **18**, which were trapped with alcohols, acids and pyrrole (cf. Scheme 1.5).

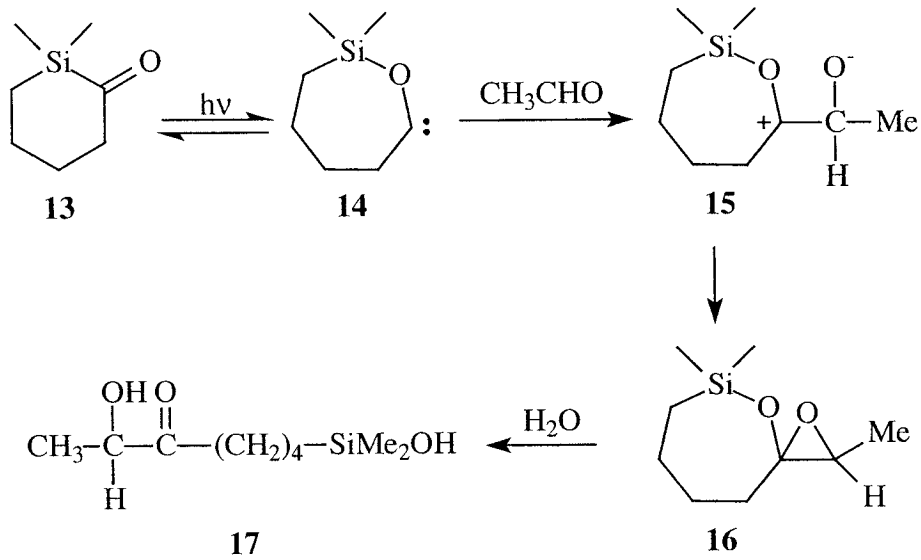

Scheme 1.4

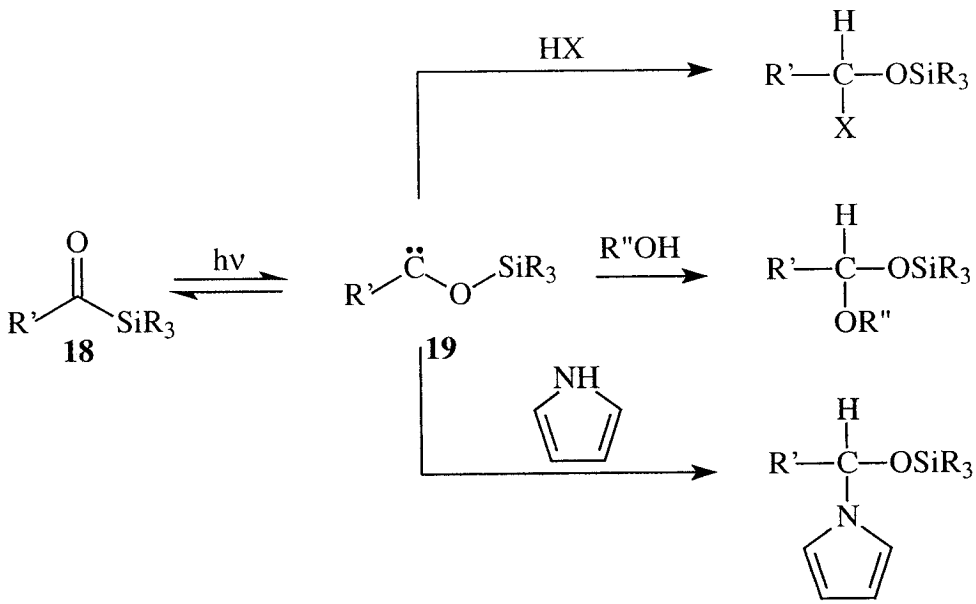

Scheme 1.5

Siloxycarbenes have also been implicated as intermediates in thermal and photochemical rearrangements of acylsilanes.[12-14,16,17] For example, Bassindale *et al.*[12] reported that the thermolysis of pivaloyltrimethylsilane (**20**) affords 2,2-dimethyl-cyclopropyloxytrimethylsilane (**22**), which has been attributed to C-H insertion in the intermediate *tert*-butyltrimethylsiloxycarbene (**21**) (cf. Scheme 1.6). As well, Hassner and Soderquist found that thermolysis of 2,2-dimethyl-2-silacyclopentanone (**23**) affords 4,4-dimethyl-4-sila-3-oxacyclohexene (**25**) and dimethylsilacyclobutane (**26**), as a result of 1,2-H migration and decarbonylation of 3,3-dimethyl-3-sila-2-oxacyclohexylidene (**24**) respectively (cf. Scheme 1.7).[14]

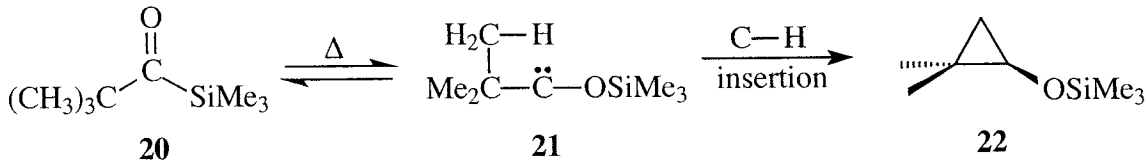

20 **21** **22**

Scheme 1.6

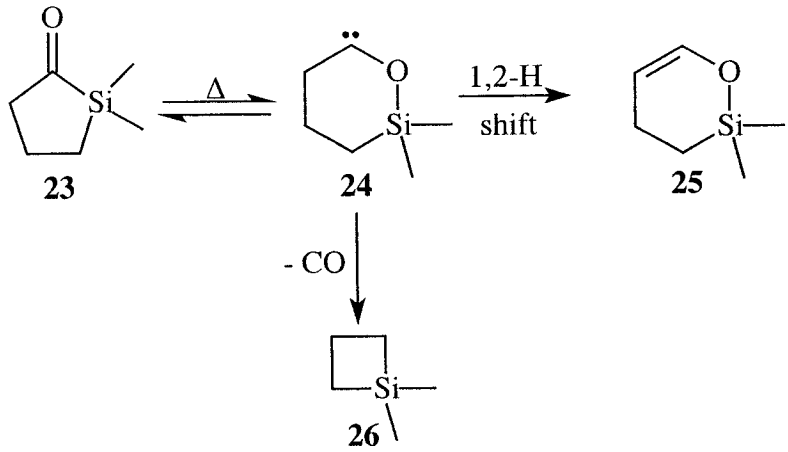

23 **24** **25** **26**

Scheme 1.7

Although siloxycarbenes are known to undergo a number of intramolecular rearrangements, essentially no attention has been paid to the mechanisms of these rearrangements. However, with the growing use of acylsilanes in organic synthesis, a knowledge and understanding of the reactivity and related properties of these species have become imperative. In this work, we attempt to shed some light onto the intramolecular reactivity of siloxycarbenes using ab initio molecular orbital theory and density-functional theory (DFT) calculations, together with the quantum theory of atoms in molecules (AIM),[18] the electron localization function (ELF),[19-23] and natural bond orbital (NBO) analysis.[24]

1.2 Carbenes

1.2.1 Electronic Structure

Carbenes are neutral reactive intermediates featuring a divalent carbon with two non-bonding electrons.[25-27] They exist in either a linear or bent geometry depending on the hybridization of the central carbene carbon (cf. Fig. 1.1). In the linear geometry, the carbene carbon is *sp*-hybridized and thus has two degenerate *p* orbitals, often denoted p_x and p_y. As a consequence, the two non-bonding electrons occupy separate *p* orbitals with parallel spin (Hund's rule) resulting in a ground-state triplet carbene. In the bent geometry, the carbene carbon is sp^2-hybridized. Apparently, bending causes the in-plane p_x orbital to acquire *s* character and thereby become stabilized, while the out-of-plane p_y orbital remains essentially unchanged.[25-27] This means that the degeneracy of the p_x and p_y orbitals is broken and the two "new" non-degenerate orbitals are referred to as σ and *p* respectively. Once the energy gap between the σ and *p* orbitals is large enough to overcome electron correlation energy (i.e. the energy required to bring the two electrons

together in the same orbital), the two electrons occupy the lower-lying σ orbital, consequently resulting in a ground-state singlet carbene.

All carbenes possess some degree of bending and so their frontier orbitals are almost always referred to as σ and ρ; the linear geometry does not actually exist.[27] This means that carbenes can have any of the four possible electronic configurations shown in Fig. 1.2. The two electrons can occupy the same orbital giving rise to the σ^2 ($^1A_1$ state) and p^2 ($^1B_1$ state) electronic configurations. On the other hand, the two electrons can occupy separate orbitals with anti-parallel spin ($^1B_1$ state) or parallel spin ($^3B_1$ state) resulting in the $\sigma^1 p^1$ electronic configuration.

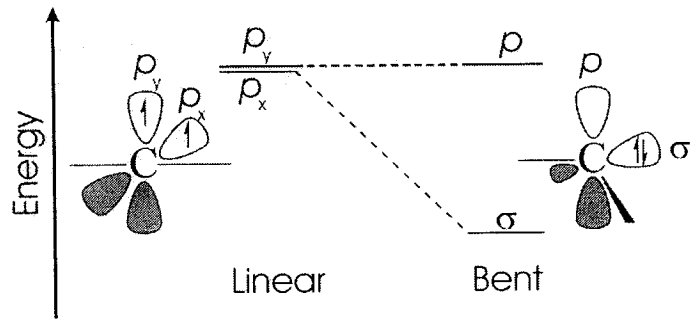

Figure 1.1 Effect of geometry on the frontier molecular orbitals and electronic structure of carbenes.

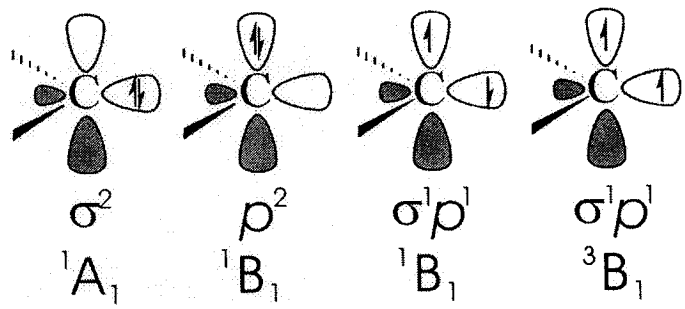

Figure 1.2 The four possible electronic configurations of carbenes.

1.2.2 Substituent Effects on Electronic Structure

Substituents can profoundly influence the ground-state spin multiplicity of carbenes and consequently dictate their reactivity.[26,27] Generally, singlet carbenes tend to be ambiphilic exhibiting both electrophilic and nucleophilic characteristics, whereas triplet carbenes tend to behave as biradicals. The influence of substituents on the ground-state spin multiplicity can be analyzed in terms of electronic and steric effects.

In terms of inductive effects, σ-electron-withdrawing substituents generally tend to favor the singlet ground-state electronic configuration whereas σ-electron-donating substituents seem to favor the triplet ground-state electronic configuration.[26,27] These effects can be understood by inspection of the orbital interaction diagrams shown in Figs. 1.3 and 1.4, assuming C_{2V} symmetry. As illustrated in Fig. 1.3, interaction between the orbitals of σ-electron-withdrawing substituents with the symmetry-adapted valence orbitals of the carbene carbon results in a large $\sigma \rightarrow p$ energy gap, which favors the singlet ground-state electronic configuration of the carbene. On the contrary, interaction between the orbitals of σ-electron-donating substituents and the symmetry-adapted valence orbitals of the carbene carbon results in a small $\sigma \rightarrow p$ energy gap, thus favoring the triplet ground-state electronic configuration (cf. Fig. 1.4). It is important to remember that σ-electron-withdrawing substituents generally tend to be more electronegative and thus have lower-energy orbitals than the carbene carbon, and vice versa for σ-electron-donating substituents.

The ground-state spin multiplicity of carbenes is even more profoundly influenced by resonance or mesomeric effects of substituents.[25-27] In the case of π-electron-donating substituents, the energy of the vacant carbene *p* orbital is raised by interaction with the

symmetric combination of the lone-pair orbitals (b_1) of substituents, while the energies of the σ orbital (a_1) of the carbene and the non-symmetric combination of the lone-pair orbitals (a_2) of substituents remain unchanged (cf. Fig. 1.5). This means that the $\sigma \rightarrow p$ energy gap increases, thus favoring the singlet state. On the other hand, in the case of π-electron-withdrawing substituents, the in-plane carbene σ orbital (a_1) is stabilized by interaction with the symmetric combination of the vacant orbitals (a_1) of the substituents, while the out-of-plane carbene *p* orbital remains unaffected (cf. Fig. 1.6). This results in an increase in the $\sigma \rightarrow p$ energy gap, which also favors the singlet state.

Steric effects can also dictate the ground-state spin multiplicity of carbenes, especially when electronic effects are negligible.[27] As mentioned earlier, singlet carbenes usually have a bent geometry whereas triplet carbenes often exist in a linear geometry. Thus, bulky substituents, which tend to minimize the extent of bending, generally seem to favor the triplet state, whereas smaller substituents, which can allow a considerable degree of bending, tend to favor the singlet state.

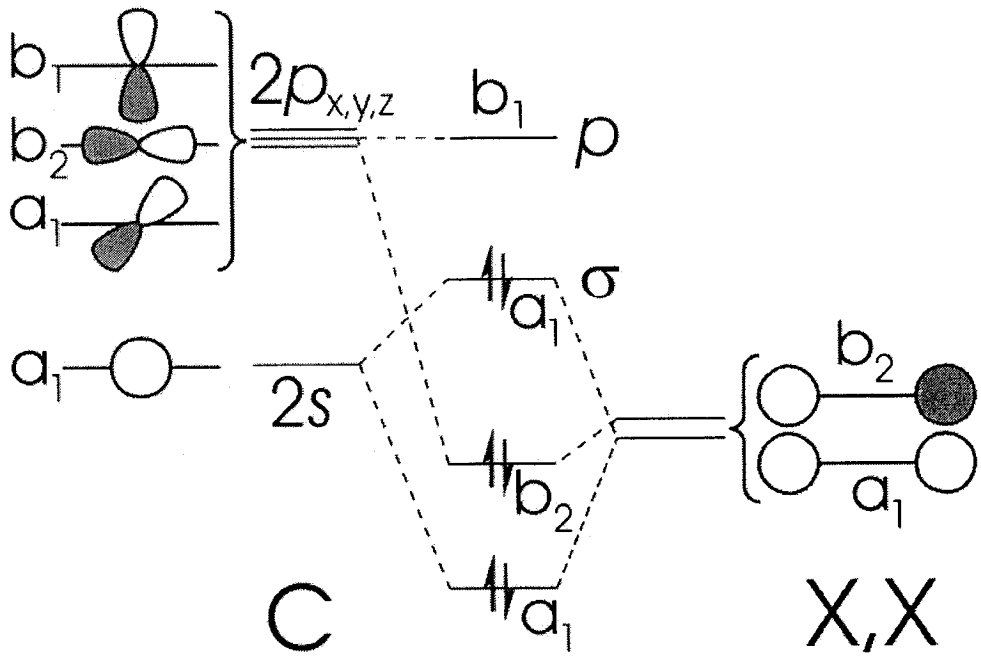

Figure 1.3 Orbital interaction diagram showing the effect of σ-electron-withdrawing substituents on the ground-state electronic structure of carbenes.

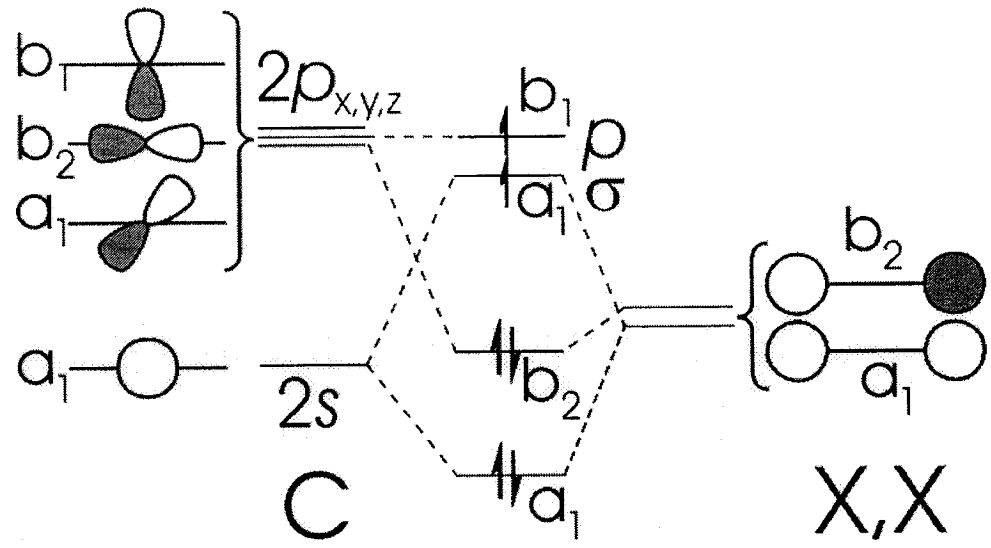

Figure 1.4 Orbital interaction diagram showing the effect of σ-electron-donating substituents on the ground-state electron configuration of carbenes.

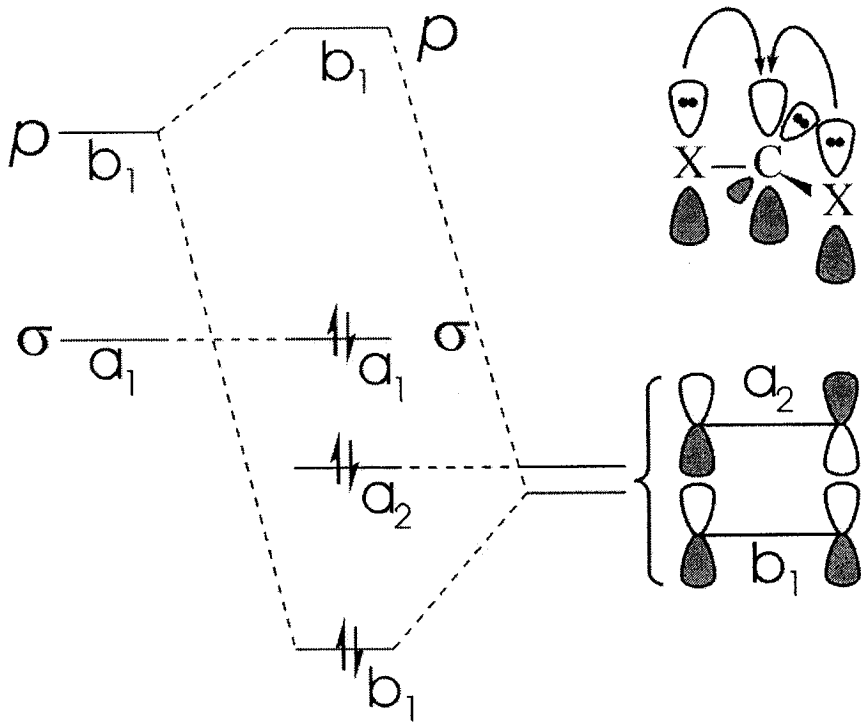

Figure 1.5 Orbital interaction diagram showing the effects of π-electron-donating substituents on ground-state electronic structure of carbenes.

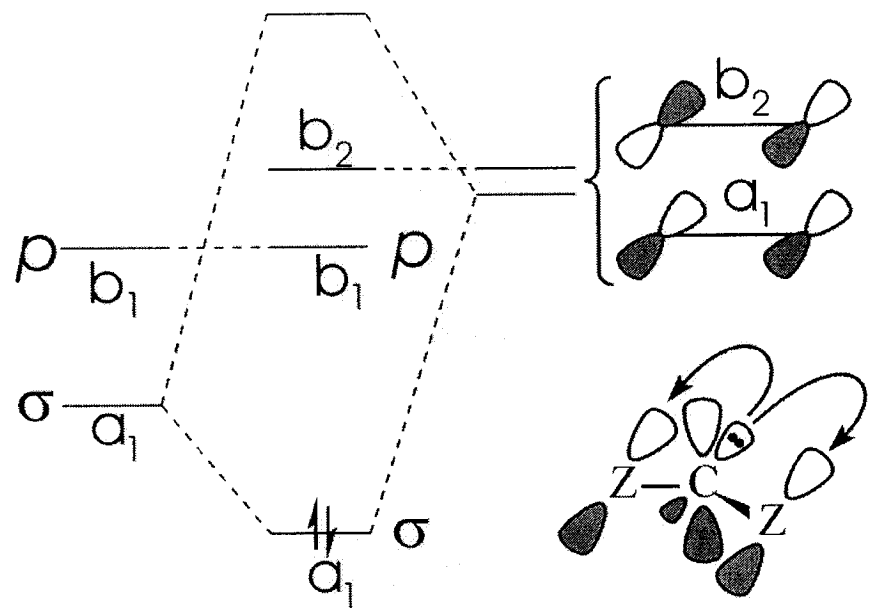

Figure 1.6 Orbital interaction diagram showing the effects of π-electron-withdrawing substituents on ground-state electronic configuration of carbenes.

1.3 Brief Survey of Pertinent Singlet Carbene Rearrangements

1.3.1 Rearrangements of Alkylcarbenes

The most common intramolecular rearrangement of singlet alkylcarbenes is the 1,2-H shift.[28-30] Experimental[28-36] and theoretical evidence[37-44] indicate that this rearrangement involves a hydride-like shift from the migration origin to the vacant carbene *p* orbital (cf. Scheme 1.8). For example, La Villa and Goodman[32] and Bonneau *et al.*[33] have reported that 1,2-H shifts in singlet alkylchlorocarbenes are accelerated by alkyl substitution at the migration origin, while Moss *et al.*[34] have found that various electron-donating substituents at the migration origin had the same effect. Similarly, Liu and Bonneau[35] and Su and Thornton[31] have observed that electron-donating substituents accelerate 1,2-H shifts in *p*-substituted benzylchlorocarbenes and benzylmethylcarbenes respectively. These findings are consistent with hydride-like shifts from the migration origin to the vacant carbene *p* orbital, where the positive charge developing at the migration origin is stabilized by electron-donating substituents. In fact, Liu and Bonneau[35] and Su and Thornton,[31] obtained Hammett ρ values of close to -1, in concordance with positive charge development at the migration origin. These findings are supported by density-functional theory (DFT) calculations, which have revealed that electron-donating substituents at the migration origin lower the activation barrier for 1,2-H migration.[43]

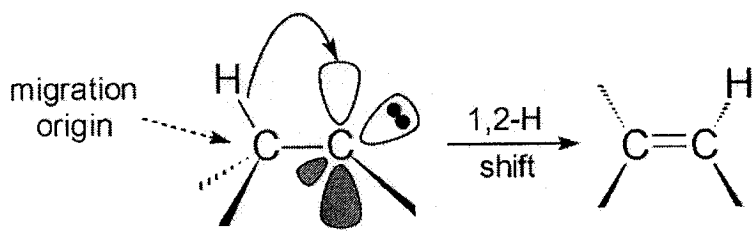

Scheme 1.8

Contrarily, electron-donating substituents attached to the carbene carbon tend to decelerate 1,2-H shifts in singlet alkylcarbenes. For example, Moss *et al.* found that 1,2-H shifts in alkylfluorocarbenes are slower than they are in alkylbromocarbenes,[34] while La Villa and Goodman found that the 1,2-H shift in methylchlorocarbene is slower than that in methylbromocarbene.[45] As well, ab initio calculations indicate that the presence of electron-donating substituents at the carbene carbon raises the barrier for 1,2-H migration.[37,38] These observations seem to suggest that the increase in negative charge density at the carbene carbon that arises from the presence of electron-donating substituents enhances somewhat repulsion of the approaching hydride-like species, consequently destabilizing the transition state and raising the barrier for 1,2-H migration. Alternatively, the increase in the activation barrier for 1,2-H migration could arise from considerable stabilization of the carbene relative to the transition state.

Singlet alkylcarbenes are also known to undergo 1,2-migrations involving other species such as alkyl,[28,34,44,46-48] phenyl,[28,36,49] silyl,[50,51] and halo[28,36,52] groups. For example, cyclopropylhalocarbenes have been found to undergo ring expansion (i.e. 1,2-alkyl shifts) to the corresponding cyclobutenes.[33,34,46-48] Similarly, dimethylbenzylchlorocarbene has been reported to undergo a 1,2-phenyl shift,[49] while methylchlorobenzylchlorocarbene[28] and dichlorobenzylchlorocarbene[52] have been found to undergo 1,2-chloro shifts. There have also been reports of 1,3-migrations in singlet alkylcarbenes including 1,3-H, 1,3-alkyl and 1,3-silyl migrations. For example, bicyclo [2.2.1] heptylidene has been reported to undergo 1,3-H migration yielding tricyclo [2.2.1.0] heptane,[53,54] while *endo*-6-trimethylsilylbicyclo [2.2.1] heptylidene and *syn*-6-trimethylsilyl bicyclo [2.2.2] octylidene have been found to rearrange by 1,3-silyl

migration to give the corresponding tricyclo [2.2.1.0] heptyl- and tricyclo [2.2.2.0] octyl-silane products respectively.[55] The mechanisms for these rearrangements are all believed to involve anion-like shifts from the migration origin to the vacant carbene *p* orbital.

1.3.2 Rearrangements of Oxy- and Dioxycarbenes

Oxy- and dioxycarbenes preferentially undergo intermolecular reactions with species such as electron-deficient alkenes,[56] alkynes,[57] and alcohols,[56,58,59] in solution rather than intramolecular rearrangements. Moreover, in the absence of carbene scavengers they tend to undergo dimerization instead of intramolecular rearrangements.[56,58,60] Nevertheless, there have been reports of a few oxy- and dioxycarbenes rearrangements. Some of these rearrangements are described briefly below.

Moss *et al.* found that phenylacyloxycarbenes rearrange by 1,2-acyl migrations affording 1,2-diketone products (cf. Scheme 1.9).[61] They provided both experimental and theoretical evidence showing that this rearrangement occurs via nucleophilic attack by the carbene lone pair at the acyl carbon. On the other hand, Venneri and Warkentin reported that methoxyallyloxycarbenes undergo 1,2-allyl migrations yielding the respective product esters (cf. Scheme 1.10).[62] They demonstrated that these rearrangements involve initial fragmentation of the dioxycarbene to methoxycarbonyl and allyl radicals which subsequently recombine to form the appropriate esters. These findings are also supported by ab initio and density-functional theory studies of methoxyallyloxycarbene rearrangements, which confirm that the fragmentation-recombination mechanism involving radicals is energetically viable.[63] There is also evidence that 1,2-benzyl migrations in *p*-substituted benzyloxymethoxycarbenes[64] and

benzyloxybenzyloxycarbenes[65] occur via a similar fragmentation-recombination mechanism involving radicals, while the ring contraction of cyclic oxy- and dioxycarbenes, which involves 1,2-alkyl migration from oxygen to the carbene carbon, occurs via a fragmentation-recombination mechanism involving singlet acyl-alkyl biradicals.[66-71]

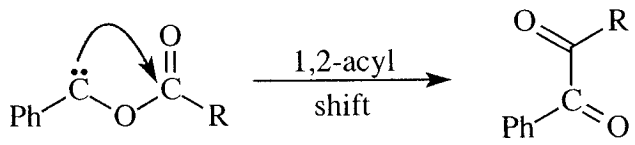

Scheme 1.9

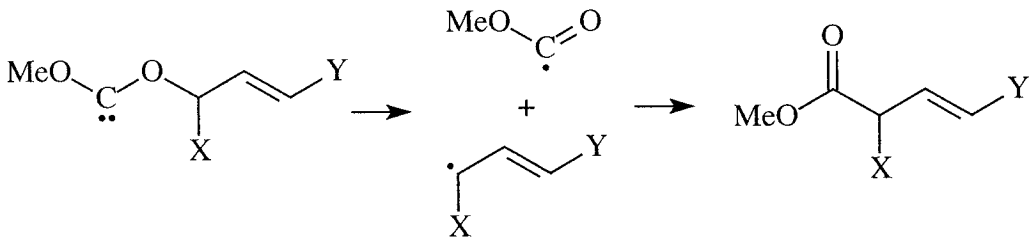

X = Ph, Y = H and X = H, Y = Ph

Scheme 1.10

Moss *et al.* have carried out a number of studies on the decarbonylation of alkoxyhalocarbenes, which afford alkyl halides.[72-81] They proposed that the mechanism for this reaction involves initial fragmentation of the alkoxyhalocarbenes to tight ion-pair intermediates comprising carbon monoxide sandwiched between a halide ion and a carbocation, followed by ion-pair collapse to form alkyl halides (cf. Scheme 1.11). Likhotvorik *et al.*[82] have also investigated the decarbonylation of alkoxyhalocarbenes and have proposed that reaction occurs via internal nucleophilic substitution which involves a tight ion-pair intermediate slightly different from that proposed by Moss *et al.* There is also evidence that a bimolecular nucleophilic substitution (S_N2) mechanism plays a minor

role in the decarbonylation of alkoxyhalocarbenes, where there is backside attack by free halide ion at the alkyl moiety of either the ion-pair intermediate or the alkoxyhalocarbene.[78,80-83] On the other hand, Crawford and Raap reported that diethoxycarbene undergoes decarbonylation resulting in diethyl ether. They suggested that the process occurs via a fragmentation-recombination mechanism involving radicals as shown in Scheme 1.12.[84] Similarly, McDonald and Krueger found evidence indicating that methoxycarbene undergoes decarbonylation via a fragmentation-recombination mechanisms involving radicals.[85] In addition, there is evidence that the decarbonylation of cyclic oxy- and dioxycarbenes involve the intermediacy of singlet biradicals.[66-71]

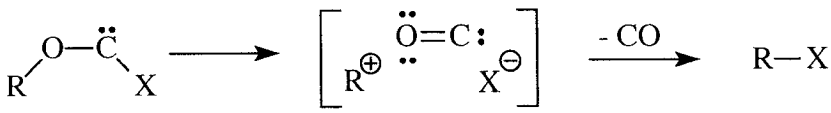

R = alkyl, X = halide

Scheme 1.11

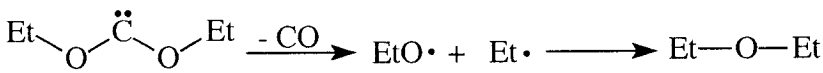

Scheme 1.12

1.4 Objectives and Outline

As implied in Section 1.1, the main objective of this work is to provide insight into the mechanisms of intramolecular rearrangements of siloxycarbenes using ab initio molecular orbital theory and density functional theory calculations, combined with the quantum theory of atoms in molecules, the electron localization function and natural bond orbital analysis. In this thesis, a detailed investigation of the mechanisms of intramolecular rearrangements of methoxy(siloxy)carbene is first described. The effects of substituents and the role of hyperconjugation in siloxycarbene rearrangements are then assessed. Finally, the mechanisms of intramolecular rearrangements of 3-sila-2-oxacyclohexylidene, a cyclic siloxycarbene, are examined.

Chapter 2.
Intramolecular Rearrangements of Methoxy(siloxy)carbene

2.1 Introduction

It has been reported that methoxytriphenylsiloxycarbene (**II**), generated by thermolysis of 2-methoxy-2-triphenylsiloxy-5,5-dimethyl-Δ^3-1,3,4-oxadiazoline (**I**), undergoes 1,2-triphenylsilyl migration and decarbonylation yielding methyl triphenylsilylformate (**III**) and methyl triphenylsilyl ether (**IV**), respectively (cf. Scheme 2.1).[86] The rate constant for thermal decomposition of oxadiazoline **I** at 110 °C was determined to be 8.1×10^{-5} s^{-1} in benzene and 6.1×10^{-5} s^{-1} in methanol, and the ratio of ester **III** to ether **IV** in benzene was found to be 1:3. Thermolysis of oxadiazoline **I** in toluene did not produce any bibenzyl and in the presence of TEMPO (2,2,6,6-tetramethylpiperidinyloxy radical), no products of radical trapping were evident. In methanol-d_4, thermolysis of **I** resulted in a small amount of carbene **II** being trapped as the deuterated orthoformate **V** (~8%), along with ester **III** and ether **IV** (unlabelled) as co-products (cf. Scheme 2.2).

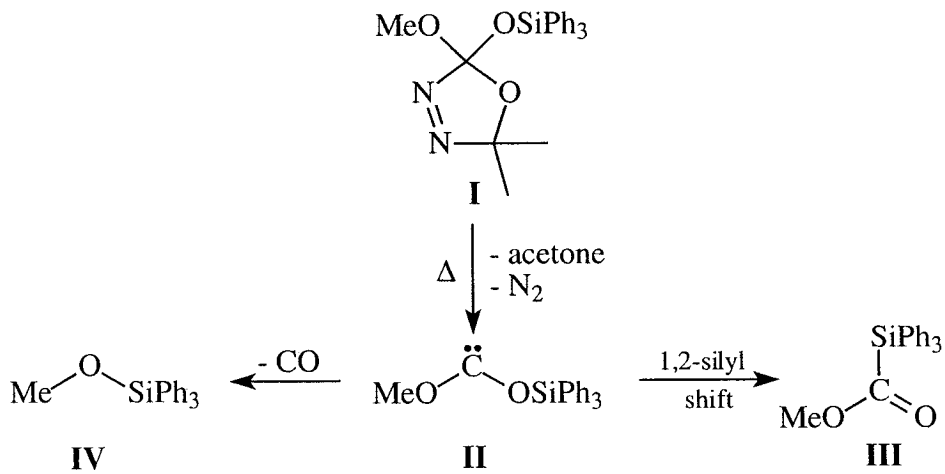

Scheme 2.1

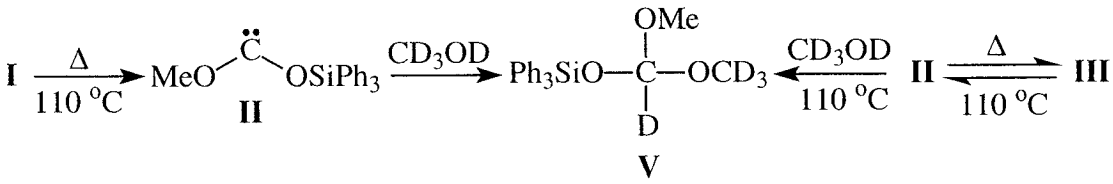

Scheme 2.2

Thermolysis of ester **III** also resulted in the formation of ether **IV**,[86] a reaction previously reported by Brook *et al.*[87] The overall rate constant at 110 °C was determined to be 6.5×10^{-6} s^{-1} in benzene and 8.2×10^{-4} s^{-1} in methanol.[86] It was also found that when ester **III** was heated in methanol-d_4, a small amount of carbene **II** was trapped as deuterated orthoformate **V** (cf. Scheme 2.2).

Although the above experimental findings do provide insight into the mechanisms of 1,2-triphenylsilyl migration and decarbonylation of carbene **II**, many questions remain unanswered. Let us first consider the possible mechanisms for 1,2-triphenylsilyl migration from oxygen to the carbene carbon. A fragmentation-recombination mechanism involving methoxycarbonyl and triphenylsilyl radicals similar to that established for 1,2-alkyl migrations in dialkoxycarbenes[62-65] is unlikely, since no bibenzyl nor products of radical trapping were detected when thermolysis of **I** was carried out in toluene and in the presence of TEMPO.[86] However, the mechanism could involve an anion-like shift of the triphenylsilyl group from oxygen to the "vacant" carbene *p* orbital (cf. Scheme 2.3a) similar to that established for 1,2-migrations in singlet alkylcarbenes.[28-30] As a matter of fact, Suh *et al.* found evidence suggesting that gas phase 1,2-alkyl migrations from oxygen to the carbene carbon in dialkoxycarbenes involve anion-like shifts from oxygen to the "vacant" carbene *p* orbital.[88] It is also possible that the mechanism for 1,2-triphenylsilyl migration involves nucleophilic attack by the carbene

lone pair at the triphenylsilyl moiety (cf. Scheme 2.3b) reminiscent of the unique mechanism proposed by Moss *et al.* for 1,2-acyl migrations in phenylacyloxycarbenes.[61] We note that the mechanism involving an anion-like shift of the triphenylsilyl group from oxygen to the carbene carbon is *symmetry-allowed* according to Woodward-Hoffmann rules,[89-93] since overlap between the $\sigma_{O\text{-}Si}$ orbital (HOMO) and the "vacant" carbene *p* orbital (LUMO) results in a favorable bonding interaction (cf. Scheme 2.3a). On the contrary, the mechanism involving front-side nucleophilic attack by the carbene lone pair at silicon is *symmetry-forbidden*,[89-93] since interaction between the carbene lone-pair n_C orbital (HOMO) and the anti-bonding $\sigma^*_{O\text{-}Si}$ orbital (LUMO) contains an unfavorable destabilizing anti-bonding component (cf. Scheme 2.3b).

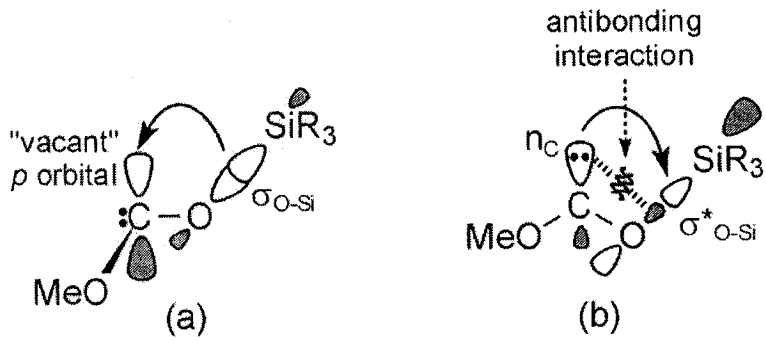

Scheme 2.3

Let us now consider the possible mechanisms for decarbonylation of carbene **II**. A fragmentation-recombination mechanism involving carbon monoxide along with either the methoxy and triphenylsilyl radicals or the methyl and triphenylsilyloxy radicals, similar to that proposed for decarbonylation of methoxycarbene[85] and diethoxycarbene[84] (cf. Scheme 1.12) is conceivable. However, since no products of radical trapping were evident when thermolysis of **I** was carried out in toluene and in the presence of TEMPO,[86] this mechanisms seems unlikely. It is also conceivable that an S_N2 reaction

involving nucleophilic attack by methanol at the triphenylsilyl moiety contributes to the decarbonylation process. In fact, decarbonylation of alkoxychlorocarbenes is thought to occur to some degree via a similar S_N2 reaction involving back-side nucleophilic attack by free chloride ions at the alkyl moiety.[78,80-83] However, since the ether **IV** produced when thermolysis of oxadiazoline **I** was carried out in methanol-d_4 was unlabelled,[86] this mechanistic pathway also seems unlikely. Thus, the mechanism for decarbonylation of carbene **II** most likely involves intramolecular front-side nucleophilic attack by either the methoxy oxygen at silicon or the siloxy oxygen at the methyl carbon. Moreover, this process could be concerted or stepwise, similar to that discussed by Schreiner *et al.* for decomposition of alkylchlorosulfites.[94,95]

Decarbonylation of carbene **II** via the concerted pathway involving front-side nucleophilic attack by either the methoxy oxygen at silicon or the siloxy oxygen at the methyl carbon would be a one-step process that occurs via a cyclic transition state, as shown in Scheme 2.4a. However, it is evident from the sketch of the frontier orbitals shown in Scheme 2.5a that this mechanism is *symmetry-forbidden* according to Woodward-Hoffmann rules,[89-93] since interaction between the in-plane "sp^2 hybridized" lone-pair n_O orbital[1] (HOMO) and the anti-bonding $\sigma^*_{O\text{-}R'}$ orbital (LUMO) contains a destabilizing anti-bonding component. On the other hand, a stepwise mechanism involving front-side nucleophilic attack by either the methoxy oxygen at silicon or the siloxy oxygen at the methyl carbon would occur via an ion-pair intermediate. The ion-pair intermediate could comprise either the methoxycarbonyl anion and the triphenylsilyl cation or the triphenylsiloxycarbonyl anion and the methyl cation, as shown in Scheme

[1] Assuming the second oxygen lone pair has considerable *p* character and is involved in π-back bonding with the vacant carbene *p* orbital.

2.4b. Moreover, formation of such an ion-pair intermediate would result in a *symmetry-allowed* reaction since it allows favorable bonding interaction between the in-plane "sp^2 hybridized" lone-pair n_O orbital (HOMO) and the vacant cation *p* orbital (LUMO) as illustrated in Scheme 2.5b. Alternatively, the ion-pair intermediate could consist of carbon monoxide sandwiched between either the methoxide ion and the triphenylsilyl cation or the triphenylsiloxide anion and the methyl cation (cf. Scheme 2.4c) similar to that proposed by Moss *et al.* for alkoxyhalocarbene decarbonylation.[72-76,78-80,83,96]

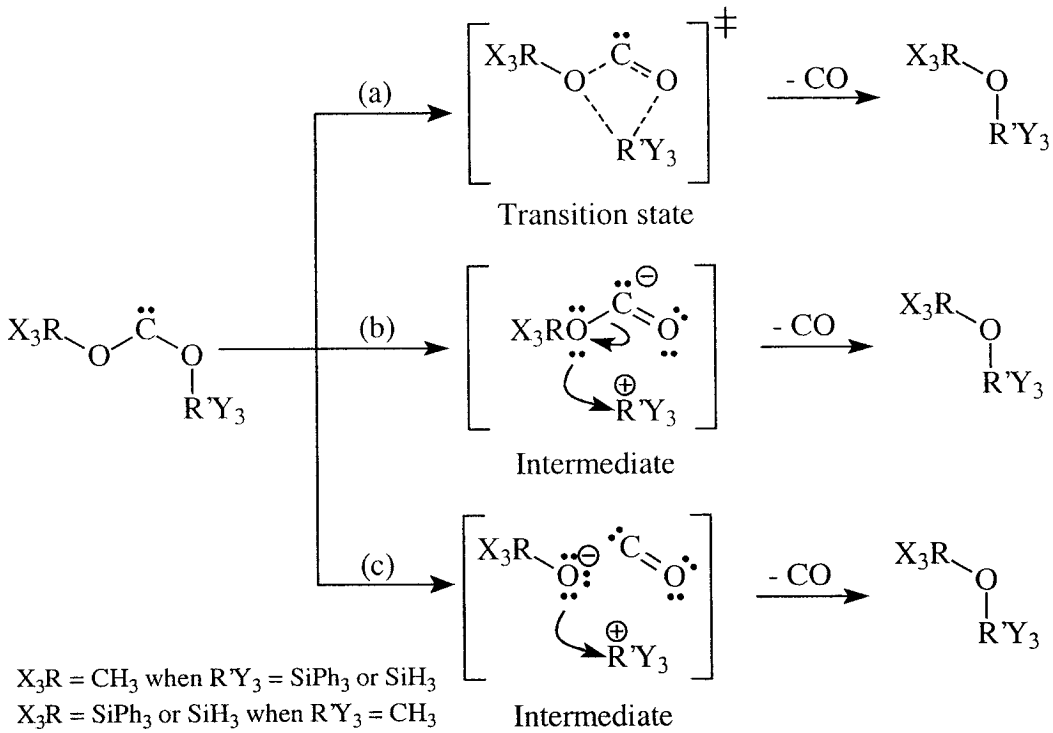

Scheme 2.4

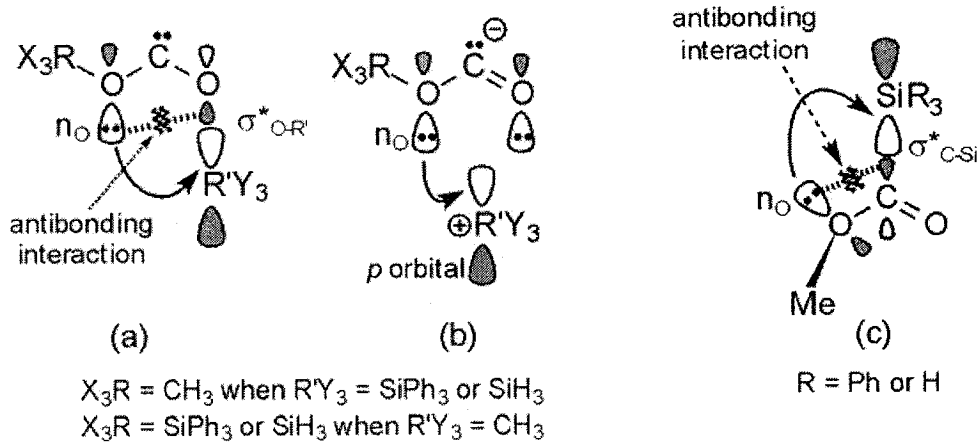

Scheme 2.5

It is also possible for decarbonylation of carbene **II** to occur via a pathway involving initial 1,2-triphenylsilyl migration to yield ester **III**, followed by a Brook rearrangement to afford ether **IV** (cf. Scheme 2.6), since ester **III** is known to undergo decarbonylation when heated.[6,86,87] However, the rate constant for decarbonylation of ester **III** in benzene is smaller than the overall rate constant for thermal decomposition of oxadiazoline **I**,[86] which means that decarbonylation of carbene **II** involving intermediate formation of ester **III** is unlikely. We note that a concerted mechanism for decarbonylation of ester **III** involving front-side nucleophilic attack by the methoxy oxygen at silicon is *symmetry-forbidden*, as evident from the sketch of the frontier orbitals in Scheme 2.5c.

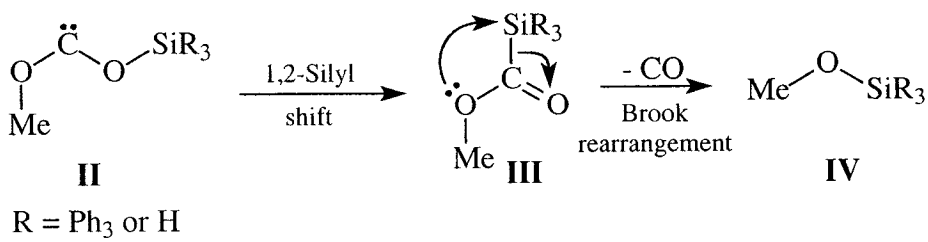

Scheme 2.6

In this chapter, we will discuss results from our investigation of the mechanisms of 1,2-silyl migration and decarbonylation in methoxy(siloxy)carbene as a model system for carbene **II**.[86,97-99] As well, we will consider the mechanism of 1,2-methyl migration for comparative purposes. As shown in Scheme 2.7, 1,2-silyl migration, 1,2-methyl migration and decarbonylation afford methyl silylformate, silyl acetate and methyl silyl ether respectively.

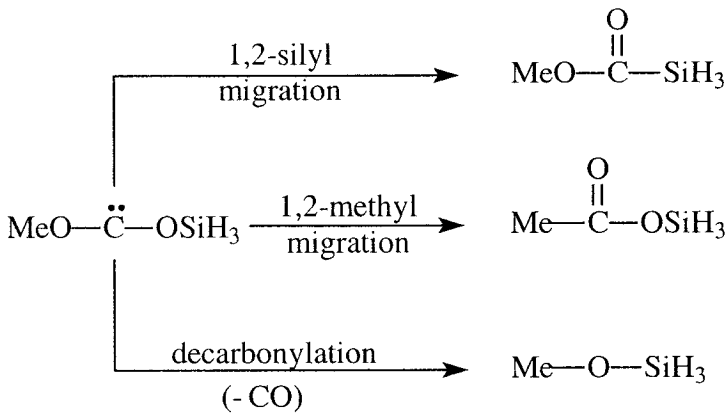

Scheme 2.7

2.2 Computational Methods

Standard ab initio molecular orbital calculations at the Hartree-Fock (HF) and second-order Møller-Plesset (MP2) levels of theory,[100,101] and hybrid density-functional theory calculations using the Becke three-parameter hybrid functional[101,102] with the Lee-Yang-Parr correlation potential[101,103] (B3LYP), were performed with the 6-311+G(2d,p) basis set.[100,101] MP2 and B3LYP calculations with medium to large-size basis sets have been found to provide reasonable geometries and reaction energetics for a number of carbene systems.[26,39,40] The 6-311+G(2d,p) basis set was chosen after performing preliminary calculations with the 6-31+G(d), 6-311+G(2d,p) and 6-311++G(2df,pd) basis sets. It was found to be the best compromise between accuracy and performance.

Calculations were performed on the closed-shell singlet (S_0) state of methoxy(siloxy)carbene since oxy- and dioxycarbenes are known to have large $S_0 \rightarrow T_1$ and $S_0 \rightarrow S_1$ energy gaps.[56,104,105] For example, the lowest triplet states of *trans-trans* and *cis-trans* dimethoxycarbene are 76.3 and 76.7 kcal/mol above their respective singlet (S_0) states based on MP2/6-31G*//HF/6-31G* calculations.[56] Moreover, computed (CIS)INDO/S//HF/6-31G* vertical $S_0 \rightarrow S_1$ energy gaps for *trans-trans* and *cis-trans* dimethoxycarbene are 104 and 109 kcal/mol, respectively.[56] In addition, vertical $S_0 \rightarrow T_1$ gaps for dihydroxycarbene, calculated at various levels of theory, lie in the range 43.4 to 66.3 kcal/mol, while the lowest energy triplet carbene is 26.4 to 50.0 kcal/mol above the lowest energy singlet carbene.[104]

Ground-state minimum-energy structures were optimized using the Berny algorithm,[106] while transition-state optimizations were performed with the eigenvector following method.[107-109] These calculations were carried out with the Gaussian 98 suite of programs.[110] Frequency calculations were performed for stationary-point characterization and to obtain thermochemical data within the rigid rotor-harmonic oscillator approximation using standard statistical mechanical method methods implemented in Gaussian 98.[111] Intrinsic reaction coordinate (IRC) calculations were also performed to confirm the identity of the transition states. The quantum theory of atoms in molecules[18] (AIM) and the electron-localization function[19-23] (ELF) were used to probe electronic structures of the optimized geometries. AIM and ELF analyses were performed with the AIMPAC series of programs[18,112,113] and TopMod package, respectively.[114] ELF isosurfaces were plotted with the SciAn program[115] using an ELF isovalue of 0.85. The ab initio and DFT methods used, as well as AIM and ELF, are described in Appendix A.

2.3 Results and Discussion

2.3.1 Ground-State Conformers of Methoxy(siloxy)carbene

Optimized geometries for the ground-state conformers of methoxy(siloxy)carbene are shown in Fig. 2.1. They are the *trans-trans* **A**, *cis-trans* **B** and the *trans-cis* **C** conformers. Calculated geometries of the transition-states for *trans-trans* to *cis-trans* isomerization $\mathbf{TS_{AB}}$ and *trans-trans* to *trans-cis* isomerization $\mathbf{TS_{AC}}$ are also shown in Fig. 2.1. We note that the computed CIS/6-31+G*//MP2/6-31+G* vertical $S_0 \rightarrow T_1$ gaps for conformers **A**, **B** and **C** of methoxy(siloxy)carbene are 57.8, 56.8, and 55.1 kcal/mol, while the $S_0 \rightarrow S_1$ gaps are 116.0, 118.1 and 118.4 kcal/mol. In addition, UMP2/6-31+G* optimizations of triplet methoxy(siloxy)carbene afforded two conformers that were 55.2 and 55.8 kcal/mol above the lowest-energy singlet (S_0) ground-state carbene conformer **A.**

Table 2.1 contains topological properties of the electronic density $\rho(r)$ at selected bond critical points[116] (BCPs) for conformers **A**, **B** and **C** of methoxy(siloxy)carbene. It is apparent that values of the BCP electronic densities $\rho_b(r)$ for the O2-C6 and C6-O7 bonds are larger than those for the C1-O2 bond. These observations suggest that the O2-C6 and C6-O7 bonds have some double-bond character. Moreover, values of the bond ellipticity, ε,[117] for the O2-C6 and C6-O7 bonds are noticeably larger than zero, indicative of the elliptical symmetry of the BCP charge density usually associated with double bonds.[18] Furthermore, gradient vector analysis of the Laplacian of the electronic density, $\nabla^2\rho(r)$,[118] revealed that the valence-shell charge concentration[119] (VSCC) of the O2, C6 and O7 atoms each contain one non-bonded maximum. Since there is usually a one-to-one mapping between local maxima in the VSCC of an atom and electron pairs of

the Lewis model,[18] these findings suggest that the O2, C6, and O7 atoms each possess one lone pair. Apparently, the additional lone pair expected on the O2 and O7 atoms is involved in π-back bonding with the vacant carbene *p* orbital, which gives rise to partial O2-C6 and C6-O7 double-bond character.

ELF isosurfaces for conformers **A**, **B** and **C** of methoxy(siloxy)carbene are shown in Fig. 2.2 and corresponding ELF basin properties are given in Table 2.2. The V(C6) *monosynaptic* (lone-pair) valence basin corresponds to the carbene lone pair while the V(O2) and V(O7) lone-pair valence basins each represents two lone pairs on the O2 and O7 atoms. The V(C1,O2), V(O2,C6), V(C6,O7) and V(O7,Si) *disynaptic* (bonding) valence basins represent the C1-O2, O2-C6, C6-O7 and O7-Si bonds. We note that the V(C1,O2), V(O2,C6) and V(C6,O7) basin populations are all less than 2.0, which is most likely due to significant basin population delocalization, as evident from the fairly large relative fluctuation values $\lambda(\Omega_i)$. From the %cross-exchange contribution data, it is apparent that delocalization of the V(C1,O2) and V(O2,C6) basin populations primarily involve the V(O2) lone-pair valence basin, while V(C6,O7) basin population delocalization mainly involves the V(O7) lone-pair valence basin. We also note that the V(O2,C6) and V(C6,O7) basin populations are larger than the V(C1,O2) basin population. Therefore, if the V(C1,O2) basin population is representative of a standard C-O single bond, then the larger V(O2,C6) and V(C6,O7) basin populations indicate that both the O2-C6 and C6-O7 bonds do indeed have some double-bond character, in agreement with the above AIM findings.

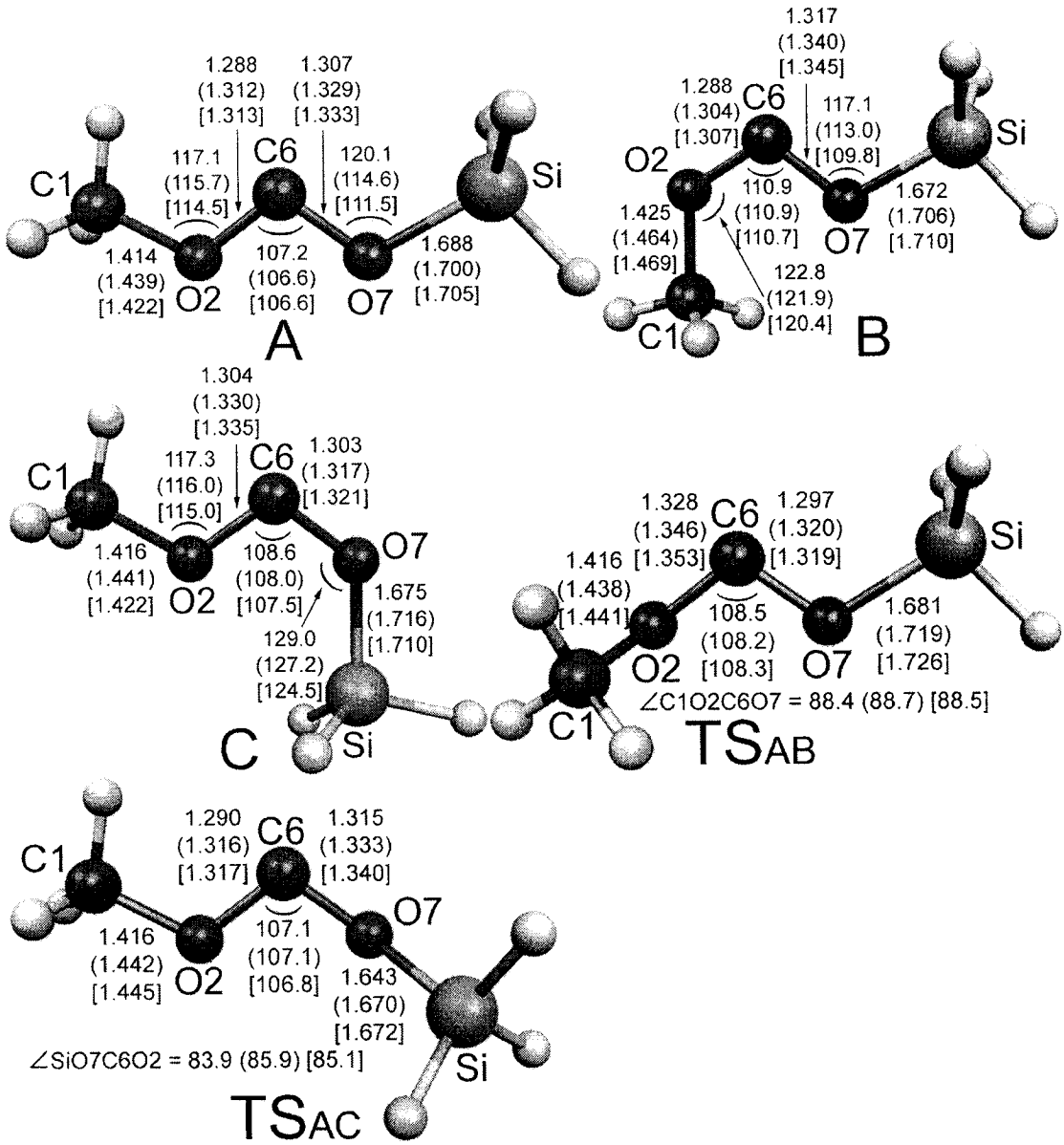

Figure 2.1 Optimized molecular geometries of the ground-state conformers of methoxy(siloxy)carbene and the transition states for conformational isomerization. Geometric parameters are given for the HF/6-311+G(2d,p), B3LYP/6-311+G(2d,p) (parentheses) and MP2/6-311+G(2d,p) [brackets] model chemistries. Bond distances and angles are in Å and degrees, respectively.

Table 2.1 Topological properties of the electronic density $\rho(r)$ at pertinent BCPs of the methoxy(siloxy)carbene conformers.[a]

	C1-O2	O2-C6	C6-O7	O7-Si
		A		
		HF/6-311+G(2d,p)		
$\rho_b(r)$ (e/Å^3)	1.68	2.30	2.19	0.89
$\nabla^2\rho_b(r)$ (e/Å^5)	-4.5	-5.4	-7.7	18.9
ε	0.01	0.21	0.28	0.05
		B3LYP/6-311+G(2d,p)		
$\rho_b(r)$ (e/Å^3)	1.62	2.19	2.11	0.84
$\nabla^2\rho_b(r)$ (e/Å^5)	-12.3	-13.2	-15.5	14.6
ε	0.01	0.13	0.17	0.05
		MP2/6-311+G(2d,p)		
$\rho_b(r)$ (e/Å^3)	1.60	2.15	2.07	0.81
$\nabla^2\rho_b(r)$ (e/Å^5)	-11.7	-10.7	-13.7	15.1
ε	0.00	0.13	0.17	0.05
		B		
		HF/6-311+G(2d,p)		
$\rho_b(r)$ (e/Å^3)	1.64	2.28	2.13	0.87
$\nabla^2\rho_b(r)$ (e/Å^5)	-6.6	-5.6	-6.7	18.6
ε	0.01	0.20	0.32	0.05
		B3LYP/6-311+G(2d,p)		
$\rho_b(r)$ (e/Å^3)	1.55	2.22	2.05	0.83
$\nabla^2\rho_b(r)$ (e/Å^5)	-11.9	-12.5	-15.0	14.3
ε	0.00	0.11	0.20	0.05
		MP2/6-311+G(2d,p)		
$\rho_b(r)$ (e/Å^3)	1.55	2.16	2.00	0.80
$\nabla^2\rho_b(r)$ (e/Å^5)	-12.3	-10.2	-13.3	14.7
ε	0.01	0.11	0.20	0.05
		C		
		HF/6-311+G(2d,p)		
$\rho_b(r)$ (e/Å^3)	1.66	2.19	2.19	0.86
$\nabla^2\rho_b(r)$ (e/Å^5)	-3.9	-5.0	-7.0	17.9
ε	0.01	0.26	0.27	0.03
		B3LYP/6-311+G(2d,p)		
$\rho_b(r)$ (e/Å^3)	1.61	2.09	2.14	0.80
$\nabla^2\rho_b(r)$ (e/Å^5)	-12.0	-13.3	-13.9	13.2
ε	0.00	0.17	0.16	0.02

(continues on next page)

Table 2.1 (Continued)

	C1-O2	O2-C6	C6-O7	O7-Si
		C		
		MP2/6-311+G(2d,p)		
$\rho_b(r)$ (e/Å^3)	1.59	2.04	2.09	0.78
$\nabla^2\rho_b(r)$ (e/Å^5)	-11.4	-11.4	-12.3	14.0
ε	0.00	0.17	0.16	0.02

[a] Obtained from AIM analysis.

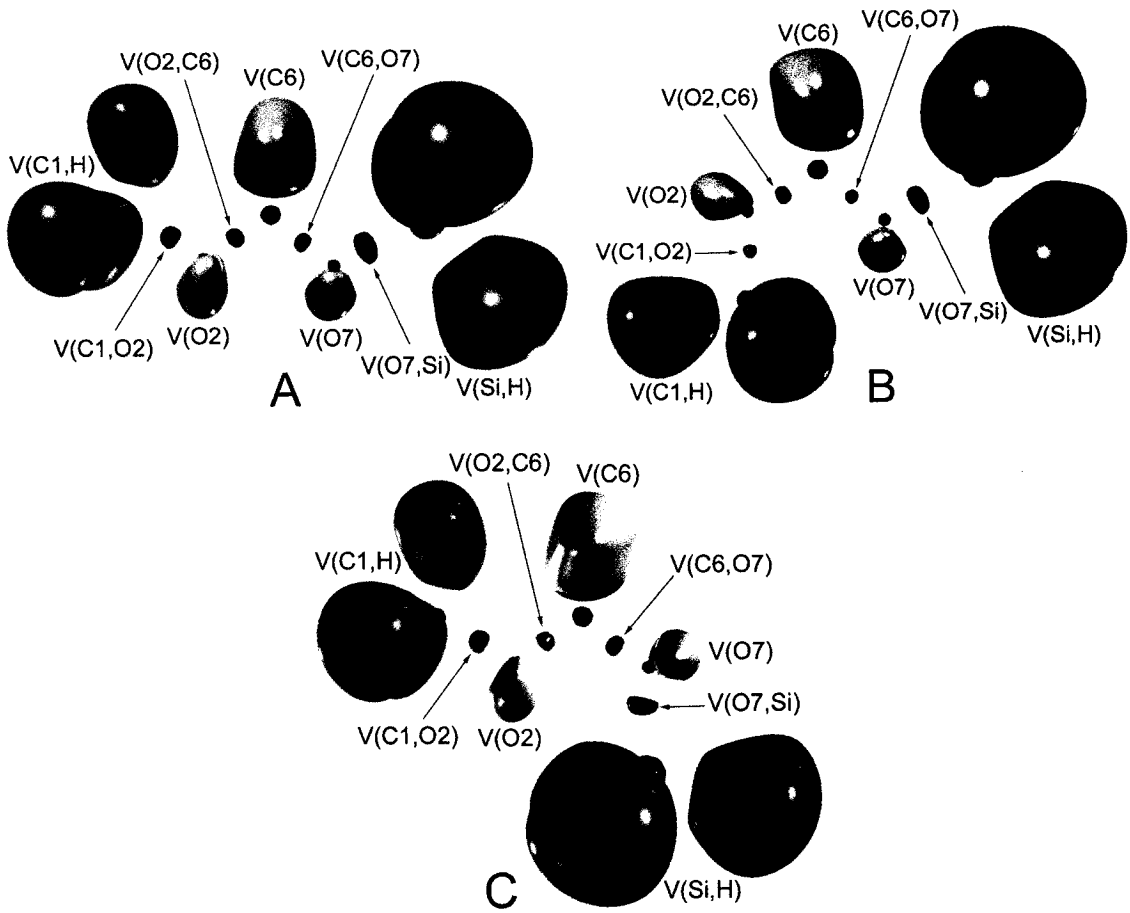

Figure 2.2 B3LYP/6-311+G(2d,p) ELF isosurfaces for the ground-state conformers of methoxy(siloxy)carbene. The basins shown are core basins (purple), disynaptic or bonding valence basins (green), monosynaptic or lone-pair valence basins (orange) and protonated valence basins (blue).

Table 2.2 Basin population $N(\Omega_i)$, relative fluctuation $\lambda(\Omega_i)$ and %cross-exchange contribution of the methoxy(siloxy)carbene conformers.[a]

Basin	$N(\Omega_i)$	$\lambda(\Omega_i)$	%Cross-exchange contribution (covariance)
			A
V(C1,O2)	1.45	0.61	V(O2) 27.6; V(O2,C6) 7.6; 3×V(C1,H) 17.2
V(O2)	4.25	0.37	V(O2,C6) 11.8; V(C1,O2) 9.5; V(C6) 3.5
V(O2,C6)	1.76	0.58	V(O2) 28.4; V(C6) 8.5; V(C1,O2) 6.3; V(C6,O7) 4.0
V(C6)	2.36	0.36	V(O2) 6.3, V(O2,C6) 6.3; V(C6,O7) 5.9; V(O7) 5.5
V(C6,O7)	1.58	0.61	V(O7) 26.6; V(O7,Si) 10.1; V(C6) 8.9; V(O2,C6) 4.4
V(O7)	3.99	0.38	V(O7,Si) 13.8; V(C6,O7) 10.5
V(O7,Si)	2.05	0.54	V(O7) 27.0; V(C6,O7) 7.8; 3×V(Si,H) 7.5
			B
V(C1,O2)	1.36	0.63	V(O2) 28.1; V(O2,C6) 8.1; 3×V(C1,H) 17.7
V(O2)	4.23	0.36	V(O2,C6) 12.1; V(C1,O2) 9.0; V(C6) 3.8
V(O2,C6)	1.86	0.57	V(O2) 27.9; V(C6) 7.7; V(C1,O2) 6.0; V(C6,O7) 3.8
V(C6)	2.34	0.35	V(O2) 6.8; V(O2,C6) 6.0; V(C6,O7) 6.0; V(O7) 5.1
V(C6,O7)	1.63	0.60	V(O7) 26.1; V(O7,Si) 10.6; V(C6) 8.7; V(O2,C6) 4.3
V(O7)	3.92	0.39	V(O7,Si) 14.1; V(C6,O7) 10.7
V(O7,Si)	2.08	0.53	V(O7) 26.4; V(C6,O7) 8.2; 3×V(Si,H) 7.2
			C
V(C1,O2)	1.41	0.62	V(O2) 29.1; V(O2,C6) 6.4, 3×V(C1,H) 17.8
V(O2)	4.42	0.36	V(O2,C6) 10.8; V(C1,O2) 9.3; V(C6) 3.4
V(O2,C6)	1.60	0.60	V(O2) 30.2; V(C6) 8.8; V(C1,O2) 5.7; V(C6,O7) 4.4
V(C6)	2.35	0.35	V(O2) 6.4; V(O2,C6) 6.0; V(O7) 6.0; V(C6,O7) 5.5
V(C6,O7)	1.60	0.60	V(O7) 26.3; V(O7,Si) 11.3; V(C6) 8.1; V(O2,C6) 4.4
V(O7)	3.92	0.38	V(O7,Si) 14.3; V(C6,O7) 10.7
V(O7,Si)	2.11	0.53	V(O7) 26.7; V(C6,O7) 8.6; 3×V(Si,H) 7.2

[a] Obtained from ELF analysis of B3LYP/6-311+G(2d,p) wave functions. The relative fluctuation $\lambda(\Omega_i)$ reflects the extent of basin population delocalization and %cross-exchange contribution refers to the percentage contribution of neighboring basins to the total basin population.

2.3.2 *FMO Analysis of Methoxy(siloxy)carbene Rearrangements*

Plots of the frontier molecular orbitals of the methoxy(siloxy)carbene conformers are shown in Fig 2.3. It is evident from these plots that the HOMO primarily comprises "*sp^2 hybridized*" lone-pair (non-bonding) orbitals on the O2, C6 and O7 atoms (n_{O2}, n_{C6} and n_{O7}), while the LUMO is essentially the $\sigma^*_{O7\text{-}Si}$ anti-bonding orbital. The computed HF/6-311+G(2d,p) HOMO/LUMO energy gaps for conformers **A**, **B** and **C** are 11.9, 11.8 and 11.8 eV respectively. These gaps seem reasonable for intramolecular reactivity when compared to the computed HF/4-31G HOMO/LUMO gap of 11.7 eV for phenylacetoxycarbene,[61] which has been found to undergo 1,2-acyl migration. In contrast, the computed HF/6-31G* HOMO/LUMO gap for dimethoxycarbene is 14.9 eV,[56] while the computed HF/4-31G HOMO/LUMO gap for methoxyphenoxycarbene is 14.1 eV.[120] The latter dioxycarbenes are not known for their intramolecular reactivity, partly because of their larger HOMO/LUMO gaps.

Based on FMO analysis, the mechanism for 1,2-silyl migration in methoxy(siloxy)carbene is predicted to occur via nucleophilic attack by the carbene lone pair at silicon rather than via an anion-like shift of the silyl group from oxygen to the "vacant" carbene *p* orbital. As pointed out earlier, the HOMO has considerable n_{C6} character while the LUMO is essentially the $\sigma^*_{O7\text{-}Si}$ anti-bonding orbital (cf. Fig. 2.3). Thus, since the n_{C6} portion of the HOMO is aligned with the $\sigma^*_{O7\text{-}Si}$ portion of the LUMO in conformers **A** and **B**, nucleophilic attack by the carbene lone pair at silicon is expected to be favorable. In contrast, a mechanism involving an anion-like shift of the silyl group from oxygen to the carbene carbon seems unlikely since the contribution of the $\sigma_{O7\text{-}Si}$ orbital to the HOMO and that of the "vacant" carbene *p* orbital to the LUMO appears to

be insignificant (cf. Fig. 2.3). Moreover, the geometries of the carbene conformers are not suitable for HOMO/LUMO interaction involving the in-plane $\sigma_{O7\text{-}Si}$ orbital and the out-of-plane carbene *p* orbital.

With regards to 1,2-methyl migration, it appears that neither nucleophilic attack by the carbene lone pair at the methyl carbon nor an anion-like shift of the methyl group from oxygen to the vacant carbene *p* orbital is favorable. For nucleophilic attack by the carbene lone pair at the methyl carbon to be favorable, the contribution of the n_{C6} orbital to the HOMO and the $\sigma^*_{C1\text{-}O2}$ orbital to the LUMO must be considerable. Indeed, the HOMO has significant n_{C6} character but the LUMO does not appear to have any $\sigma^*_{C1\text{-}O2}$ character (cf. Fig. 2.3). Consequently, in conformers **A** and **C** where the n_{C6} orbital would be aligned with the $\sigma^*_{C1\text{-}O2}$ anti-bonding orbital, nucleophilic attack by the carbene lone pair at the methyl carbon is expected to be unfavorable. The alternative mechanism involving an anion-like shift of the methyl group from oxygen to the carbene carbon is also expected to be unfavorable because the contribution of the $\sigma_{C1\text{-}O2}$ orbital to the HOMO and the "vacant" carbene *p* orbital to the LUMO appears to be negligible.

We now consider the mechanism for methoxy(siloxy)carbene decarbonylation involving intramolecular front-side nucleophilic attack by the methoxy oxygen O2 at silicon and by the siloxy oxygen O7 at the methyl carbon C1 in terms of FMO theory. In conformer **C**, where the n_{O2} part of the HOMO is aligned with the $\sigma^*_{O7\text{-}Si}$ portion of the LUMO (cf. Fig. 2.3), nucleophilic attack by O2 at Si is expected to be favorable. On the contrary, even though the n_{O7} portion of the HOMO is aligned with the $\sigma^*_{C1\text{-}O2}$ portion of the LUMO in conformer **B**, nucleophilic attack by the siloxy oxygen O7 at the methyl carbon C1 is not expected to be favorable because the LUMO lacks $\sigma^*_{C1\text{-}O2}$ character.

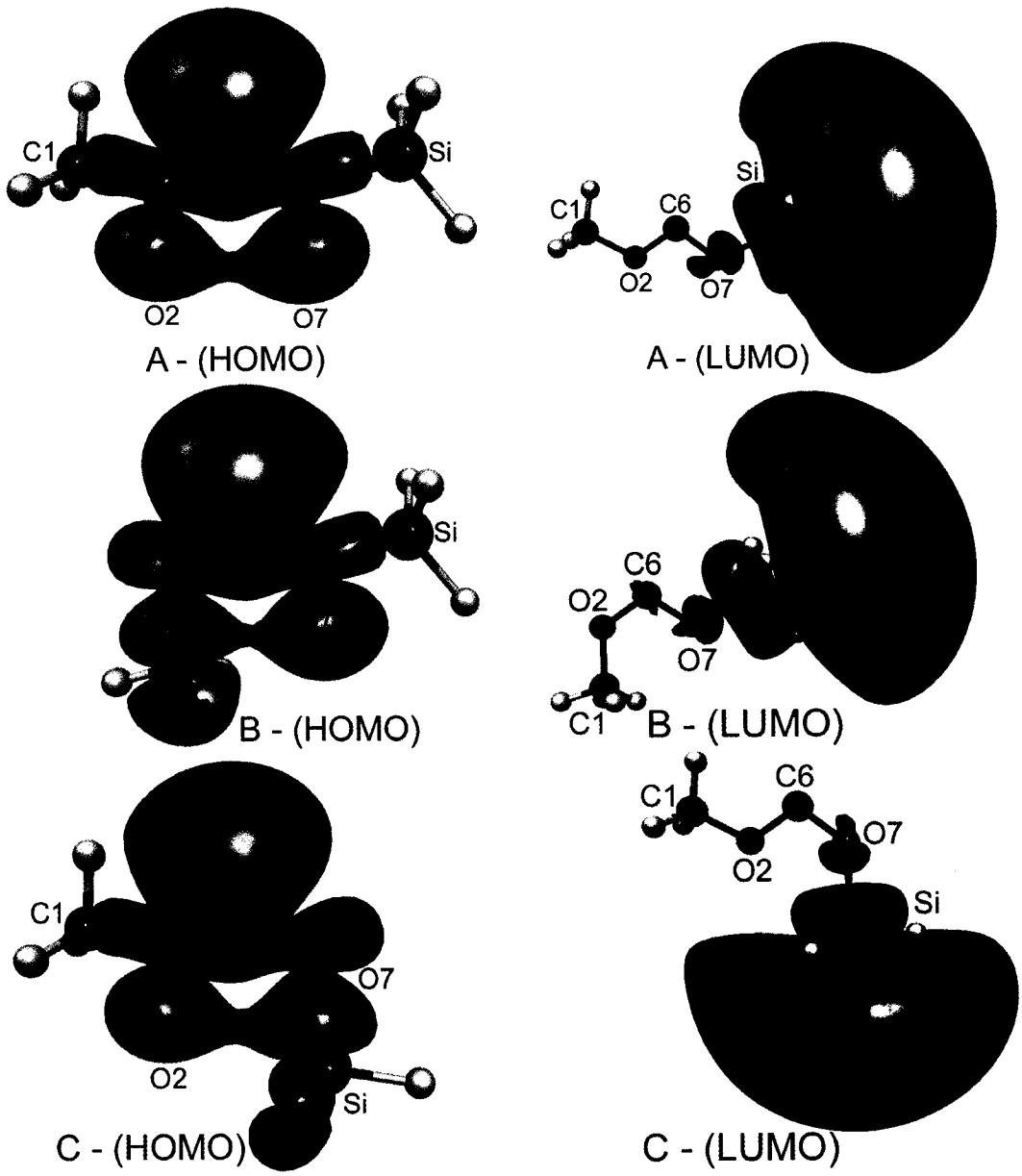

Figure 2.3 Computed HF/6-311+G(2d,p) frontier molecular orbitals of conformers **A**, **B** and **C** of methoxy(siloxy)carbene.

2.3.3 Mechanism for 1,2-Silyl Migration

The optimized transition-state geometries, denoted $\mathbf{TS_{AD}}$ and $\mathbf{TS_{BE}}$, for 1,2-silyl migration in conformers **A** and **B** of methoxy(siloxy)carbene are shown in Fig. 2.4. Optimized geometries of the products, *anti*-methyl silylformate **D** and *syn*-methyl silylformate **E** are also shown in Fig. 2.4. Relative to conformers **A** and **B** (cf. Fig. 2.1), there is significant shrinkage of the ∠C6O7Si angle, together with modest lengthening and shortening of the O7-Si and C6-O7 bonds, respectively, in $\mathbf{TS_{AD}}$ and $\mathbf{TS_{BE}}$. In addition, both $\mathbf{TS_{AD}}$ and $\mathbf{TS_{BE}}$ are planar, indicating that silyl migration occurs in the plane containing the carbene lone pair. These features are consistent with nucleophilic attack by the carbene lone pair at silicon, in concert with modest O7-Si bond dissociation and C6-O7 double-bond formation.

The changes in geometry in going from **A** and **B** to $\mathbf{TS_{AD}}$ and $\mathbf{TS_{BE}}$ are reflected in the topological properties of the electronic density (cf. Tables 2.1 and 2.3). The ∠C6O7Si angle shrinkage results in weak C6-Si bond formation, as indicated by the low $\rho_b(r)$ and positive $\nabla^2\rho_b(r)$ values (cf. Table 2.3).[121] As well, the shortening and lengthening of the C6-O7 and O7-Si bonds are accompanied by an increase and a decrease in the $\rho_b(r)$ values, respectively. These observations are in accord with nucleophilic attack by the carbene C6 lone pair at silicon, in concert with C6-O7 double-bond formation and O7-Si bond dissociation. We note that the outrageously large ε values for the developing and the dissociating C6-Si and O7-Si bonds in $\mathbf{TS_{AD}}$ and $\mathbf{TS_{BE}}$ (cf. Table 2.3) most likely arise from the structural instability of these bonds.[122]

Contour plots of the Laplacian of the electronic density overlaid by bonds or *bond paths* at selected points along the reaction path for 1,2-silyl migration in conformers **A**

and **B** are displayed in Figure 2.5. These plots basically summarize the changes in the electronic charge distribution and molecular structure that occurs during 1,2-silyl migration. Negative intrinsic reaction coordinate (IRC) values correspond to the reactant side of the reaction path, positive IRC values correspond to the product side of the reaction path and an IRC value of zero represents the transition state. It can be seen that the region of charge concentration corresponding to the carbene C6 lone pair becomes polarized towards Si as the reaction progresses from reactant (negative IRC values), through the transition state (an IRC value of zero) and onto product (positive IRC values), indicative of nucleophilic attack by the carbene lone pair at silicon.

The changes in the electronic charge distribution during 1,2-silyl migration result in three regions of structural stability corresponding to a *reactant region*, an intermediate *ring-structure region* and a *product region*, each of which persists for several geometric configurations along the reaction path (cf. Fig. 2.5). The plots for IRC = -0.59620, 0.00000 and 0.49519 $amu^{1/2}$ bohr for 1,2-silyl migration in **A**, and IRC = -0.59531, 0.00000 and 0.59672 $amu^{1/2}$ bohr for 1,2-silyl migration in **B**, are in the reactant, ring-structure and product regions of structural stability, respectively. This sequence of changes in molecular structure is characteristic of a *bifurcation mechanism*.[18] At some point between the *reactant* and *ring-structure* regions, a unique and unstable critical point appears in the electronic charge distribution. This critical point, referred to as a *bifurcation catastrophe point*, is a minimum in $\rho(r)$ along the line connecting the C6 and Si nuclei (positive curvature), a maximum along a line perpendicular to the C6O7Si plane (negative curvature) and a point of inflexion on a line originating from infinity and terminating at either the C6-O7 or O7-Si bond critical point (zero curvature). Further

motion along the IRC results in a bifurcation of this unstable critical point into a new C6-Si bond critical point (BCP) and C6-O7-Si ring critical point (RCP). As motion along the IRC continues, the RCP migrates towards the dissociating O7-Si BCP and when they coalesce, the system has reached a second *bifurcation catastrophe point.* As motion along the IRC continues, the O7-Si bond becomes annihilated and the system enters the product region of structural stability. Thus, the changes in molecular structure that accompanies 1,2-silyl migration in methoxy(siloxy)carbene involving nucleophilic attack by the carbene lone pair at silicon occur via a *bifurcation mechanism.*

ELF isosurfaces for $\mathbf{TS_{AD}}$ and $\mathbf{TS_{BE}}$ are shown in Fig. 2.6 and corresponding ELF basin properties are collected in Table 2.4. Inspection of the ELF isosurfaces reveals that the V(C6) lone-pair basins in **A** and **B** (cf. Fig. 2.2) turn into the V(C6,Si) bonding basins in $\mathbf{TS_{AD}}$ and $\mathbf{TS_{BE}}$ (cf. Fig. 2.6), indicative of nucleophilic attack by the carbene lone pair at silicon. In addition, the V(O7) lone-pair basins in **A** and **B** change shape in $\mathbf{TS_{AD}}$ and $\mathbf{TS_{BE}}$, as they develop into carbonyl oxygen lone pairs, while the V(O7,Si) basins migrate towards O7, in keeping with O7-Si bond dissociation.[123] As a matter of fact, the V(O7,Si) basins are located 0.636 Å away from O7 in **A** and **B**, and 0.580 Å away from O7 in $\mathbf{TS_{AD}}$ and $\mathbf{TS_{AB}}$. We note that the V(C6,O7) basin populations increase in $\mathbf{TS_{AD}}$ and $\mathbf{TS_{BE}}$ (cf. Table 2.4) relative to **A** and **B** (cf. Table 2.2), consistent with the developing C6-O7 double bond. We also note that the V(O7,Si) basin populations for the dissociating O7-Si bond increases in $\mathbf{TS_{AD}}$ and $\mathbf{TS_{BE}}$ relative to **A** and **B**. The latter observation most likely results from additional cross-exchange contribution involving the new V(C6,Si) bonding basin in $\mathbf{TS_{AD}}$ and $\mathbf{TS_{BE}}$.

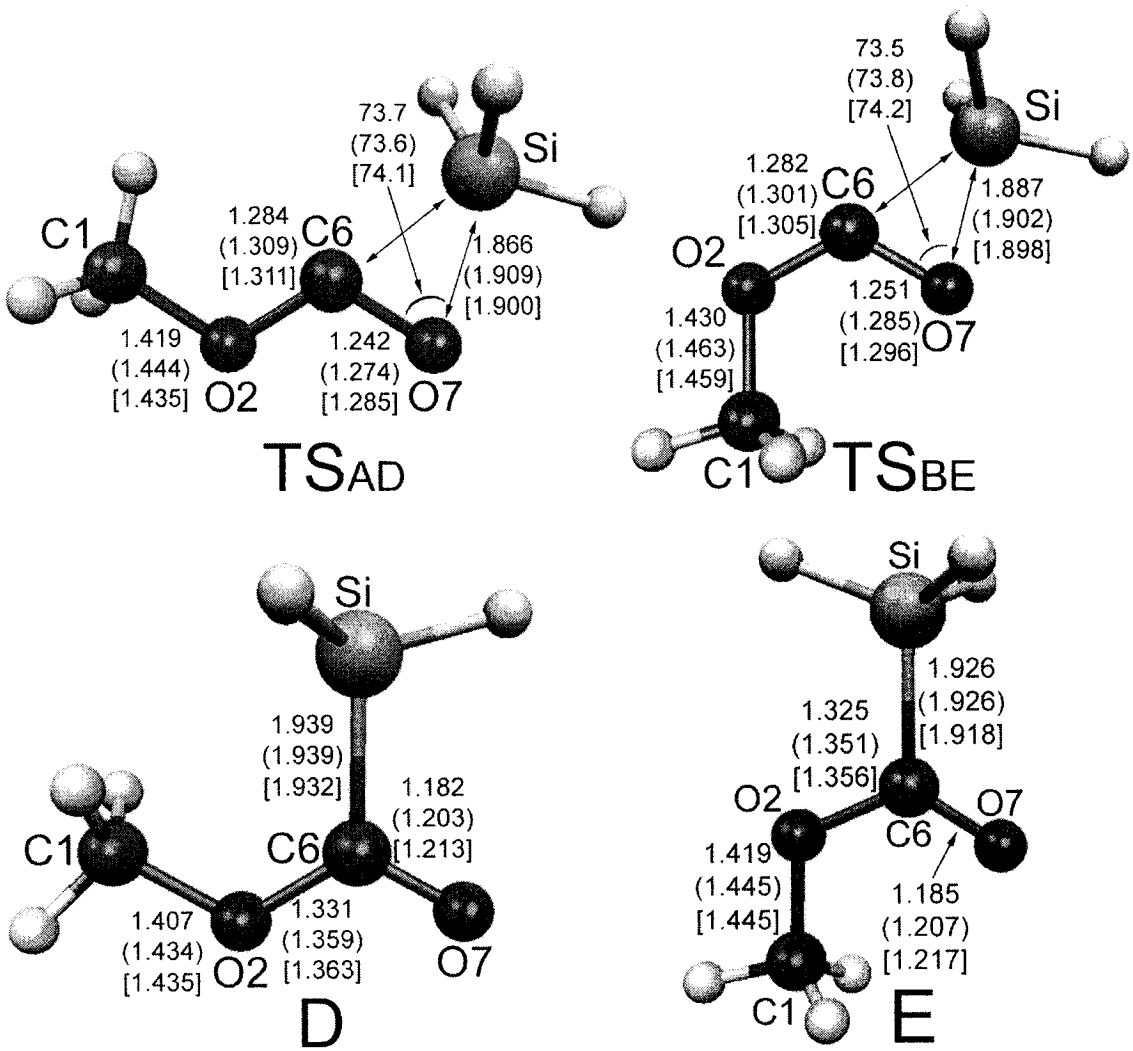

Figure 2.4 Optimized molecular geometries of the transition-states for 1,2-silyl migration in methoxy(siloxy)carbene, and the products *anti*- and *syn*-methyl silylformate. Geometric parameters are given for HF/6-311+G(2d,p), B3LYP/6-311+G(2d,p) (parentheses), and MP2/6-311+G(2d,p) [brackets] model chemistries. Bond lengths and angles are in Å and degrees.

Table 2.3 Topological properties of the electronic density at pertinent BCPs of the transition states for 1,2-silyl migration in the methoxy(siloxy)carbene conformers.[a]

	O2-C6	C6-O7	C6-Si	O7-Si
		TS_{AD}		
		HF/6-311+G(2d,p)		
$\rho_b(r)$ (e/Å^3)	2.33	2.66	0.51	0.49
$\nabla^2\rho_b(r)$ (e/Å^5)	-5.8	-9.2	6.1	9.7
ε	0.16	0.07	0.61	1.48
		B3LYP/6-311+G(2d,p)		
$\rho_b(r)$ (e/Å^3)	2.21	2.48	0.52	0.52
$\nabla^2\rho_b(r)$ (e/Å^5)	-13.2	-17.3	4.1	6.8
ε	0.08	0.03	0.85	1.34
		MP2/6-311+G(2d,p)		
$\rho_b(r)$ (e/Å^3)	2.16	2.38	0.50	0.51
$\nabla^2\rho_b(r)$ (e/Å^5)	-10.8	-15.0	4.9	7.4
ε	0.08	0.03	2.03	1.05
		TS_{BE}		
		HF/6-311+G(2d,p)		
$\rho_b(r)$ (e/Å^3)	2.34	2.59	0.51	0.49
$\nabla^2\rho_b(r)$ (e/Å^5)	-6.2	-8.6	6.2	9.4
ε	0.15	0.10	0.50	1.57
		B3LYP/6-311+G(2d,p)		
$\rho_b(r)$ (e/Å^3)	2.25	2.41	0.52	0.52
$\nabla^2\rho_b(r)$ (e/Å^5)	-13.0	-16.8	4.2	6.9
ε	0.08	0.06	0.85	1.08
		MP2/6-311+G(2d,p)		
$\rho_b(r)$ (e/Å^3)	2.19	2.31	0.49	0.51
$\nabla^2\rho_b(r)$ (e/Å^5)	-10.7	-14.6	4.9	7.5
ε	0.07	0.06	1.85	0.96

[a] Obtained from AIM analysis.

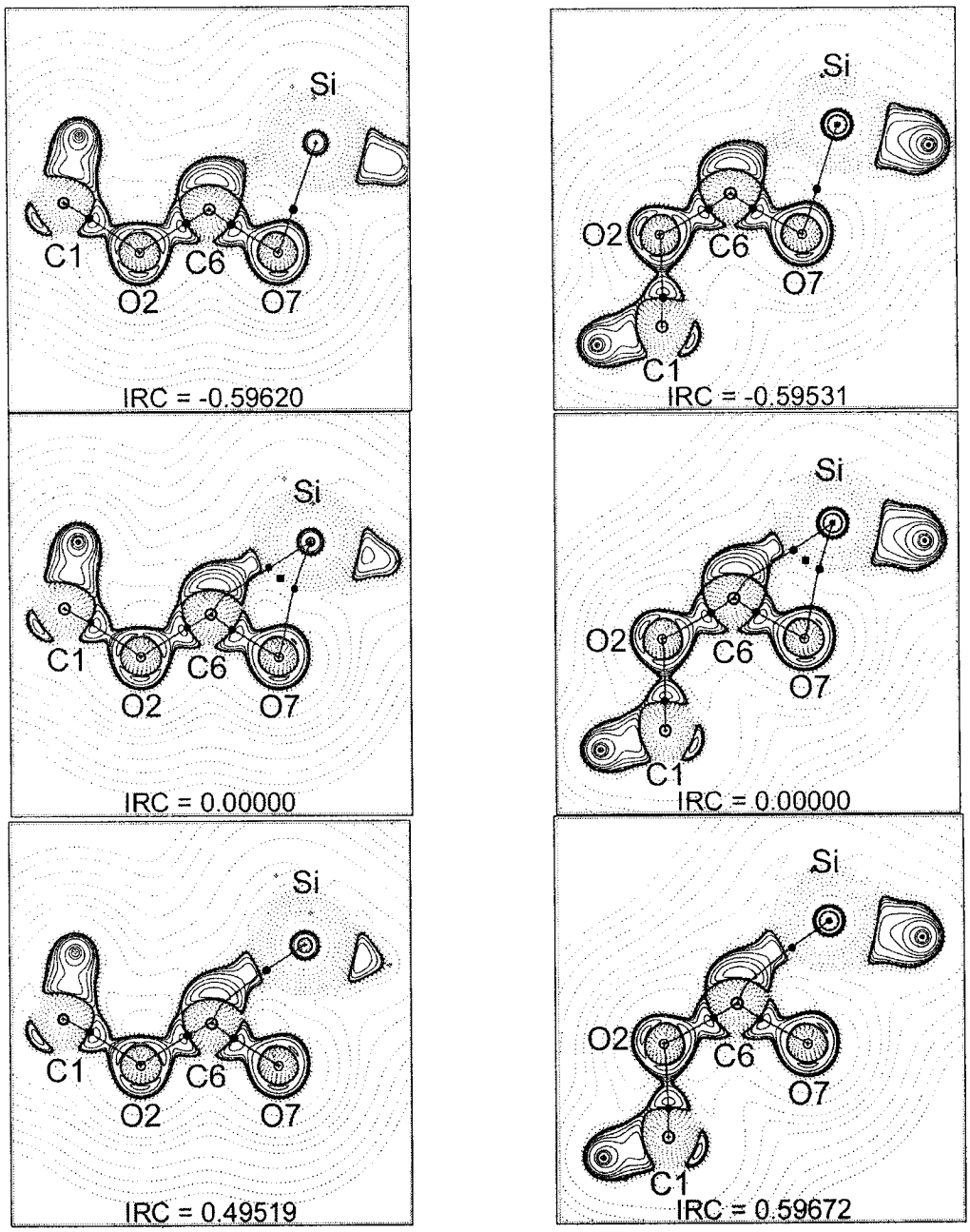

Figure 2.5 B3LYP/6-311+G(2d,p) contour plots of the Laplacian of $\rho(r)$ overlaid by bond paths in the O2C6O7 plane at selected IRC values for 1,2-silyl migration in methoxy(siloxy)carbene. The plots on the left and right are for conformers **A** and **B**, respectively. Plots for IRC = -0.59620, 0.00000 and 0.49519 amu$^{1/2}$ bohr for **A**, and -0.59531, 0.00000 and 0.59672 amu$^{1/2}$ bohr for **B**, are in the reactant, ring-structure and product regions of structural stability, respectively. Solid and broken contours represent regions of charge concentration and charge depletion, while solid round and square dots denote BCPs and RCPs.

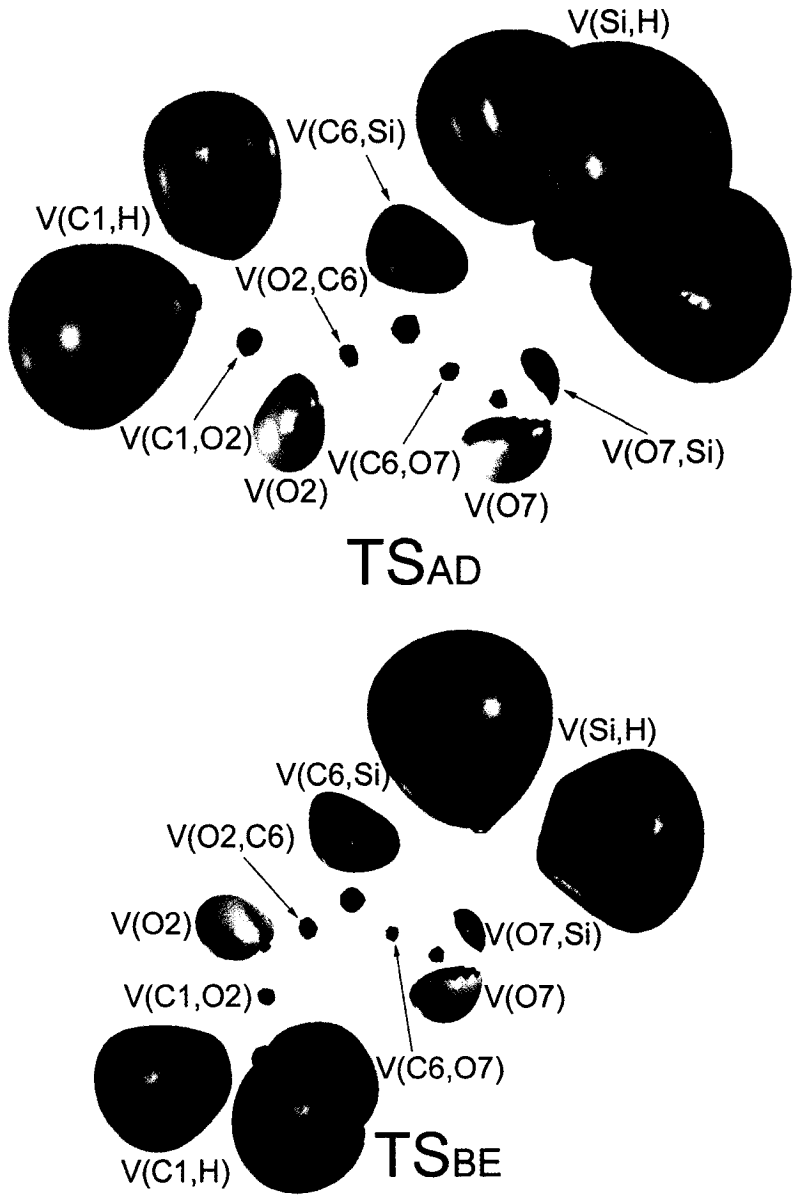

Figure 2.6 B3LYP/6-311+G(2d,p) ELF isosurfaces of the transition states for 1,2-silyl migration in methoxy(siloxy)carbene. The basins are core basins (purple), bonding basins (green), lone-pair basins (orange) and protonated basins (blue).

Table 2.4 Basin population $N(\Omega_i)$, relative fluctuation $\lambda(\Omega_i)$ and %cross-exchange contribution of the transition states for 1,2-silyl migration in methoxy(siloxy)carbene.[a]

Basin	$N(\Omega_i)$	$\lambda(\Omega_i)$	%Cross-exchange contribution (covariance)
			TS_{AD}
V(C1,O2)	1.42	0.62	V(O2) 28.9; V(O2,C6) 7.0; 3×V(C1,H) 17.6
V(O2)	4.38	0.36	V(C1,O2) 9.4; V(O2,C6) 11.4;
V(O2,C6)	1.67	0.60	V(O2) 29.9; V(C1,O2) 6.0; V(C6,Si) 8.4; V(C6,O7) 4.2
V(C6,Si)	2.43	0.43	V(O2,C6) 5.8; V(C6,O7) 6.2; V(O7,Si) 5.0; 3×V(Si,H) 7.9
V(C6,O7)	1.76	0.60	V(C6,Si) 8.6; V(O7) 22.9; V(O2,C6) 4.0; V(O7,Si) 13.7
V(O7)	3.45	0.40	V(C6,O7) 11.6; V(O7,Si) 15.6
V(O7,Si)	2.32	0.52	V(O7) 23.4; V(C6,O7) 10.4;V(C6,Si) 5.2; 3×V(Si,H) 4.8
			TS_{BE}
V(C1,O2)	1.49	0.61	V(O2) 28.7; V(O2,C6) 8.1; 3×V(C1,H) 17.6
V(O2)	4.22	0.35	V(C1,O2) 9.1; V(O2,C6) 12.1
V(O2,C6)	1.92	0.56	V(C1,O2) 6.0;V(O2) 28.4; V(C6,Si) 7.1; V(C6,O7) 4.4
V(C6,Si)	2.24	0.39	V(O2,C6) 5.4;V(C6,O7) 6.2; V(O7,Si) 5.0; 3×V(Si,H) 7.9
V(C6,O7)	1.88	0.58	V(C6,Si) 8.2; V(O7) 22.5; V(O7,Si) 13.2; V(O2,C6) 4.4
V(O7)	3.49	0.40	V(C6,O7) 11.8; V(O7,Si) 15.2
V(O7,Si)	2.31	0.51	V(O7) 23.5; V(C6,O7) 10.6; V(C6,Si) 5.3; 3×V(Si,H) 4.9

[a] Obtained from ELF analysis of B3LYP/6-311+G(2d,p) wave functions. The relative fluctuation $\lambda(\Omega_i)$ reflects the extent of basin population delocalization and %cross-exchange contribution refers to the percentage contribution of neighboring basins to the total basin population.

2.3.4 *Mechanism for 1,2-Methyl Migration*

The optimized transition-state geometries, denoted $\mathbf{TS_{AF}}$ and $\mathbf{TS_{CG}}$, for 1,2-methyl migration in conformers **A** and **C** of methoxy(siloxy)carbene, together with the products *anti*-silyl acetate **F** and *syn*-silyl acetate **G**, are shown in Fig. 2.7. As can be seen, there is tremendous ∠C1O2C6 angle shrinkage, in concert with significant C1-O2 bond lengthening and modest O2-C6 bond shortening in $\mathbf{TS_{AF}}$ and $\mathbf{TS_{CG}}$ relative to **A** and **C** (cf. Fig. 2.1), respectively. In addition, the ∠C1O2C6O7 dihedral angle in both $\mathbf{TS_{AF}}$ and $\mathbf{TS_{CG}}$ suggests that the methyl group rotates out-of-plane during migration most likely for better alignment of the $\sigma_{C1\text{-}O2}$ bond with the "vacant" carbene *p* orbital. These features are consistent with an anion-like shift of the methyl group from oxygen to the "vacant" carbene *p* orbital.

Table 2.5 contains topological properties of the electronic density at pertinent BCPs for $\mathbf{TS_{AF}}$ and $\mathbf{TS_{CG}}$. It is apparent that the C1-O2 bond lengthening observed is accompanied by a tremendous decrease in $\rho_b(r)$ (except for the HF/6-311+G(2d,p) computed values, presumably due to the lack of electron correlation) while the O2-C6 bond shortening results in an increase in $\rho_b(r)$ in going from **A** and **C** (cf. Table 2.1) to $\mathbf{TS_{AF}}$ and $\mathbf{TS_{CG}}$, respectively. These features are consistent with significant C1-O2 bond dissociation, in concert with modest O2-C6 double-bond formation in $\mathbf{TS_{AF}}$ and $\mathbf{TS_{CG}}$. Significant C1-O2 bond dissociation is also reflected in the fact that the sign of $\nabla^2\rho_b(r)$ changes from negative to positive.[121]

Contour plots of the Laplacian of the electronic density overlaid by bond paths at selected points along the reaction path for 1,2-methyl migration in conformer **A** are shown in Fig. 2.8. The plots are in the C1O2C6 migration plane and the O2C6O7 carbene

valence plane. From the sequence of plots in Fig. 2.8, it can be seen that while the bond path from C1 switches from O2 to C6, the region of charge concentration corresponding to the carbene C6 lone pair remains intact, consistent with a mechanism for 1,2-methyl migration involving an anion-like shift from oxygen to the "vacant" carbene *p* orbital.

The sequence of plots in Fig. 2.8 reveals that there are two regions of structural stability corresponding to reactant and product regions. The plots for IRC = -0.00990 and 0.00000 $amu^{1/2}$ bohr, where the bond path from C1 terminates at O2, are in the reactant region of structural stability, while those for IRC = 0.11990 $amu^{1/2}$ bohr, where the bond path from C1 terminates at C6, are in the product region of structural stability. The plots for IRC = 0.05990, where the bond path from C1 terminates at the O2-C6 BCP, corresponds to a unique and unstable structure that is transitional between C1-O2 bond dissociation and C1-C6 bond formation. Since the O2 and C6 atoms are in essence competing for the line of maximum charge density from C1, this unique arrangement of bond paths is referred to as a *conflict structure*,[18] and the overall change in molecular structure is said to occur by a *conflict mechanism*.[18] Thus, it appears that 1,2-methyl migration involving an anion-like shift from oxygen to the "vacant" carbene *p* orbital occur via a conflict mechanism.

ELF isosurfaces for $\mathbf{TS_{AF}}$ and $\mathbf{TS_{CG}}$ are shown in Fig. 2.9 and ELF basin properties are collected in Table 2.6. Inspection of the ELF isosurfaces reveals that the V(C1,O2) bonding basin in **A** and **C** (cf. Fig. 2.2) completely disappears in $\mathbf{TS_{AF}}$ and $\mathbf{TS_{CG}}$ (cf. Fig. 2.9), indicative of complete C1-O2 bond cleavage. As well, the V(O2) lone-pair basin in **A** and **C** splits into V_1(O2) and V_2(O2) lone-pair basins in $\mathbf{TS_{AF}}$ and $\mathbf{TS_{CG}}$, which appear as a $V_1(O2)\cup V_2(O2)$ superbasin in Fig. 2.9. The latter observation is

consistent with O2-C6 carbonyl group formation, even though the V(O2,C6) basin populations in **A** and **C** (cf. Table 2.2) remain essentially unchanged in $\mathbf{TS_{AF}}$ and $\mathbf{TS_{CG}}$ (cf. Table 2.6). However, the most important information garnered from inspection of the ELF isosurfaces is the fact the V(C6) lone-pair basin corresponding to the carbene C6 lone pair in **A** and **C** (cf. Fig. 2.2) remains intact in $\mathbf{TS_{AF}}$ and $\mathbf{TS_{CG}}$ (cf. Fig. 2.2), consistent with an anion-like shift of the methyl group from oxygen to the "vacant" carbene *p* orbital.

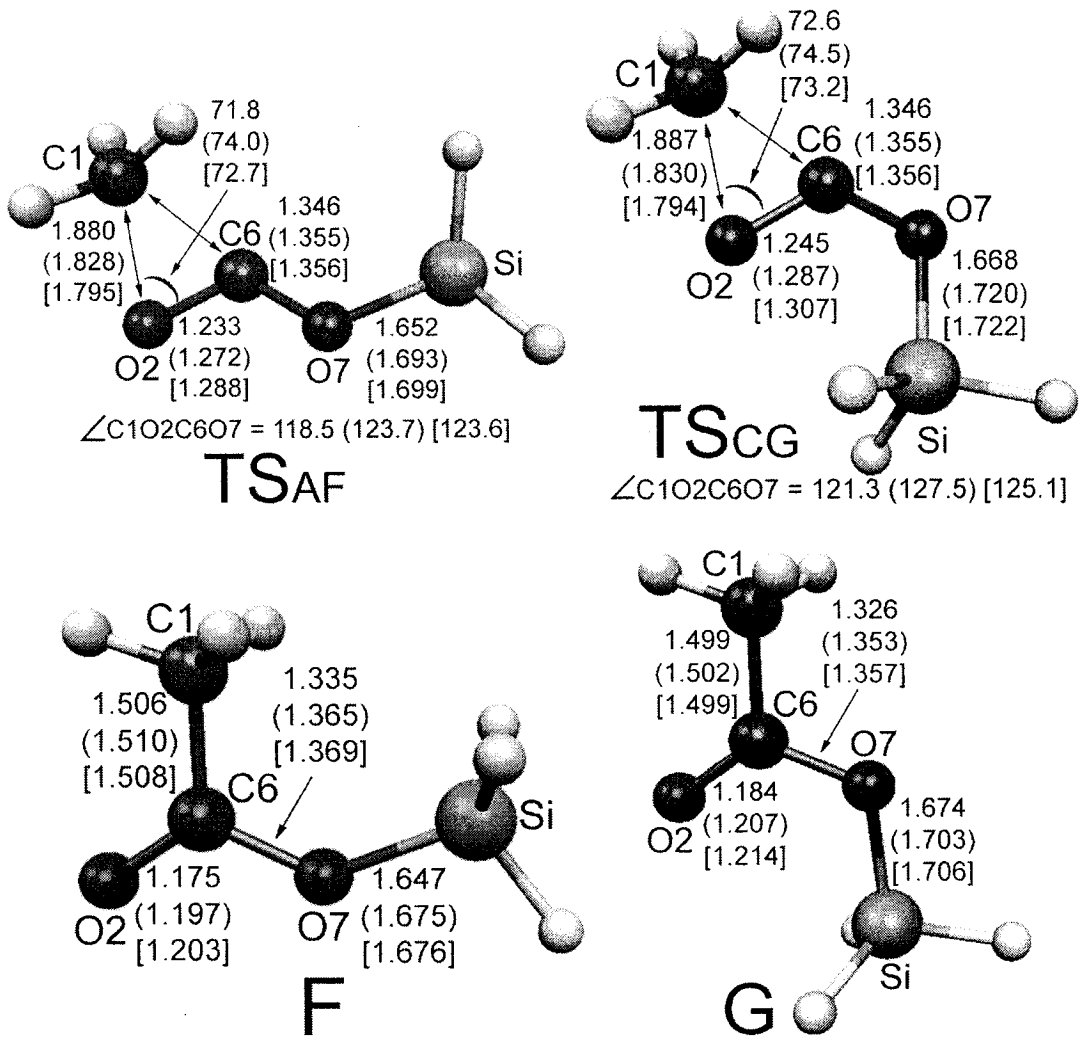

Figure 2.7 Optimized molecular geometries of the transition states for 1,2-methyl migration in methoxy(siloxy)carbene, and the products *anti*- and *syn*-silyl acetate. Geometric parameters are given for the HF/6-311+G(2d,p), B3LYP/6-311+G(2d,p) (parentheses), and MP2/6-311+G(2d,p) [brackets] model chemistries. Bond lengths and angles are in Å and degrees, respectively.

Table 2.5 Topological properties of the electronic density at pertinent BCPs of the transition states for 1,2-methyl migration in methoxy(siloxy)carbene.[a]

	C1-O2	O2-C6	C6-O7	O7-Si
		TS_{AF}		
		HF/6-311+G(2d,p)		
$\rho_b(r)$ (e/Å^3)	1.83	3.12	2.03	0.88
$\nabla^2\rho_b(r)$ (e/Å^5)	18.0	-4.9	-11.2	20.6
ε	0.07	0.17	0.11	0.05
		B3LYP/6-311+G(2d,p)		
$\rho_b(r)$ (e/Å^3)	0.68	2.49	1.98	0.85
$\nabla^2\rho_b(r)$ (e/Å^5)	3.2	-17.9	-15.8	15.0
ε	0.84	0.11	0.19	0.05
		MP2/6-311+G(2d,p)		
$\rho_b(r)$ (e/Å^3)	0.72	2.38	1.96	0.82
$\nabla^2\rho_b(r)$ (e/Å^5)	3.0	-16.7	-15.0	15.5
ε	0.90	0.11	0.19	0.05
		TS_{CG}		
		HF/6-311+G(2d,p)		
$\rho_b(r)$ (e/Å^3)	1.61	2.12	2.23	0.85
$\nabla^2\rho_b(r)$ (e/Å^5)	-5.9	-14.2	-5.5	18.2
ε	0.01	0.39	0.28	0.02
		B3LYP/6-311+G(2d,p)		
$\rho_b(r)$ (e/Å^3)	0.67	2.40	2.08	0.79
$\nabla^2\rho_b(r)$ (e/Å^5)	3.2	-18.0	-14.6	12.9
ε	0.67	0.11	0.18	0.03
		MP2/6-311+G(2d,p)		
$\rho_b(r)$ (e/Å^3)	0.72	2.27	2.04	0.77
$\nabla^2\rho_b(r)$ (e/Å^5)	2.9	-16.7	-13.6	13.6
ε	0.73	0.12	0.18	0.03

[a] Obtained from AIM analysis.

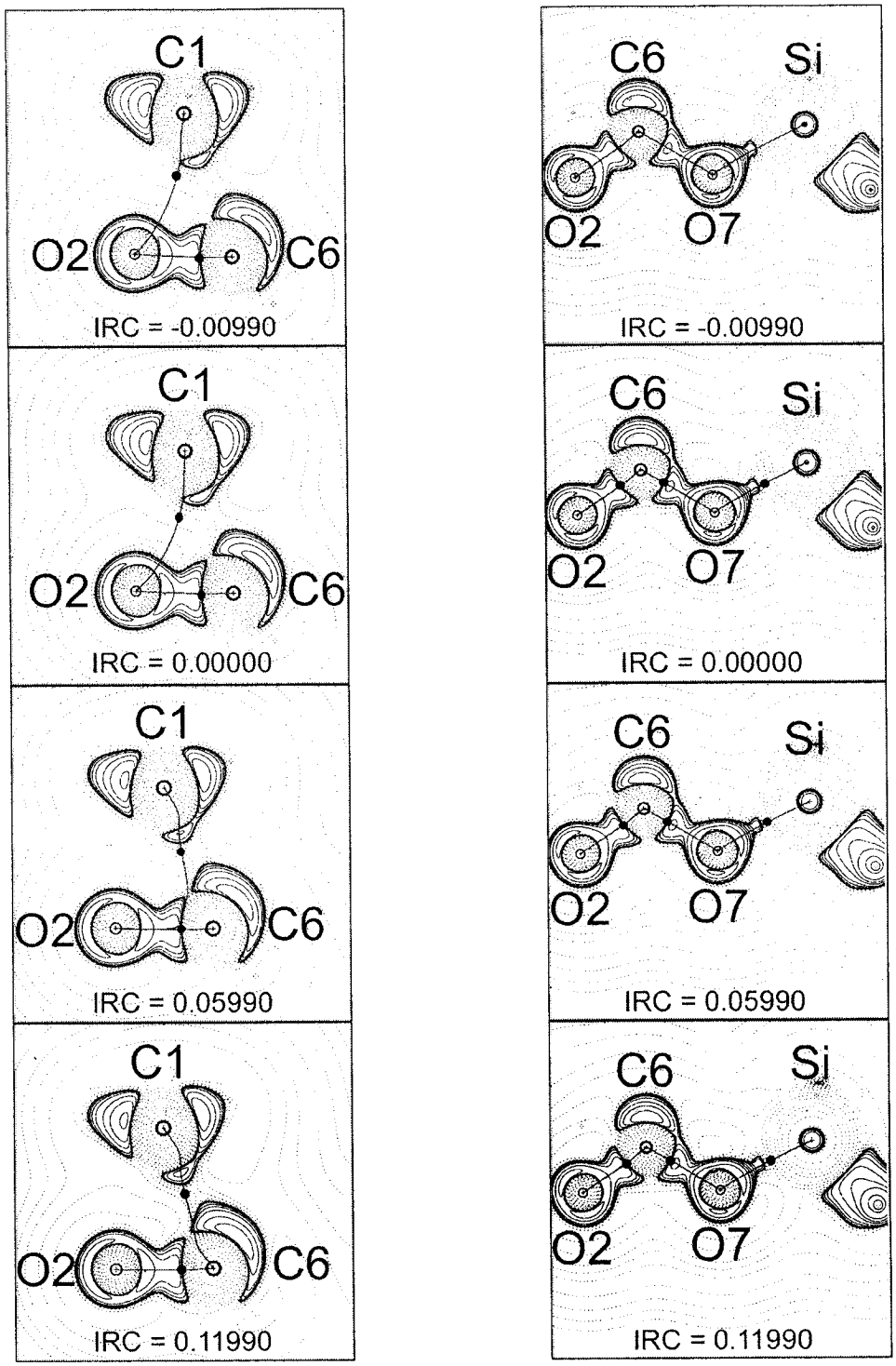

Figure 2.8 HF/6-311+G(2d,p) contour plots of the Laplacian of $\rho(r)$ overlaid by bond paths for 1,2-methyl migration in *trans-trans* methoxy(siloxy)carbene in the C1O2C6 (left) and O2C6O7 (right) planes. Plots for IRC = -0.00990 and 0.00000 amu$^{1/2}$ bohr are in the reactant region of structural stability, while those for IRC = 0.11990 amu$^{1/2}$ bohr are in the product region of structural stability. The plots for IRC = 0.05990 amu$^{1/2}$ bohr represents a conflict structure. Solid round dots denote BCPs.

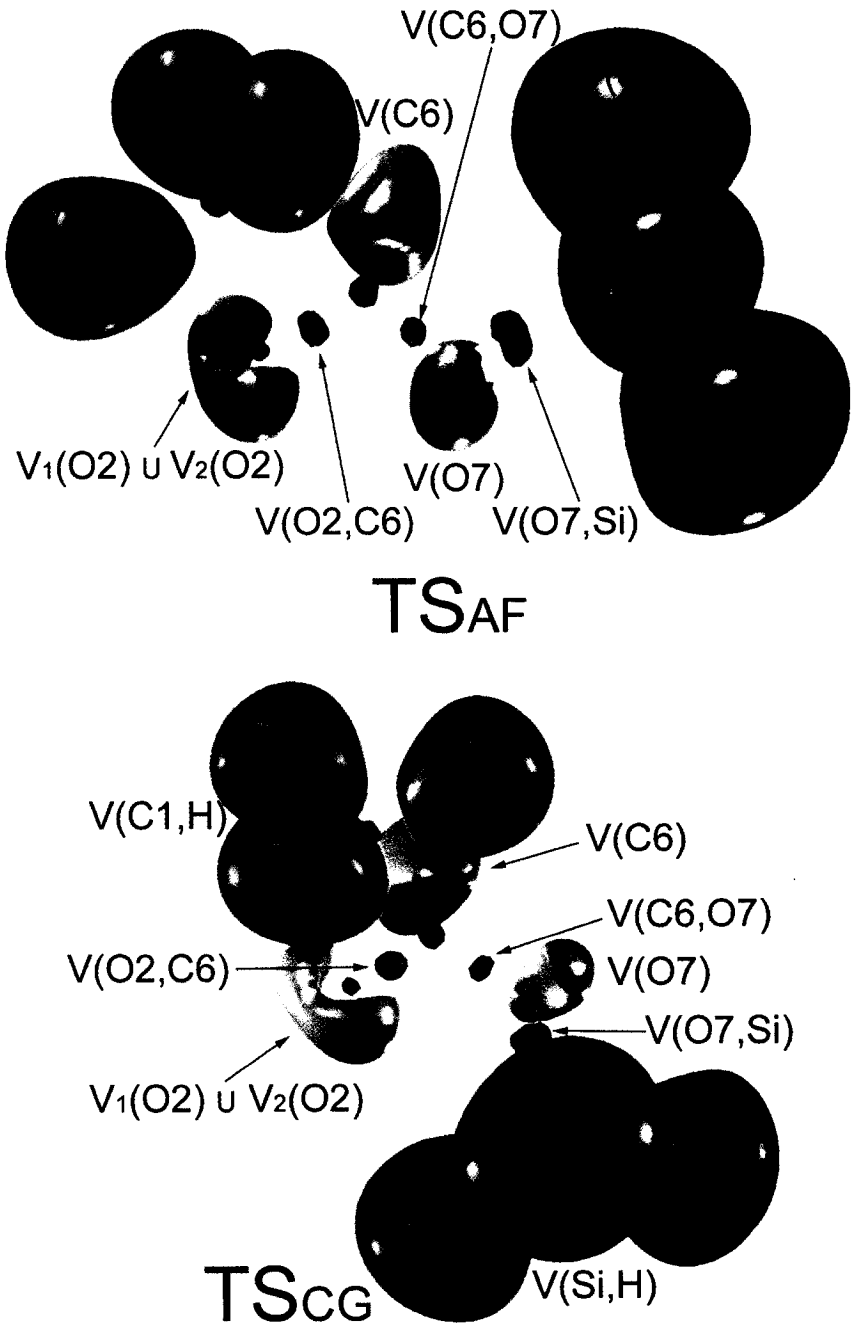

Figure 2.9 B3LYP/6-311+G(2d,p) ELF isosurfaces of the transition states for 1,2-methyl migration in methoxy(siloxy)carbene. The basins shown are core basins (purple), bonding valence basins (green), lone-pair valence basins (orange) and protonated valence basins (blue).

Table 2.6 Basin population $N(\Omega_i)$, relative fluctuation $\lambda(\Omega_i)$ and %cross-exchange contribution of the transition states for 1,2-methyl migration in methoxy(siloxy)carbene.[a]

Basin	$N(\Omega_i)$	$\lambda(\Omega_i)$	%Cross-exchange contribution (covariance)
			TS_{AF}
V_1(O2)	2.67	0.47	V_2(O2) 17.5; V(O2,C6) 11.2
V_2(O2)	2.69	0.45	V_1(O2) 17.5; V(O2,C6) 11.2
V(O2,C6)	1.77	0.59	V_1(O2) 17.1; V_2(O2) 17.1; V(C6) 8.5; V(C6,O7) 3.4
V(C6)	2.24	0.46	V(O2,C6) 6.7; V(C6,O7) 5.4, V_1(O2) 5.4; V_2(O2) 4.0
V(C6,O7)	1.39	0.64	V(C6) 8.8; V(O7) 29.4; V(O2,C6) 4.4;V(O7,Si) 10.3
V(O7)	4.11	0.38	V(C6,O7) 9.7; V(O7,Si) 14.6
V(O7,Si)	2.14	0.54	V(O7) 28.0; V(C6,O7) 6.5; 3×V(Si,H) 7.0
			TS_{CG}
V_1(O2)	2.63	0.46	V_2(O2) 18.4; V(O2,C6) 11.1
V_2(O2)	2.82	0.46	V_1(O2) 17.1; V(O2,C6) 11.0
V(O2,C6)	1.75	0.60	V_1(O2) 16.7; V_2(O2) 17.8; V(C6) 8.1; V(C6,O7) 4.0
V(C6)	2.17	0.46	V(O2,C6) 6.4; V(C6,O7) 5.5, V_1(O2) 3.7; V_2(O2) 5.5
V(C6,O7)	1.53	0.62	V(C6) 8.0; V(O7) 27.8; V(O2,C6) 4.6;V(O7,Si) 10.6
V(O7)	4.16	0.37	V(C6,O7) 10.1; V(O7,Si) 13.5
V(O7,Si)	1.99	0.55	V(O7) 28.3; V(C6,O7) 8.1; 3×V(Si,H) 7.6

[a] Obtained from ELF analysis of B3LYP/6-311+G(2d,p) wave functions. The relative fluctuation $\lambda(\Omega_i)$ reflects the extent of basin population delocalization and %cross-exchange contribution refers to the percentage contribution of neighboring basins to the total basin population.

2.3.4 *Decarbonylation Involving Front-side Attack by the Methoxy Oxygen at Silicon*

The optimized transition-state geometry for intramolecular front-side nucleophilic attack by the methoxy oxygen O2 at silicon in conformer **C** of methoxy(siloxy)carbene, denoted $\mathbf{TS_{CH}}$, is shown in Fig. 2.10. Computed minimum-energy structures of the products, carbon monoxide and methyl silyl ether **H**, can also be found in Fig. 2.10. Relative to conformer **C** (cf. Fig. 2.1), there is considerable shrinkage of the ∠C6O7Si angle, along with modest lengthening of the O2-C6 and O7-Si bonds, and shortening of the C6-O7 bond in $\mathbf{TS_{CH}}$. These features are consistent with nucleophilic attack by the methoxy oxygen O2 at silicon, in concert with moderate O2-C6 and O7-Si bond dissociation, and C6-O7 triple-bond formation. We must point out that IRC calculations confirm that $\mathbf{TS_{CH}}$ corresponds to the transition state for decarbonylation of conformer **C**, which implies that the reaction is concerted. We also note that the dissociating O7-Si bond is shorter than the developing O2-Si bond in $\mathbf{TS_{CH}}$, indicative of an early transition state with a low activation barrier according to Hammond's postulate.[124]

Plots of bond distance versus intrinsic reaction coordinate (IRC) for decarbonylation of conformer **C** via $\mathbf{TS_{CH}}$ are shown in Fig. 2.11a. As mentioned earlier, negative IRC values correspond to the reactant side of the reaction coordinate, positive IRC values correspond to the product side of the reaction coordinate and an IRC value of zero corresponds to the transition state. The plots in Fig. 2.11a show that there is moderate lengthening of the O2-C6 and O7-Si bonds, and shortening of the C6-O7 bond, as the decarbonylation of **C** approaches $\mathbf{TS_{CH}}$. More importantly, they reveal the synchronicity of the reaction in that the rates of O2-C6 and O7-Si bond dissociation, and C6-O7 triple-bond formation, are essentially identical. Thus, it is clear from Fig. 2.11a

that decarbonylation of conformer **C** involving front-side nucleophilic attack by the methoxy oxygen O2 at silicon is a concerted reaction (i.e. one step process with no intermediates) that occurs with remarkable synchronicity (i.e. bond formation and dissociation occur at the same rate in going from reactant to the transition state).

Topological properties of the electronic density at pertinent BCPs for $\mathbf{TS_{CH}}$ are collected in Table 2.7. It can be seen from the table that a new O2-Si bond with low $\rho_b(r)$ and positive $\nabla^2\rho_b(r)$ develops in $\mathbf{TS_{CH}}$ as a result of the shrinkage of the ∠C6O7Si angle that reduces the distance between the O2 and Si atoms. At the same time, values of $\rho_b(r)$ for the lengthening O2-C6 and O7-Si bonds decrease slightly, while those for the shortening C6-O7 bond increase slightly, in $\mathbf{TS_{CH}}$ relative to **C** (cf. Table 2.1). These observations are consistent with slight O2-C6 and O7-Si bond dissociation, and modest C6-O7 triple-bond formation. The modest changes in $\rho_b(r)$ for the O2-C6, O7-Si and C6-O7 bonds are also reflected in the fact that the sign of $\nabla^2\rho_b(r)$ remains unchanged. Indeed, the sign of $\nabla^2\rho_b(r)$ for the O7-Si bond remains positive because of the inherent ionic character of this bond.[18] However, significant O2-C6 bond dissociation would normally be accompanied by a sign change in $\nabla^2\rho_b(r)$ from negative to positive.[121] As well, considerable C6-O7 triple-bond formation would result in a sign change in $\nabla^2\rho_b(r)$ from negative to positive, since $\nabla^2\rho_b(r)$ is positive for the C≡O triple bond.[18] We note that values of ε for the C6-O7 bond are close to zero in $\mathbf{TS_{CH}}$ reflecting the incipient cylindrical symmetry of the developing triple bond. In contrast, values of ε for the dissociating O2-C6 and O7-Si bonds increase in $\mathbf{TS_{CH}}$ relative to those for conformer **C** (cf. Table 2.1), indicative of the structural instability of these dissociating bonds.[122]

Plots of BCP electronic density versus IRC for decarbonylation of conformer **C** via $\mathbf{TS_{CH}}$ are shown in Fig. 2.11b. The plot basically shows the changes in BCP electronic density for the dissociating and developing bonds during the course of the reaction. It can be seen that the decrease in $\rho_b(r)$ for the O2-C6 and O7-Si bonds, as well as the increase in $\rho_b(r)$ for the C6-O7 bond, are moderate and occur essentially at the same rate as the reaction proceeds from conformer **C** towards $\mathbf{TS_{CH}}$. These observations offer further support to the notion that decarbonylation of conformer **C** involving front-side nucleophilic attack by the methoxy oxygen O2 at silicon is a concerted reaction that occurs with considerable synchronicity.

The ELF isosurface for $\mathbf{TS_{CH}}$ is displayed in Fig. 2.12 and corresponding ELF basin properties are provided in Table 2.8. It is evident that part of the V(O2) lone-pair basin in conformer **C** (cf. Fig. 2.2) turns into the V(O2,Si) bonding basin in $\mathbf{TS_{CH}}$. Also apparent from the figure is the fact that the V(O2,C6) and V(O7,Si) basins shift closer to the O2 and O7 nuclei respectively in going from **C** to $\mathbf{TS_{CH}}$, indicative of O2-C6 and O7-Si bond dissociation.[123] In fact, the V(O2,C6) and V(O7,Si) basins are located 0.632 Å and 0.633 Å away from the O2 and O7 nuclei respectively in **C**, while they are located 0.567 Å and 0.596 Å away from the O2 and O7 nuclei in $\mathbf{TS_{CH}}$. In addition, the V(O2,C6) and V(O7,Si) basin populations decrease, while the V(C6,O7) basin population increases in $\mathbf{TS_{CH}}$ relative to **C** (Table 2.2). These observations are in keeping with nucleophilic attack by the methoxy oxygen O2 at silicon, in concert with O2-C6 and O7-Si bond dissociation, and C6-O7 triple-bond formation.

It appears that since the $\sigma^*_{O7\text{-}Si}$ orbital is primarily localized on the more electropositive silicon atom, the destabilizing anti-bonding component of the $n_{O2} \rightarrow \sigma^*_{O7\text{-}Si}$

HOMO/LUMO interaction for nucleophilic attack by the methoxy oxygen O2 at silicon (cf. Scheme 2.5a) is small enough to allow this *symmetry-forbidden* reaction to be *concerted* and *synchronous*. Natural bond orbital (NBO) analysis[24] with the HF/6-311+G(2d,p) model chemistry reveals that the polarization coefficients for the $\sigma^*_{O7\text{-}Si}$ orbital of conformer **C** are 14% on O7 and 86% on Si. This means that $\sigma^*_{O7\text{-}Si}$ orbital lobes are considerably smaller on O7 than they are on Si (cf. Scheme 2.5a). Therefore, only modest O2-C6 and O7-Si bond dissociation is needed to overcome the destabilizing anti-bonding component of the $n_{O2} \rightarrow \sigma^*_{O7\text{-}Si}$ interaction between orbital lobes of opposite sign and at the same time allow favorable bonding interaction between lobes of the same sign. We note that the computed HF/6-311+G(2d,p), B3LYP/6-311+G(2d,p) and MP2/6-311+G(2d,p) dipole moments increase from 2.62, 2.70 and 2.72 D in conformer **C** to 3.60, 3.40 and 3.42 D in $\mathbf{TS_{CH}}$; increases that are consistent with the modest changes in geometry and electronic structure, and hence a concerted and synchronous process.

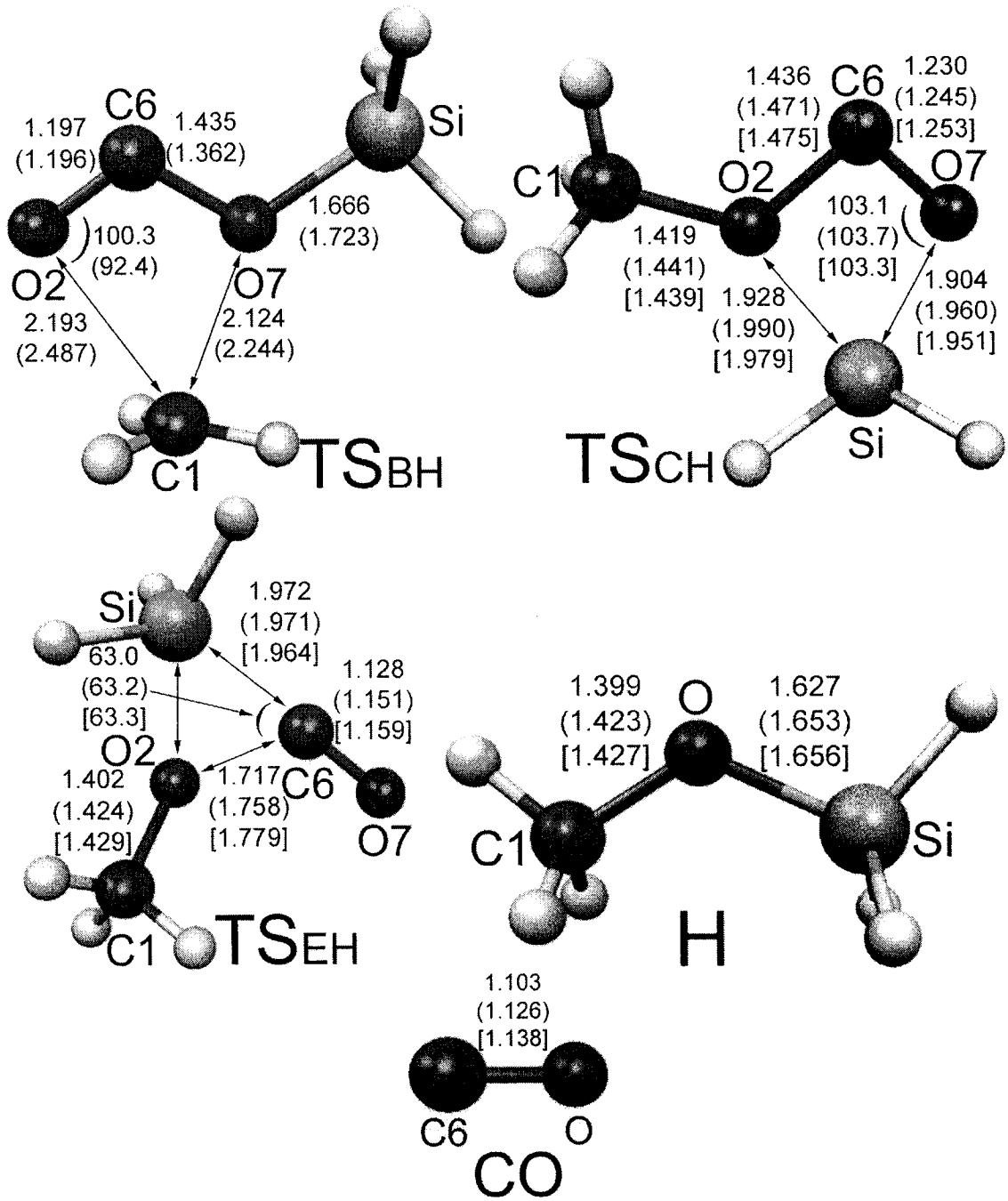

Figure 2.10 Optimized geometries of the transition states for decarbonylation of methoxy(siloxy)carbene and *syn*-methyl silylformate, along with products methyl silyl ether and carbon monoxide. Geometric parameters are given for HF/6-311+G(2d,p), B3LYP/6-311+G(2d,p) (parentheses) and MP2/6-311+G(2d,p) [brackets] model chemistries. Bond lengths and angles are given in Å and degrees respectively.

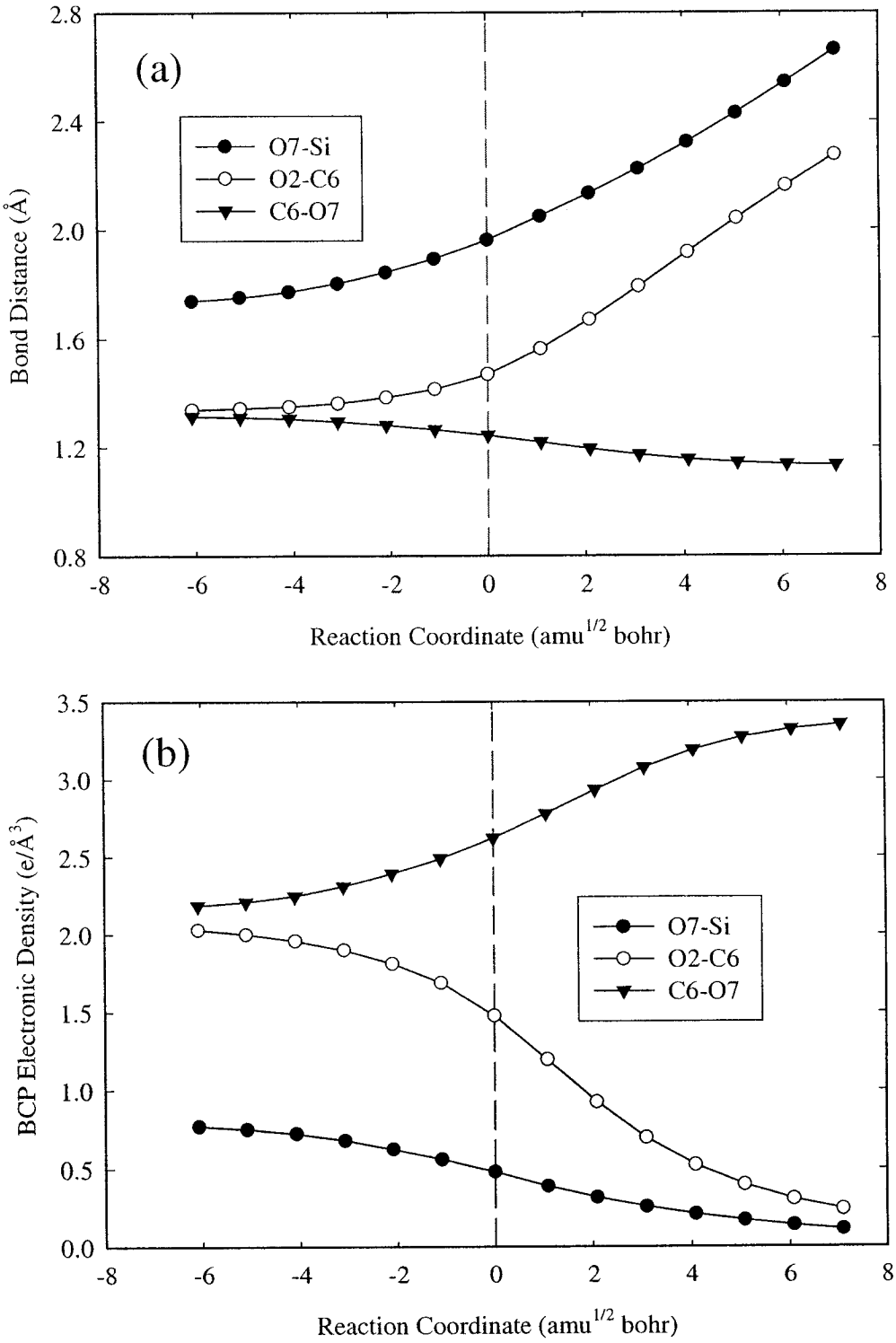

Figure 2.11 Plots of (a) bond distance versus intrinsic reaction coordinate and (b) BCP electronic density versus intrinsic reaction coordinate for decarbonylation of *trans-cis* methoxy(siloxy)carbene, based on IRC calculations with the B3LYP/6-311+G(2d,p) model chemistry.

Table 2.7 Topological properties of the electronic density at pertinent BCPs of the transition states for decarbonylation of methoxy(siloxy)carbene.[a]

	C1-O2	O2-C6	C6-O7	O7-Si	O2-Si
			TS_{CH}		
			HF/6-311+G(2d,p)		
$\rho_b(r)$ (e/Å^3)	1.59	1.55	2.73	0.50	0.42
$\nabla^2\rho_b(r)$ (e/Å^5)	-1.9	-4.5	-10.2	7.5	6.7
ε	0.01	0.98	0.02	0.10	0.45
			B3LYP/6-311+G(2d,p)		
$\rho_b(r)$ (e/Å^3)	1.53	1.48	2.62	0.48	0.41
$\nabla^2\rho_b(r)$ (e/Å^5)	-10.8	-10.2	-15.5	4.0	3.6
ε	0.01	0.27	0.01	0.13	0.47
			MP2/6-311+G(2d,p)		
$\rho_b(r)$ (e/Å^3)	1.54	1.43	2.61	0.45	0.38
$\nabla^2\rho_b(r)$ (e/Å^5)	-4.4	-8.4	-13.6	6.0	5.4
ε	0.02	0.81	0.02	0.15	0.51
	C1-O2	C1-O7	O2-C6	C6-O7	O7-Si
			TS_{BH}		
			HF/6-311+G(2d,p)		
$\rho_b(r)$ (e/Å^3)	0.30	0.31	2.93	1.54	0.89
$\nabla^2\rho_b(r)$ (e/Å^5)	2.8	3.0	-5.3	-7.0	18.8
ε	0.62	0.25	0.00	0.75	0.06
			B3LYP/6-311+G(2d,p)		
$\rho_b(r)$ (e/Å^3)	0.19	0.28	2.91	1.90	0.79
$\nabla^2\rho_b(r)$ (e/Å^5)	1.7	2.4	-7.3	-12.8	13.1
ε	0.13	0.12	0.00	0.26	0.06

[a] Obtained from AIM analysis.

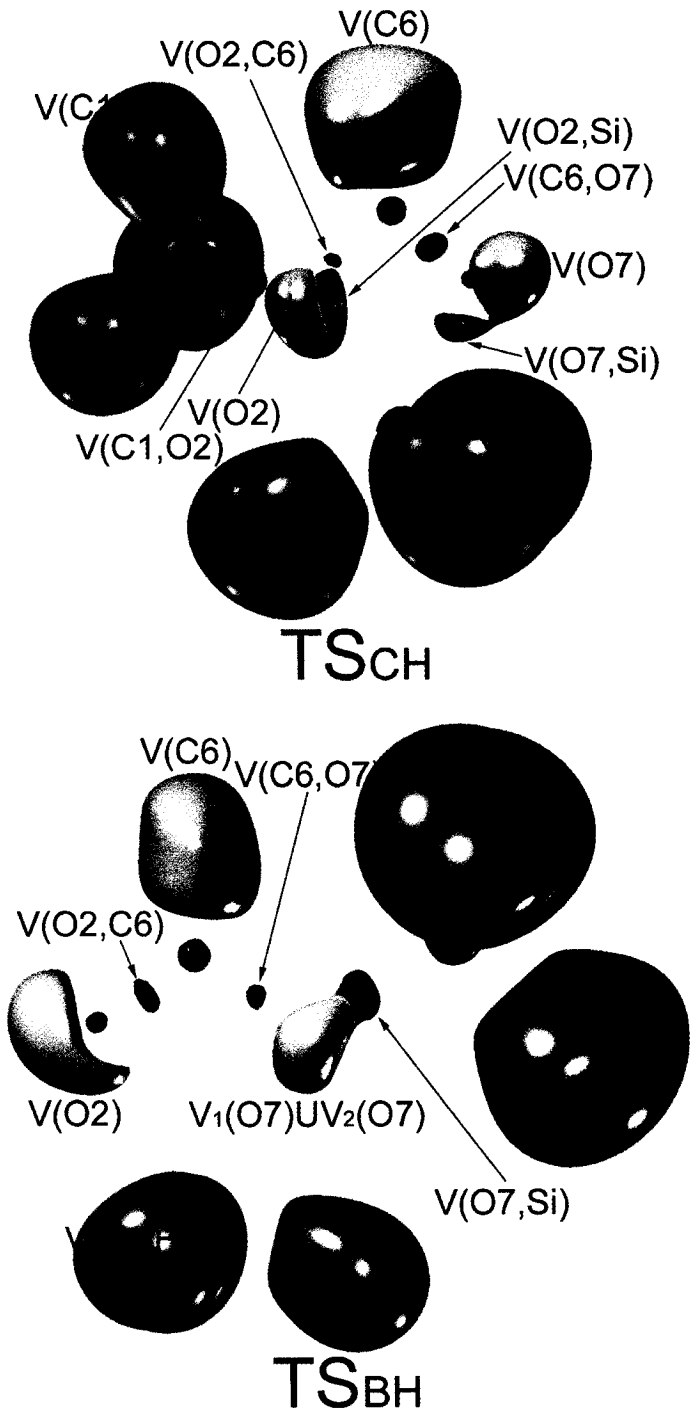

Figure 2.12 B3LYP/6-311+G(2d,p) ELF isosurfaces of the transition states for decarbonylation of methoxy(siloxy)carbene. The basins are core basins (purple), bonding valence basins (green), lone-pair valence basins (orange) and protonated valence basins (blue).

Table 2.8 Basin population $N(\Omega_i)$, relative fluctuation $\lambda(\Omega_i)$ and %cross-exchange contribution of the transition state for the decarbonylation of methoxy(siloxy)carbene.[a]

Basin	$N(\Omega_i)$	$\lambda(\Omega_i)$	%Cross-exchange contribution (covariance)
			TS_{CH}
V(C1,O2)	1.26	0.64	V(O2) 15.3; V(O2,Si) 18.6; 3×V(C1,H) 19.4
V(O2)	2.09	0.54	V(C1,O2) 9.1; V(O2,Si) 18.1; V(O2,C6) 9.1
V(O2,Si)	2.94	0.48	V(O2) 12.9; V(C1,O2) 7.8; V(O2,C6) 7.8;
V(O2,C6)	1.14	0.68	V(O2) 16.7; V(O2.Si) 20.2; V(C6) 9.7; V(C6,O7) 5.3
V(C6)	2.41	0.34	V(O2,C6); V(C6,O7) 7.1; V(O7) 6.7
V(C6,O7)	2.03	0.56	V(C6) 8.4; V(O7) 22.7; V(O7,Si) 11.8
V(O7)	3.56	0.40	V(C6,O7) 13.0; V(O7,Si) 13.3
V(O7,Si)	1.97	0.56	V(O7) 24.0; V(C6,O7) 12.2; 3×V(Si,H) 6.12
			TS_{BH}
V(O2)	5.08	0.30	V(O2,C6) 14.4; V(C6) 4.3
V(O2,C6)	2.24	0.54	V(O7) 32.7; V(C6) 8.1
V(C6)	2.09	0.47	V(O2) 10.3; V(O2,C6) 8.5; V(C6,O7) 5.7
V(C6,O7)	1.32	0.65	V_1(O7) 16; V_2(O7) 16.0; V(O7,Si) 6.9; V(O2,C6) 5.3; V(C6) 9.2
V_1(O7)	2.27	0.53	V_2(O7) 13.7; V(C6,O7) 9.4; V(O7,Si) 12.4
V_2(O7)	2.14	0.54	V_1(O7) 14.5; V(C6,O7) 9.8; V(O7,Si) 12.6
V(O7,Si)	1.71	0.58	V_1(O7) 16.5; V_2(O7) 15.9; V(C6,O7) 5.3; 3×V(Si,H) 7.64

[a] Obtained from ELF analysis of B3LYP/6-311+G(2d,p) wave functions. The relative fluctuation $\lambda(\Omega_i)$ reflects the extent of basin population delocalization and %cross-exchange contribution refers to the percentage contribution of neighboring basins to the total basin population.

2.3.5 *Decarbonylation Involving Front-side Attack by the Siloxy Oxygen at Carbon*

The computed molecular geometry of the transition state for decarbonylation of methoxy(siloxy)carbene involving intramolecular front-side nucleophilic attack by the siloxy oxygen O7 at the methyl carbon C1, denoted $\mathbf{TS_{BH}}$, is shown in Fig. 2.10. This geometry was obtained from optimizations with the HF/6-311+G(2d,p) and B3LYP/6-311+G(2d,p) model chemistries. We were unable to locate this transition state on the MP2/6-311+G(2d,p) potential energy surface.

Relative to conformer **B** (cf. Fig. 2.1), there is significant shrinkage of the ∠C1O2C6 angle in $\mathbf{TS_{BH}}$. This is accompanied by tremendous C1-O2 bond elongation, along with modest O2-C6 bond shortening and C6-O7 bond lengthening. These features are consistent with nucleophilic attack by the siloxy oxygen O7 at methyl carbon C1, in concert with significant C1-O2 bond cleavage, modest O2-C6 triple-bond formation and slight C6-O7 bond dissociation. The tremendous C1-O2 bond elongation, along with modest O2-C6 bond shortening and C6-O7 bond lengthening, suggests that considerable ionic character develops in the transition state resulting in characteristics resembling that of a tight ion-pair intermediate comprising a methyl cation and a siloxycarbonyl anion, as illustrated in Scheme 2.4b. In fact, the HF/6-311+G(2d,p) and B3LYP/6-311+G(2d,p) computed ∠HC1H angles in $\mathbf{TS_{BH}}$ are 117.8° and 118.3° respectively, which is close to the 120° angle expected for a methyl cation. However, IRC calculations confirm that $\mathbf{TS_{BH}}$ is the transition state for decarbonylation of conformer **B**, suggesting that the reaction is concerted. We also note that the dissociating C1-O2 bond is longer than the developing C1-O7 bond, which is indicative of a late transition state with a high activation barrier according to Hammond's postulate.[124]

Plots of bond distance versus IRC for decarbonylation of conformer **B** via $\mathbf{TS_{BH}}$ are shown in Fig. 2.13a. These plots clearly reveal that the rate of C1-O2 bond lengthening is significantly greater than the rate of O2-C6 bond shortening and C6-O7 bond lengthening as the reaction progresses from conformer **B** towards $\mathbf{TS_{BH}}$. Thus, it is apparent that even though the transition state for decarbonylation of conformer **B** involving front-side nucleophilic attack by the siloxy oxygen O7 at the methyl carbon C1 corresponds to a concerted reaction, it is an *asynchronous* process with significant C1-O2 bond fragmentation at the transition state.

Topological properties of the electronic density at selected BCPs for $\mathbf{TS_{BH}}$ are given in Table 2.7. The shrinkage of the ∠C1O2C6 angle in $\mathbf{TS_{BH}}$ relative to **B**(cf. Fig. 2.1), narrows the separation of the C1 and O7 atoms enough that it results in the appearance of a weak C1-O7 bond, as indicated by the low $\rho_b(r)$ and positive $\nabla^2\rho_b(r)$.[121] At the same time, values of $\rho_b(r)$ for the lengthening C1-O2 bond decrease dramatically, while they increase and decrease slightly for the shortening O2-C6 and lengthening C6-O7 bonds, respectively, in $\mathbf{TS_{BH}}$ relative to **B** (cf. Table 2.1). The features are consistent with nucleophilic attack by the siloxy oxygen O7 at the methyl carbon C1, in concert with tremendous C1-O2 bond dissociation, modest O2-C6 triple-bond formation and slight C6-O7 bond dissociation. Moreover, the sign of $\nabla^2\rho_b(r)$ for the C1-O2 bond changes from negative in **B** (cf. Table 2.1) to positive in $\mathbf{TS_{BH}}$ (cf. Table 2.7), while it remains unchanged for the O2-C6 and C6-O7 bonds, consistent with the magnitude of the changes in $\rho_b(r)$ observed.[121] We note that values of ε for the C1-O2 and C6-O7 bonds are quite large in $\mathbf{TS_{BH}}$ (cf. Table 2.7), consistent with bond fragmentation,[122] while they approach zero for the O2-C6 bond, indicative of the incipient cylindrical symmetry

usually associated with a triple bond.[18] We also note that the low $\rho_b(r)$ and positive $\nabla^2\rho_b(r)$ values for the C1-O2 and C1-O7 bonds in Table 2.7 are indicative of a weakly bound methyl group in $\mathbf{TS_{BH}}$;[121] features that can be associated with an ion-pair intermediate comprising a methyl cation and a siloxycarbonyl anion.

Fig. 2.13b contains plots of BCP electronic density versus IRC for the decarbonylation of conformer **B** via $\mathbf{TS_{BH}}$. The plots clearly show that the rate of decrease in $\rho_b(r)$ for the C1-O2 bond is substantially greater than the rate of increase in $\rho_b(r)$ for the O2-C6 bond and the rate of decrease in $\rho_b(r)$ for the C6-O7 bond, as the decarbonylation of **B** approaches $\mathbf{TS_{BH}}$. These observations support the notion that decarbonylation of conformer **B** involving front-side nucleophilic attack by the siloxy oxygen O7 at the methyl carbon C1 is asynchronous.

Figure 2.12 contains the ELF isosurface for $\mathbf{TS_{BH}}$ and the corresponding ELF basin properties are given in Table 2.8. Features resembling that of an ion-pair intermediate comprising a methyl cation and a siloxycarbonyl anion (cf. Scheme 2.4b) are reflected in the ELF isosurface. The two O2 lone pairs, the carbene C6 lone pair and the two O7 lone pairs of the apparent siloxycarbonyl anion are represented by the V(O2), V(C6) and $V_1(O7)\chi V_2(O7)$ basins, respectively, while the absence of V(C1,O2) and V(C1,O7) basins indicates that the apparent methyl cation and siloxycarbonyl anion are held together by ionic bonding.[20,21,23,44,114] In addition, the V(O2,C6) and V(C6,O7) basin populations 2.24 and 1.32 in $\mathbf{TS_{BH}}$ are consistent with an O2-C6 double bond and a C6-O7 single bond.

The asynchronous nature of this decarbonylation reaction may be due to the fairly sizeable destabilizing component of the $n_{O7} \rightarrow \sigma^*_{C1\text{-}O2}$ HOMO/LUMO interaction (cf.

Scheme 2.5a) because even though the $\sigma^*_{C1\text{-}O2}$ orbital is primarily localized on the more electropositive C1 atom, localization on the O2 atom is not insignificant. NBO analysis of the HF/6-311+G(2d,p) wave function for conformer **B** indicates that the polarization coefficients for the $\sigma^*_{C1\text{-}O2}$ orbital are 70% on C1 and 30% on O2 (compared to 86% on Si and 14% on O7 for the $\sigma^*_{O7\text{-}Si}$ orbital of conformer **C**). Thus, considerable C1-O2 or C6-O7 bond dissociation is required to overcome the destabilizing anti-bonding component of the $n_{O7} \rightarrow \sigma^*_{C1\text{-}O2}$ interaction between orbital lobes of opposite sign and simultaneously allow favorable bonding interaction between orbital lobes of the same sign (cf. Scheme 2.5a). In this case, there is greater dissociation of the weaker C1-O2 bond since, as discussed earlier, the C6-O7 bond of conformer **B** has double-bond character. Furthermore, significant C1-O2 bond dissociation effectively allows the n_{O2} and n_{O7} lone-pair orbitals to interact favorably with the "vacant cationic *p* orbital" on the C1 atom in $\mathbf{TS_{BH}}$ in a manner similar to that of a tight ion-pair intermediate made up of the methyl cation and the siloxycarbonyl anion, (cf. Scheme 2.5b). We also note that the computed HF/6-311+G(2d,p) dipole moment increases from 2.69 D in conformer **B** to 5.53 D in $\mathbf{TS_{BH}}$; an increase of 2.84 D (compared to a 0.98 D increase between conformer **C** and $\mathbf{TS_{CH}}$), consistent with the development of significant ionic character in the transition state.

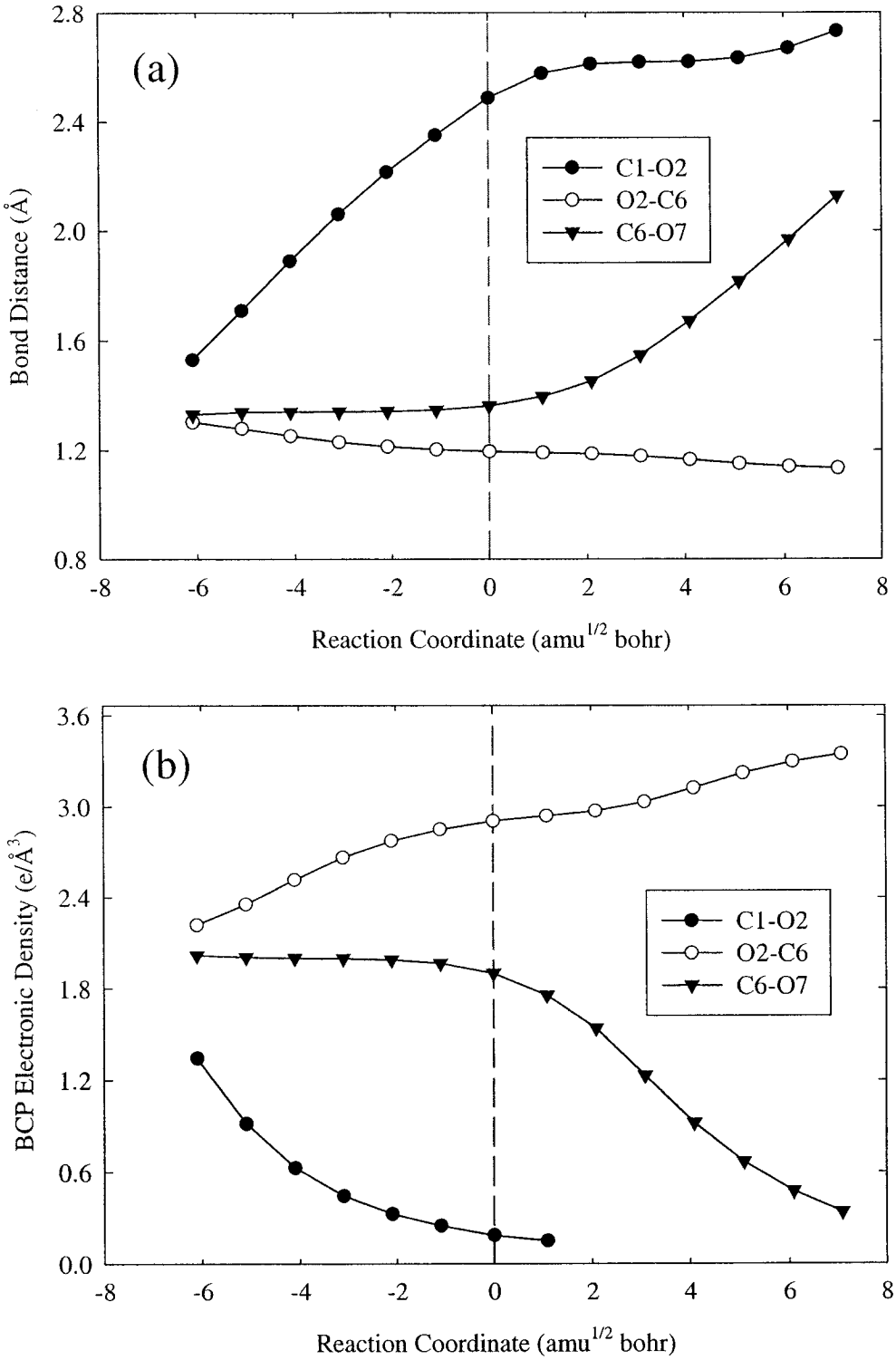

Figure 2.13 Plots of (a) bond distance versus intrinsic reaction coordinate and (b) BCP electronic density versus intrinsic reaction coordinate for decarbonylation of *cis-trans* methoxy(siloxy)carbene, based on IRC calculations with the B3LYP/6-311+G(2d,p) model chemistry.

2.3.6 Decarbonylation of Methyl Silylformate via the Brook Rearrangement

As discussed earlier, decarbonylation of methoxy(siloxy)carbene could involve initial 1,2-silyl migration followed by a Brook ester rearrangement, as outlined in Scheme 2.6. Since we have already discussed the mechanism for 1,2-silyl migration, we will dedicate this section to the mechanism for decarbonylation of methyl silylformate via the Brook rearrangement. Inspection of the computed HF/6-311+G(2d,p) frontier molecular orbitals of methyl silylformate revealed that the pertinent orbitals for nucleophilic attack by the methoxy oxygen O2 at silicon are the HOMO-1 and the LUMO+1 rather than the HOMO and LUMO. The HOMO-1 and LUMO+1 for *syn*-methyl silylformate **E** are shown in Fig. 2.14. It is obvious from these plots that the HOMO-1 has considerable n_{O2} character while the LUMO+1 has significant $\sigma^*_{C6\text{-}Si}$ character. However, the calculated HF/6-311+G(2d,p) energy gap between these orbitals is 14.8 eV, which may be too large for favorable interaction and thus, nucleophilic attack by the methoxy oxygen O2 at Si. In fact, this gap is comparable to the HOMO/LUMO gaps of dimethoxycarbene[56] and methoxyphenoxycarbene,[120] which rarely undergo intramolecular rearrangement.

The optimized transition-state geometry $\mathbf{TS_{EH}}$ for decarbonylation of *syn*-methyl silylformate **E** involving front-side nucleophilic attack by the methoxy oxygen O2 at silicon is shown in Fig. 2.10. IRC calculations confirmed that $\mathbf{TS_{EH}}$ is the transition state for decarbonylation of **E**. Relative to **E** (cf. Fig. 2.4), there is tremendous shrinkage of the ∠O2C6Si angle and elongation of the O2-C6 bond, along with modest C6-O7 bond shortening and C6-Si bond lengthening in $\mathbf{TS_{EH}}$. In addition, the methyl group rotates out-of-plane in $\mathbf{TS_{EH}}$, most likely for better alignment of an O2 lone pair with Si. These observations are in keeping with nucleophilic attack by the methoxy oxygen O2 at

silicon, in concert with O2-C6 and C6-Si bond dissociation, and C6-O7 triple-bond formation. Moreover, the plots of bond distance versus IRC provided in Appendix B (cf. Fig. B2a) clearly show that the rate of O2-C6 bond lengthening is considerably greater than the rate C6-Si bond elongation as decarbonylation of **E** approaches $\mathbf{TS_{EH}}$, indicative of an asynchronous process.

Table 2.9 contains topological properties of the electronic density at selected BCP for **E** and $\mathbf{TS_{EH}}$. It is apparent that nucleophilic attack by O2 at Si in **E** results in the development of a weak O2-Si bond with low $\rho_b(r)$ and a positive $\nabla^2\rho_b(r)$ in $\mathbf{TS_{EH}}$. Simultaneously, $\rho_b(r)$ decreases tremendously for the dissociating O2-C6 bond and slightly for the dissociating C6-Si bond, while it increases noticeably for the developing C6-O7 triple bond in $\mathbf{TS_{EH}}$ relative to **E**. In addition, plots of the BCP electronic density versus IRC given in Appendix B (cf. Fig. B2b), reveal that the rate of decrease in $\rho_b(r)$ for the O2-C6 bond is significantly greater than that for the C6-Si bond, which is a reflection of the asynchronous nature of this intramolecular reaction.

ELF isosurfaces for **E** and $\mathbf{TS_{EH}}$ are shown in Fig. 2.15 and corresponding topological properties can be found in Table 2.10. It can be seen from the ELF isosurfaces that part of the V(O2) basin in **E** is converted into the V(O2,Si) basin in $\mathbf{TS_{EH}}$, consistent with nucleophilic attack by O2 at Si, while the V(O2,C6) basin in **E** disappears in $\mathbf{TS_{EH}}$, indicative of complete O2-C6 bond fragmentation. However, the V(C6,Si) basin population for the dissociating C6-Si bond actually increases in $\mathbf{TS_{EH}}$ relative to **E**, most likely as a result of additional cross exchange with the developing V(O2,Si) basin. Also, the V(C6,O7) basin population increases while the

$V_1(O7) \cup V_2(O7)$ superbasin is reduced to a single V(O7) basin with a smaller population in going from **E** to $\mathbf{TS_{EH}}$, consistent with C6-O7 triple-bond formation.

The asynchronous nature of the Brook rearrangement of *syn*-methyl silylformate **E** can be attributed to the fairly sizeable destabilizing anti-bonding component of the $n_{O2} \rightarrow \sigma^*_{C6\text{-}Si}$ interaction (cf. Scheme 2.5c), because even though the $\sigma^*_{C6\text{-}Si}$ orbital is primarily localized on Si, there is still a considerable degree of localization on C6. NBO analysis of the HF/6-311+G(2d,p) wave function for **E** revealed that the polarization coefficients for the $\sigma^*_{C6\text{-}Si}$ bond are 69% on Si and 31% on C6. This means that tremendous O2-C6 bond dissociation is necessary to overcome the destabilizing anti-bonding component of the $n_{O2} \rightarrow \sigma^*_{C6\text{-}Si}$ interaction between orbital lobes of opposite sign and allow favorable bonding interaction between orbital lobes of the same sign. We note that $\mathbf{TS_{EH}}$ has significant ionic character which is reflected in the low $\rho_b(r)$ values and the positive $\nabla^2\rho_b(r)$ values of the O2-C6 bond, as well as the O2-Si and C6-Si bonds (cf. Table 2.9). This is in keeping with experimental findings that the rate of decarbonylation of ester **III** is much faster in relatively polar methanol than it is in non-polar benzene.[86]

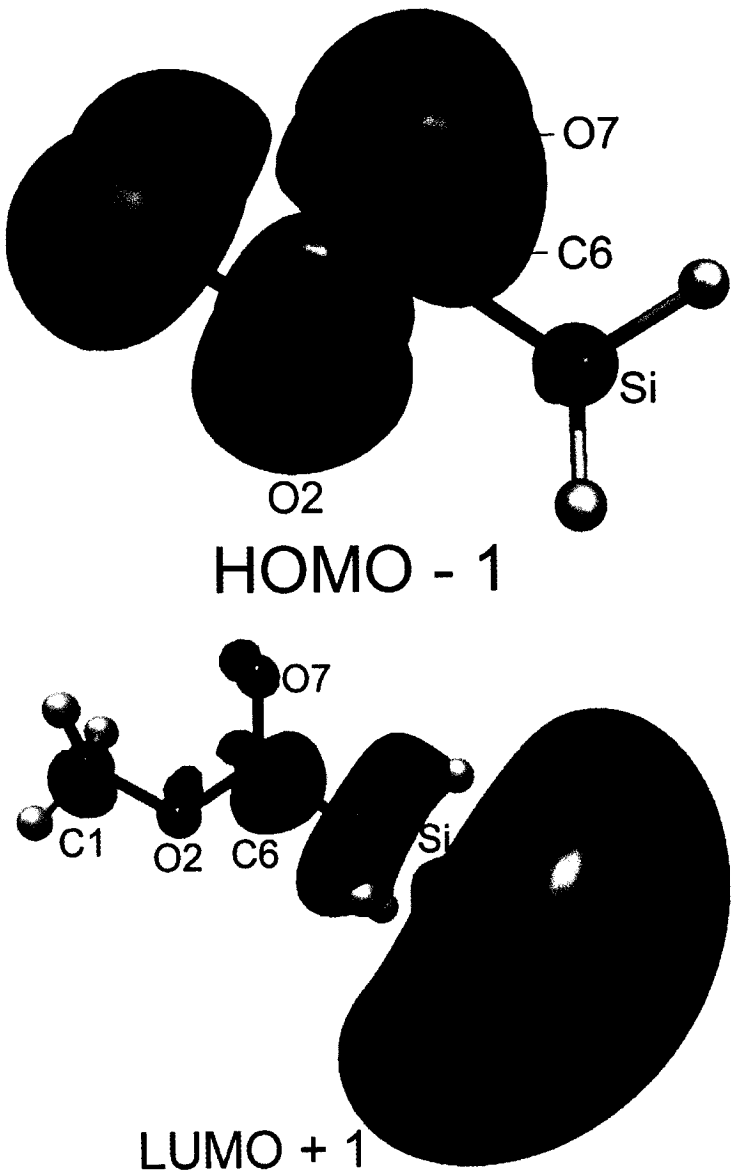

Figure 2.14 Computed HF/6-311+G(2d,p) frontier molecular orbitals for *syn*-methyl silylformate.

Table 2.9 Topological properties of the electronic density at pertinent BCPs for *syn*-methyl silylformate and its decarbonylation transition state.[a]

	C1-O2	O2-C6	C6-O7	C6-Si	O2-Si
			E		
			HF/6-311+G(2d,p)		
$\rho_b(r)$ (e/Å^3)	1.65	2.14	3.04	0.78	
$\nabla^2\rho_b(r)$ (e/Å^5)	-5.0	-10.1	-5.04	4.1	
ε	0.00	0.09	0.09	0.07	
			B3LYP/6-311+G(2d,p)		
$\rho_b(r)$ (e/Å^3)	1.60	2.04	2.87	0.77	
$\nabla^2\rho_b(r)$ (e/Å^5)	-12.4	-17.1	-12.7	2.1	
ε	0.00	0.00	0.09	0.08	
			MP2/6-311+G(2d,p)		
$\rho_b(r)$ (e/Å^3)	1.59	1.99	2.77	0.75	
$\nabla^2\rho_b(r)$ (e/Å^5)	-12.3	-15.8	-10.6	3.5	
ε	0.00	0.01	0.10	0.07	
			TS_{EH}		
			HF/6-311+G(2d,p)		
$\rho_b(r)$ (e/Å^3)	1.73	0.87	3.43	0.42	0.54
$\nabla^2\rho_b(r)$ (e/Å^5)	-8.4	3.7	8.5	7.0	5.7
ε	0.02	0.28	0.08	0.42	0.20
			B3LYP/6-311+G(2d,p)		
$\rho_b(r)$ (e/Å^3)	1.68	0.82	3.21	0.44	0.56
$\nabla^2\rho_b(r)$ (e/Å^5)	-13.9	4.5	0.1	4.7	3.8
ε	0.01	0.24	0.04	0.59	0.18
			MP2/6-311+G(2d,p)		
$\rho_b(r)$ (e/Å^3)	1.65	0.79	3.10	0.43	0.55
$\nabla^2\rho_b(r)$ (e/Å^5)	-13.6	4.6	3.9	5.0	4.9
ε	0.02	0.28	0.02	0.49	0.24

[a] Obtained from AIM analysis.

Table 2.10 Basin population $N(\Omega_i)$ relative fluctuation $\lambda(\Omega_i)$ and %cross-exchange contribution for *syn*-methyl silylformate and its transition state for decarbonylation.[a]

Basin	$N(\Omega_i)$	$\lambda(\Omega_i)$	%Cross Exchange Contribution (covariance)
			E
V(C1,O2)	1.40	0.62	V(O2) 29.3; V(O2,C6) 6.4; 3×V(C1,H) 18.6
V(O2)	4.50	0.34	V(C1,O2) 9.2; V(O2,C6) 10.5
V(O2,C6)	1.58	0.61	V(O2) 30.3; V(C6,Si) 7.1; V(C1,O2) 5.8; V(C6,O7) 5.8
V(C6,O7)	2.22	0.57	V_1(O7) 17.8; V_2(O7) 17.4; V(C6,Si) 7.8; V(C6,O7) 4.1
V_1(O7)	2.75	0.45	V_2(O7) 18.5; V(C6,O7) 14.2
V_2(O7)	2.65	0.46	V_1(O7) 19.2; V(C6,O7) 14.3
V(C6,Si)	2.34	0.45	V(C6,O7) 7.4; V(O2,C6) 4.8; 3×V(Si,H) 11.7
			TS_{EH}
V(C1,O2)	1.21	0.66	V(O2) 25.2; V(O2,Si) 13.4; 3×V(C1,H) 20.1
V(O2)	3.89	0.40	V(C1,O2) 7.7; V(O2,Si) 14.4
V(O2,Si)	2.15	0.54	V(O2) 25.9; V(C1,O2) 7.4
V(C6,O7)	2.67	0.51	V(C6,Si) 9.5; V(O7) 32.6
V(O7)	4.82	0.30	V(C6,O7) 17.9, V(C6,Si) 4.8
V(C6,Si)	2.70	0.43	V(O7) 8.5; V(C6,O7) 9.3; V(O2,Si) 4.1; V(O2) 6.7; 3×V(Si,H) 7.0

[a] Obtained from ELF analysis of B3LYP/6-311+G(2d,p) wave functions. The relative fluctuation $\lambda(\Omega_i)$ reflects the extent of basin population delocalization and %cross-exchange contribution refers to the percentage contribution of neighboring basins to the total basin population.

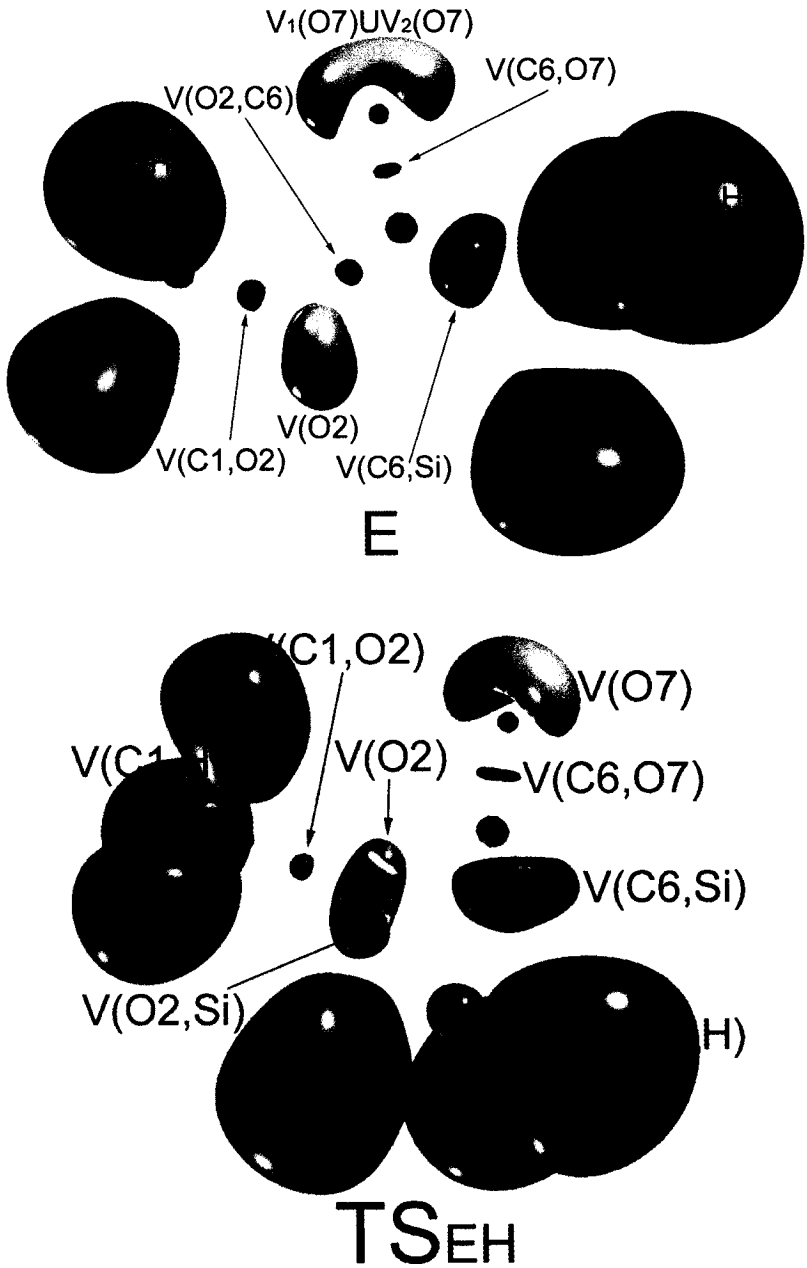

Figure 2.15 B3LYP/6-311+G(2d,p) ELF isosurfaces for *syn*-methyl silylformate and its decarbonylation transition state. The basins are core basins (purple), bonding valence basins (green), lone-pair valence basins (orange) and protonated valence basins (blue).

2.3.7 *Thermodynamics of Methoxy(siloxy)carbene Rearrangements*

Relative Gibbs free energies and relative enthalpies with respect to conformer **A** of methoxy(siloxy)carbene are given in Table 2.11. These data reveal that of the three ground-state conformers of methoxy(siloxy)carbene (cf. Fig. 2.1), conformer **A** is the most stable. The barriers for *trans-trans* to *cis-trans* isomerization (via $\mathbf{TS_{AB}}$) are noticeably higher than those for *trans-trans* to *trans-cis* isomerization (via $\mathbf{TS_{AC}}$), which suggests that the O2-C6 bond of conformer **A** has more double-bond character than the C6-O7 bond. As a matter of fact, $\rho_b(r)$ for the O2-C6 bond of **A** is greater than that for the C6-O7 bond according to AIM analysis (cf. Table 2.1), while the V(O2,C6) basin population for the O2-C6 bond of **A** is slightly greater than the V(C6,O7) basin population for the C6-O7 bond according to ELF analysis (cf. Table 2.2). These findings support the notion that the O2-C6 bond of conformer **A** has greater double-bond character than the C6-O7 bond.

Let us now consider the energetics of 1,2-silyl and 1,2-methyl migration in methoxy(siloxy)carbene. The barriers for 1,2-silyl migration in conformers **A** and **B** of methoxy(siloxy)carbene (via $\mathbf{TS_{AD}}$ and $\mathbf{TS_{BE}}$) are considerably lower than those for 1,2-methyl migration in conformer **A** and **C** (via $\mathbf{TS_{AF}}$ and $\mathbf{TS_{CG}}$), as evident from Table 2.11 and the relative Gibbs free-energy profile in Fig. 2.16. These observations are in keeping with predictions made earlier on the basis of FMO theory. We note that the HF/6-311+G(d,p) barriers appear to be overestimated as is usually the case, due to the neglect of electron correlation energy.[26,39,40,125] However, computed B3LYP and MP2 barriers have been found to be fairly reliable when compared to experimental data.[26,39,40,61] The B3LYP/6-311+G(2d,p) and MP2/6-311+G(2d,p) Gibbs free-energy

barriers for 1,2-silyl migration seem quite reasonable when compared with the experimentally determined Gibbs free energy barrier of 9.9 kcal/mol for 1,2-benzoyl migration in phenylbenzyloxycarbene.[61]

We now turn to the energetics of methoxy(siloxy)carbene decarbonylation. It is evident from Table 2.11 and the Gibbs free-energy profile Fig. 2.17 that the decarbonylation pathway involving front-side nucleophilic attack by the methoxy oxygen O2 at silicon in conformer **C** (via $\mathbf{TS_{CH}}$) is much more favorable than that involving front-side nucleophilic attack by the siloxy oxygen O7 at the methyl carbon C1 in conformer **B** (via $\mathbf{TS_{BH}}$). These results are in accord with predictions made earlier on the basis of FMO theory and Hammond's postulate. The decarbonylation pathway involving initial 1,2-silyl migration in the methoxy(siloxy)carbene conformer **B** (via $\mathbf{TS_{BE}}$) followed by a Brook rearrangement of *syn*-methyl silylformate **E** (via $\mathbf{TS_{EH}}$) is also unfavorable because of the thermodynamic stability of **E**. The finding that the Brook rearrangement of **E** involving front-side nucleophilic attack by the methoxy oxygen O2 at silicon (via $\mathbf{TS_{EH}}$) is energetically unfavorable is also in keeping with the predictions made earlier on the basis of FMO theory.

Table 2.11 Relative Gibbs free energies and enthalpies for intramolecular rearrangement of methoxy(siloxy)carbene.[a]

	HF/6-311+G(2d,p)		B3LYP/6-311+G(2d,p)		MP2/6-311+G(2d,p)	
	ΔG	ΔH	ΔG	ΔH	ΔG	ΔH
A	0.0	0.0	0.0	0.0	0.0	0.0
B	3.5	2.9	2.2	1.8	1.9	1.4
C	3.5	2.9	2.2	1.8	1.9	1.4
TS_{AB}	17.2	16.5	17.6	17.2	18.8	18.0
TS_{AC}	7.3	6.7	7.6	6.8	8.4	7.9
D	-7.2	-7.2	-15.8	-15.9	-17.4	-17.5
E	-15.5	-15.6	-24.4	-23.1	-26.0	-24.7
TS_{AD}	20.1	19.6	10.6	9.9	9.0	8.4
TS_{BE}	20.1	18.8	9.5	9.1	8.1	7.4
F	-50.3	-50.4	-53.1	-53.2	-57.6	-57.7
G	-56.8	-57.6	-58.9	-59.6	-63.8	-64.3
TS_{AF}	61.1	60.7	45.3	45.2	45.4	45.2
TS_{CG}	62.0	61.3	45.8	45.2	46.1	45.3
H + CO	-51.9	-41.2	-42.4	-31.7	-48.9	-38.2
TS_{BH}	67.7	67.7	40.0	40.4	-	-
TS_{CH}	27.6	27.3	19.5	19.7	17.8	17.8
TS_{EH}	25.3	25.4	10.1	9.8	5.2	5.0

[a] Gibbs free energies and enthalpies are in kcal/mol at 298.15 K and 1.0 atm all relative to **A**. HF/6-311+G(2d,p), B3LYP/6-311+G(2d,p) and MP2/6-311+G(2d,p) Gibbs free energies for **A** are -517.887744, -519.782877, -518.709658 hartrees respectively, while the relative enthalpies are -517.848743, -519.743471, and -518.670694 hartrees respectively.

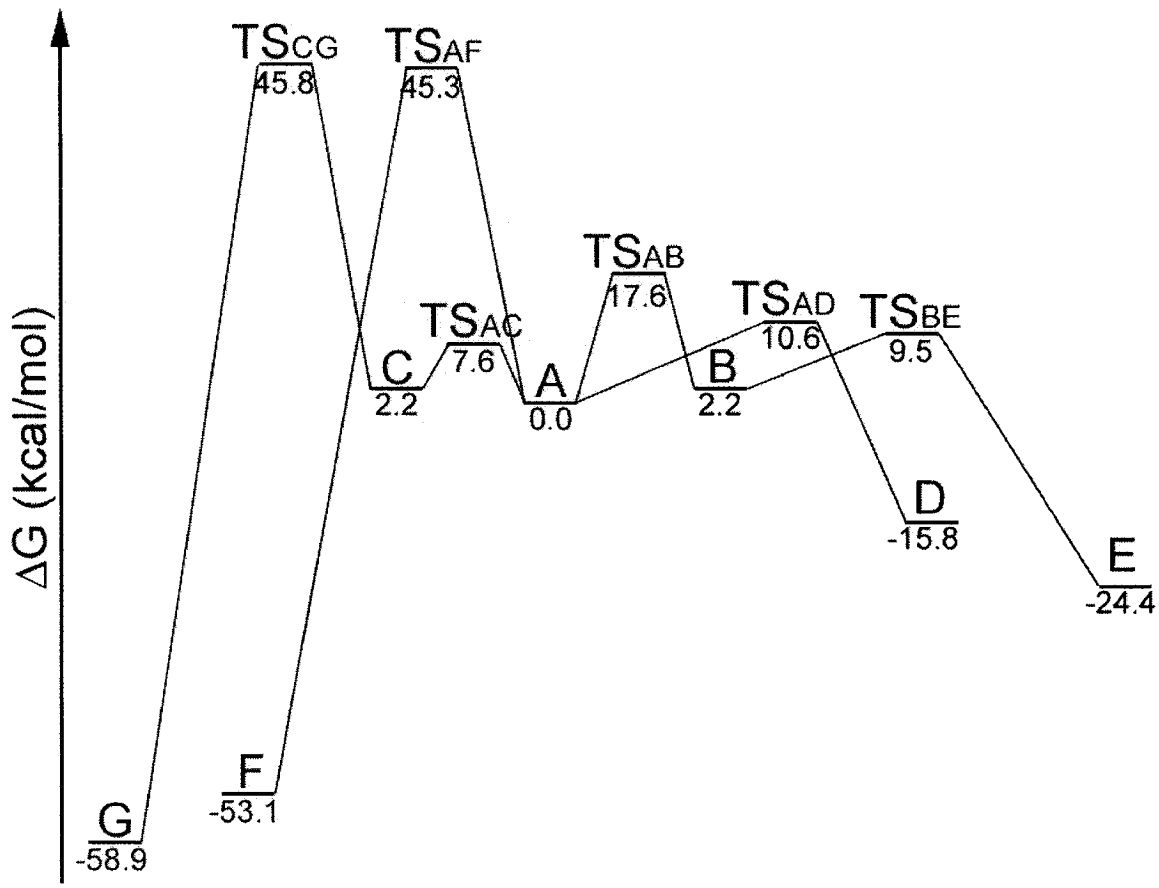

Figure 2.16 Relative B3LYP/6-311+G(2d,p) Gibbs free-energy profile for 1,2-silyl and 1,2-methyl migration in methoxy(siloxy)carbene at 298.15 K and 1.0 atm.

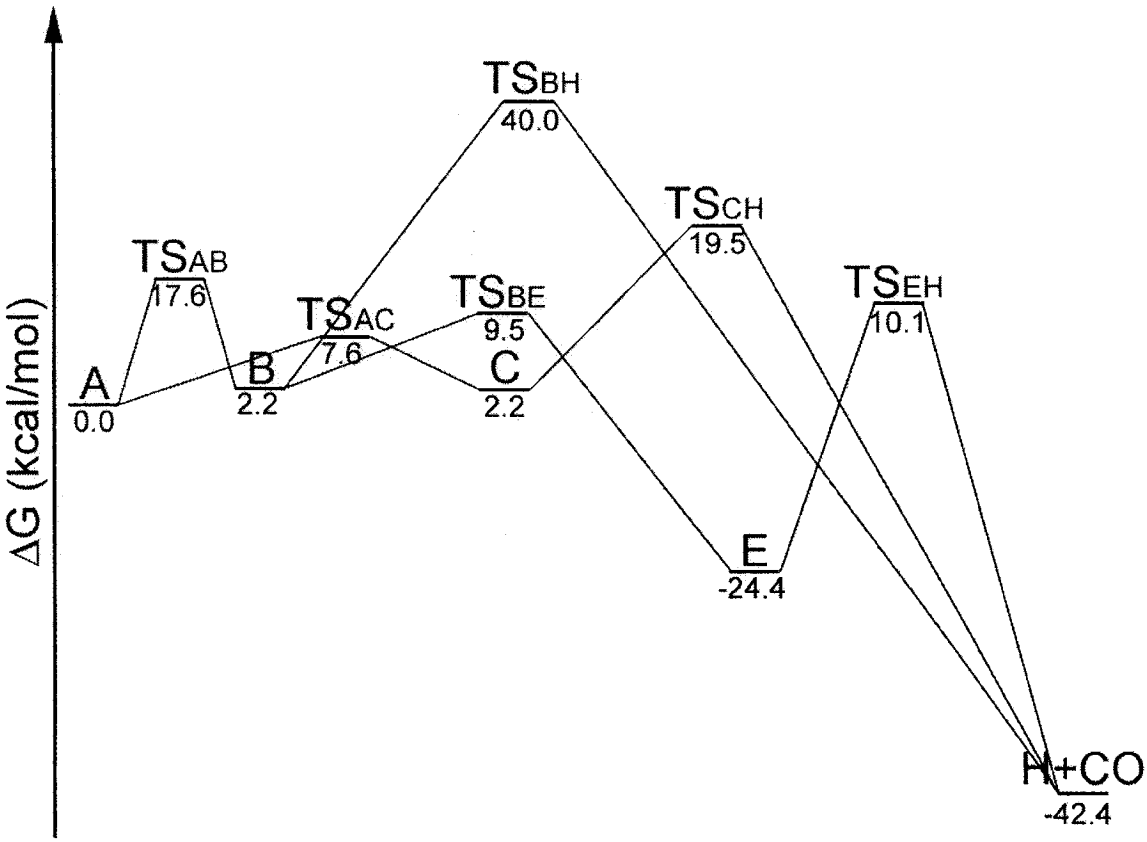

Figure 2.17 Relative B3LYP/6-311+G(2d,p) Gibbs free energy profile for decarbonylation pathways of methoxy(siloxy)carbene at 298.15 K and 1.0 atm.

2.4 Conclusion

Ab initio molecular orbital theory and hybrid density-functional theory calculations combined with frontier molecular orbital (FMO) theory, the quantum theory of atoms in molecules (AIM) and the electron-localization function (ELF) were used to investigate the mechanisms of 1,2-silyl migration, 1,2-methyl migration and decarbonylation of methoxy(siloxy)carbene. It was found that 1,2-silyl migration occurs via front-side nucleophilic attack by the carbene lone pair at silicon, which is *symmetry-forbidden* according to Woodward-Hoffman rules. In contrast, 1,2-methyl migration was shown to involve an anion-like shift of the methyl group from oxygen to the "vacant" carbene *p* orbital, a *symmetry-allowed* process. However, the *symmetry-forbidden* 1,2-silyl migration turns out to be considerably more favorable than the *symmetry-allowed* 1,2-methyl migration according to the computed reaction energetics.

For decarbonylation of methoxy(siloxy)carbene, pathways involving intramolecular front-side nucleophilic attack by the methoxy oxygen at silicon and by the siloxy oxygen at the methyl carbon, as well as that involving initial 1,2-silyl migration followed by a Brook ester rearrangement, were investigated. The pathway involving front-side nucleophilic attack by the methoxy oxygen at silicon was found to be *concerted* and *synchronous*. On the contrary, even though the pathway involving front-side nucleophilic attack by the siloxy oxygen at the methyl carbon was found to be *concerted*, it was *asynchronous*, with transition-state features resembling that of a tight ion-pair intermediate comprising a methyl cation and a siloxycarbonyl anion. Of the three decarbonylation pathways investigated, it appears that that involving front-side nucleophilic attack by the methoxy oxygen at silicon is the most viable energetically.

Chapter 3
Substituent Effects and the Role of Hyperconjugation in Siloxycarbene Rearrangements

3.1 Introduction

In the previous chapter, we presented evidence indicating that 1,2-silyl migration from oxygen to the carbene carbon of methoxy(siloxy)carbene involves front-side nucleophilic attack by the carbene lone pair at silicon. We also provided evidence showing that decarbonylation of methoxy(siloxy)carbene occurs via front-side nucleophilic attack by the methoxy oxygen at silicon. Since the proposed mechanisms are *symmetry-forbidden* (cf. Scheme 2.3b and 2.5a) and somewhat unique, we thought that it would be of interest to investigate the effects of substituents on these intramolecular rearrangements. In addition, an investigation of substituent effects would provide a convenient opportunity to examine the role of hyperconjugation in these intramolecular rearrangements.

Substituent effects are most often evaluated in terms of Hammett free-energy relationships. These relationships have provided valuable insight into the mechanisms of a number of singlet carbene rearrangements and reactions.[31,35,61,65,126,127] For example, Su and Thornton[31] and Liu and Bonneau[35] investigated the effects of substituents on 1,2-H migrations in a number of *p*-substituted benzylmethylcarbenes and *p*-substituted benzylchlorocarbenes, respectively. Logarithmic plots of the rate constants (log *k*) versus substituent constants (σ_p and σ^+) yielded Hammett reaction constants (ρ) close to -1.0, consistent with the positive charge development at the migration origin that accompanies a hydride-like shift to the vacant carbene *p* orbital. Similarly, Moss *et al.* investigated 1,2-acyl migrations in phenylacyloxycarbenes.[61] A Hammett plot of log *k* versus σ_p for

1,2-benzoyl migrations in *p*-substituted benzoyloxyphenylcarbenes afforded a ρ value of -0.96, in keeping with nucleophilic attack by the carbene lone pair at the acyl carbon. In other words, π-electron-donating substituents stabilize the acyl moiety in the transition state as it migrates with cation-like character to the carbon lone pair.[128] A variant of the Hammett relationship known as the *dual-substituent-parameter* (DSP) *equation*,[129] has also been applied to studies of carbene reactivity.[126,127] For example, Rondan *et al.*[126] and Moss *et al.*[127] examined the dependence of carbene stabilization energies and the carbene selectivity index on σ^+_R and σ_I for the cycloaddition of singlet carbenes to alkenes. In both studies, the coefficients of σ^+_R and σ_I were negative and positive, respectively, indicating that π-electron-donating and σ-electron-withdrawing substituents stabilize carbenes and increase their selectivity.

It is widely believed that hyperconjugation dictates which rearrangements predominate when multiple rearrangements of singlet carbenes are possible. For example, Nickon *et al.*,[130] Freeman *et al.*[131] and Kyba *et al.*[132] found that 1,2-H migrations in 2-norbornylidenes occur preferentially from the *exo* position rather than the *endo* position. Similarly, Press and Shechter,[133] and Kyba *et al.*,[134,135] reported that 1,2-H migrations in cyclohexylidenes occur with a noticeable preference for *axial* migration over *equatorial* migration. The observed selectivities have been attributed to stronger hyperconjugative interaction between the *exo* C-H bond and the vacant carbene *p* orbital in 2-norbonylidenes, and between the *axial* C-H bond and the vacant carbene *p* orbital in cyclohexylidenes. These findings are supported by ab initio calculations which have revealed that the *exo* C-H bond is longer than the *endo* C-H bond in 2-norbornylidenes, and that the *axial* C-H bond is longer than its *equatorial* counterpart in cyclohexylidenes.

There have also been reports that 1,2-H migrations in singlet alkylchlorocarbenes bearing β-electronegative substituents X afford the thermodynamically less stable *Z*-alkene isomers as the major products over their *E*-alkene counterparts.[32,33,136-138] The observed Z-selectivity is believed to be due to the fact that the *cis*-carbene conformers are more stable that the corresponding *trans*-carbene conformers.[32,33,42,136-139] The greater stabilization of the *cis*-carbene conformers arises from *negative hyperconjugative interaction* between the carbene lone-pair orbital and the $\sigma^*_{C\text{-}X}$ anti-bonding orbital, which is unlikely in the *trans*-carbene conformers because of poor orbital alignment.

In this chapter, we report the results from our investigation of substituent effects and the role of hyperconjugation in 1,2-silyl migration and decarbonylation of methoxy(substituted-siloxy)carbenes,[140] which afford methyl substituted-silylformates and methyl substituted-silyl ethers, respectively, as outlined in Scheme 3.1. We will first discuss the molecular geometries and electronic structures of the carbene conformers as a function of substituents, as well as the changes in molecular geometries and electronic structures during the carbene rearrangements. We will then discuss the effects of substituents in terms of Hammett free-energy relationships and assess the role of hyperconjugation in the intramolecular carbene rearrangements.

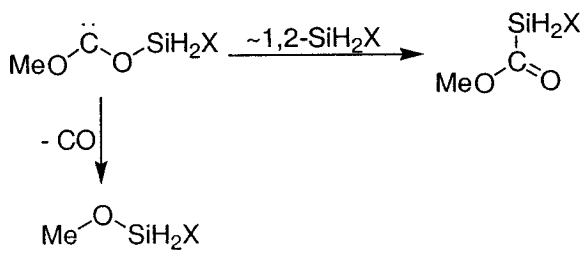

X = -H, -F, -Cl, -OH, -SH, $-NH_2$, -CN, -CCH

Scheme 3.1

3.2 Computational Methods

Ab initio molecular orbital theory calculations at the Hartree-Fock (HF) and second-order Møller-Plesset (MP2) levels of theory,[100,101] and density functional theory calculations using the Becke three-parameter hybrid-exchange functional with the Lee-Yang-Parr correlation potential (B3LYP)[101-103] were performed with the 6-311+G(2d,p) basis set[100,101] using the Gausian98 suite of programs.[110] Minimum-energy and transition-state geometries were obtained using the Berny algorithm[106] and the eigenvector following method[107-109] respectively, and frequency calculations were performed for stationary-point characterization. Thermochemical data were obtained within the rigid-rotor harmonic-oscillator approximation using standard statistical methods implemented in Gaussian98.[111] Natural bond orbital (NBO) analysis was performed to determine atomic charges from natural population analysis (NPA) and to obtain stabilization energies due to hyperconjugation which were estimated from second-order perturbation-energy analysis and calculated by deletion of the appropriate Fock matrix elements,[24] using the NBO program version 3.1[141] available in Gaussian98. Atoms in molecules (AIM) analysis[18] was also carried out to determine bond critical point[116] (BCP) electronic densities $\rho_b(r)$ using the AIMPAC suite of programs.[18,112,113] Brief descriptions of the ab initio and DFT methods used, as well as AIM and NBO, are provided in Appendix A.

3.3 Results and Discussion

3.3.1 Changes in Molecular Geometry

Figures 3.1, 3.2 and 3.3 display minimum-energy geometries of the *trans-trans* **A(X)**, *cis-trans* **B(X)** and *trans-cis* **C(X)** conformers of a number of methoxy(substituted-siloxy)carbenes.[142] Optimized molecular geometries of the transition states for 1,2-silyl migration in conformers **A(X)** and **B(X)**, denoted $\mathbf{TS_{AD}(X)}$ and $\mathbf{TS_{BE}(X)}$, are shown in Figs. 3.4 and 3.5, while those for decarbonylation of conformers **C(X)**, denoted $\mathbf{TS_{CH}(X)}$, are shown in Fig. 3.6. Interestingly, it appears that the presence of σ-electron-withdrawing substituents on the silyl moiety of the carbene conformers causes the ∠C6O7Si angle to shrink, the O7-Si and O2-C6 bonds to shorten, and the C6-O7 and C1-O2 bonds to lengthen. As a matter of fact, good linear correlations are obtained for plots of the ∠C6O7Si angle and the O7-Si, C6-O7, O2-C6 and C1-O2 bond lengths versus Swain-Lupton modified Hammett substituent constants,[143,144] σ_I. Plots of the ∠C6O7Si angle and the O7-Si bond length versus σ_I for conformers **A(X)** are shown in Fig. 3.7, while those for conformers **B(X)** and **C(X)** are available in Appendix C (cf. Figs. C1 to C4). In addition, plots of the C1-O2, O2-C6 and C6-O7 bond lengths versus σ_I for conformers **A(X)**, **B(X)** and **C(X)** are provided in Appendix C (cf. Figs. C5 to C13). It is worthy to note that the dependence of the ∠C6O7Si angle on σ_I is considerably greater for conformers **A(X)** and **B(X)** than for conformers **C(X)**. Also noteworthy, is the fact that the dependence of the ∠C6O7Si angle on σ_I for conformers **B(X)** is slightly greater than that for conformers **A(X)**. For instance, plots of the computed MP2/6-311+G(2d,p) ∠C6O7Si angle versus σ_I have slopes of -12.9, -17.6

and -4.7 for conformers **A(X)**, **B(X)** and **C(X)**, respectively. We will address the aforementioned observations later on.

Let us now examine the changes in geometry in going from the parent ground-state carbene conformers to the transition states for 1,2-silyl migration and decarbonylation. In the case of 1,2-silyl migration, there is considerable shrinkage of the ∠C6O7Si angles, in concert with modest lengthening of the O7-Si bonds and shortening of the C6-O7 bonds in going from conformers **A(X)** and **B(X)** in Figs. 3.1 and 3.2 to $\mathbf{TS_{AD}(X)}$ and $\mathbf{TS_{BE}(X)}$ in Figs. 3.4 and 3.5. These observations are consistent with nucleophilic attack by the carbene C6 lone pair at silicon, in concert with O7-Si bond dissociation and C6-O7 double-bond formation. The planarity of $\mathbf{TS_{AD}(X)}$ and $\mathbf{TS_{BE}(X)}$ indicates that silyl migration occurs in the plane containing the carbene lone pair, which further supports the above conclusion. In regards to decarbonylation, both the ∠O2C6O7 and ∠C6O7Si angles decrease considerably, while there is modest elongation of the O2-C6 and O7-Si bonds, and shortening of the C6-O7 bonds in going from conformers **C(X)** in Fig. 3.3 to $\mathbf{TS_{CH}(X)}$ in Fig. 3.6. These changes in geometry are consistent with nucleophilic attack by the methoxy oxygen O2 at silicon, along with O2-C6 and O7-Si bond dissociation, and C6-O7 triple-bond formation.

3.3.2 Changes in Electronic Structure

In light of the above observations that the presence of σ-electron-withdrawing substituents on the silyl moiety of the ground-state conformers of methoxy(substituted-siloxy)carbenes shortens the O7-Si and O2-C6 bonds, and lengthens the C6-O7 and C1-O2 bonds, we investigated the dependence of the bond critical point[116] (BCP) electronic densities $\rho_b(r)$ for these bonds on the σ-electron-withdrawing ability of

substituents. It turns out that σ-electron-withdrawing substituents do indeed lead to an increase in the values of $\rho_b(r)$ for the O7-Si and O2-C6 bonds, and a decrease in the values of $\rho_b(r)$ for the C6-O7 and C1-O2 bonds, consistent with the changes observed in the bond lengths. Moreover, fairly reasonable linear correlations are obtained for plots of the BCP electronic densities $\rho_b(r)$ versus σ_I, which are provided in Appendix C (cf. Figs. C14 to C25).

The changes in geometry mentioned above in the transition states for 1,2-silyl migration and decarbonylation relative to the parent ground-state carbene conformers are also reflected in the BCP electronic densities $\rho_b(r)$ presented in Tables 3.1 and 3.2. In regards to 1,2-silyl migration, the shrinkage of the ∠C6O7Si angles in going from conformers **A(X)** and **B(X)** to $\mathbf{TS_{AD}(X)}$ and $\mathbf{TS_{BE}(X)}$ generally results in the formation of new C6-Si bonds with low $\rho_b(r)$ values in $\mathbf{TS_{AD}(X)}$ and $\mathbf{TS_{BE}(X)}$, while the shortening and lengthening of the C6-O7 and O7-Si bonds are accompanied by increases and decreases in the $\rho_b(r)$ values, respectively. We note that C6-Si bond formation is not apparent in some of the transition states for 1,2-silyl migration where weaker σ-electron-withdrawing substituents are attached to the silyl moiety (cf. Tables 3.1 and 3.2). On the other hand, C6-Si bond formation and complete O7-Si bond annihilation are clearly evident in the transition states for 1,2-silyl migration when strongly σ-electron-withdrawing substituents are present on the silyl moiety. For decarbonylation, the shrinkage of the ∠O2C6O7 and ∠C6O7Si angles in going from conformers **C(X)** to $\mathbf{TS_{CH}(X)}$ is followed by the emergence of new O2-Si bonds with low $\rho_b(r)$ values in $\mathbf{TS_{CH}(X)}$, while O2-C6 and O7-Si bond lengthening is accompanied by a decrease in the

$\rho_b(r)$ values and C6-O7 bond shortening is followed by an increase in the $\rho_b(r)$ values (cf. Tables 3.1 and 3.2).

To gain further insight into the electronic structure changes in going from the ground-state conformers of methoxy(substituted-siloxy)carbenes to the transition states for 1,2-silyl migration and decarbonylation, we carried out NBO analysis. The electronic structure of the ground-state carbene conformers is most likely a hybrid of the three resonance structures shown in Scheme 3.2. Our NBO analysis was performed using the resonance-structure description shown in Scheme 3.2a for the wave functions of the ground-state carbene conformers and transition states for 1,2-silyl migration and decarbonylation. As can be seen from Tables 3.3 and 3.4, this resonance-structure description (or Lewis structure) accounts for more than 98.7% of the total electronic density of the ground-state carbene conformers and more than 97.5% of that of the transition states for 1,2-silyl migration and decarbonylation.

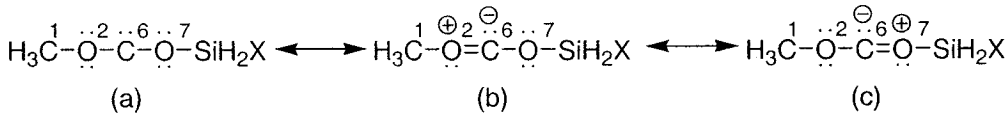

Scheme 3.2

The O2 and O7 atoms of conformers **A(X)**, **B(X)** and **C(X)** each have an in-plane σ-type lone-pair NBO, hereafter denoted as $n(\sigma)_{O2}$ and $n(\sigma)_{O7}$, and an out-of-plane π-type lone-pair NBO, henceforth denoted as $n(\pi)_{O2}$ and $n(\pi)_{O7}$. Figure 3.8 displays these NBOs for the *trans-trans* conformer of methoxy(siloxy)carbene **A(H)**. The stabilization energies that arise from $n(\pi)_{O2} \rightarrow p_{C6}$ and $n(\pi)_{O7} \rightarrow p_{C6}$ delocalization (or π-back bonding) in the carbene conformers (where p_{C6} represents the out-of-plane vacant carbene *p* orbital on

C6), estimated by second-order NBO perturbation-energy analysis, clearly indicate that the O2-C6 and C6-O7 bonds have considerable double-bond character (cf. Tables 3.3 and 3.4). For 1,2-silyl migration, the stabilization energies that arise from $n(\sigma)_{C6} \rightarrow \sigma^*_{O7\text{-}Si}$ interaction illustrated in Scheme 3.2a and $n(\pi)_{O7} \rightarrow p_{C6}$ back bonding, increase dramatically in going from conformers **A(X)** and **B(X)** to $\mathbf{TS_{AD}(X)}$ and $\mathbf{TS_{BE}(X)}$, respectively (cf. Table 3.3). This is indicative of nucleophilic attack by the carbene lone pair at silicon, in concert with C6-O7 double-bond formation. In addition, the stabilization energies that result from $n(\pi)_{O2} \rightarrow p_{C6}$ back bonding in conformers **A(X)** and **B(X)** decrease only slightly in $\mathbf{TS_{AD}(X)}$ and $\mathbf{TS_{BE}(X)}$, which means that π–back bonding from O2 to C6 helps stabilize the transition states for 1,2-silyl migration. In regards to decarbonylation, the stabilization energies due to $n(\sigma)_{O2} \rightarrow \sigma^*_{O7\text{-}Si}$ interaction illustrated in Scheme 3.3a increase tremendously in $\mathbf{TS_{CH}(X)}$ relative to conformers **C(X)** as can be seen in Table 3.4, indicative of nucleophilic attack by the methoxy oxygen O2 at silicon. The stabilization energies due to $n(\pi)_{O2} \rightarrow p_{C6}$ back donation decrease significantly while those that result from $n(\pi)_{O7} \rightarrow p_{C6}$ back donation increase considerably, in keeping with the loss of double-bond character of the dissociating O2-C6 bond and C6-O7 triple-bond formation.

Table 3.5 summarizes the changes in atomic charges in the transition states for 1,2-silyl migration and decarbonylation relative to the parent ground-state methoxy(substituted-siloxy)carbene conformers. For 1,2-silyl migration in conformers **A(X)** and **B(X)**, there is considerable negative charge accumulation at Si and positive charge development at O7 in $\mathbf{TS_{AD}(X)}$ and $\mathbf{TS_{BE}(X)}$. This is accompanied by modest positive charge buildup at O2 and negative charge buildup at C6. These findings are

consistent with nucleophilic attack by the carbene C6 lone pair at silicon, in unison with C6-O7 double-bond formation, O7-Si bond dissociation, and some $n(\pi)_{O2} \rightarrow p_{C6}$ back bonding that facilitates transition-state stabilization. The charge development at C6 most likely depends on the extent of C6-Si bond formation, C6-O7 double-bond formation and $n(\pi)_{O2} \rightarrow p_{C6}$ back bonding. For decarbonylation of conformers **C(X)**, there is modest negative charge buildup at Si and positive charge buildup at C6, along with sizeable negative charge development at O2 and positive charge development at O7 in $\mathbf{TS_{CH}(X)}$. These findings are consistent with nucleophilic attack by the methoxy oxygen O2 at Si, together with O2-C6 and O7-Si bond dissociation, and C6-O7 triple-bond formation.

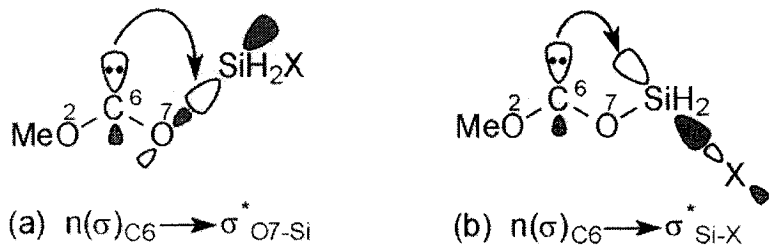

Scheme 3.2

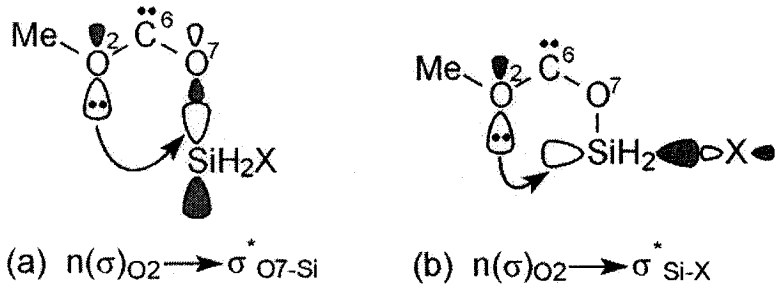

Scheme 3.3

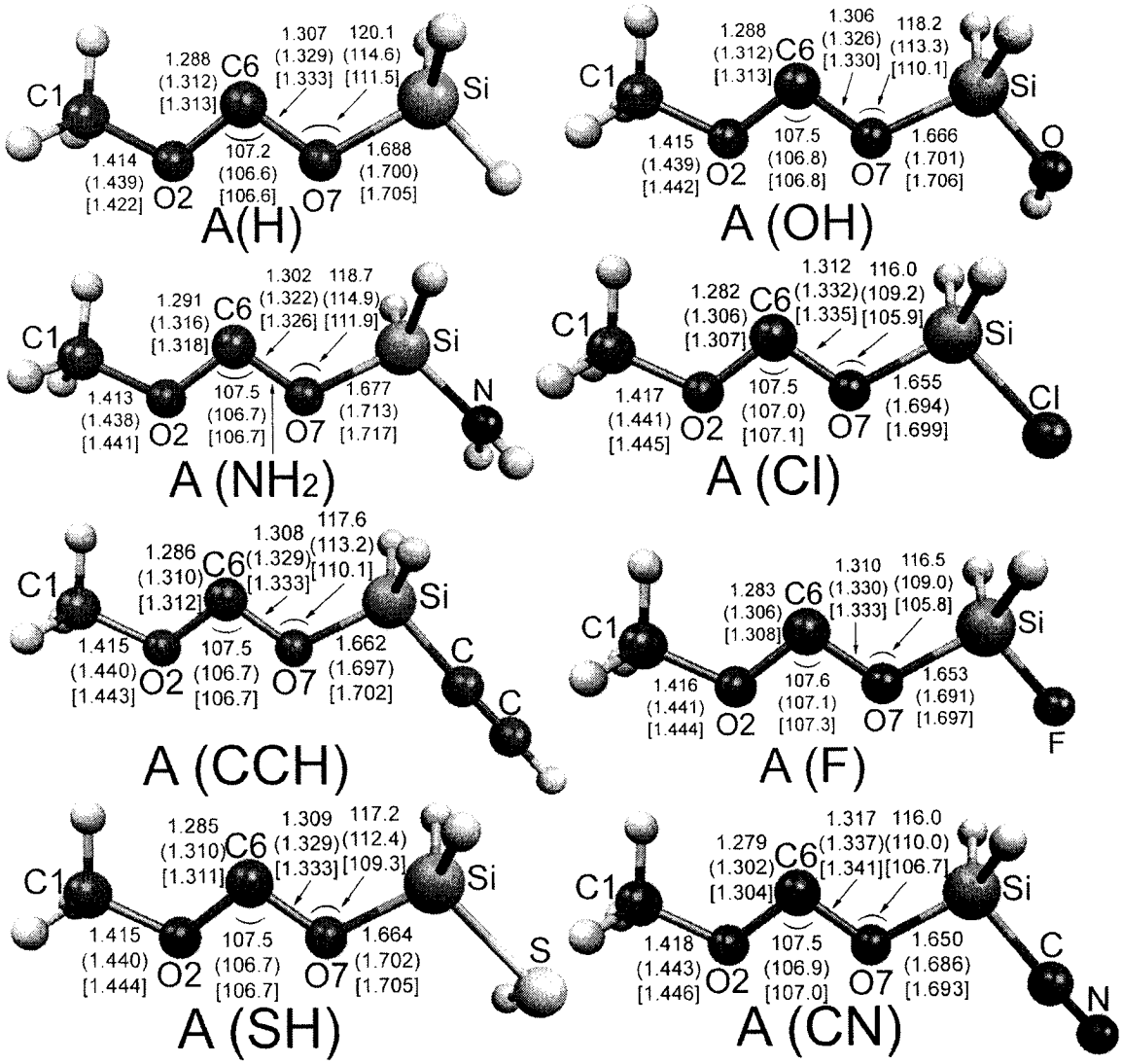

Figure 3.1 Optimized molecular geometries of the *trans-trans* conformers of methoxy(substituted-siloxy)carbenes **A(X)**. Geometric parameters are given for HF/6-311+G(2d,p), B3LYP/6-311+G(2d,p) (parentheses), and MP2/6-311+G(2d,p) [brackets] model chemistries. Bond lengths and angles are in Å and degrees respectively.

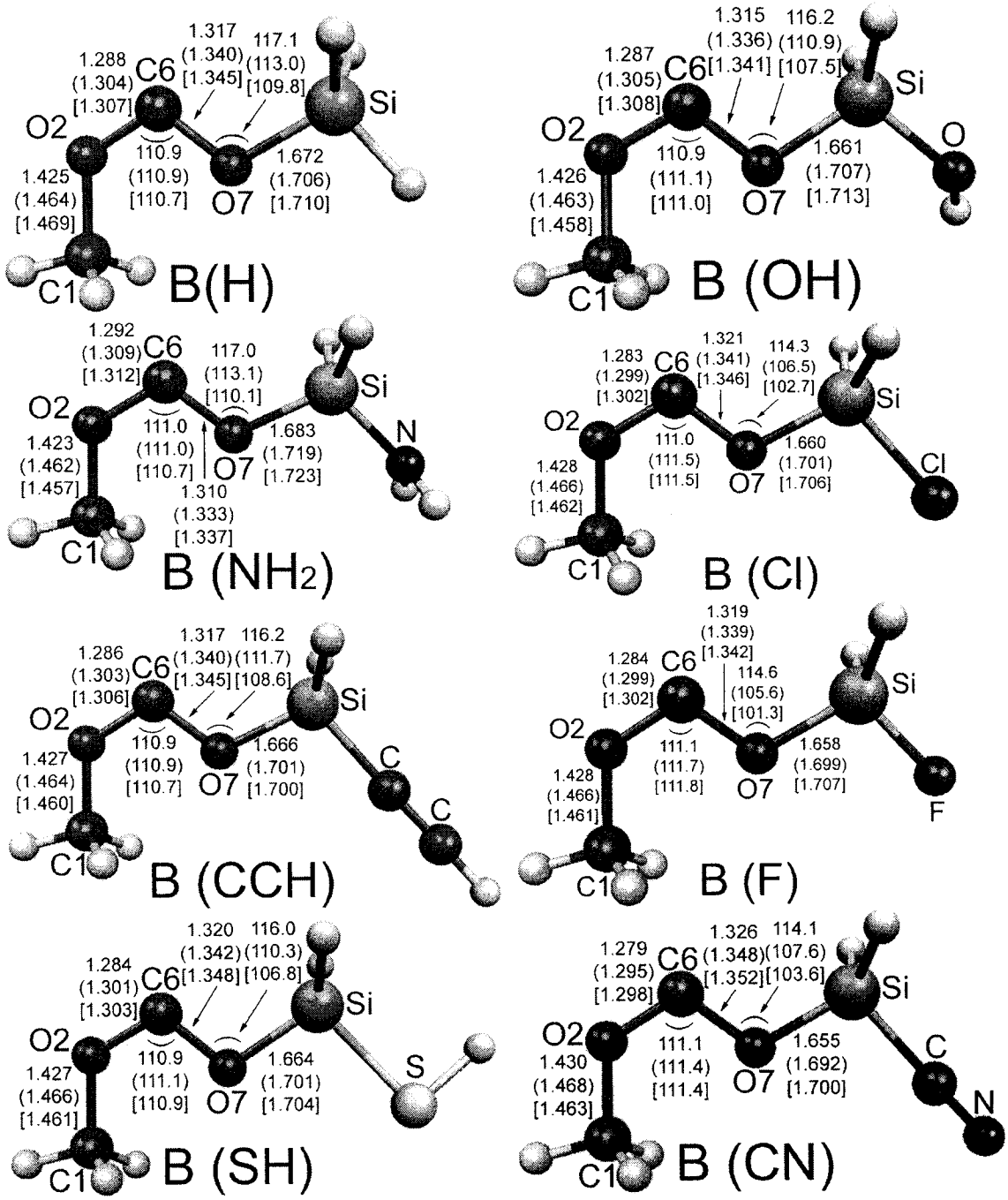

Figure 3.2 Optimized molecular geometries of the *cis-trans* conformers of methoxy(substituted-siloxy)carbene **B(X)**. Geometric parameters are given for HF/6-311+G(2d,p), B3LYP/6-311+G(2d,p) (parentheses), and MP2/6-311+G(2d,p) [brackets] model chemistries. Bond lengths and angles are in Å and degrees respectively.

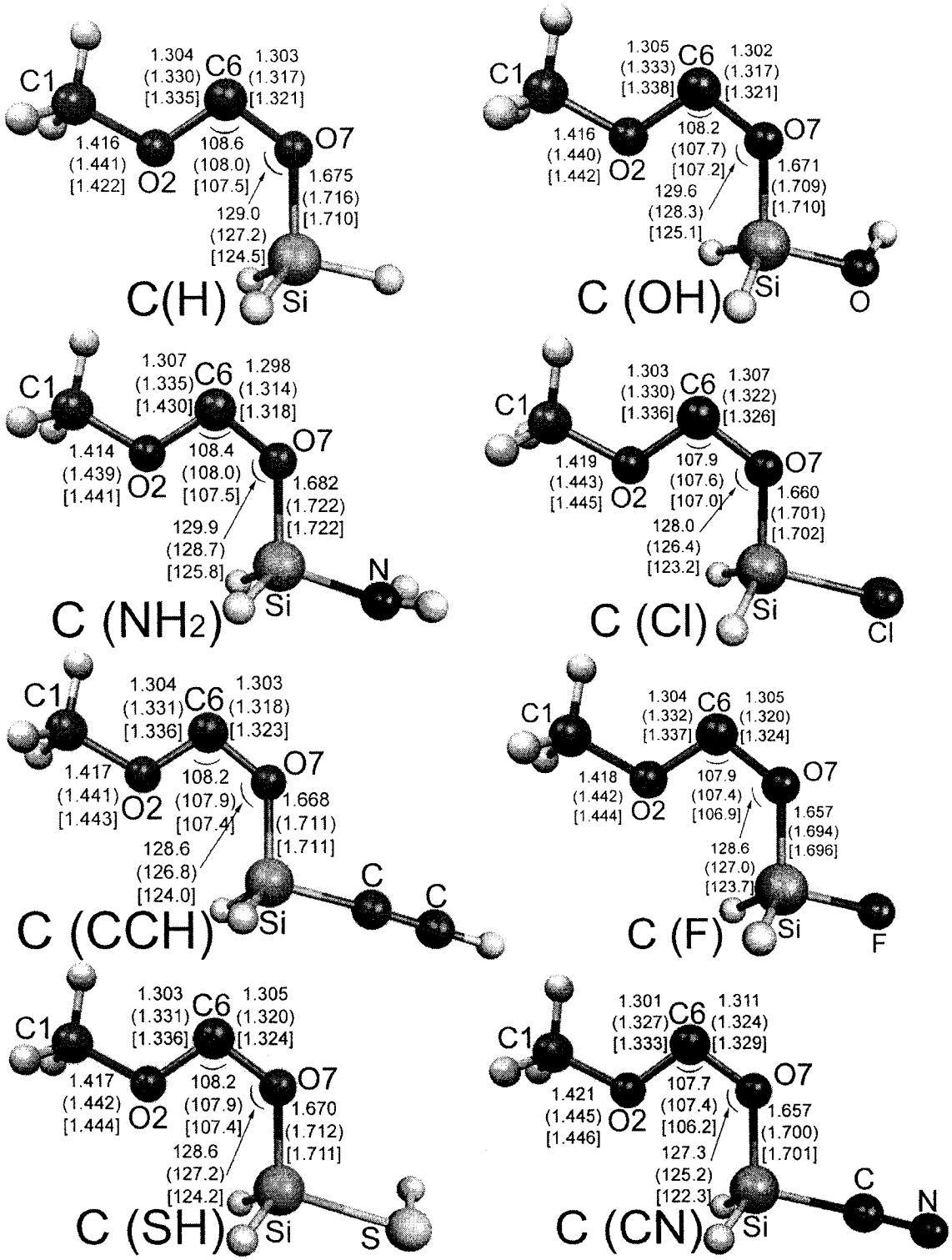

Figure 3.3 Optimized molecular geometries of the *trans-cis* conformers of methoxy(substituted-siloxy)carbenes **C(X)**. Geometric parameters are given for HF/6-311+G(2d,p), B3LYP/6-311+G(2d,p) (parentheses), and MP2/6-311+G(2d,p) [brackets] model chemistries. Bond lengths and angles are in Å and degrees respectively.

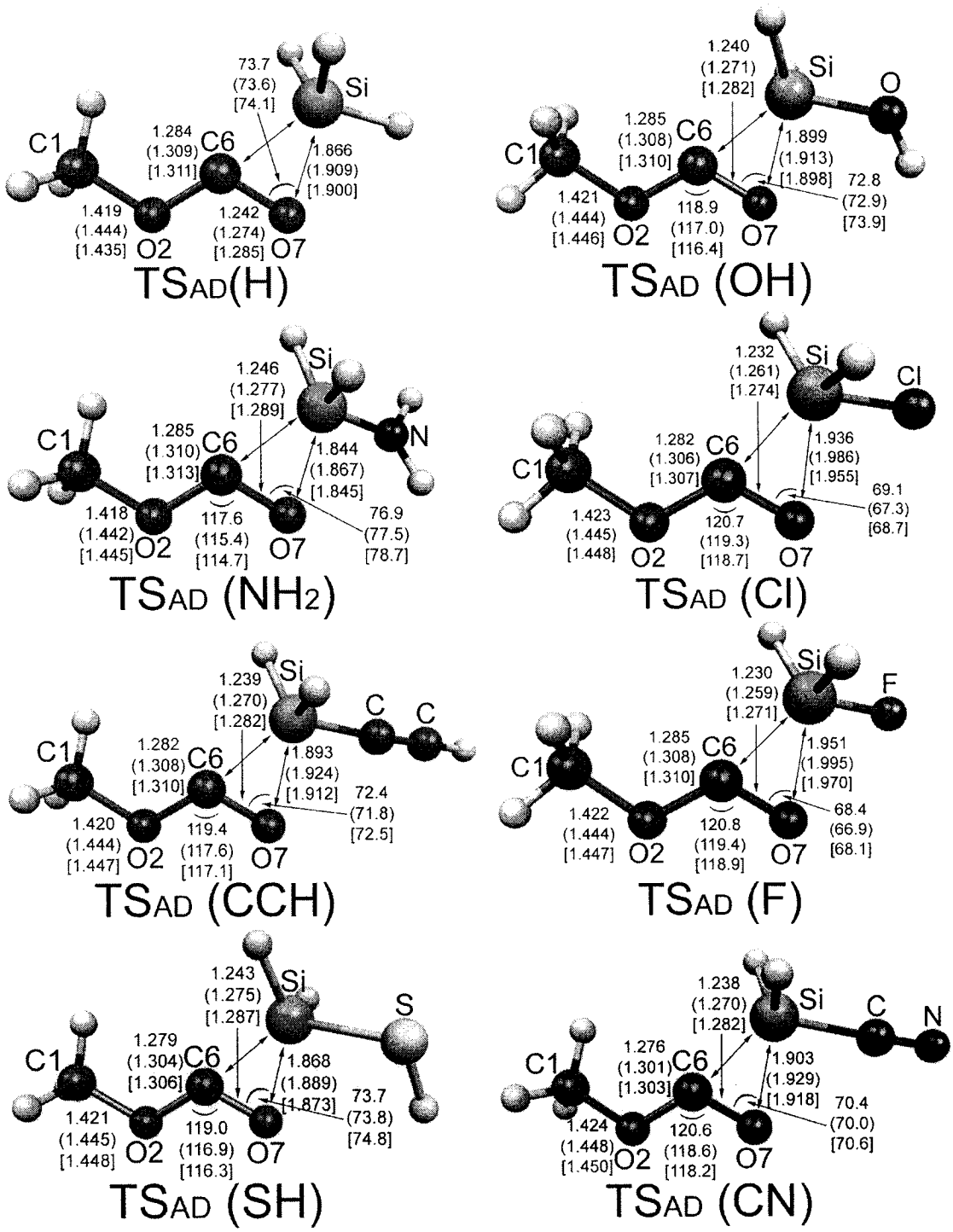

Figure 3.4 Optimized molecular geometries of the transition states for 1,2-silyl migrations in the *trans-trans* conformers of methoxy(substituted-siloxy)carbenes **TS_{AD}(X)**. Geometric parameters are given for the HF/6-311+G(2d,p), B3LYP/6-311+G(2d,p) (parentheses), and MP2/6-311+G(2d,p) [brackets] model chemistries. Bond lengths and angles are in Å and degrees, respectively.

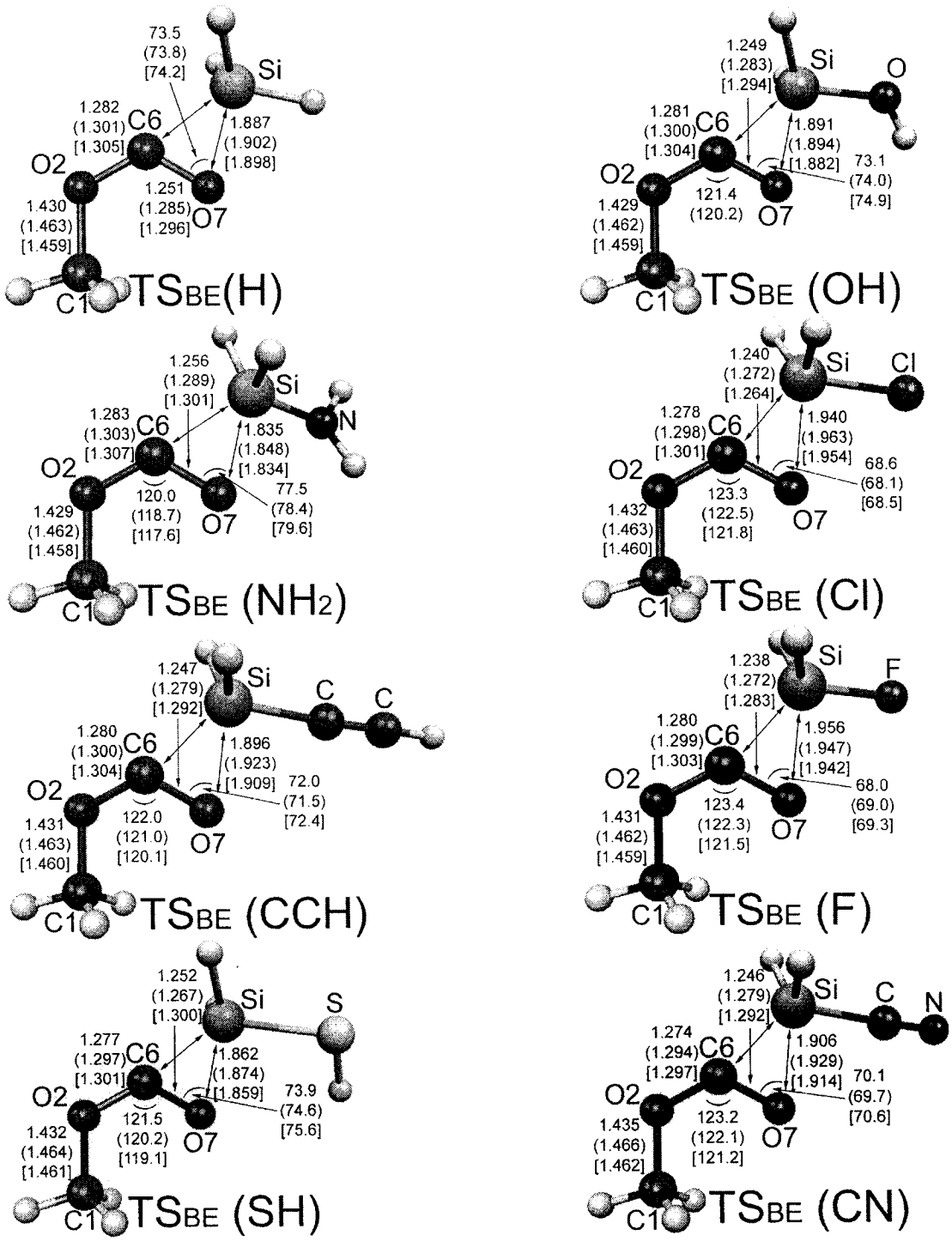

Figure 3.5 Optimized molecular geometries of the transition states for 1,2-silyl migrations in the *cis-trans* conformers of methoxy(substituted-siloxy)carbene $\mathbf{TS_{BE}(X)}$. Geometric parameters are given for the HF/6-311+G(2d,p), B3LYP/6-311+G(2d,p) (parentheses), and MP2/6-311+G(2d,p) [brackets] model chemistries. Bond lengths and angles are in Å and degrees, respectively.

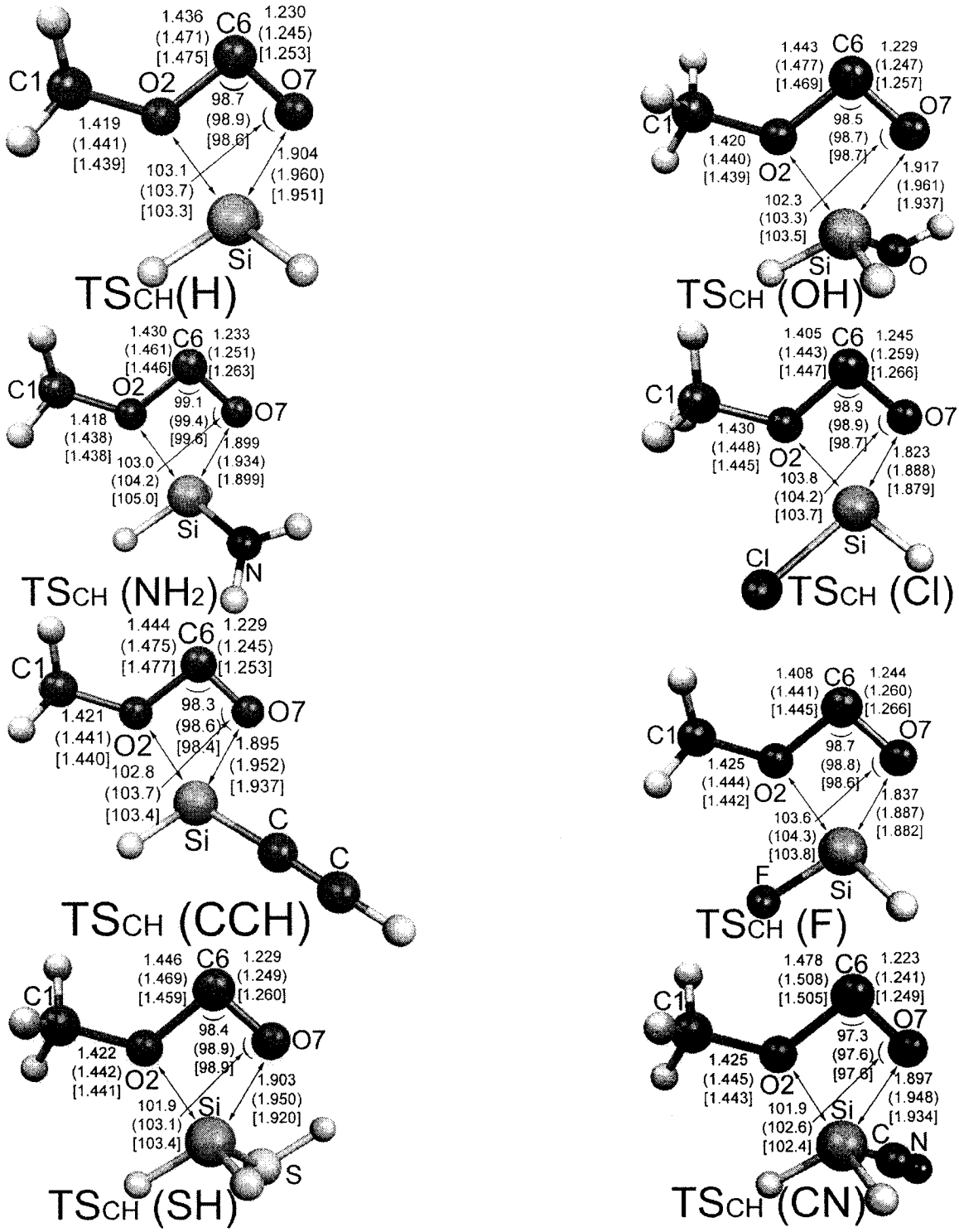

Figure 3.6 Optimized molecular geometries of the transition states for decarbonylation of the *trans-cis* conformers of methoxy(substituted-siloxy)carbenes **TS_{CH}(X)**. Geometric parameters are given for HF/6-311+G(2d,p), B3LYP/6-311+G(2d,p) (parentheses), and MP2/6-311+G(2d,p) [brackets] model chemistries. Bond lengths and angles are in Å and degrees respectively.

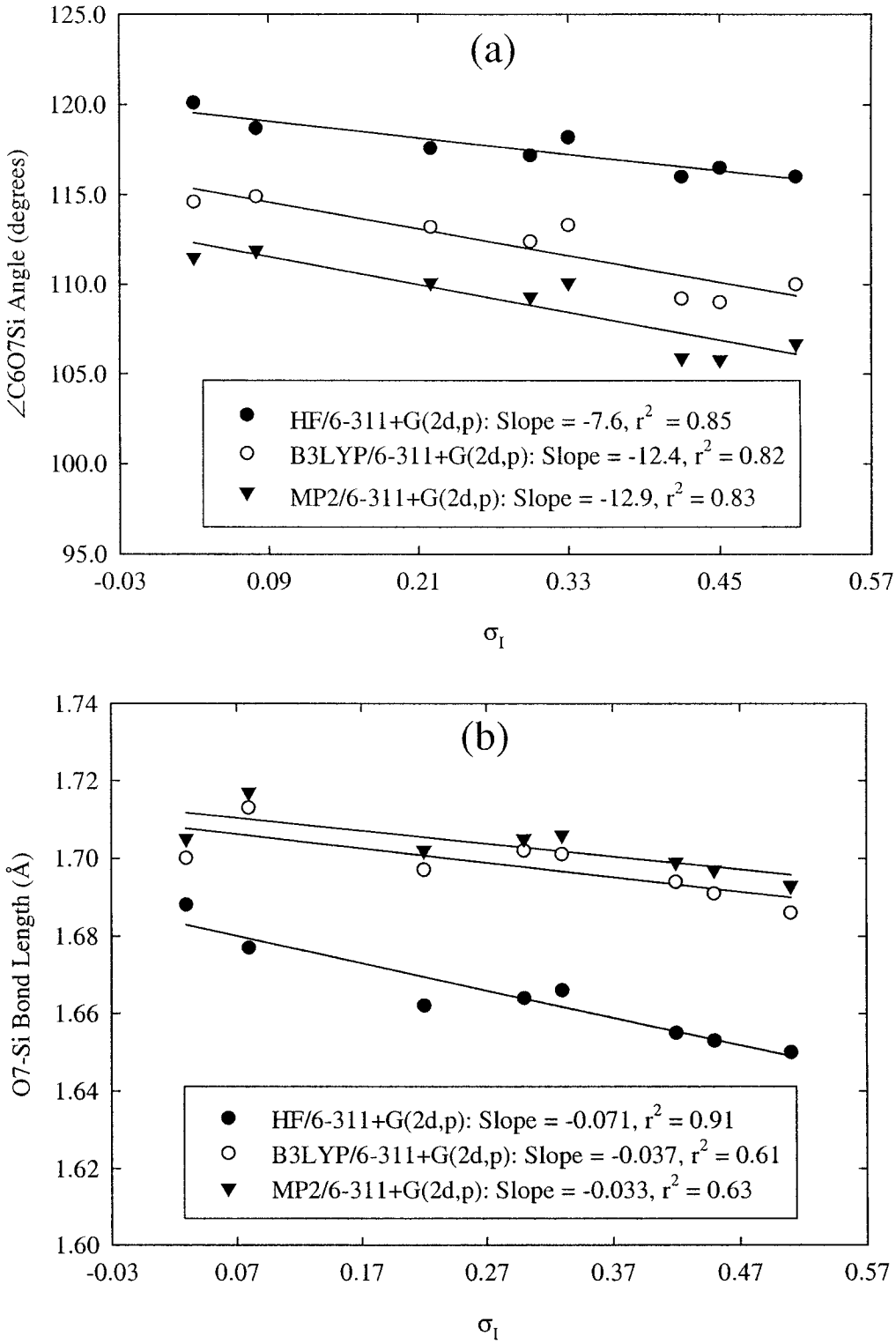

Figure 3.7 Plots of (a) the ∠C6O7Si angle and (b) the O7-Si bond length versus σ_I for conformers **A(X)** of methoxy(substituted-siloxy)carbenes.

Table 3.1 MP2/6-311+G(2d,p) BCP electronic densities of the ground-state conformers of methoxy(substituted-siloxy)carbenes.[a]

X	σ_I	C1-O2	O2-C6	C6-O7	O7-Si
			A(X)		
H	0.03	1.596	2.152	2.070	0.811
NH_2	0.08	1.607	2.126	2.101	0.791
CCH	0.22	1.593	2.159	2.066	0.827
SH	0.30	1.590	2.161	2.066	0.822
OH	0.33	1.598	2.149	2.082	0.818
Cl	0.42	1.583	2.181	2.062	0.843
F	0.45	1.586	2.178	2.073	0.846
CN	0.51	1.573	2.200	2.034	0.853
			B(X)		
H	0.03	1.548	2.164	2.002	0.800
NH_2	0.08	1.562	2.138	2.036	0.780
CCH	0.22	1.543	2.172	1.999	0.818
SH	0.30	1.536	2.186	1.989	0.824
OH	0.33	1.552	2.162	2.021	0.806
Cl	0.42	1.532	2.197	2.007	0.828
F	0.45	1.535	2.195	2.028	0.825
CN	0.51	1.521	2.216	1.976	0.839
			C(X)		
H	0.03	1.587	2.036	2.089	0.781
NH_2	0.08	1.599	2.013	2.108	0.769
CCH	0.22	1.584	2.034	2.083	0.798
SH	0.30	1.570	2.062	2.105	0.805
OH	0.33	1.589	2.026	2.089	0.795
Cl	0.42	1.573	2.036	2.063	0.822
F	0.45	1.577	2.029	2.073	0.830
CN	0.51	1.561	2.048	2.053	0.824

[a] BCP electronic densities are in e/Å^3 and were obtained from AIM analysis. The σ_I values are Swain-Lupton modified Hammett substituent constants[143] for field/inductive effects of σ-electron-withdrawing/donating substituents. HF/6-311+G(2d,p) and B3LYP/6-311+G(2d,p) BCP electronic densities are available in Appendix C.

Table 3.2 MP2/6-311+G(2d,p) BCP electronic densities of the transition states for 1,2-silyl migration and decarbonylation of methoxy(substituted-siloxy)carbenes.[a]

X	C1-O2	O2-C6	C6-O7	O7-Si	C6-Si
			TS_{AD}		
H	1.572	2.160	2.381	0.513	0.499
NH_2	1.582	2.151	2.347	0.578	-
CCH	1.567	2.167	2.399	0.511	0.533
SH	1.562	2.185	2.362	0.551	-
OH	1.572	2.166	2.387	0.518	0.504
Cl	1.558	2.184	2.442	-	0.605
F	1.566	2.171	2.461	-	0.610
CN	1.547	2.205	2.400	-	0.581
			TS_{BE}		
H	1.532	2.192	2.311	0.512	0.494
NH_2	1.543	2.179	2.270	0.589	-
CCH	1.528	2.201	2.333	0.509	0.531
SH	1.524	2.215	2.285	0.564	-
OH	1.537	2.196	2.312	0.531	-
Cl	1.521	2.219	2.381	-	0.608
F	1.528	2.210	2.382	-	0.593
CN	1.508	2.239	2.334	-	0.580
			TS_{CH}		
	C1-O2	O2-C6	C6-O7	O7-Si	O2-Si
H	1.559	1.456	2.533	0.469	0.405
NH_2	1.568	1.560	2.465	0.526	0.351
CCH	1.555	1.448	2.530	0.488	0.417
SH	1.547	1.510	2.486	0.512	0.400
OH	1.558	1.478	2.507	0.485	0.400
Cl	1.519	1.551	2.460	0.555	0.416
F	1.536	1.559	2.457	0.551	0.405
CN	1.534	1.357	2.553	0.489	0.474

[a] BCP electronic densities are in e/Å^3 and were obtained from AIM analysis. HF/6-311+G(2d,p) and B3LYP/6-311+G(2d,p) BCP electronic densities are available in Appendix C.

Table 3.3 Estimated HF/6-311+G(2d,p)//MP2/6-311+G(2d,p) stabilization energies that arise from delocalization in the *trans-trans* and *cis-trans* conformers of methoxy(substituted-siloxy)carbenes and the transition states for 1,2-silyl migration.[a]

X	%Lewis structure	$n(\pi)_{O2} \rightarrow p_{C6}$	$n(\pi)_{O7} \rightarrow p_{C6}$	$n(\sigma)_{C6} \rightarrow \sigma^*_{O7\text{-}Si}$
		A(X)		
H	98.8	107.87	92.77	6.64
NH_2	98.8	104.21	97.23	5.01
CCH	98.9	109.05	92.62	6.80
SH	98.9	109.55	92.59	7.43
OH	98.8	107.58	94.82	5.28
Cl	98.9	112.68	92.87	8.74
F	98.8	112.02	94.78	6.91
CN	98.9	116.10	88.61	8.94
		B(X)		
H	98.7	110.77	86.50	7.01
NH_2	98.8	106.87	91.05	5.36
CCH	98.8	112.10	86.29	7.27
SH	98.9	114.11	85.32	9.15
OH	98.8	110.41	89.56	6.01
Cl	98.8	115.96	88.44	10.68
F	98.7	115.28	91.91	9.31
CN	98.8	119.38	84.13	10.63
		TS_{AD}(X)		
H	97.7	103.23	185.85	77.12
NH_2	98.0	102.62	167.80	59.80
CCH	97.9	103.85	194.05	81.26
SH	98.1	107.27	176.66	69.71
OH	97.9	103.99	183.11	66.09
Cl	97.9	104.65	214.41	76.62
F	97.7	102.19	221.90	71.20
CN	97.9	109.49	198.51	86.36
		TS_{BE}(X)		
H	97.5	108.44	168.72	73.39
NH_2	98.1	107.46	150.41	54.11
CCH	98.0	109.15	176.90	79.49
SH	98.2	112.59	157.94	64.18
OH	98.0	109.00	164.01	60.68
Cl	98.0	110.03	196.33	75.26
F	97.8	108.72	194.85	68.56
CN	97.9	115.15	180.39	84.73

[a] Stabilization energies are in kcal/mol and were estimated by second-order NBO perturbation-energy analysis of HF/6-311+G(2d,p) wave functions generated from MP2/6-311+G(2d,p) geometries. %Lewis structure is the percentage of the total electronic density accounted for by the resonance-structure representation in Scheme 3.1a.

Table 3.4 Estimated HF/6-311+G(2d,p)//MP2/6-311+G(2d,p) stabilization energies that arise from delocalization in the *trans-cis* conformer of methoxy(substituted-siloxy)carbenes and the transition states for decarbonylation.[a]

X	%Lewis structure	$n(\pi)_{O2} \rightarrow p_{C6}$	$n(\pi)_{O7} \rightarrow p_{C6}$	$n(\sigma)_{O2} \rightarrow \sigma^*_{O7\text{-}Si}$
		C(X)		
H	98.8	91.44	94.26	3.75
NH_2	98.8	89.36	97.82	2.74
CCH	98.9	91.11	93.75	3.84
SH	99.0	91.68	92.61	3.81
OH	98.8	90.74	94.53	2.82
Cl	99.0	91.46	91.15	4.04
F	98.9	90.67	92.34	3.15
CN	98.9	92.54	88.73	4.72
		TS_{CH}(X)		
H	98.3	31.80	182.92	64.50
NH_2	98.4	38.98	170.20	50.59
CCH	98.5	31.17	186.58	66.20
SH	98.6	35.00	175.48	59.75
OH	98.4	34.06	182.03	58.56
Cl	98.7	37.72	161.59	58.57
F	98.5	38.65	162.02	53.36
CN	98.5	26.91	189.53	74.26

[a] Stabilization energies are in kcal/mol and were estimated by second-order NBO perturbation-energy analysis of HF/6-311+G(2d,p) wave functions generated from MP2/6-311+G(2d,p) geometries. %Lewis structure is the percentage of the total electronic density accounted for by the resonance-structure representation in Scheme 3.1a.

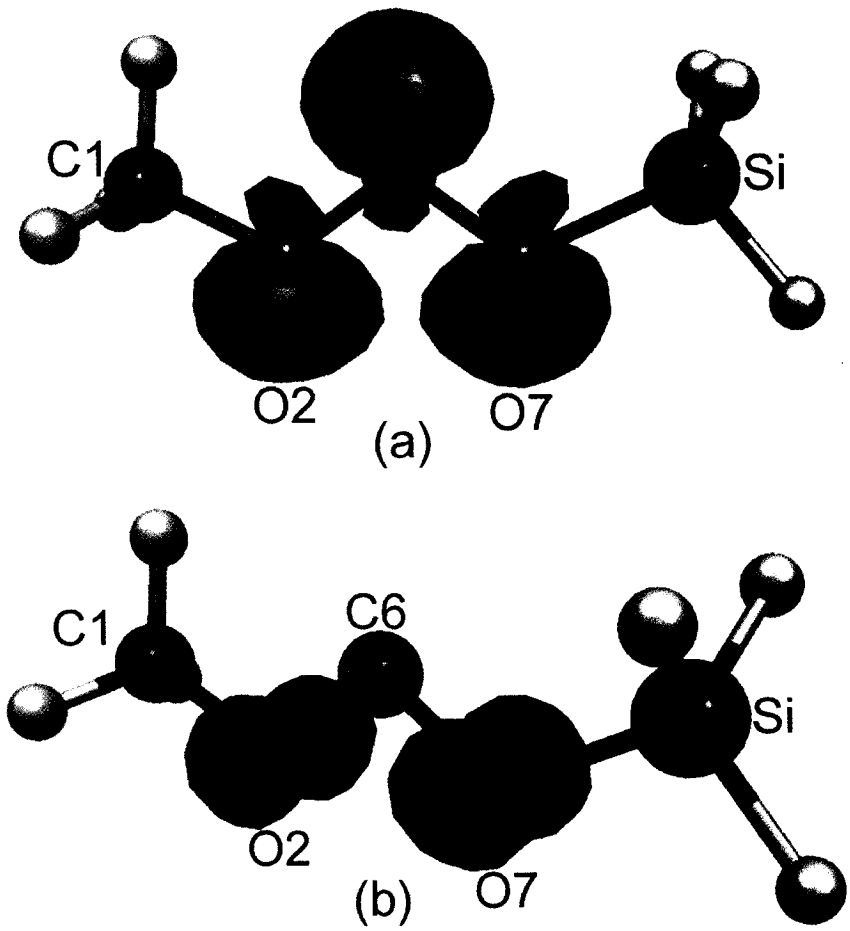

Figure 3.8 Plots of (a) the in-plane σ-type lone-pair NBOs on the O2, C6 and O7 atoms and (b) the out-of-plane π-type lone-pair NBOs on the O2 and O7 atoms of the *trans-trans* conformer of methoxy(siloxy)carbene, obtained from NBO analysis of the HF/6-311+G(2d,p) wave function.

Table 3.5 Changes in MP2/6-311+G(2d,p) NPA atomic charges in the transition states relative to the parent carbene conformers.[a]

X	C1	O2	C6	O7	Si
			TS_{AD}(X) relative to **A(X)**		
H	0.0002	0.0214	-0.0073	0.1822	-0.1939
NH_2	0.0009	0.0235	-0.0036	0.1593	-0.1619
CCH	0.0005	0.0228	-0.0034	0.1968	-0.2159
SH	0.0007	0.0243	-0.0032	0.1846	-0.1873
OH	0.0008	0.0226	-0.0085	0.1836	-0.2194
Cl	0.0003	0.0188	-0.0129	0.2285	-0.2331
F	0.0003	0.0159	-0.0190	0.2319	-0.2542
CN	0.0005	0.0217	-0.0006	0.2098	-0.2270
			TS_{BE}(X) relative to **B(X)**		
H	0.0034	0.0243	-0.0226	0.1708	-0.1751
NH_2	0.0029	0.0249	-0.0139	0.1436	-0.1443
CCH	0.0049	0.0257	-0.0219	0.1861	-0.1972
SH	0.0040	0.0250	-0.0229	0.1679	-0.1873
OH	-0.0385	0.0840	-0.0488	0.1462	-0.1757
Cl	0.0064	0.0211	-0.0359	0.2128	-0.2038
F	0.0065	0.0183	-0.0346	0.2023	-0.2180
CN	0.0058	0.0232	-0.0211	0.1941	-0.1982
			TS_{CH}(X) relative to **C(X)**		
H	0.0034	-0.1272	0.0531	0.1079	-0.0668
NH_2	0.0066	-0.0905	0.0204	0.1243	-0.0539
CCH	0.0041	-0.1095	0.0217	0.1486	-0.0666
SH	0.0051	-0.1039	0.0226	0.1384	-0.0678
OH	0.0058	-0.1101	0.0221	0.1353	-0.0757
Cl	0.0033	-0.0972	0.0260	0.1290	-0.0610
F	0.0071	-0.0927	0.0205	0.1284	-0.0924
CN	0.0030	-0.1252	0.0309	0.1585	-0.0645

[a] Obtained from NBO analysis. HF/6-311+G(2d,p) and B3LYP/6-311+G(2d,p) atomic charges are available in Appendix C.

3.3.3 Hammett Free-Energy Relationships

The Hammett free-energy relationship for rate data is given by eq (3.1), where k_X and k_H are the rate constants for the substituted and un-substituted (parent) compounds, and σ and ρ are the Hammett substituent and reaction constants, respectively. This expression can be re-written in terms of Gibbs free energies as eq (3.2), where ΔG_{TS} and ΔG^{H}_{TS} are the Gibbs free energies of activation for the substituted and parent compounds.

Computed Gibbs free-energy and enthalpy barriers for 1,2-silyl migration in conformers **A(X)** and **B(X)** via $\mathbf{TS_{AD}(X)}$ and $\mathbf{TS_{BE}(X)}$, respectively, and for decarbonylation of conformers **C(X)** via $\mathbf{TS_{CH}(X)}$, are given in Table 3.6. Absolute Gibbs free energies and enthalpies are available in Appendix C. We note that the HF/6-311+G(2d,p) model chemistry overestimates ΔG_{TS} and ΔH_{TS}, when compared to the more reliable B3LYP/6-311+G(2d,p) and MP2/6-311+G(2d,p) model chemistries, due to the neglect of electronic correlation.[100,101,125] Hammett plots of ΔG_{TS} versus Swain-Lupton modified Hammett substituent constants, σ_I,[143] for 1,2-silyl migration and decarbonylation are shown in Figs. 3.9 and 3.10, respectively.

$$\log\left(\frac{k_X}{k_H}\right) = \rho\sigma \tag{3.1}$$

$$\Delta G_{TS} = \Delta G^{H}_{TS} - 2.303RT\rho\sigma \tag{3.2}$$

In regards to 1,2-silyl migration in conformers **A(X)** and **B(X)**, fairly reasonable linear correlations are obtained for Hammett plots of ΔG_{TS} versus σ_I, as evident in Fig. 3.9. In fact, the correlation seems to improve with higher levels of theory, which presumably yield more accurate relative Gibbs free energies. The Hammett plots clearly show that the Gibbs free-energy barriers are lowered by σ-electron-withdrawing

substituents. This lowering of the Gibbs free-energy barriers is most likely due to the fact that σ-electron-withdrawing substituents stabilize the sizeable negative charge accumulation at Si in $\mathbf{TS_{AD}(X)}$ and $\mathbf{TS_{BE}(X)}$ that accompanies nucleophilic attack by the carbene lone pair at silicon (cf. Tables 3.5). The relatively large positive Hammett ρ values (cf. Fig. 3.9) suggest that 1,2-silyl migration in conformers **A(X)** and **B(X)** is quite sensitive to the presence of σ-electron-withdrawing substituents on the silyl moiety, with slightly greater sensitivity for 1,2-silyl migration in conformers **B(X)**. In regards to the decarbonylation of conformers **C(X)**, although it appears from the Hammett plots in Fig. 3.10 that the Gibbs free-energy barriers are generally lowered by σ-electron-withdrawing substituents, the correlation coefficients (r^2) suggest that there is effectively no correlation between ΔG_{TS} and σ_I. In other words, the Gibbs free-energy barriers are quite insensitive to the presence of σ-electron-withdrawing substituents on the silyl moiety. This lack of sensitivity is most likely due to the fact that stabilization of the meager negative charge buildup at Si (cf. Table 3.5) in $\mathbf{TS_{CH}(X)}$ by σ-electron-withdrawing substituents is not as meaningful as that of the more substantial negative charge buildup at Si in $\mathbf{TS_{AD}(X)}$ and $\mathbf{TS_{BE}(X)}$.

Table 3.6 Gibbs free-energy and enthalpy barriers for 1,2-silyl migration and decarbonylation in methoxy(substituted-siloxy)carbenes.[a]

X	HF/6-311+G(2d,p)		B3LYP/6-311+G(2d,p)		MP2/6-311+G(2d,p)	
	ΔG_{TS}	ΔH_{TS}	ΔG_{TS}	ΔH_{TS}	ΔG_{TS}	ΔH_{TS}
	TS_{AD}(X) for 1,2-Silyl Migration					
H	20.1	19.6	10.6	9.9	9.0	8.4
NH_2	19.5	18.4	10.3	9.5	8.9	7.9
CCH	20.4	19.7	10.7	9.9	8.6	7.9
SH	18.4	17.2	8.8	7.6	7.1	5.9
OH	18.6	17.7	8.8	7.5	7.2	6.0
Cl	18.3	17.8	7.4	7.0	6.0	5.4
F	17.3	16.8	6.0	6.0	5.0	4.6
CN	17.5	16.8	7.8	7.1	5.9	5.2
	TS_{BE}(X) for 1,2-Silyl Migration					
H	16.5	15.9	7.4	7.3	6.2	6.0
NH_2	16.5	15.2	8.5	7.5	7.0	6.0
CCH	16.8	16.0	7.5	7.4	6.0	5.5
SH	14.3	12.7	6.0	4.7	4.9	2.4
OH	15.8	13.0	6.3	5.7	4.9	3.7
Cl	14.2	13.4	4.3	3.9	2.9	2.6
F	12.6	12.3	3.4	2.9	2.1	1.6
CN	13.3	12.5	3.5	4.1	2.8	2.5
	TS_{CH}(X) for Decarbonylation					
H	24.1	24.4	17.3	17.9	15.9	16.4
NH_2	22.7	22.1	16.5	15.8	13.7	13.2
CCH	25.5	25.4	18.3	18.5	15.6	15.7
SH	23.0	22.5	16.2	15.6	13.5	12.9
OH	24.5	23.6	17.3	16.5	14.4	13.9
Cl	23.2	22.1	16.6	15.9	13.9	13.2
F	21.6	21.1	15.5	15.0	13.5	13.1
CN	24.0	23.8	17.2	17.0	14.2	14.2

[a] Values of ΔG_{TS} and ΔH_{TS} are in kcal/mol at 298.15 K and 1.0 atm. Gibbs free-energy barriers are the difference in Gibbs free-energy between the transition states and their parent carbene conformers, while the enthalpy barriers are the enthalpy difference between the transition states and their parent carbene conformers.

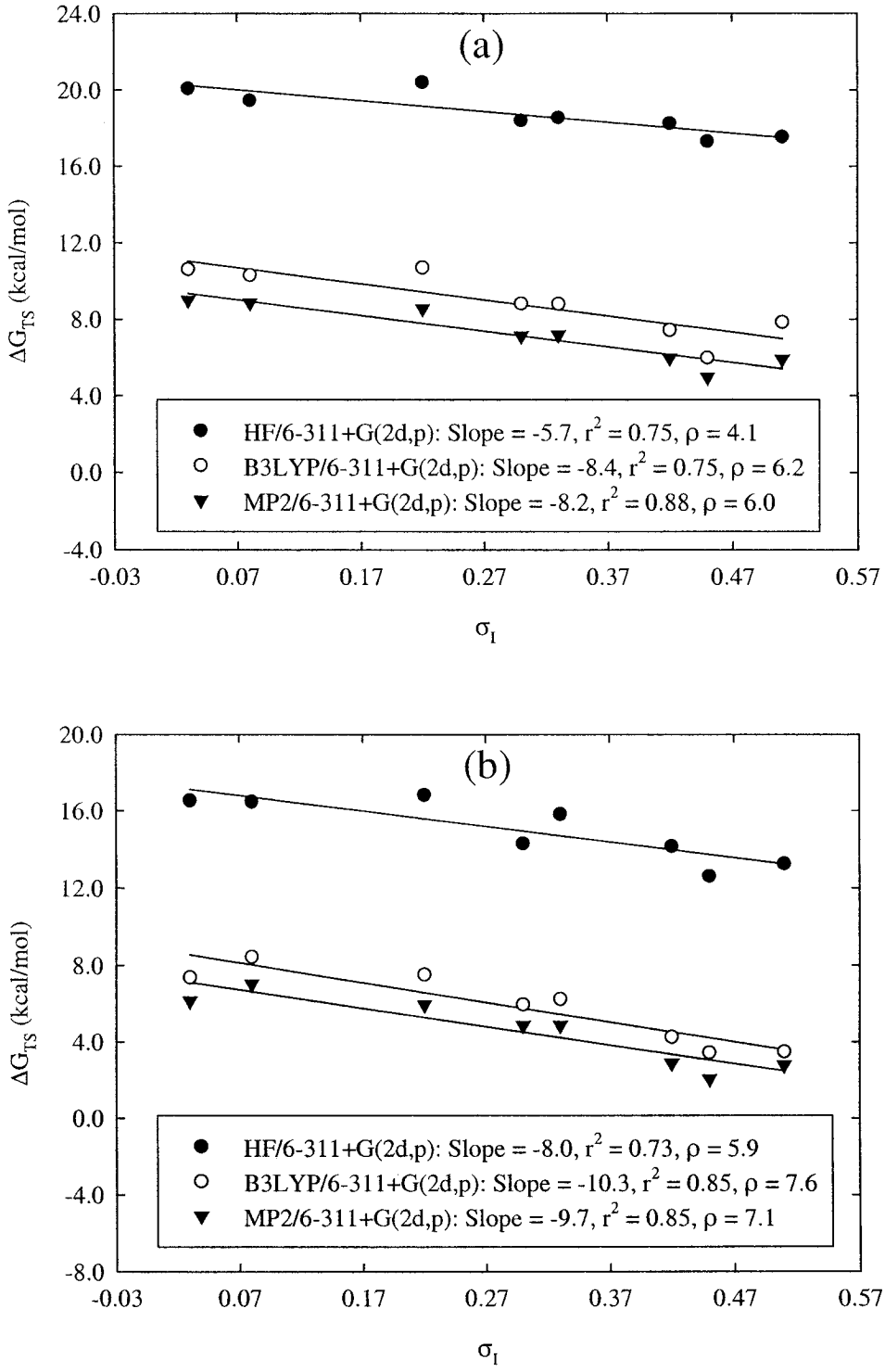

Figure 3.9 Hammett plots of ΔG_{TS} versus σ_I for 1,2-silyl migration in (a) conformers **A(X)** and (b) conformers **B(X)** of methoxy(substituted-siloxy)carbenes. Values of ρ are Hammett reaction constants.

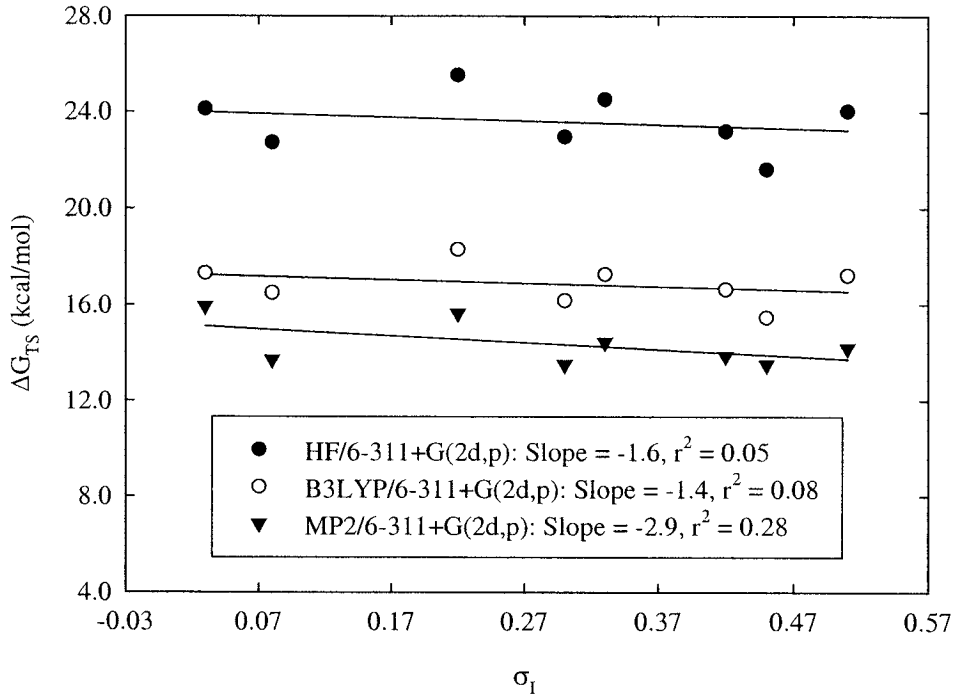

Figure 3.10 Hammett plots of ΔG_{TS} versus σ_I for decarbonylation of conformers **C(X)** of methoxy(substituted-siloxy)carbenes.

3.3.4 Role of Hyperconjugation

To assess the role of negative hyperconjugation in the ground-state conformers of methoxy(substituted-siloxy)carbenes in 1,2-silyl migration and decarbonylation, we investigated the relationship between the activation enthalpies and stabilization energies due to hyperconjugation. The relevant hyperconjugative interactions are the $n(\sigma)_{C6} \rightarrow \sigma^*_{O7\text{-}Si}$ and $n(\sigma)_{C6} \rightarrow \sigma^*_{Si\text{-}X}$ interactions for 1,2-silyl migration in conformers **A(X)** and **B(X)** shown in Scheme 3.2, and the $n(\sigma)_{O2} \rightarrow \sigma^*_{O7\text{-}Si}$ and $n(\sigma)_{O2} \rightarrow \sigma^*_{Si\text{-}X}$ interactions for decarbonylation of conformers **C(X)** shown in Scheme 3.3. Stabilization energies due to these hyperconjugative interactions, obtained from NBO analysis of HF/6-311+G(2d,p) wave functions based on MP2/6-311+G(2d,p) optimized geometries by deletion of the appropriate Fock matrix elements, are collected in Table 3.7. Stabilization energies due to $n(\sigma)_{C6} \rightarrow RY^*_{Si}$ hyperconjugation in conformers **A(X)** and **B(X)**, and $n(\sigma)_{O2} \rightarrow RY^*_{Si}$ hyperconjugation in conformers **C(X)** (where RY^*_{Si} denotes the Rydberg NBOs on silicon) have also been included in Table 3.7.

We mentioned earlier that the presence of σ-electron-withdrawing substituents on the silyl moiety of the methoxy(substituted-siloxy)carbene conformers seems to cause the ∠C6O7Si angle to shrink, the O7-Si and O2-C6 bonds to shorten and the C1-O2 and C6-O7 bonds to lengthen. We also mentioned that σ-electron-withdrawing substituents cause the BCP electronic densities $\rho_b(r)$ of the O7-Si and O2-C6 bonds to increase, and the C1-O2 and C6-O7 bonds to decrease. The shrinkage of the ∠C6O7Si angle that accompanies an increase in the σ-electron-withdrawing ability of substituents is most likely due to an increase in the combined $n(\sigma)_{C6} \rightarrow \sigma^*_{O7\text{-}Si}$, $n(\sigma)_{C6} \rightarrow \sigma^*_{Si\text{-}X}$ and $n(\sigma)_{C6} \rightarrow RY^*_{Si}$ hyperconjugative interactions in conformers **A(X)** and **B(X)**, and to the

$n(\sigma)_{O2}\rightarrow\sigma^*_{O7\text{-}Si}$ and $n(\sigma)_{O2}\rightarrow\sigma^*_{Si\text{-}X}$ hyperconjugative interactions in conformers **C(X)**. As a matter of fact, excellent linear correlations are obtained for plots of the ∠C6O7Si angle versus the total stabilization energy $E^{(tot)}_{stab}$ that arises from the combined $n(\sigma)_{C6}\rightarrow\sigma^*_{O7\text{-}Si}$, $n(\sigma)_{C6}\rightarrow\sigma^*_{Si\text{-}X}$ and $n(\sigma)_{C6}\rightarrow RY^*_{Si}$ hyperconjugative interactions in conformers **A(X)** and **B(X)**, and $n(\sigma)_{O2}\rightarrow\sigma^*_{O7\text{-}Si}$ and $n(\sigma)_{O2}\rightarrow\sigma^*_{Si\text{-}X}$ hyperconjugative interactions in conformers **C(X)**. Plots of the ∠C6O7Si angles versus total stabilization energies $E^{(tot)}_{stab}$ due to the pertinent hyperconjugative interactions for conformers **A(X)** are shown in Figs 3.11, while those for conformers **B(X)** and **C(X)** are provided in Appendix C (cf. Figs. C26 and C27). We also noted earlier that the dependence of the ∠C6O7Si angle on σ_I is considerably greater for conformers **A(X)** and **B(X)** than for conformers **C(X)**, while that for conformers **B(X)** is slightly greater than that for conformers **A(X)**. The former observation most likely arises because the combined $n(\sigma)_{C6}\rightarrow\sigma^*_{O7\text{-}Si}$, $n(\sigma)_{C6}\rightarrow\sigma^*_{Si\text{-}X}$ and $n(\sigma)_{C6}\rightarrow RY^*_{Si}$ interactions in **A(X)** and **B(X)** are significantly greater than $n(\sigma)_{O2}\rightarrow\sigma^*_{O7\text{-}Si}$ and $n(\sigma)_{O2}\rightarrow\sigma^*_{Si\text{-}X}$ hyperconjugation in **C(X)**, while the latter finding arises because the combined $n(\sigma)_{C6}\rightarrow\sigma^*_{O7\text{-}Si}$, $n(\sigma)_{C6}\rightarrow\sigma^*_{Si\text{-}X}$ and $n(\sigma)_{C6}\rightarrow RY^*_{Si}$ hyperconjugative interactions in conformers **B(X)** are slightly stronger than that in the corresponding conformers **A(X)** (cf. Table 3.7).

The O7-Si and O2-C6 bond shortening in the carbene conformers likely results from a strengthening of $n(\sigma)_{O7}\rightarrow\sigma^*_{Si\text{-}X}$ and $n(\sigma)_{O2}\rightarrow\sigma^*_{C6\text{-}O7}$ hyperconjugation depicted in Schemes 3.4a and 3.4c that accompanies an increase in the σ-electron-withdrawing ability of substituents, while the C6-O7 and C1-O2 bond lengthening probably arises from a weakening of $n(\sigma)_{O7}\rightarrow\sigma^*_{O2\text{-}C6}$ and $n(\sigma)_{O2}\rightarrow\sigma^*_{C1\text{-}H}$ hyperconjugation shown in Schemes 3.4b and 3.4d. Apparently, the strengthening of $n(\sigma)_{O7}\rightarrow\sigma^*_{Si\text{-}X}$

hyperconjugation by σ-electron-withdrawing substituents results in a weakening of $n(\sigma)_{O7}\rightarrow\sigma^*_{O2\text{-}C6}$ and $n(\sigma)_{O2}\rightarrow\sigma^*_{C1\text{-}H}$ hyperconjugation, and a strengthening of $n(\sigma)_{O2}\rightarrow\sigma^*_{C6\text{-}O7}$ hyperconjugation. More explicitly, the presence of σ-electron-withdrawing substituents on the silyl moiety causes an increase in $n(\sigma)_{O7}\rightarrow\sigma^*_{Si\text{-}X}$ charge transfer (hyperconjugation), which consequently reduces $n(\sigma)_{O7}\rightarrow\sigma^*_{O2\text{-}C6}$ charge transfer, hence the O7-Si bond shortening and C6-O7 bond lengthening. The C6-O7 bond lengthening increases bond polarization and thus lowers the energy of the $\sigma^*_{C6\text{-}O7}$ orbital, which results in stronger $n(\sigma)_{O2}\rightarrow\sigma^*_{C6\text{-}O7}$ hyperconjugation and thus O2-C6 bond shortening. Finally, the increase in $n(\sigma)_{O2}\rightarrow\sigma^*_{C6\text{-}O7}$ charge transfer lowers $n(\sigma)_{O2}\rightarrow\sigma^*_{C1\text{-}H}$ charge transfer, which results in a weakening of the C1-O2 bond. In fact, fairly good linear correlations are obtained for plots of the O7-Si bond lengths versus stabilization energies due to $n(\sigma)_{O7}\rightarrow\sigma^*_{Si\text{-}X}$ hyperconjugation, and the C6-O7 bond lengths versus stabilization energies due to $n(\sigma)_{O7}\rightarrow\sigma^*_{O2\text{-}C6}$ hyperconjugation, which support the above conclusions. These plots are available in Appendix C (cf. Fig. C28 to C33). Linear correlations between the O2-C6 bond length versus $n(\sigma)_{O2}\rightarrow\sigma^*_{C6\text{-}O7}$ stabilization energies and the C1-O2 bond length versus $n(\sigma)_{O2}\rightarrow\sigma^*_{C1\text{-}H}$ stabilization energies also likely exist.

It is evident from the activation enthalpies in Table 3.6 that 1,2-silyl migration in conformers **A(X)** and **B(X)** via $\mathbf{TS_{AD}(X)}$ and $\mathbf{TS_{BE}(X)}$, respectively, is considerably more favorable than decarbonylation of conformers **C(X)** via $\mathbf{TS_{CH}(X)}$. This is most likely due to the fact that the $n(\sigma)_{C6}\rightarrow\sigma^*_{O7\text{-}Si}$, $n(\sigma)_{C6}\rightarrow\sigma^*_{Si\text{-}X}$ and $n(\sigma)_{C6}\rightarrow RY^*_{Si}$ hyperconjugative interactions in conformers **A(X)** and **B(X)** are collectively greater than the combined $n(\sigma)_{O2}\rightarrow\sigma^*_{O7\text{-}Si}$, $n(\sigma)_{O2}\rightarrow\sigma^*_{Si\text{-}X}$ and $n(\sigma)_{O2}\rightarrow RY^*_{Si}$ hyperconjugative interactions in conformers **C(X)**, as evident from the stabilization energies $E^{(tot)}_{stab}$ in Table 3.7. The

stronger $n(\sigma)_{C6} \rightarrow \sigma^*_{O7\text{-}Si}$, $n(\sigma)_{C6} \rightarrow \sigma^*_{Si\text{-}X}$ and $n(\sigma)_{C6} \rightarrow RY^*_{Si}$ hyperconjugative interactions in the **A(X)** and **B(X)** conformers compared to the $n(\sigma)_{O2} \rightarrow \sigma^*_{O7\text{-}Si}$, $n(\sigma)_{O2} \rightarrow \sigma^*_{Si\text{-}X}$ and $n(\sigma)_{O2} \rightarrow RY^*_{Si}$ hyperconjugative interactions in the **C(X)** conformers are primarily due to the fact that the $n(\sigma)_{C6}$ orbital energies are higher than the $n(\sigma)_{O2}$ orbital energies (cf. Table 3.8). In addition, the closer proximity of the C6 and Si atoms in conformers **A(X)** and **B(X)** compared to the O2 and Si atoms in conformers **C(X)** facilitates $n(\sigma)_{C6} \rightarrow \sigma^*_{O7\text{-}Si}$, $n(\sigma)_{C6} \rightarrow \sigma^*_{Si\text{-}X}$ and $n(\sigma)_{C6} \rightarrow RY^*_{Si}$ hyperconjugation.

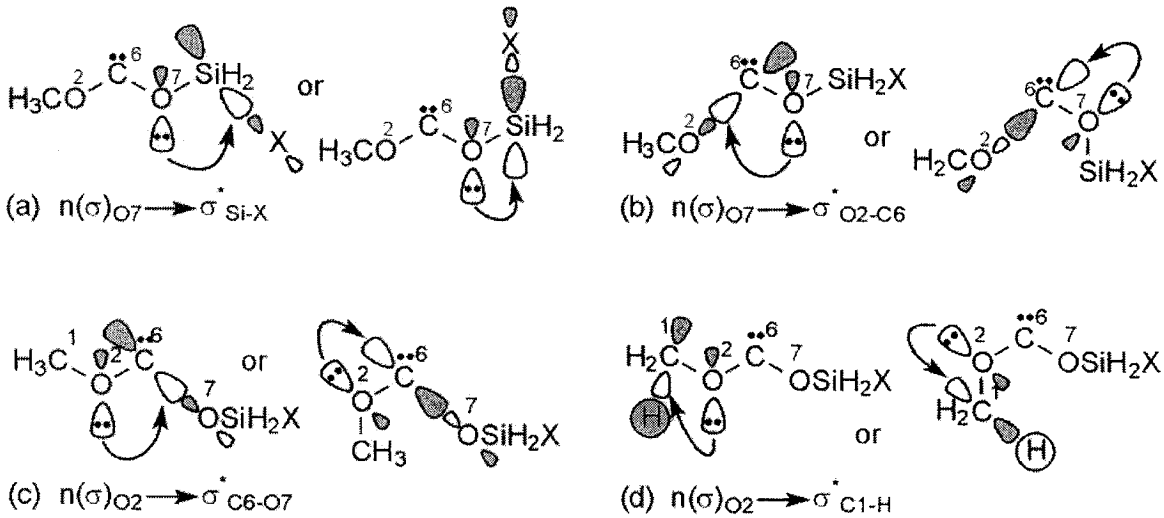

Scheme 3.4

It is also apparent from the activation enthalpies in Table 3.6 that 1,2-silyl migration in conformers **B(X)** is slightly more favorable than that in their **A(X)** counterparts. This is primarily due to the smaller $n(\sigma)_{C6} \rightarrow \sigma^*_{O7\text{-}Si}$ and $n(\sigma)_{C6} \rightarrow \sigma^*_{Si\text{-}X}$ orbital energy gaps in conformers **B(X)**, which result from higher $n(\sigma)_{C6}$ and lower $\sigma^*_{O7\text{-}Si}$ and $\sigma^*_{Si\text{-}X}$ orbital energies (cf. Table 3.8). Apparently, since the $n(\sigma)_{O2}$ orbital is antiperiplanar to the $n(\sigma)_{C6}$ orbital in the **A(X)** conformers (cf. Scheme 3.5), interaction between these non-bonding orbitals is essentially non-existent. In contrast, the $n(\sigma)_{O2}$

orbital is synperiplanar to the $n(\sigma)_{C6}$ orbital in the **B(X)** conformers, which maximizes interaction and consequently raises the $n(\sigma)_{C6}$ orbital energy (cf. Scheme 3.5). In other words, the α-effect,[91] which refers to the increase in nucleophilicity of a nucleophilic site observed when it is flanked by lone-pair-carrying atoms, is at a minimum in conformers **A(X)** and at a maximum in conformers **B(X)**. On the other hand, the lower $\sigma^*_{O7\text{-}Si}$ and $\sigma^*_{Si\text{-}X}$ orbital energies in conformers **B(X)** relative to their **A(X)** counterparts most likely arises from greater polarization of the O7-Si and Si-X bonds as a result of differences in the orientation and magnitude of the net molecular dipole moments between these two types of carbene conformers. In fact, the magnitudes of polarization coefficients on the electronegative O7 atom and the electropositive Si atom of the $\sigma^*_{O7\text{-}Si}$ orbital in conformers **B(X)** are indeed smaller and larger, respectively, than those in the corresponding conformers **A(X)** (cf. Table 3.8), indicative of the greater polarization of the O7-Si bond in the **B(X)** conformers. Similarly, the magnitudes of the polarization coefficients of the $\sigma^*_{Si\text{-}X}$ orbitals are larger on the more electropositive Si atoms and smaller on the more electronegative X atoms in the **B(X)** conformers than in the corresponding **A(X)** conformers (cf. Table 3.8), consistent with greater polarization of the Si-X bond in conformers **B(X)**.

Plots of activation enthalpies ΔH_{TS} for 1,2-silyl migration and decarbonylation versus total HF/6-311+G(2d,p)//MP2/6-311+G(2d,p) stabilization energies $E^{(tot)}_{stab}$ due to $n(\sigma)_{C6}\rightarrow\sigma^*_{O7\text{-}Si}$, $n(\sigma)_{C6}\rightarrow\sigma^*_{Si\text{-}X}$ and $n(\sigma)_{C6}\rightarrow RY^*_{Si}$ hyperconjugation in conformers **A(X)** and **B(X)**, and $n(\sigma)_{O2}\rightarrow\sigma^*_{O7\text{-}Si}$ and $n(\sigma)_{O2}\rightarrow\sigma^*_{Si\text{-}X}$ hyperconjugation in conformers **C(X)** hyperconjugation are shown in Figs. 3.12 and 3.13, respectively. Similar plots of ΔH_{TS} versus stabilization energies $E^{(tot)}_{stab}$ computed with the less rigorous HF/6-311+G(2d,p)

and B3LYP/6-311+G(2d,p) model chemistries are provided in Appendix C (cf. Figs C34 to C39). For 1,2-silyl migration, ΔH_{TS} generally seems to decrease with increasing $E^{(tot)}_{stab}$, suggesting that stronger hyperconjugative interaction in the ground-state carbene conformers **A(X)** and **B(X)** lower the activation enthalpies (cf. Figs. 12). We note however that the correlations for plots of ΔH_{TS} versus stabilization energies $E^{(tot)}_{stab}$ are generally quite poor. The best correlations are obtained for plots of ΔH_{TS} versus computed HF/6-311+G(2d,p)//MP2/6-311+G(2d,p) stabilization energies $E^{(tot)}_{stab}$ in Fig. 12. In regards to decarbonylation of conformers **C(X)**, there is effectively no correlation between ΔH_{TS} and $E^{(tot)}_{stab}$. This may be an indication that the activation enthalpies for decarbonylation of conformers **C(X)** are independent of $n(\sigma)_{O2} \rightarrow \sigma^*_{O7\text{-}Si}$ and $n(\sigma)_{O2} \rightarrow \sigma^*_{Si\text{-}X}$ hyperconjugation.

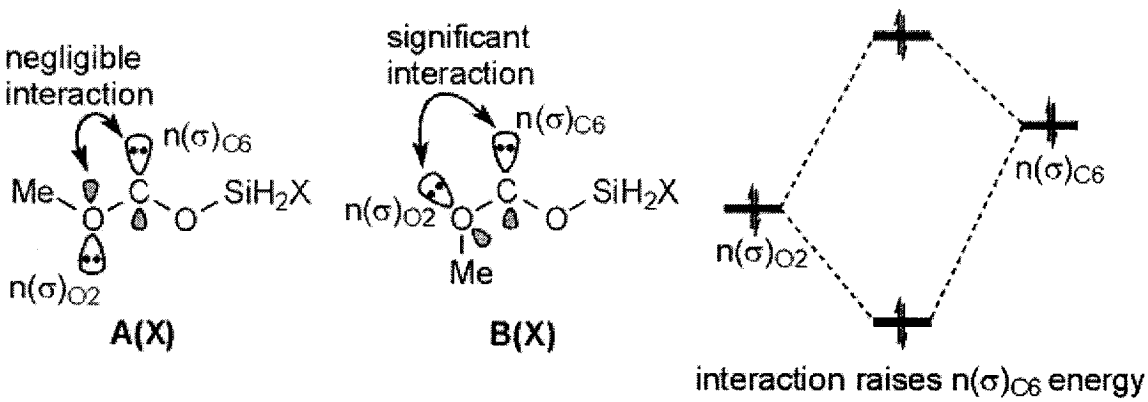

Scheme 3.5

Table 3.7 HF/6-311+G(2d,p)//MP2/6-311+G(2d,p) stabilization energies due to hyperconjugation in methoxy(substituted-siloxy)carbenes.[a]

X	$n(\sigma)_{C6}\rightarrow\sigma^*_{O7\text{-}Si}$	$n(\sigma)_{C6}\rightarrow\sigma^*_{Si\text{-}X}$	$n(\sigma)_{C6}\rightarrow RY^*_{Si}$	$E^{(tot)}_{stab}$
		A(X)		
H	5.32	2.05	1.97	9.33
NH_2	3.94	2.08	4.99	11.01
CCH	5.40	2.64	5.72	13.75
SH	5.78	3.12	4.06	12.96
OH	4.18	2.18	4.22	10.58
Cl	6.70	4.17	6.29	17.16
F	5.38	3.33	5.71	14.42
CN	6.97	3.50	5.18	15.65
		B(X)		
H	5.44	2.51	1.92	9.87
NH_2	4.02	2.66	4.34	11.03
CCH	5.57	3.23	2.55	11.35
SH	6.88	3.75	6.28	16.91
OH	4.51	3.07	4.39	11.97
Cl	7.70	5.80	7.62	21.12
F	6.87	5.42	7.91	20.19
CN	8.03	4.92	6.10	19.05
		C(X)		
	$n(\sigma)_{O2}\rightarrow\sigma^*_{O7\text{-}Si}$	$n(\sigma)_{O2}\rightarrow\sigma^*_{Si\text{-}X}$	$n_{O2}\rightarrow RY^*_{Si}$	$E^{(tot)}_{stab}$
H	3.31	2.11	0.00	5.42
NH_2	2.39	2.09	0.00	4.47
CCH	3.37	2.44	0.00	5.81
SH	3.31	2.56	0.00	5.86
OH	2.47	2.03	0.00	4.50
Cl	3.51	2.80	0.00	6.31
F	2.76	2.29	0.00	5.04
CN	4.11	2.95	0.00	7.06

[a] Stabilization energies are in kcal/mol and were obtained from NBO analysis by deletion of specific Fock matrix elements. $E^{(tot)}_{stab}$ is the sum of the stabilization energies that arises from the $n(\sigma)_{C6}\rightarrow\sigma^*_{O7\text{-}Si}$, $n(\sigma)_{C6}\rightarrow\sigma^*_{Si\text{-}X}$ and all $n(\sigma)_{C6}\rightarrow RY^*_{Si}$ interactions in conformers **A(X)** and **B(X)**, and from the $n(\sigma)_{O2}\rightarrow\sigma^*_{O7\text{-}Si}$ and $n(\sigma)_{O2}\rightarrow\sigma^*_{Si\text{-}X}$ interactions in conformers **C(X)**. HF/6-311+G(2d,p) and B3LYP/6-311+G(2d,p) stabilization energies are available in Appendix C.

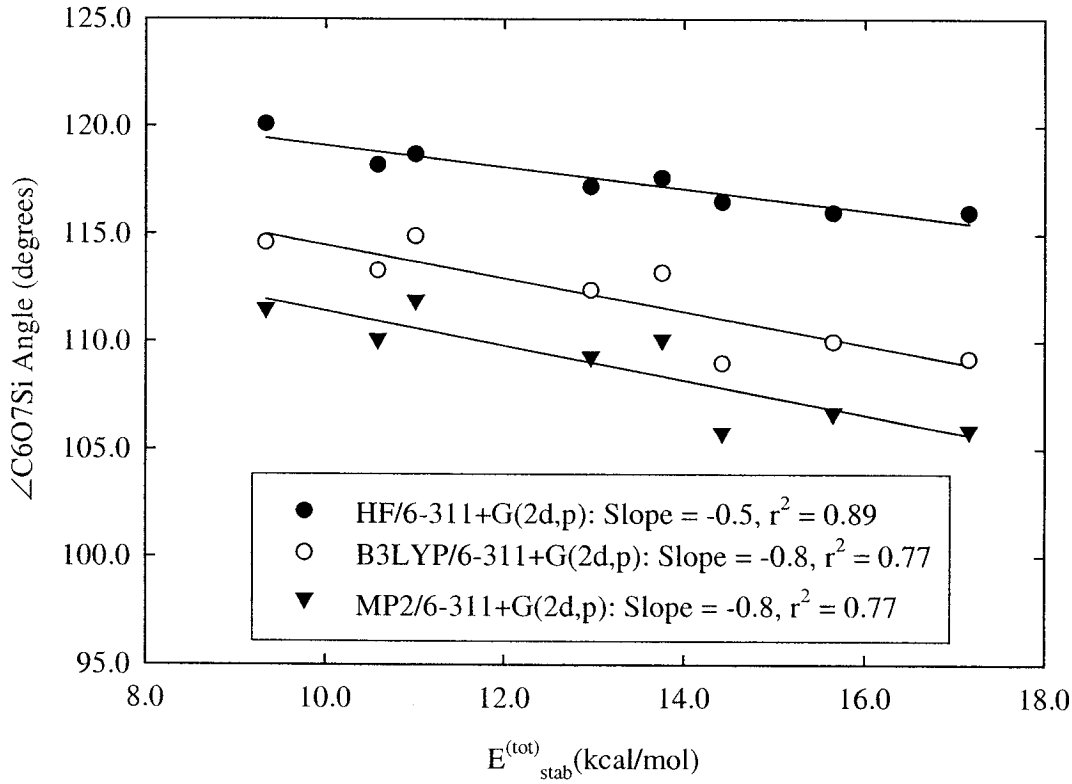

Figure 3.11 Plots of the ∠C6O7Si angles of methoxy(substituted-siloxy)carbene conformers **A(X)** versus stabilization energies $E^{(tot)}_{stab}$ due to hyperconjugation.

Table 3.8 HF/6-311+G(2d,p)//MP2/6-311+G(2d,p) NBO energies and polarization coefficients for methoxy(substituted-siloxy)carbenes.[a]

X	$n(\sigma)_{C6}$	$\sigma^*_{O7\text{-}Si}$	$c_{(O7)}$[b]	$c_{(Si)}$[b]	$\sigma^*_{Si\text{-}X}$	$c_{(Si)}$[c]	$c_{(X)}$[c]
				A(X)			
H	-0.5111	0.3623	0.3720	-0.9282	0.3979	0.7897	-0.6135
NH_2	-0.5037	0.3873	0.3650	-0.9310	0.4742	0.9041	-0.4273
CCH	-0.5119	0.3798	0.3736	-0.9276	0.4820	0.8643	-0.5030
SH	-0.5141	0.3485	0.3715	-0.9284	0.3058	0.8333	-0.5528
OH	-0.5127	0.3966	0.3633	-0.9317	0.4534	0.9260	-0.3776
Cl	-0.5203	0.3518	0.3711	-0.9286	0.3137	0.8725	-0.4886
F	-0.5221	0.3953	0.3627	-0.9319	0.4239	0.9400	-0.3411
CN	-0.5309	0.3546	0.3919	-0.9200	0.4250	0.8486	-0.5290
				B(X)			
H	-0.4920	0.3506	0.3674	-0.9301	0.3951	0.7910	-0.6119
NH_2	-0.4840	0.3768	0.3604	-0.9328	0.4731	0.9049	-0.4256
CCH	-0.4929	0.3699	0.3687	-0.9295	0.4780	0.8650	-0.5018
SH	-0.4960	0.3422	0.3656	-0.9308	0.2986	0.8349	-0.5504
OH	-0.4928	0.3854	0.3585	-0.9335	0.4492	0.9264	-0.3764
Cl	-0.4999	0.3380	0.3653	-0.9309	0.3103	0.8737	-0.4864
F	-0.5010	0.3800	0.3561	-0.9345	0.4215	0.9406	-0.3394
CN	-0.5110	0.3426	0.3712	-0.9285	0.4213	0.8632	-0.5049
				C(X)			
X	$n(\sigma)_{O2}$	$\sigma^*_{O7\text{-}Si}$	$c_{(O7)}$[b]	$c_{(Si)}$[b]	$\sigma^*_{Si\text{-}X}$	$c_{(Si)}$[c]	$c_{(X)}$[c]
H	-0.8180	0.3436	0.3800	-0.9250	0.4010	0.7885	-0.6151
NH_2	-0.8123	0.3732	0.3714	-0.9285	0.4756	0.9032	-0.4292
CCH	-0.8210	0.3619	0.3823	-0.9241	0.4849	0.8632	-0.5049
SH	-0.8233	0.3331	0.3790	-0.9254	0.3069	0.8319	-0.5549
OH	-0.8211	0.3814	0.3700	-0.9290	0.4546	0.9252	-0.3795
Cl	-0.8312	0.3381	0.3797	-0.9251	0.3148	0.8709	-0.4915
F	-0.8324	0.3824	0.3707	-0.9288	0.4231	0.9391	-0.3435
CN	-0.8414	0.3376	0.3871	-0.9220	0.4270	0.8608	-0.5089

[a] NBO energies are in atomic units. [b] Polarization coefficients $c_{(O7)}$ and $c_{(Si)}$ are for $\sigma^*_{O7\text{-}Si}$. [c] Polarization coefficients $c_{(Si)}$ and $c_{(X)}$ are for $\sigma^*_{Si\text{-}X}$. HF/6-311+G(2d,p) and B3LYP/6-311+G(2d,p) NBO energies are available in Appendix C.

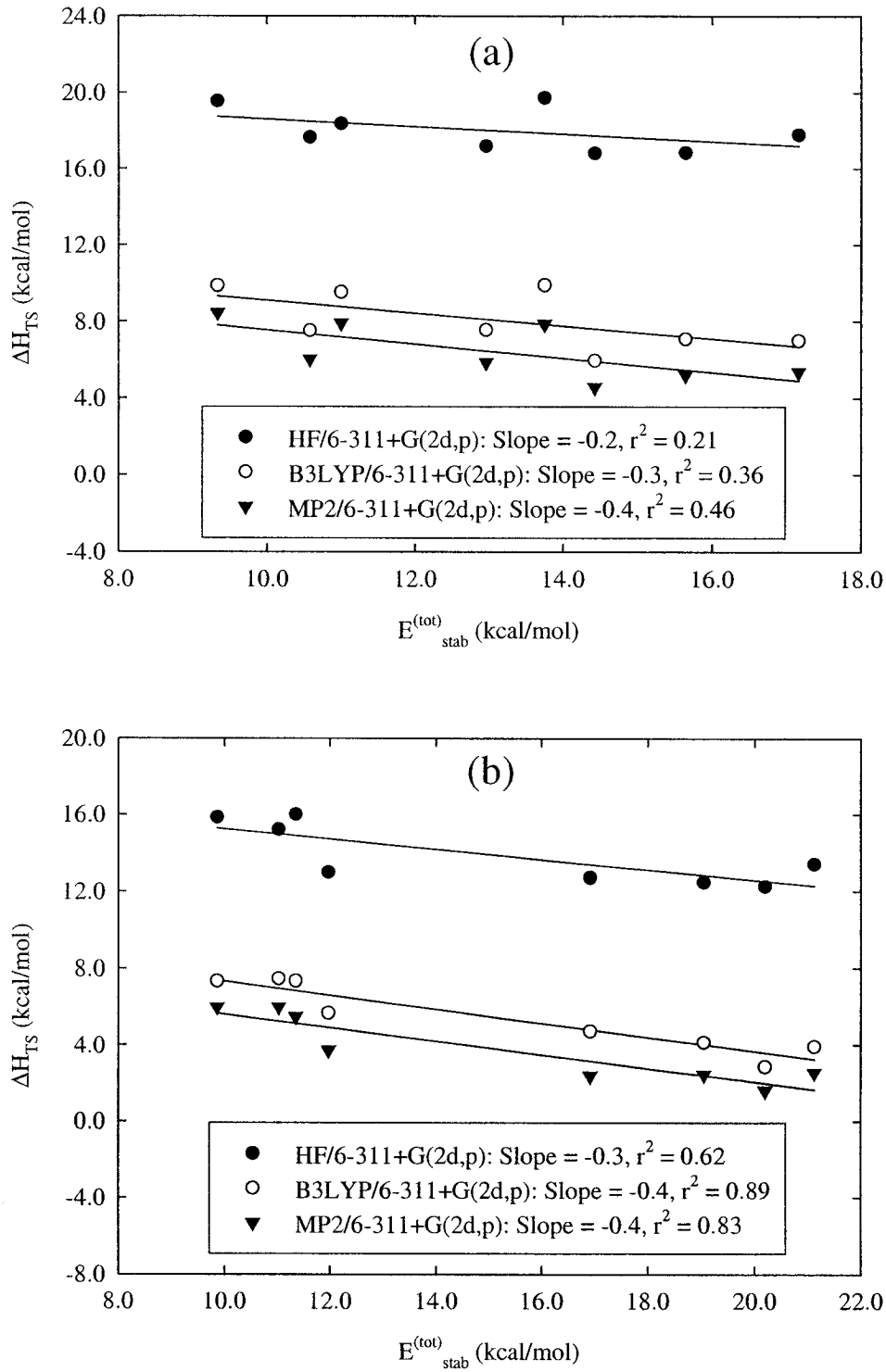

Figure 3.12 Plots of activation enthalpies for 1,2-silyl migration versus HF/6-311+G(2d,p)//MP2/6-311+G(2d,p) stabilization energies due to hyperconjugation in (a) conformers **A(X)** and (b) conformers **C(X)** of methoxy(substituted-siloxy)carbenes.

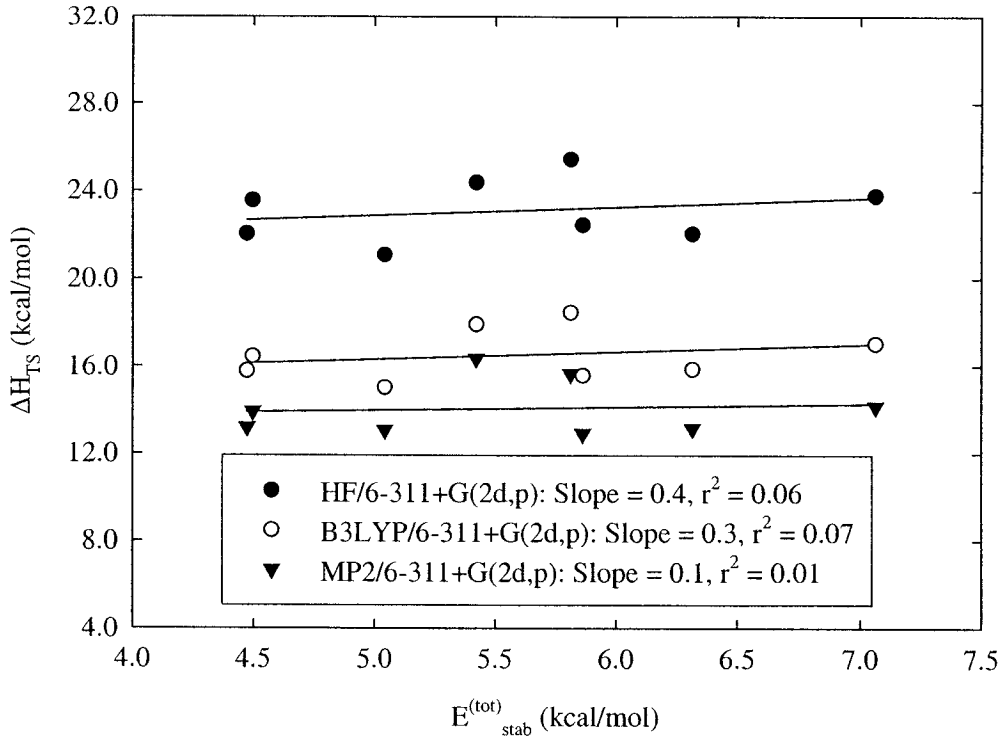

Figure 3.13 Plots of activation enthalpies for decarbonylation versus HF/6-311+G(2d,p)//MP2/6-311+G(2d,p) stabilization energies due to hyperconjugative interaction in conformers **C(X)** of methoxy(substituted-siloxy)carbenes.

3.4 Conclusion

The effects of substituents on 1,2-silyl migration and decarbonylation of methoxy(substituted-siloxy)carbenes have been investigated and it has been found that, in general, σ-electron-withdrawing substituents lower the activation barriers for these intramolecular reactions. However, although good linear Hammett correlations are obtained for 1,2-silyl migration, those obtained for decarbonylation are very poor. The finding that σ-electron-withdrawing substituents lower the activation barriers for 1,2-silyl migration and decarbonylation supports our earlier conclusions that 1,2-silyl migration and decarbonylation occur via front-side nucleophilic attack by the carbene lone pair at silicon and by the methoxy oxygen at silicon, respectively. The role of hyperconjugation in 1,2-silyl migration and decarbonylation of methoxy(substituted-siloxy)carbenes has also been investigated. The finding that 1,2-silyl migration is energetically more viable than decarbonylation seems to be primarily related to the fact that hyperconjugative interaction between the carbene lone pair $n(\sigma)_{C6}$ and the $\sigma^*_{O7\text{-}Si}$ orbital is stronger than that between the in-plane methoxy oxygen lone pair $n(\sigma)_{O2}$ and the $\sigma^*_{O7\text{-}Si}$ orbital. However, while the activation enthalpies for 1,2-silyl migration seem to decrease linearly with stronger hyperconjugative interaction, there appears to be no correlation between the activation enthalpies for decarbonylation and the strength of hyperconjugation.

Chapter 4.
Intramolecular Rearrangements of 3-Sila-2-Oxacyclohexylidene

4.1 Introduction

Cyclic alkoxycarbenes have been known to undergo a number of intramolecular rearrangements, including 1,2-H migration, ring contraction and decarbonylation.[66-68] Particular attention has been paid to the mechanism of ring contraction, not only because it is an intriguing problem, but also because it is closely related to the photochemical ring expansion of cycloalkanones.[70,145-147] Experimental evidence seems to indicate that this reaction occurs via both a concerted mechanism involving an anion-like shift from oxygen to the "vacant" carbene *p* orbital and a stepwise fragmentation-recombination mechanism involving an acyl-alkyl biradical intermediate.[66-68] Decarbonylation is also believed to involve initial fragmentation to an acyl-alkyl biradical, which thereafter loses carbon monoxide to afford a dialkyl biradical.[66-68] The latter biradical then collapses to the appropriate cycloalkane product.

In the previous chapters, we provided evidence showing that 1,2-silyl migration and decarbonylation of methoxy(siloxy)carbenes occur via front-side nucleophilic attack by the carbene lone pair at silicon and by the methoxy oxygen at silicon, respectively. In light of these findings, we thought that it would be of interest to investigate the mechanisms of 1,2-silyl migration (i.e. ring contraction) and decarbonylation, as well as 1,2-H migration, in a cyclic siloxycarbene such as 3-sila-2-oxacyclohexylidene **A** (cf. Scheme 4.1). Although cyclic siloxycarbenes have been generated by thermolysis and photolysis of acylsilanes, research has focused primarily on their intermolecular reactivity with species such as alkenes, alcohols, acids, aldehydes and ketones.[6,10,11,14]

3,3-Dimethyl-3-sila-2-oxacyclohexylidene has been reported to undergo ring contraction, decarbonylation and 1,2-H migration,[14] but to our knowledge, the mechanisms of these intramolecular rearrangements have never been investigated, presumably because of the assumption that they are no different from the analogous rearrangements of cyclic alkoxycarbenes.[66-68]

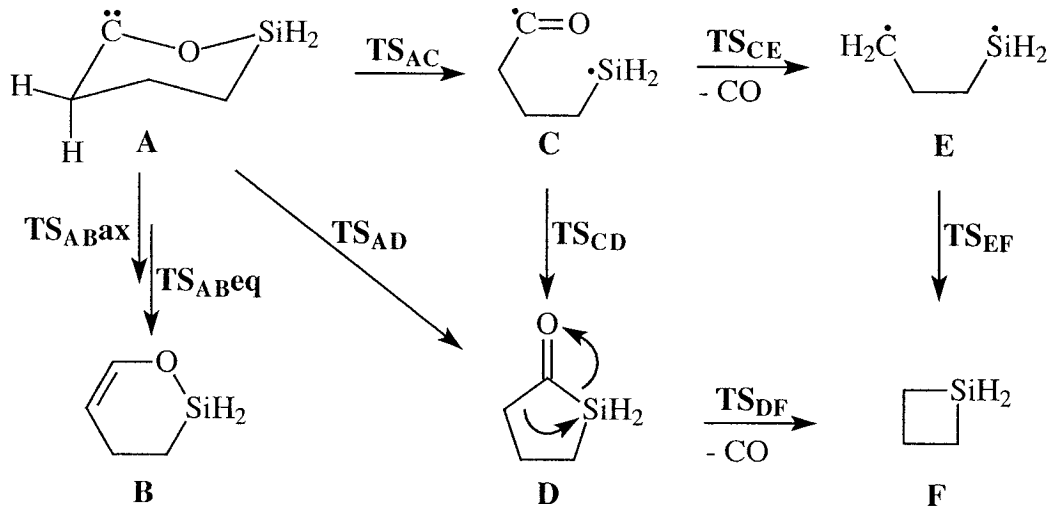

Scheme 4.1

The mechanism for 1,2-H migration in 3-sila-2-oxacyclohexylidene **A** is expected to involve a typical hydride-like shift to the "vacant" carbene *p* orbital.[28-30,38,39,41] However, the mechanisms for ring contraction and decarbonylation are expected to be a bit more complicated. As shown in Scheme 4.1, ring contraction of **A** could occur via a concerted mechanism, or a stepwise mechanism involving the acyl-silyl biradical intermediate **C**. Moreover, the concerted mechanism could involve either an anion-like shift of the silyl group from oxygen to the "vacant" carbene *p* orbital or front-side nucleophilic attack by the carbene lone pair at silicon. Assuming **A** exists in a chair-like conformation, ring contraction involving an anion-like shift of the silyl group from oxygen to the "vacant" carbene *p* orbital is expected to be favorable since the relevant

frontier orbitals are appropriately aligned (cf. Scheme 4.2a). Moreover, it is clear from the sketch of the frontier orbitals in Scheme 4.2a that this mechanism is *symmetry-allowed* according to Woodward-Hoffmann rules,[89-93] since interaction between the $\sigma_{O\text{-}Si}$ orbital (HOMO) and the "vacant" carbene *p* orbital (LUMO) leads to a favorable bonding interaction. In contrast, ring contraction involving front-side nucleophilic attack by the carbene lone pair at silicon is not expected to be favorable because of poor alignment of the relevant frontier orbitals (cf. Scheme 4.2b) and because the 'rigid' carbene ring structure may present difficulties in achieving appropriate alignment of the pertinent frontier orbitals. Furthermore, it is evident from the sketch of the frontier orbitals in Scheme 4.2b that the latter mechanism is *symmetry-forbidden*, since interaction between the carbene lone-pair n_C orbital (HOMO) and the $\sigma^*_{O\text{-}Si}$ orbital (LUMO) contains a destabilizing anti-bonding component.

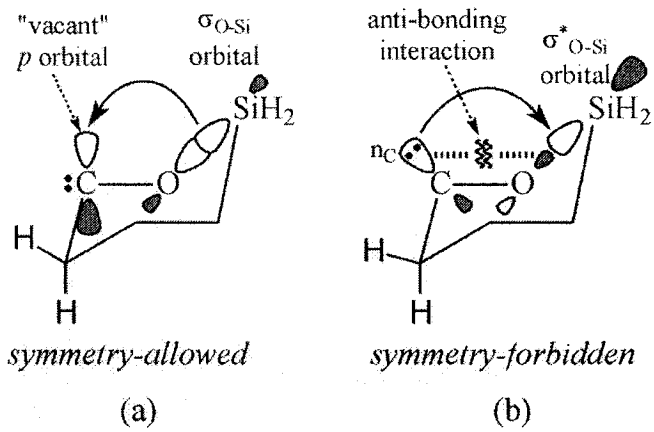

Scheme 4.2

Finally, decarbonylation of 3-sila-2-oxacyclohexylidene **A** could occur via two distinct pathways, both of which are shown in Scheme 4.1. The first pathway is that involving initial fragmentation to afford the acyl-silyl biradical **C**, followed by loss of carbon monoxide to yield the silabutane biradical **E**, which then collapses to

silacyclobutane **F** (cf. Scheme 4.1). This is similar to the mechanism proposed for decarbonylation of cyclic alkoxycarbenes.[66-68] The second pathway involves initial ring contraction to give silacyclopentanone **D**, followed by decarbonylation to yield **F** (cf. Scheme 4.1). The mechanism for decarbonylation of **D** in Scheme 4.1 resembles somewhat that proposed by Brook for decarbonylation of methyl triphenylsilylformate involving nucleophilic attack by the methoxy oxygen at silicon.[6]

In this chapter, we report results from our investigation of the mechanisms of intramolecular rearrangements of 3-sila-2-oxacyclohexylidene **A** based on hybrid density-functional theory calculations combined with the quantum theory of atoms in molecules and the electron localization function.[148] We will first discuss the geometry of carbene **A**, and then focus on the mechanisms of 1,2-H migration, ring contraction and decarbonylation as outlined in Scheme 4.1.

4.2 General Approach and Computational Methods

To shed light onto the mechanisms of intramolecular rearrangements of 3-sila-2-oxacyclohexylidene **A**, we performed a series of hybrid density-functional theory (DFT) calculations using the Becke three-parameter hybrid functional[101,102] with the Lee-Yang-Parr correlation potential[101,103] (B3LYP) and the Perdew-Burke-Ernzerhof one-parameter hybrid exchange-correlation functional[149-152] (PBE1PBE), in combination with the 6-311+G(2d,p) and cc-pVTZ basis sets. Broken-symmetry unrestricted density-functional theory (BS-UDFT), where the HOMO and LUMO are mixed to destroy α,β spin and spatial symmetries,[153] was used to characterize all open-shell singlet biradical species while restricted density-functional theory (RDFT) was used for closed-shell singlet

species. BS-UDFT, particularly BS-UB3LYP, has been found to provide reasonable descriptions of open-shell singlet biradical species.[154] In this work, BS-UB3LYP and BS-UPBE1PBE methods were used to characterize the biradical intermediates **C** and **E**, and the transition states $\mathbf{TS_{AC}}$, $\mathbf{TS_{CD}}$, $\mathbf{TS_{CE}}$ and $\mathbf{TS_{EF}}$ (cf. Scheme 4.1). The calculations were performed using the Gaussian98 suite of programs.[110] Geometry optimizations were performed with the default Berny algorithm[106] for minimum-energy structures and the eigenvector-following method[107-109] for transition-state structures. Frequency calculations were performed for stationary-point characterization and to obtain thermochemical data within the rigid rotor-harmonic oscillator approximation using standard statistical mechanics expressions implemented in Gaussian98.[111] Intrinsic reaction coordinate (IRC) calculations were also performed to confirm the identity of the computed transition states. The quantum theory of atoms in molecules[18] (AIM) and the electron localization function[19-23] (ELF) were used to probe changes in electronic charge distribution and hence molecular structure. AIM analysis was carried out with the AIMPAC suite of programs[18,112,113] and AIM2000,[155] while ELF analysis was performed with the TopMod program package.[114] All ELF isosurfaces were plotted with the SciAn program[115] using an ELF isovalue of 0.85. Natural bond orbital (NBO) analysis[24] was also carried out with the NBO program version 3.1[141] available in Gaussian98, to shed some light onto geometric features of **A**.

4.3 Results and Discussion

4.3.1 Geometry of 3-Sila-2-oxacyclohexylidene

The minimum-energy structure of 3-sila-2-oxacyclohexylidene **A**, along with selected geometric parameters, is shown in Fig. 4.1. It appears that this *pseudo* half-chair conformer of **A** is the only minimum-energy conformer that exists, presumably because the C2-O bond has significant double-bond character which results in cyclohexene-like characteristics (i.e. half-chair conformation). This double-bond character is reflected in the fact that the C2-O bond in **A** is shorter than it is in 4-sila-3-oxacyclohexene **B** (cf. Fig. 4.1). The double-bond character is also evident from the topological properties of the electronic density given in Table 4.1, where values of $\rho_b(r)$ for the C2-O bond in **A** are larger than those in **B**. Values of the bond ellipticity ε for the C2-O bond in **A** are also greater than zero, consistent with the elliptical symmetry of the BCP charge density usually associated with double bonds.[117] In comparison, values of ε for the C2-O bond in **B** are all essentially zero, reflecting the cylindrical symmetry of the BCP charge density that is characteristic of single bonds. From the ELF basin properties given in Table 4.2, it is apparent that the population of the V(C2,O) basin in **A** is larger than it is in **B**, further supporting the notion that the C2-O bond in **A** has some double-bond character. We also note that natural bond orbital (NBO) analysis[24] reveals that the most suitable Lewis-structure description of the B3LYP and PBE1PBE wave functions of **A** is with the C2-O bond as a double bond.

The pseudo axial C1-H4 bond of **A** is slightly longer than the pseudo equatorial C1-H3 bond (cf. Fig. 4.1). Similar observations have been reported for singlet cyclohexylidene derivatives and have been attributed to stronger hyperconjugative

interaction between the axial $\sigma_{C\text{-}H}$ orbital and the vacant carbene *p* orbital.[40,44] According to second-order NBO perturbation-energy analysis, the B3LYP/6-311+G(2d,p), B3LYP/cc-pVTZ and PBE1PBE/6-311+G(2d,p) stabilization energies that arise from axial $\sigma_{C1\text{-}H4} \rightarrow p_{C2}$ hyperconjugation are 9.2, 9.2 and 10.0 kcal/mol respectively, while those due to equatorial $\sigma_{C1\text{-}H3} \rightarrow p_{C2}$ hyperconjugation are 3.7, 3.6 and 4.5 kcal/mol. These findings support the notion that the longer axial C1-H4 bond arises from greater hyperconjugative interaction between the axial $\sigma_{C1\text{-}H4}$ orbital and the "vacant" carbene *p* orbital.

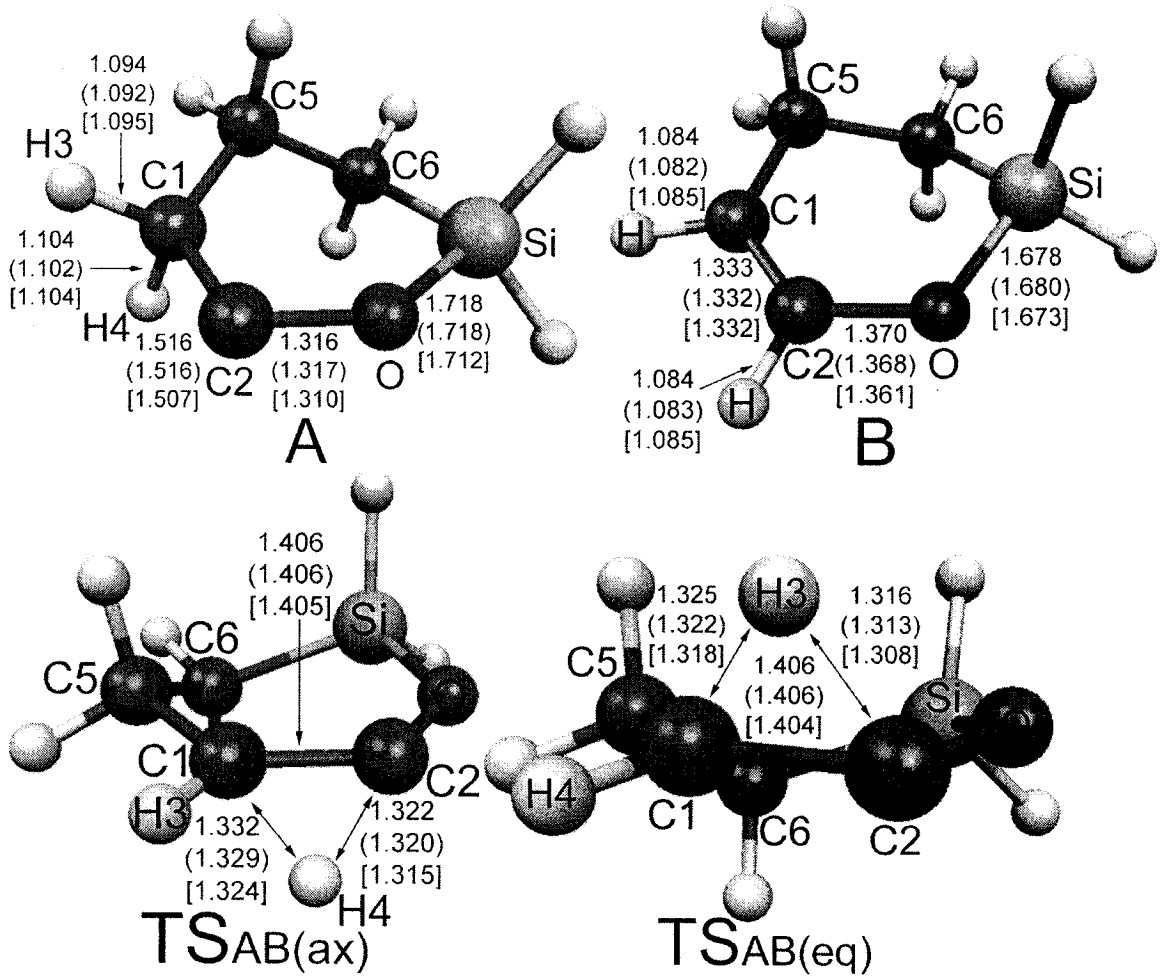

Figure 4.1 Optimized molecular geometries of 3-sila-2-oxacyclohexylidene, 4-sila-3-oxacyclohexene, and the transition states for axial and equatorial 1,2-H migration. Bond distances are given for B3LYP/6-311+G(2d,p), B3LYP/cc-pVTZ (parentheses) and PBE1PBE/6-311+G(2d,p) [brackets] model chemistries. Bond lengths are in Å.

Table 4.1 Topological properties of electronic density at important BCPs for 3-sila-2-oxacyclohexylidene, 4-sila-3-oxacyclohexene and the transition states for axial and equatorial 1,2-H migration.[a]

	C1-C2	C1-H3	C1-H4	C2-O	O-Si
			A		
			B3LYP/6-311+G(2d,p)		
$\rho_b(r)$ (e/Å^3)	1.72	1.86	1.78	2.06	0.80
$\nabla^2\rho_b(r)$ (e/Å^5)	-13.8	-22.1	-20.4	-7.3	13.1
ε	0.02	0.03	0.03	0.48	0.01
			B3LYP/cc-pVTZ		
$\rho_b(r)$ (e/Å^3)	1.77	1.92	1.84	2.06	0.80
$\nabla^2\rho_b(r)$ (e/Å^5)	-16.6	-26.3	-24.2	-4.0	15.3
ε	0.02	0.03	0.03	0.48	0.02
			PBE1PBE/6-311+G(2d,p)		
$\rho_b(r)$ (e/Å^3)	1.75	1.84	1.77	2.08	0.81
$\nabla^2\rho_b(r)$ (e/Å^5)	-14.5	-21.9	-20.3	-5.0	13.8
ε	0.02	0.03	0.03	0.48	0.01
			TS_{AB}(ax)		
			B3LYP/6-311+G(2d,p)		
$\rho_b(r)$ (e/Å^3)	2.08	1.91	1.13	1.87	0.87
$\nabla^2\rho_b(r)$ (e/Å^5)	-20.3	-23.5	-2.3	-12.1	15.4
ε	0.16	0.03	2.03	0.42	0.04
			B3LYP/cc-pVTZ		
$\rho_b(r)$ (e/Å^3)	2.13	1.98	1.17	1.88	0.87
$\nabla^2\rho_b(r)$ (e/Å^5)	-24.1	-27.9	-3.4	-8.8	17.6
ε	0.19	0.03	2.11	0.44	0.05
			PBE1PBE/6-311+G(2d,p)		
$\rho_b(r)$ (e/Å^3)	2.07	1.90	1.16	1.90	0.88
$\nabla^2\rho_b(r)$ (e/Å^5)	-20.3	-23.4	-2.7	-10.0	16.1
ε	0.17	0.03	2.02	0.44	0.04
			TS_{AB}(eq)		
			B3LYP/6-311+G(2d,p)		
$\rho_b(r)$ (e/Å^3)	2.07	1.15	1.91	1.85	0.88
$\nabla^2\rho_b(r)$ (e/Å^5)	-20.2	-2.5	-23.6	-12.1	15.6
ε	0.18	2.07	0.03	0.42	0.04
			B3LYP/cc-pVTZ		
$\rho_b(r)$ (e/Å^3)	2.13	1.19	1.98	1.87	0.87
$\nabla^2\rho_b(r)$ (e/Å^5)	-24.0	-3.6	-28.0	-9.1	17.8
ε	0.20	2.16	0.03	0.44	0.05
			PBE1PBE/6-311+G(2d,p)		
$\rho_b(r)$ (e/Å^3)	2.07	1.18	1.90	1.88	0.89
$\nabla^2\rho_b(r)$ (e/Å^5)	-20.2	-2.9	-23.4	-10.0	16.3
ε	0.18	2.10	0.03	0.44	0.04

Table 4.1 (Continued)

	C1-C2	C1-H	C2-H	C2-O	O-Si
			B		
			B3LYP/6-311+G(2d,p)		
$\rho_b(r)$ (e/Å^3)	2.36	1.89	1.95	1.89	0.88
$\nabla^2\rho_b(r)$ (e/Å^5)	-26.3	-23.0	-24.8	-14.0	16.2
ε	0.39	0.03	0.05	0.01	0.06
			B3LYP/cc-pVTZ		
$\rho_b(r)$ (e/Å^3)	2.42	1.96	2.02	1.91	0.87
$\nabla^2\rho_b(r)$ (e/Å^5)	-30.4	-27.4	-29.5	-11.2	18.3
ε	0.41	0.03	0.05	0.01	0.06
			PBE1PBE/6-311+G(2d,p)		
$\rho_b(r)$ (e/Å^3)	2.35	1.88	1.94	1.92	0.89
$\nabla^2\rho_b(r)$ (e/Å^5)	-26.2	-22.9	-24.7	-12.3	16.9
ε	0.40	0.03	0.05	0.00	0.06

[a] Obtained from AIM analysis.

Table 4.2 Basin population $N(\Omega_i)$, relative fluctuation $\lambda(\Omega_i)$ and %cross-exchange contribution for 3-sila-2-oxacyclohexylidene, 4-sila-3-oxacyclohexene and the transition states for axial and equatorial 1,2-H migration.[a]

Basin	$N(\Omega_i)$	$\lambda(\Omega_i)$	%Cross-exchange contribution[b]
			A
V(C1,C2)	2.03	0.50	V(C2) 9.5; V(C1,H3) 8.0; V(C1,H4) 8.5; V(C1,C5) 6.5
V(C1,H3)	1.98	0.34	V(C1,H4) 9.6; V(C1,C2) 7.0; V(C1,C5) 8.0; V(C2) 2.0
V(C1,H4)	1.94	0.35	V(C1,H3) 9.8; V(C1,C2) 7.3; V(C1,C5) 8.8; V(C2) 2.1
V(C2)	2.23	0.34	V(C1,C2) 8.5; V(C2,O) 6.3; V(O) 5.8
V(C2,O)	1.76	0.58	V(C1,C2) 8.5; V(C2) 8.0; V(O) 24.0; V(O,Si) 12.6
V(O)	3.53	0.40	V(C2,O) 11.9; V(O,Si) 15.0; V(C2) 3.7
V(O,Si)	2.24	0.52	V(O) 23.8; V(C2,O) 9.9; V(C6,Si) 2.2
			TS_{AB}(ax)
V(C1,C2)	2.26	0.50	V(C2) 9.3; V(C1,H3) 7.6; V(C1,H4,C2) 10.7
V(C1,H3)	2.08	0.32	V(C1,C2) 8.3; V(C1,C5) 7.3; V(C1,H4,C2) 6.8
V(C1,H4C2)	1.58	0.52	V(C2) 13.4; V(C1,H3) 8.9; V(C1,C2) 15.3; V(C1,C5) 5.9
V(C2)	2.14	0.42	V(C1,C2) 9.8; V(C1,H4,C2) 9.8; V(O) 5.6; V(C2,O) 5.1
V(C2,O))	1.32	0.64	V(C2) 8.5; V(O) 29.2; V(O,Si) 10.8; V(C1,C2) 6.9
V(O)	4.24	0.36	V(C2,O) 9.0; V(O,Si) 14.0; V(C2) 2.8
V(O,Si)	2.01	0.55	V(O) 29.5; V(C2,O) 7.0
			TS_{AB}(eq)
V(C1,C2)	2.25	0.50	V(C1,H3,C2) 10.8; V(C1,C5) 6.7; V(C2,O) 3.6; V(C2) 9.4
V(C1,H3,C2)	1.59	0.52	V(C1,H4) 8.9; V(C1,C5) 5.7; V(C1,C2) 15.2; V(C2) 13.3
V(C1,H4)	2.08	0.32	V(C1,H3,C2) 6.8; V(C1,C5) 7.3; V(C1,C2) 8.3; V(C2) 2.4
V(C2)	2.15	0.41	V(C1,H3,C2) 9.7; V(C1,C2) 9.7; V(C2,O) 5.1; V(O) 5.6
V(C2,O)	1.31	0.64	V(C1,C2) 6.2; V(O,Si) 10.8; V(C2) 8.5;V(O) 29.2
V(O)	4.19	0.37	V(O,Si) 14.4; V(C2,O) 9.1; V(C2) 2.9
V(O,Si)	2.08	0.54	V(O) 29.3; V(C2,O) 6.8
			B
V(C1,H)	2.12	0.32	V_1(C1,C2) 7.7, V_2(C1,C2) 7.7; V(C1,C5) 7.2
V_1(C1,C2)	1.87	0.55	V_2(C1,C2) 14.6; V(C1,H) 8.1; V(C2,H) 8.6; V(C1,C5) 7.0
V_2(C1,C2)	1.85	0.55	V_1(C1,C2) 14.8; V(C1,H) 8.7; V(C2,H) 8.7; V(C1,C5) 7.1
V(C2,H)	2.16	0.30	V_1(C1,C2) 7.0; V_2(C1,C2) 7.4; V(C2,O) 4.2
V(C2,O)	1.42	0.63	V(O) 29.1; V(O,Si) 9.9; V(C2,H) 6.4; V_1(C1,C2) 5.0
V(O)	4.30	0.36	V(C2,O) 9.6; V(O,Si) 13.6, V_1(C1,C2) 1.2; V_2(C1,C2) 1.2
V(O,Si)	1.90	0.56	V(C2,O) 7.7; V(O) 31.7; V(C6,Si) 2.7

[a] Obtained from ELF analysis of B3LYP/6-311+G(2d,p) wave functions. [b] Contributions of neighboring basins to the total basin population.

4.3.2 Mechanism for 1,2-H Migration

The optimized transition-state structures for 1,2-H migration from the axial and equatorial positions, $\mathbf{TS_{AB}(ax)}$ and $\mathbf{TS_{AB}(eq)}$, are shown in Fig. 4.1. For axial 1,2-H migration, the dissociating C1-H4 bond lengthens while the developing C1-C2 double bond shortens in $\mathbf{TS_{AB}(ax)}$ relative to **A** (cf. Fig. 4.1). The computed B3LYP/6-311+G(2d,p), B3LYP/cc-pVTZ and PBE1PBE/6-311+G(2d,p) ∠H4C1C2O dihedral angles of 106.1°, 106.4° and 106.3° respectively in $\mathbf{TS_{AB}(ax)}$, suggest that axial H4 migration occurs essentially perpendicular to the carbene valence plane (i.e. the plane containing the C1, C2 and O atoms). Simultaneously, the non-migrating equatorial H3 atom moves into the carbene valence plane, as is evident from the calculated B3LYP/6-311+G(2d,p), B3LYP/cc-pVTZ and PBE1PBE/6-311+G(2d,p) ∠H3C1C2O dihedral angles of 175.0°, 174.8° and 175.2° respectively. Similarly, for equatorial 1,2-H migration, the dissociating C1-H3 bond lengthens while the developing C1-C2 double bond shortens in $\mathbf{TS_{AB}(eq)}$ relative to **A** (cf. Fig. 4.1). The computed B3LYP/6-311+G(2d,p), B3LYP/cc-pVTZ and PBE1PBE/6-311+G(2d,p) ∠H3C1C2O dihedral angles of 104.5°, 104.8° and 104.6° clearly indicate that the equatorial H3 atom migrates perpendicular to the carbene valence plane, while the non-migrating axial H4 atom becomes co-planar with the carbene valence plane, which is reflected in the calculated B3LYP/6-311+G(2d,p), B3LYP/cc-pVTZ and PBE1PBE/6-311+G(2d,p) ∠H4C1C2O dihedral angles of 177.0°, 176.9° and 177.4°. These observations suggest that both axial and equatorial 1,2-H migration involves hydride-like shifts from the C1 atom to the "vacant" carbene *p* orbital on the C2 atom, perpendicular to the carbene valence plane. The co-planarity of the non-migrating H3 and H4 atoms with the carbene valence plane

in $\mathbf{TS_{AB}(ax)}$ and $\mathbf{TS_{AB}(eq)}$ respectively, is indicative of the development of partial cation-like character at C1 and/or ultimately C1-C2 double-bond formation.

The dissociation of the axial C1-H4 and equatorial C1-H3 bonds in $\mathbf{TS_{AB}(ax)}$ and $\mathbf{TS_{AB}(eq)}$ respectively, is reflected in the topological properties of the electronic density given in Table 4.1; values of $\rho_b(r)$ decrease for the C1-H4 and C1-H3 bonds in $\mathbf{TS_{AB}(ax)}$ and $\mathbf{TS_{AB}(eq)}$ respectively relative to **A**. Values of ε also increase dramatically for the C1-H4 bond in $\mathbf{TS_{AB}(ax)}$ and the C1-H3 bond in $\mathbf{TS_{AB}(eq)}$, consistent with the structural instability of these dissociating bonds.[122] On the other hand, values of $\rho_b(r)$ and ε for the C1-C2 bond increase appreciably in $\mathbf{TS_{AB}(ax)}$ and $\mathbf{TS_{AB}(eq)}$ relative to **A**, indicative of the incipient double-bond formation.[117]

Figure 4.2 contains contour plots of the Laplacian of the electronic density overlaid by bonds or *bond paths* in the H3C1C2 plane of migration and the C1C2O carbene valence plane at selected points along the reaction path for equatorial 1,2-H migration. As mentioned in Chapter 2, negative intrinsic reaction coordinate (IRC) values correspond to the reactant side of the reaction path, positive IRC values correspond to the product side of the reaction path and an IRC value of zero represents the transition state. It can be seen that the bond paths from H3 terminate at C1 for IRC = -0.19984 and 0.00000 $amu^{1/2}$ bohr, whereas they terminate at C2 for IRC = 0.08982 and 0.19982 $amu^{1/2}$ bohr, while the region of charge concentration corresponding to the carbene C2 lone pair is essentially identical for all four IRC values (cf. Fig. 4.2). In other words, the carbene C2 lone pair remains intact while the bond path from H3 switches from C1 to C2, which is consistent with a hydride-like shift from C1 to the "vacant" carbene *p* orbital on C2.

The changes in electronic charge distribution during equatorial 1,2-H migration result in two regions of structural stability (i.e. structures which persist for several geometric configurations along the reaction path) corresponding to a reactant region and a product region (Fig. 4.2). The plots for IRC = -0.19984 and 0.00000 $amu^{1/2}$ bohr, where the bond path from H3 terminates at C1, are in the reactant region of structural stability, while those for IRC = 0.08982 and 0.19982 $amu^{1/2}$ bohr, where the bond path from H3 terminates at C2, are in the product region of structural stability. At some point between IRC = 0.00000 and 0.08982 $amu^{1/2}$ bohr, the bond path from H3 terminates at the C1-C2 bond critical point (BCP). This arrangement of bond paths corresponds to a unique and unstable structure that is transitional between C1-H3 bond dissociation and C2-H3 bond formation. Since the C1 and C2 atoms are in essence competing for the line of maximum electronic density from H3, this arrangement of bond paths is referred to as a conflict structure,[18] and the overall change in molecular structure is said to occur via a conflict mechanism.[18] Thus, it appears that the changes in molecular structure that accompanies 1,2-H migration involving a hydride-like shift from C1 to the "vacant" carbene *p* orbital on C2 occur via a conflict mechanism.

ELF isosurfaces for **A**, $\mathbf{TS_{AB}(ax)}$, $\mathbf{TS_{AB}(eq)}$ and **B** are shown in Fig. 4.3, and corresponding ELF basin properties can be found in Table 4.2. For axial 1,2-H migration, it is apparent that the V(C1,H4) protonated valence basin in **A** develops into the V(C1,H4,C2) trisynaptic valence basin in $\mathbf{TS_{AB}(ax)}$ while the V(C2) lone-pair valence basin remains unchanged (cf. Fig. 4.3). Likewise, for equatorial 1,2-H migration, the V(C1,H3) protonated valence basin in **A** turns into the V(C1,H3,C2) trisynaptic valence basin in $\mathbf{TS_{AB}(eq)}$ while the V(C2) lone-pair valence basin remains essentially unaltered

(cf. Fig. 4.3). These observations are in keeping with a hydride-like shift to the "vacant" carbene *p* orbital. In addition, the V(C1,C2) basin population increases in **TS_{AB}(ax)** and **TS_{AB}(eq)** relative to **A**, in accord with imminent C1-C2 double-bond formation (cf. Table 4.2). Formation of the V(C1,H4,C2) and V(C1,H3,C2) trisynaptic basins, which in essence corresponds to three-center two-electron bonds, suggests that the migrating H4 and H3 atoms in **TS_{AB}(ax)** and **TS_{AB}(eq)**, respectively, share their bonding electrons with both the C1 and C2 atoms. We note that the populations of the V(C1,H4,C2) and V(C1,H3,C2) basins in **TS_{AB}(ax)** and **TS_{AB}(eq)** are smaller than those of the parent V(C1,H4) and V(C1,H3) basins in **A**, which is most likely due to greater population delocalization, as reflected in the larger values of the relative fluctuation $\lambda(\Omega_i)$ given in Table 4.2.

Relative Gibbs free energies and relative enthalpies for **A**, **B**, **TS_{AB}(ax)** and **TS_{AB}(eq)** can be found in Table 4.3, and a relative Gibbs free-energy profile is shown in Fig. 4.4. It is apparent from Table 4.3 and Fig. 4.4 that axial 1,2-H migration via **TS_{AB}(ax)** is slightly more favorable than equatorial 1,2-H migration via **TS_{AB}(eq)**. Thus, even though axial $\sigma_{C1\text{-}H4} \rightarrow p_{C2}$ hyperconjugation is stronger than equatorial $\sigma_{C1\text{-}H3} \rightarrow p_{C2}$ hyperconjugation according to second-order NBO perturbation-energy analysis, only a slight preference for axial 1,2-H migration is observed. This is consistent with the experimental observation that 1,2-H migrations in 4-*tert*-butyl-2-substituted-cyclohexylidenes occur with little axial preference,[133,134] a finding that is further supported by theoretical calculations of 1,2-H migrations in cyclohexylidenes.[40,135]

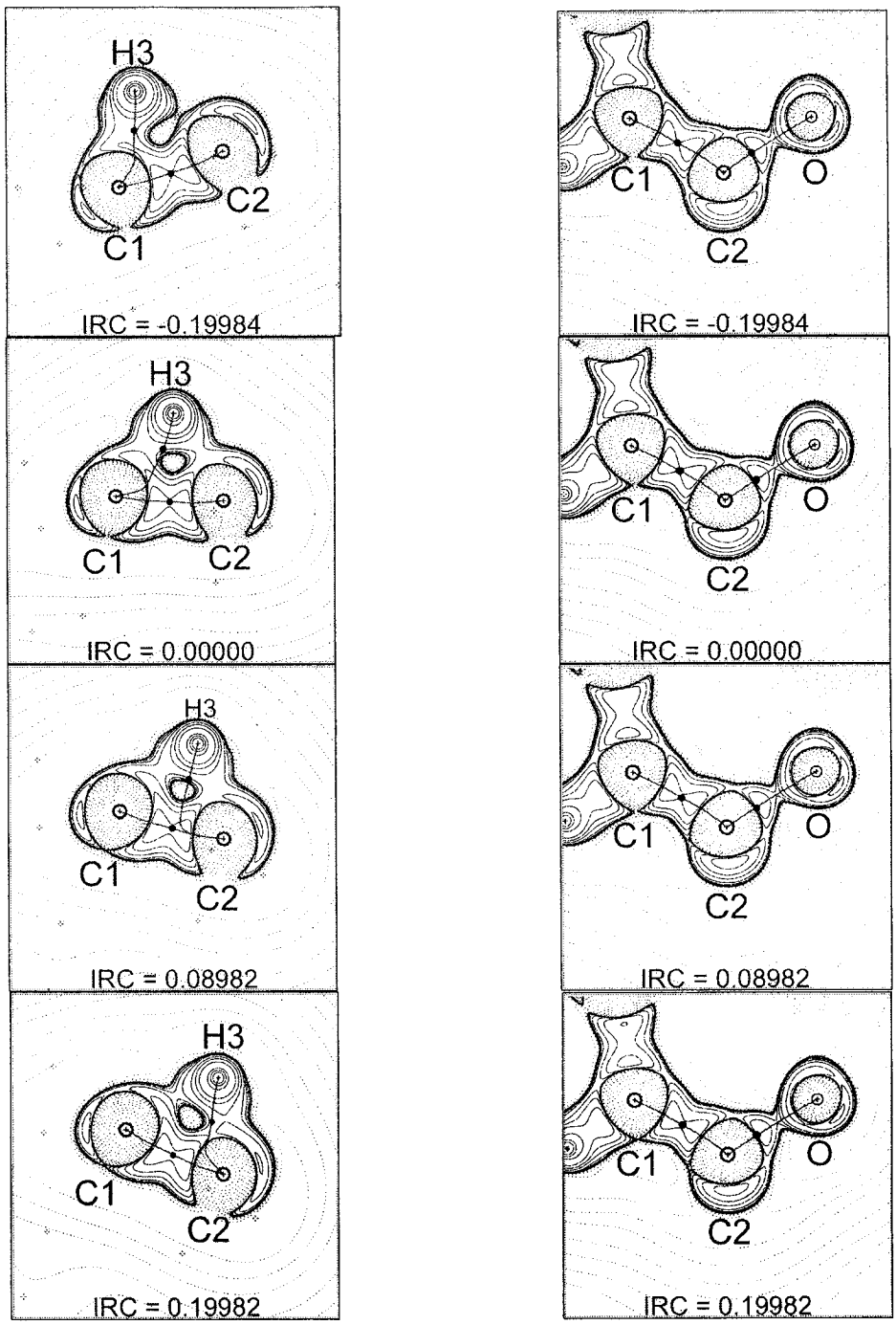

Figure 4.2 B3LYP/6-311+G(2d,p) contour plots of the Laplacian of the electronic density overlaid by bond paths in the H3C1C2 plane of migration (left) and the C1C2O carbene valence plane (right) at selected IRC values for equatorial 1,2-H migration. The plots for IRC = -0.19984 and 0.00000 amu$^{1/2}$ bohr are in the reactant region of structural stability, while those for IRC = 0.08982 and 0.19982 amu$^{1/2}$ bohr are in the product region of structural stability. Solid and broken contours represent regions of charge concentration and charge depletion, while solid round dots identify positions of BCPs. Note that some bond paths may have deviated out-of-plane.

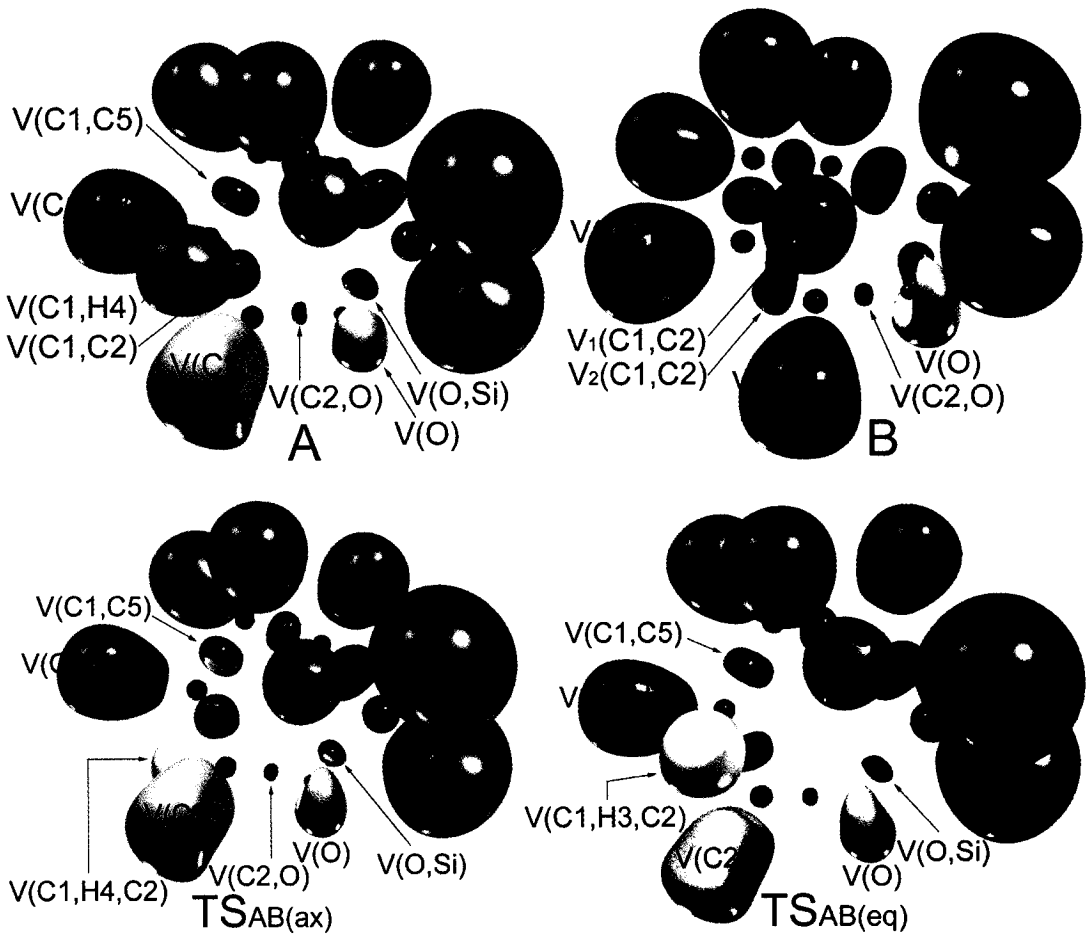

Figure 4.3 B3LYP/6-311+G(2d,p) ELF isosurfaces for 3-sila-2-oxacyclohexylidene, 4-sila-3-oxacyclohexene and the transition states for axial and equatorial 1,2-H migration. The basins shown are core basins (purple), protonated valence basins (blue), disynaptic valence basins (green), trisynaptic valence basins (yellow) and lone-pair valence basins (orange).

Table 4.3 Relative Gibbs free energies and relative enthalpies for intramolecular rearrangements of 3-sila-2-oxacyclohexylidene.[a]

	B3LYP/6-311+G(2d,p)		B3LYP/cc-pVTZ		PBE1PBE/6-311+G(2d,p)	
	ΔG	ΔH	ΔG	ΔG	ΔH	ΔG
A	0.0	0.0	0.0	0.0	0.0	0.0
TS_{AB}(ax)	16.6	16.2	16.4	16.0	14.7	14.3
TS_{AB}(eq)	17.3	17.1	17.1	16.9	15.4	15.2
B	-50.6	-50.9	-51.0	-51.3	-51.5	-51.7
TS_{AC}	27.0	28.2	27.5	28.6	26.5	27.6
C	25.8	28.6	26.5	29.1	25.0	27.7
TS_{AD}	19.2	18.4	19.2	18.2	15.9	14.9
TS_{CD}	27.0	29.2	27.8	29.9	26.2	28.3
D	-32.6	-32.4	-31.4	-31.3	-35.3	-35.2
TS_{CE}	38.5	42.6	38.9	43.0	41.5	45.5
TS_{DF}	18.0	19.1	18.4	19.3	16.9	17.8
E+CO	23.2	38.1	23.4	37.9	28.2	42.5
TS_{EF}+CO	24.5	37.7	24.9	38.1	29.6	42.7
F+CO	-30.9	-19.6	-30.6	-19.3	-27.6	-16.3

[a] Gibbs free energies and enthalpies are given in kcal/mol at 298.15 K and 1.0 atm relative to **A**. The B3LYP/6-311+G(2d,p), B3LYP/cc-pVTZ and PBE1PBE/6-311+G(2d,p) Gibbs free energies for **A** are -521.917353, -521.933184 and -521.492899 hartrees respectively. The B3LYP/6-311+G(2d,p), B3LYP/cc-pVTZ and PBE1PBE/6-311+G(2d,p) enthalpies for **A** are -521.879593, -521.895387 and -521.455132 hartrees respectively.

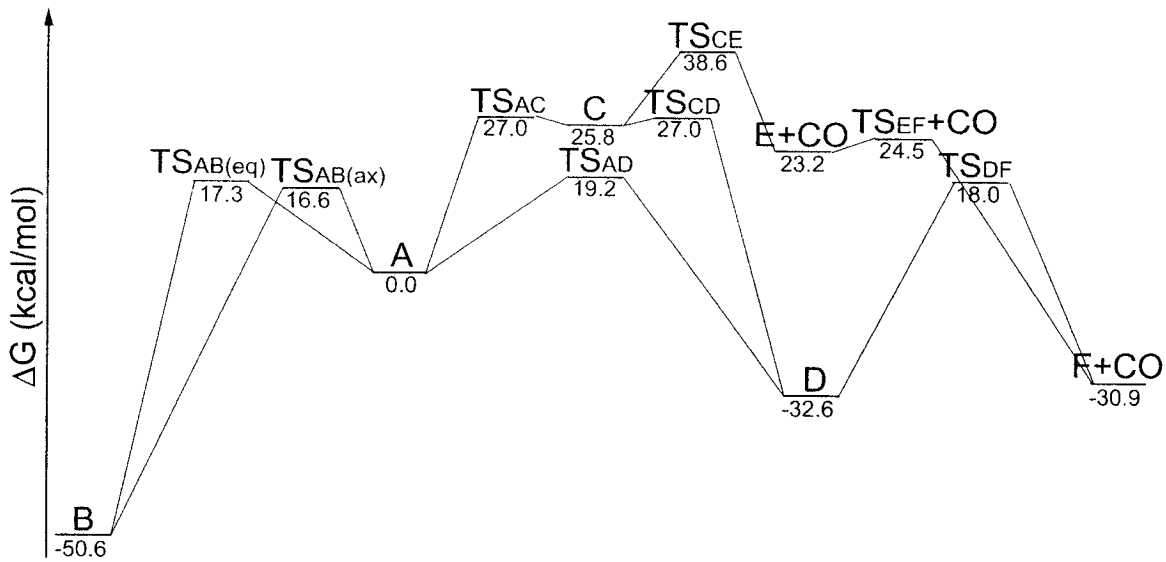

Figure 4.4 Relative B3LYP/6-311+G(2d,p) Gibbs free-energy profile for intramolecular rearrangements of 3-sila-2-oxacyclohexylidene at 298.15 K and 1.0 atm.

4.3.3 Mechanism for Ring Contraction

The mechanism for ring contraction of 3-sila-2-oxacyclohexylidene **A** could be concerted or stepwise, as outlined in Scheme 4.1. Let us first consider the mechanism for ring contraction via the concerted pathway. Computed geometric structures for the transition state $\mathbf{TS_{AD}}$ and product silacyclopentanone **D** are shown in Fig. 4.5. When compared with **A** in. Fig. 4.1, it is evident that the O-Si bond lengthens and the C2-O bond shortens in $\mathbf{TS_{AD}}$, consistent with O-Si bond dissociation and C2-Si double-bond formation. The computed B3LYP/6-311+G(2d,p), B3LYP/cc-pVTZ and PBE1PBE/6-311+G(2d,p) ∠C1C2OSi dihedral angles of 114.7°, 114.7° and 113.9° for $\mathbf{TS_{AD}}$ suggest that the $\sigma_{O\text{-}Si}$ bond is essentially aligned with the "vacant" carbene *p* orbital (i.e. both are perpendicular to the C1C2O plane), which seems to be in accord with an anion-like shift of the silyl group from oxygen to the carbene carbon. However, as will be discussed below, our AIM and ELF investigation shows that the latter inference is likely erroneous.

Figure 4.6 contains contour plots of the Laplacian of the electronic density overlaid by bond paths in the C2OSi plane at selected points along the reaction path for ring contraction of **A**. From the sequence of plots in the figure, it can be seen that the region of charge concentration corresponding to the carbene C2 lone pair becomes polarized towards Si as the reaction progresses from the reactant side of the reaction path (negative IRC values) to the product side of the reaction path (positive IRC values). This observation is clearly indicative of nucleophilic attack by the carbene lone pair at silicon, which is in contrast to the above conclusion.

The changes in electronic charge distribution during ring contraction of **A** result in three regions of structural stability corresponding to a reactant region, an intermediate

ring-structure region and a product region (cf. Fig. 4.6). The plots for IRC = -1.08707 and 0.00000 $amu^{1/2}$ bohr are in the reactant region of structural stability, while those for IRC = 0.39476 and 0.59321 $amu^{1/2}$ bohr are in the ring-structure and product regions of structural stability, respectively. This sequence of changes in molecular structure is characteristic of a bifurcation mechanism.[18] At some point between IRC = 0.00000 and 0.39476 $amu^{1/2}$ bohr, as the C2 and Si nuclei approach each other, a unique and unstable critical point appears in the electronic charge distribution. This critical point, referred to as a bifurcation catastrophe point,[18] is a minimum in $\rho(r)$ along the line connecting the C2 and Si nuclei (positive curvature), a maximum along a line perpendicular to the C2OSi plane (negative curvature), and a point of inflexion on a line originating from infinity and terminating at either the C2-O or O-Si BCP (zero curvature). Further motion along the reaction path results in the bifurcation of this unstable critical point into a new C2-Si BCP and C2-O-Si ring critical point (RCP). As motion along the reaction path continues, the RCP migrates towards the dissociating O-Si BCP and when they eventually coalesce, the system has reached a second bifurcation catastrophe point. Continued motion along the reaction path eventually results in complete annihilation of the O-Si bond path and the system enters the product region of structural stability. Thus, the changes in molecular structure accompanying the ring contraction of **A** involving front-side nucleophilic attack by the carbene lone pair at silicon, occur via a bifurcation mechanism.

Topological properties of the electronic density for $\mathbf{TS_{AD}}$ and **D** are given in Table 4.4. Values of $\rho_b(r)$ for the O-Si and C2-O bonds decrease and increase, respectively, in $\mathbf{TS_{AD}}$ relative to **A** (cf. Table 4.1), consistent with O-Si bond dissociation and C2-O double-bond formation. The large ε values for the dissociating O-Si bond and the

developing C2-O double bond in $\mathbf{TS_{AD}}$ most likely results from the unsymmetrical distribution of the BCP electronic density due to the developing ring-structure region of structural stability (cf. Fig. 4.6).[18] The large ε values for the C2-O bond in $\mathbf{TS_{AD}}$ can also be attributed to the incipient elliptical symmetry of the BCP electronic density usually associated with double bonds.[117]

ELF isosurfaces for $\mathbf{TS_{AD}}$ and **D** are shown in Fig. 4.7, and corresponding ELF basin properties are collected in Table 4.5. Close inspection of the ELF isosurfaces reveals that the V(C2) lone-pair basin in **A** (cf. Fig. 4.3) turns into the V(C2,Si) bonding basin in $\mathbf{TS_{AD}}$, which is clearly indicative of nucleophilic attack by the carbene lone pair at silicon, in accord with the AIM findings above. We note also that the V(O,Si) basin in **A** shifts slightly towards oxygen in $\mathbf{TS_{AD}}$. As a matter of fact, the V(O,Si) basin is located 0.627 Å and 0.576 Å away from oxygen in **A** and $\mathbf{TS_{AD}}$ respectively. This shift in the V(O,Si) basin is consistent with O-Si bond dissociation, since it is known that the bonding valence basin corresponding to a dissociating bond tends to shift towards the more electronegative atom.[21] It is also apparent from the ELF isosurfaces that the V(O,Si) basin in **A** (cf. Fig. 4.3) acquires some lone-pair basin character in $\mathbf{TS_{AD}}$ (cf. Fig. 4.7), as it becomes part of the $V_1(O) \cup V_2(O)$ superbasin of the C2-O carbonyl group in **D**. We note that the V(O,Si) basin population increases in $\mathbf{TS_{AD}}$ (cf. Table 4.5) relative to **A** (cf. Table 4.2), which is most likely due to added cross-exchange contribution that arises from the developing V(C2,Si) basin in $\mathbf{TS_{AD}}$. As well, the V(C2,O) basin population also increases in $\mathbf{TS_{AD}}$ relative to **A**, in keeping with C2-O double-bond formation. The increase in the V(C2,O) basin population in $\mathbf{TS_{AD}}$ relative to **A** may also be partly due to additional cross-exchange contribution from the developing V(C2,Si) basin in $\mathbf{TS_{AD}}$.

Thus, it is quite clear from both AIM and ELF analyses that ring contraction of 3-sila-2-oxacyclohexylidene **A** via the concerted pathway involves front-side nucleophilic attack by the carbene lone pair at silicon.

We now consider the ring contraction of 3-sila-2-oxacyclohexylidene **A** via the stepwise biradical pathway, involving initial fragmentation via $\mathbf{TS_{AC}}$ to the acyl-silyl biradical **C**, followed by collapse via $\mathbf{TS_{CD}}$ to silacyclopentanone **D** (cf. Scheme 4.1). The optimized molecular geometries for $\mathbf{TS_{AC}}$, **C** and $\mathbf{TS_{CD}}$, together with selected geometric parameters, are shown in Fig. 4.5. Fragmentation of **A** to **C** via $\mathbf{TS_{AC}}$ involves considerable lengthening of the O-Si bond and shortening of the C2-O bond in going from **A** (cf. Fig. 4.1) to $\mathbf{TS_{AC}}$. This is accompanied by a sizeable decrease in $\rho_b(r)$ for the O-Si bond and an increase in $\rho_b(r)$ for the C2-O bond in $\mathbf{TS_{AC}}$ (cf. Table 4.6) relative to **A** (cf. Table 4.1). These observations are consistent with O-Si bond fragmentation and C2-O double-bond formation. In the subsequent ring closure of **C** to **D** via $\mathbf{TS_{CD}}$, the distance between the C2 and Si atoms decreases while that between the O and Si atoms increases in $\mathbf{TS_{CD}}$ relative to **C** (cf. Fig. 4.5), in keeping with C2-Si bond formation and O-Si bond dissociation. We note that the bond length and values of $\rho_b(r)$ for the C2-O bond remain essentially unchanged in going from **C** to $\mathbf{TS_{CD}}$, suggesting that C2-O double-bond formation is essentially complete in biradical **C**.

A plot of the Mulliken atomic spin densities for **C** can be found in Fig. 4.8 and selected AIM atomic spin densities for $\mathbf{TS_{AC}}$, **C** and $\mathbf{TS_{CD}}$ are collected in Table 4.7. From the Mulliken spin densities for **C** in Fig. 4.8, it can be seen that the α-spin density is localized on the C2 and O atoms while the β-spin density is almost solely centered on the Si atom. This is supported by the AIM atomic spin densities in Table 4.7 which show

that the α-spin density values are highest on the C2 and O atoms while the β-spin density values are highest on the Si atom. These findings confirm that **C** is indeed an acyl-silyl biradical where the α- and β-spin densities are primarily localized on the C2 and Si atoms respectively. It is also evident that the atomic spin densities on C2, O and Si increase in going from **A** to **C** via $\mathbf{TS_{AC}}$, consistent with biradical formation. We also note that in the transition state $\mathbf{TS_{CD}}$ for ring closure of biradical **C** to afford **D**, the α- and β-spin densities are still largely localized on the C2 and Si atoms respectively. This localization of spin densities should facilitate C2-Si bond formation and hence ring closure.

Thermochemical data for ring contraction of 3-sila-2-oxacyclohexylidene **A** via the concerted and stepwise biradical pathways can be found in Table 4.3 and Fig. 4.4. It is evident from these data that ring contraction via the concerted pathway (i.e. via $\mathbf{TS_{AD}}$) is considerably more favorable than that via the stepwise biradical pathway (i.e. via $\mathbf{TS_{AC}}$, **C** and $\mathbf{TS_{CD}}$). Thus, it can be concluded that ring contraction of **A** occurs via a concerted mechanism involving front-side nucleophilic attack by the carbene lone pair at silicon, rather than a stepwise mechanism involving the intermediacy of an acyl-silyl biradical.

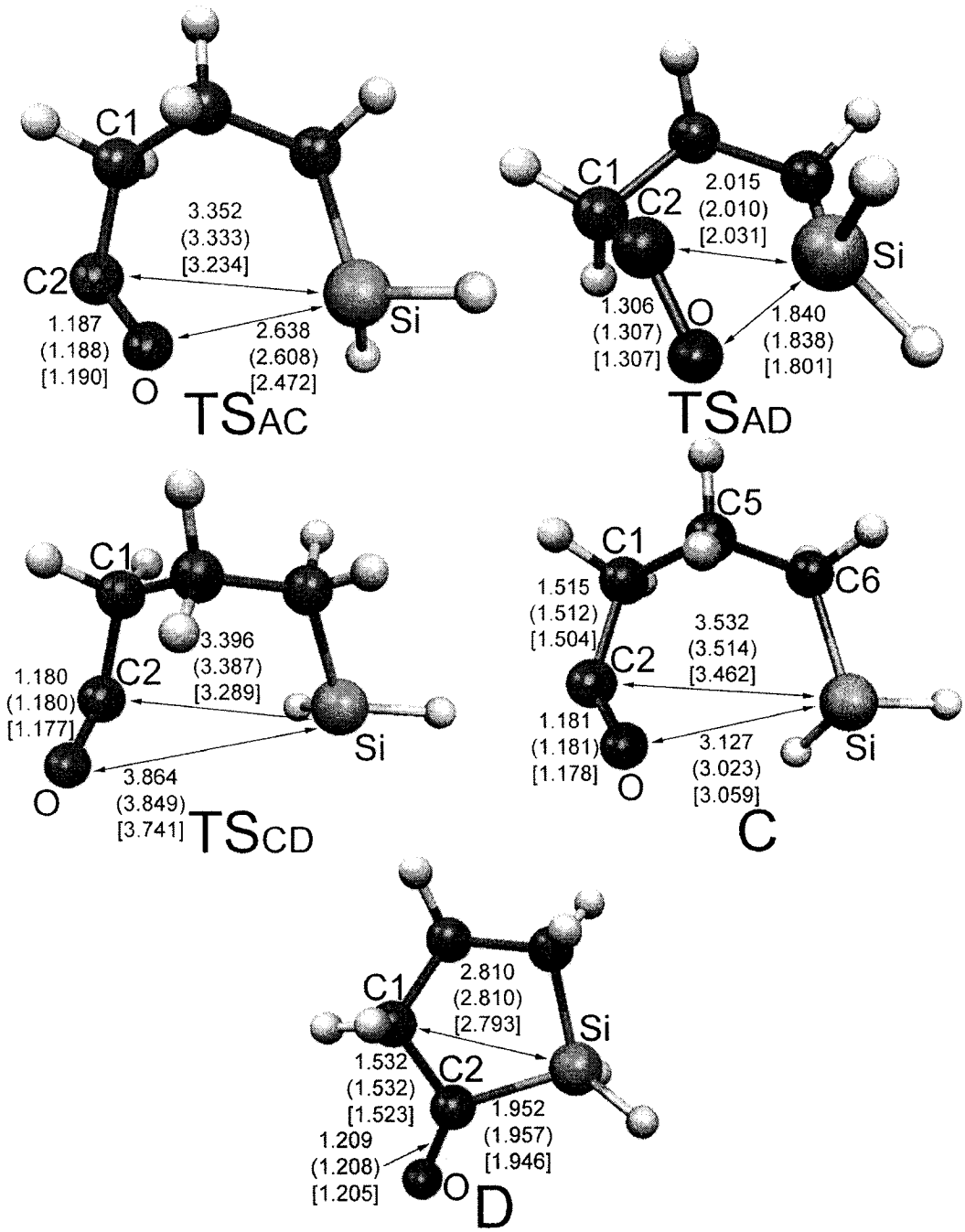

Figure 4.5 Optimized molecular geometries for $\mathbf{TS_{AC}}$, $\mathbf{TS_{AD}}$, $\mathbf{TS_{CD}}$, **C** and **D**. Interatomic distances are given for the B3LYP/6-311+G(2d,p), B3LYP/cc-pVTZ (parentheses) and PBE1PBE/6-311+G(2d,p) [brackets] model chemistries. Bond lengths are in units of Å.

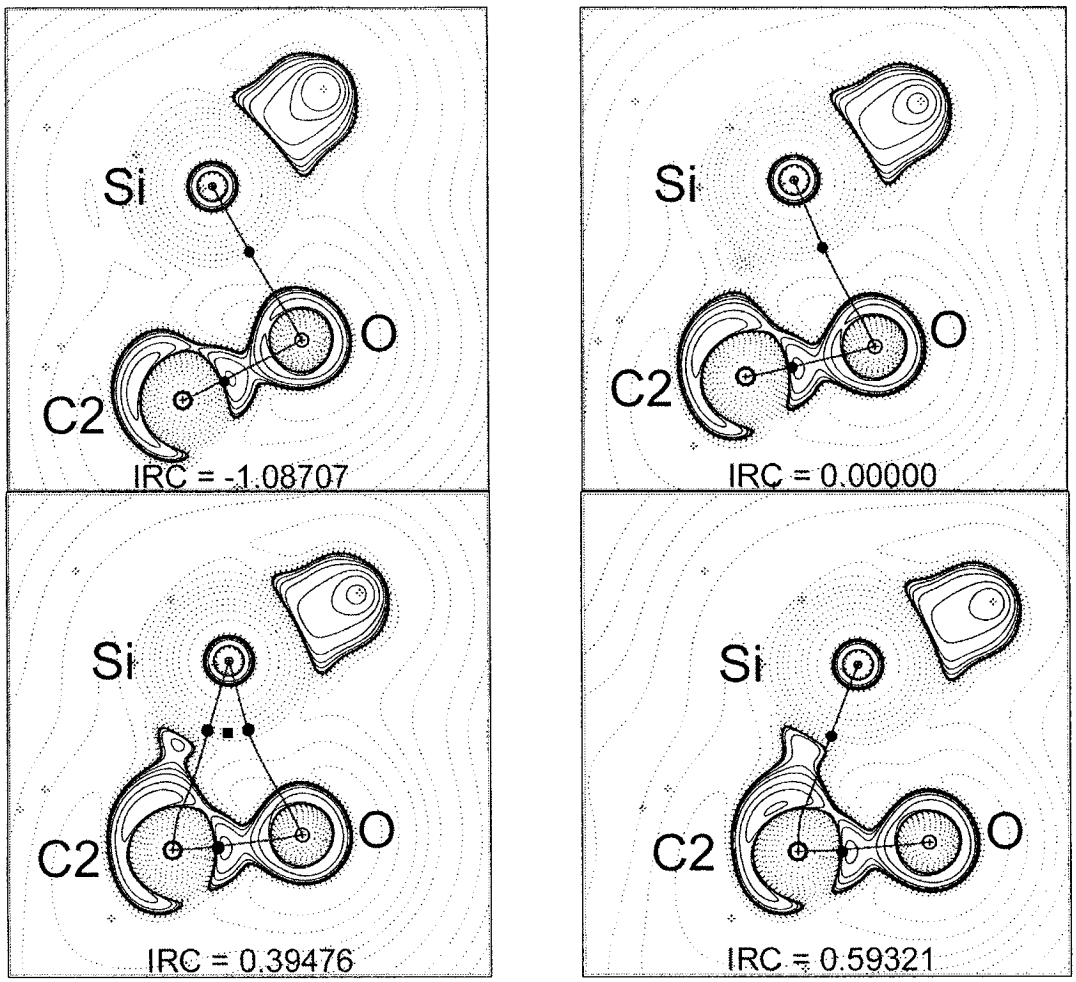

Figure 4.6 B3LYP/6-311+G(2d,p) contour plots of the Laplacian of the electronic density overlaid by bond paths in the C2OSi plane at selected IRC values for ring contraction of 3-sila-2-oxacyclohexylidene. Plots for IRC = -1.08707 and 0.00000 amu$^{1/2}$ bohr are in the reactant region of structural stability, while those for IRC = 0.39476 and 0.59321 amu$^{1/2}$ bohr are in the ring-structure and product regions of structural stability. Solid and broken contours represent regions of charge concentration and charge depletion, while solid round and square dots identify positions of BCPs and RCPs. Note that some bond paths may have deviated out-of-plane.

Table 4.4 Topological properties of the electronic density at pertinent BCPs for the transition state for ring contraction and silacyclopentanone.[a]

	TS_{AD}		
	C1-C2	C2-O	O-Si
	B3LYP/6-311+G(2d,p)		
$\rho_b(r)$ (e/Å^3)	1.82	2.25	0.59
$\nabla^2\rho_b(r)$ (e/Å^5)	-15.8	-13.3	8.4
ε	0.02	0.27	0.46
	B3LYP/cc-pVTZ		
$\rho_b(r)$ (e/Å^3)	1.87	2.25	0.60
$\nabla^2\rho_b(r)$ (e/Å^5)	-19.0	-11.4	10.0
ε	0.02	0.25	0.50
	PBE1PBE/6-311+G(2d,p)		
$\rho_b(r)$ (e/Å^3)	1.84	2.24	0.64
$\nabla^2\rho_b(r)$ (e/Å^5)	-16.4	-11.4	10.1
ε	0.02	0.30	0.28
	D		
	C1-C2	C2-O	C2-Si
	B3LYP/6-311+G(2d,p)		
$\rho_b(r)$ (e/Å^3)	1.65	2.82	0.76
$\nabla^2\rho_b(r)$ (e/Å^5)	-12.3	-8.8	1.0
ε	0.03	0.04	0.02
	B3LYP/cc-pVTZ		
$\rho_b(r)$ (e/Å^3)	1.69	2.83	0.75
$\nabla^2\rho_b(r)$ (e/Å^5)	-14.8	-4.8	2.0
ε	0.03	0.05	0.03
	PBE1PBE/6-311+G(2d,p)		
$\rho_b(r)$ (e/Å^3)	1.68	2.84	0.76
$\nabla^2\rho_b(r)$ (e/Å^5)	-13.1	-6.2	1.6
ε	0.03	0.05	0.02

[a] Obtained from AIM analysis.

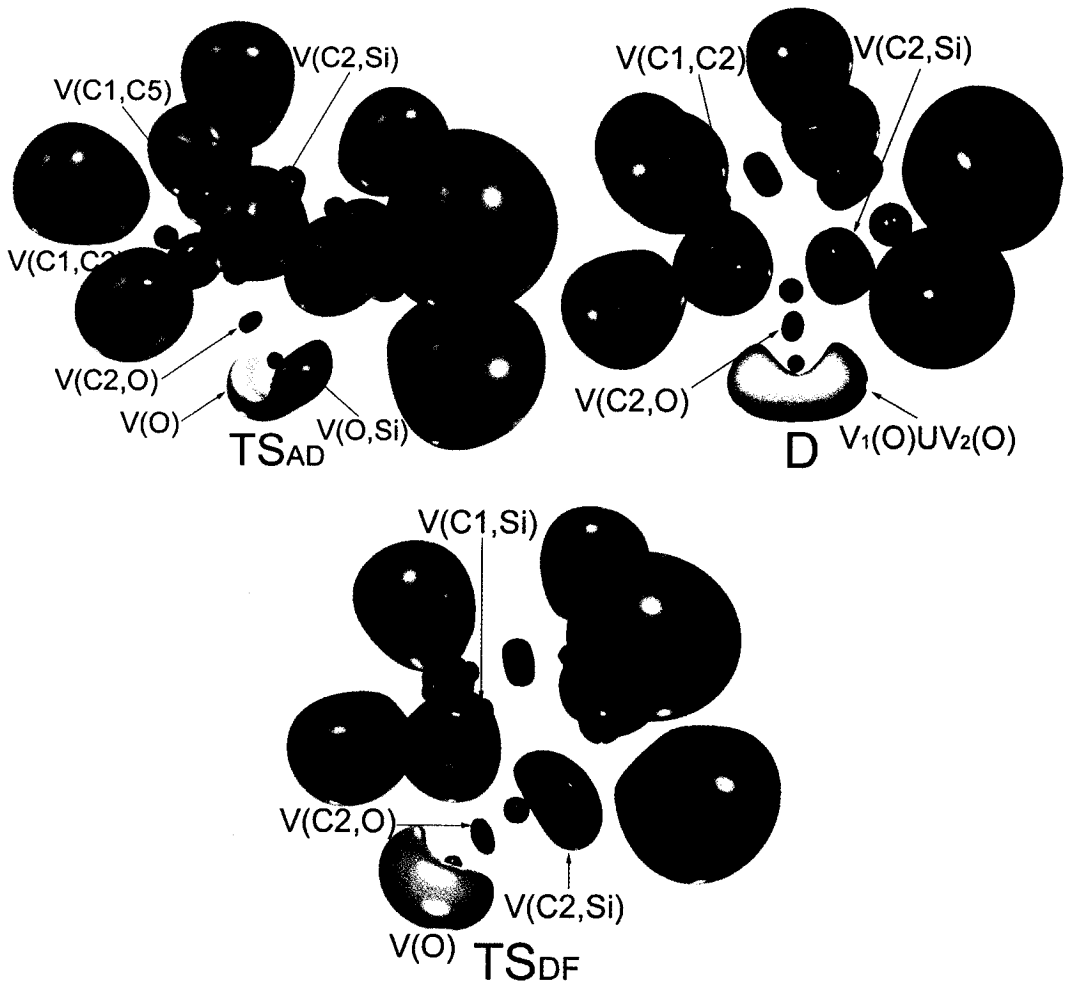

Figure 4.7 B3LYP/6-311+G(2d,p) ELF isosurfaces for $\mathbf{TS_{AD}}$, **D** and $\mathbf{TS_{DF}}$. The basins shown are core basins (purple), protonated valence basins (blue), disynaptic valence basins (green) and lone-pair valence basins (orange).

Table 4.5 Basin population $N(\Omega_i)$, relative fluctuation $\lambda(\Omega_i)$ and %cross-exchange contribution of $\mathbf{TS_{AD}}$, **D** and $\mathbf{TS_{DF}}$.[a]

Basin	$N(\Omega_i)$	$\lambda(\Omega_i)$	%Cross-exchange contribution[b]
			TS_{AD}
V(C1,C2)	2.03	0.50	V(C2,Si) 9.4; V(C1,H3) 7.9; V(C1,H4) 7.9; V(C1,C5) 6.4
V(C2,O)	1.69	0.60	V(O) 18.9; V(O,Si) 17.8; V(C2,Si) 8.9; V(C1,C2) 5.9
V(C2,Si)	2.32	0.42	V(C1,C2) 8.2; V(C2,O) 6.5; V(O,Si) 5.6; V(O) 3.9
V(O,Si)	2.78	0.48	V(O) 19.4; V(C2,O) 10.8; V(C2,Si) 4.7
V(O)	2.99	0.42	V(O,Si) 18.1; V(C2,O) 10.7; V(C2,Si) 3.0
			D
V(C1,C2)	1.99	0.51	V(C2,Si) 8.5; V(C1,H3) 8.0; V(C1,H4) 8.0; V(C2,O) 6.5
V(C2,O)	2.30	0.56	V_1(O) 17.4; V_2(O) 16.5; V(C2,Si) 7.4; V(C1,C2) 5.7
V(C2,Si)	2.22	0.45	V(C1,C2) 7.7; V(C2,O) 7.7
V_1(O)	2.55	0.45	V_2(O) 18.0; V(C2,O) 14.9
V_2(O)	2.67	0.44	V_1(O) 17.2; V(C2,O) 15.0
			TS_{DF}
V(C1,Si)	1.30	0.66	V(C2,Si) 13.8; V(C1,C5) 9.2; V(C1,H) 10.8
V(C2,Si)	2.83	0.43	V(C2,O) 9.5; V(O) 8.1; V(C1,Si) 6.4
V(C2,O)	2.64	0.52	V(O) 32.6; V(C2,Si) 10.2
V(O)	4.87	0.30	V(C2,O) 17.7; V(C2,Si) 4.7

[a] Obtained from ELF analysis of B3LYP/6-311+G(2d,p) wave functions. [b] Contribution of neighboring basins to the total basin population.

Table 4.6 Topological properties of the electronic density at important bond critical points for $\mathbf{TS_{AC}}$, **C** and $\mathbf{TS_{CD}}$.

	C1-C2	C2-O	O-Si
	TS_{AC}		
	B3LYP/6-311+G(2d,p)		
$\rho_b(r)$ (e/Å^3)	1.64	2.90	0.17
$\nabla^2\rho_b(r)$ (e/Å^5)	-12.5	0.0	1.0
ε	0.01	0.09	0.02
	B3LYP/cc-pVTZ		
$\rho_b(r)$ (e/Å^3)	1.69	2.89	0.19
$\nabla^2\rho_b(r)$ (e/Å^5)	-15.3	4.0	1.0
ε	0.02	0.09	0.01
	PBE1PBE/6-311+G(2d,p)		
$\rho_b(r)$ (e/Å^3)	1.68	2.86	0.24
$\nabla^2\rho_b(r)$ (e/Å^5)	-13.4	2.5	1.0
ε	0.01	0.11	0.03
	C		
	B3LYP/6-311+G(2d,p)		
$\rho_b(r)$ (e/Å^3)	1.62	2.96	0.06
$\nabla^2\rho_b(r)$ (e/Å^5)	-12.2	-0.3	0.6
ε	0.01	0.06	0.32
	B3LYP/cc-pVTZ		
$\rho_b(r)$ (e/Å^3)	1.68	2.96	0.08
$\nabla^2\rho_b(r)$ (e/Å^5)	-15.0	2.0	0.7
ε	0.02	0.06	0.27
	PBE1PBE/6-311+G(2d,p)		
$\rho_b(r)$ (e/Å^3)	1.66	2.97	0.07
$\nabla^2\rho_b(r)$ (e/Å^5)	-13.1	2.2	0.6
ε	0.01	0.05	0.37
	TS_{CD}		
	B3LYP/6-311+G(2d,p)		
$\rho_b(r)$ (e/Å^3)	1.59	2.97	-
$\nabla^2\rho_b(r)$ (e/Å^5)	-11.6	-0.2	-
ε	0.01	0.05	-
	B3LYP/cc-pVTZ		
$\rho_b(r)$ (e/Å^3)	1.64	2.97	-
$\nabla^2\rho_b(r)$ (e/Å^5)	-14.2	3.4	-
ε	0.02	0.05	-
	PBE1PBE/6-311+G(2d,p)		
$\rho_b(r)$ (e/Å^3)	1.63	2.98	-
$\nabla^2\rho_b(r)$ (e/Å^5)	-12.4	2.2	-
ε	0.01	0.05	-

[a] Obtained from AIM analysis.

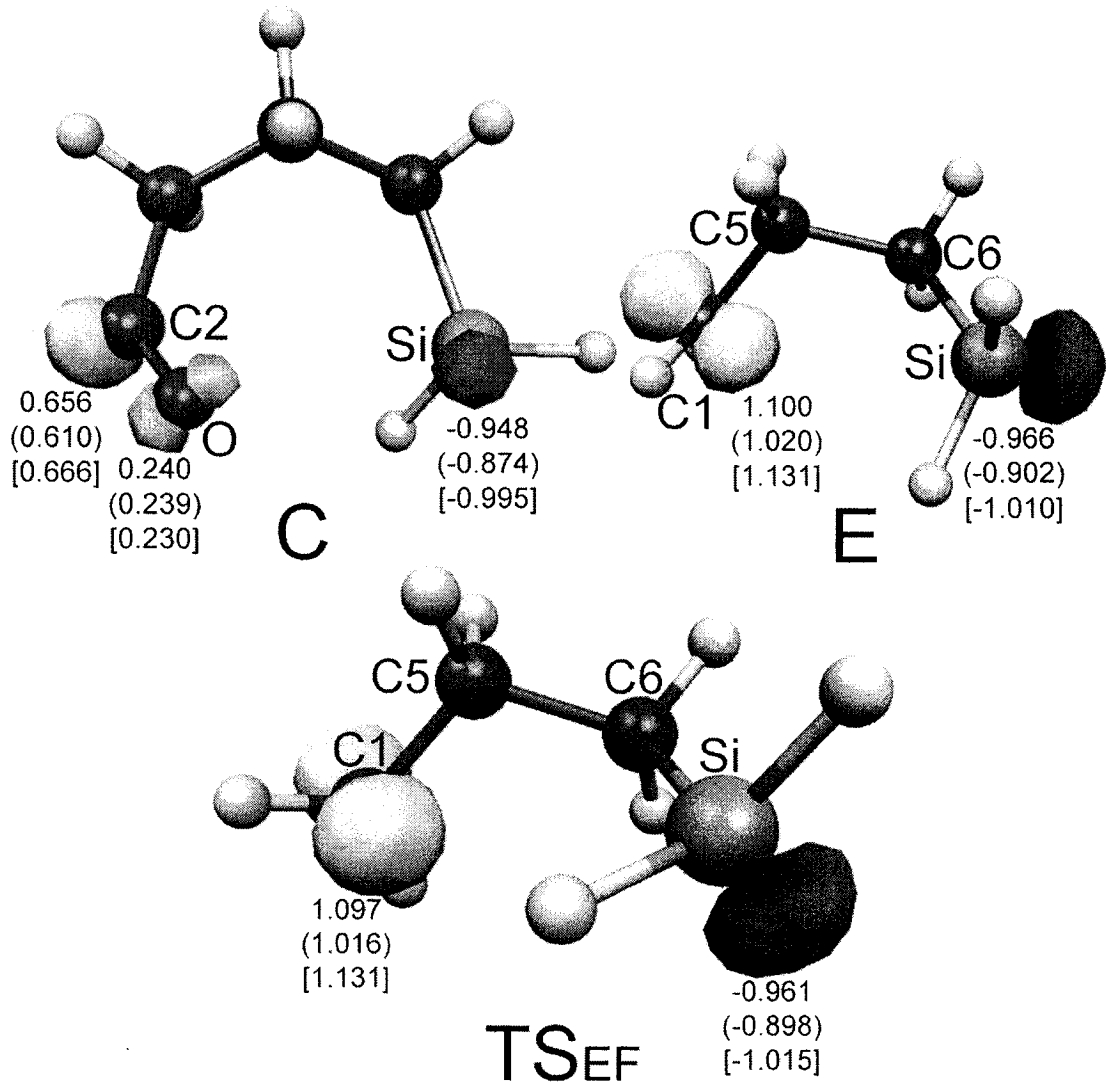

Figure 4.8 Plots of Mulliken atomic spin densities for **C**, **E** and $\mathbf{TS_{EF}}$. Spin density values are shown for B3LYP/6-311+G(2d,p), B3LYP/cc-pVTZ (parentheses) and PBE1PBE/6-311+G(2d,p) [brackets]. Positive and negative values denote α and β spin densities.

Table 4.7 AIM atomic spins densities for TS_{AC}, **C**, TS_{CD}, TS_{CE}, **E** and TS_{EF}.[a]

	C1	C2	C5	C6	O	Si
			TS_{AC}			
B3LYP/6-311+G(2d,p)	0.098	0.522	0.017	-0.048	0.179	-0.613
B3LYP/cc-pVTZ	0.096	0.516	0.017	0.049	0.175	-0.596
PBE1PBE/6-311+G(2d,p)	0.088	0.498	0.015	-0.039	0.150	-0.563
			C			
B3LYP/6-311+G(2d,p)	0.115	0.577	0.027	-0.059	0.229	-0.722
B3LYP/cc-pVTZ	0.113	0.573	0.026	-0.060	0.231	-0.707
PBE1PBE/6-311+G(2d,p)	0.111	0.593	0.027	-0.057	0.226	-0.731
			TS_{CD}			
B3LYP/6-311+G(2d,p)	0.125	0.564	0.010	-0.064	0.248	-0.733
B3LYP/cc-pVTZ	0.125	0.567	0.010	-0.066	0.247	-0.722
PBE1PBE/6-311+G(2d,p)	0.121	0.583	0.010	-0.061	0.233	-0.737
			TS_{CE}			
B3LYP/6-311+G(2d,p)	0.637	0.174	0.000	-0.059	0.096	-0.740
B3LYP/cc-pVTZ	0.634	0.175	-0.004	-0.056	0.097	-0.731
PBE1PBE/6-311+G(2d,p)	0.648	0.144	0.000	-0.062	0.080	-0.749
			E			
B3LYP/6-311+G(2d,p)	0.873	-	0.032	0.000		-0.743
B3LYP/cc-pVTZ	0.871	-	0.004	0.050		-0.734
PBE1PBE/6-311+G(2d,p)	0.883	-	0.008	0.046		-0.752
			TS_{EF}			
B3LYP/6-311+G(2d,p)	0.867	-	0.020	0.034		-0.738
B3LYP/cc-pVTZ	0.867	-	0.020	0.038		-0.731
PBE1PBE/6-311+G(2d,p)	0.880	-	0.022	0.039		-0.751

[a] Positive and negative values denote α- and β-spin densities respectively. Spin densities taken as the difference in the α- and β-electron populations, obtained by integration of the spin densities over the atomic basins.

4.3.4 Mechanism for Decarbonylation

The decarbonylation of 3-sila-2-oxacyclohexylidene **A** could involve initial formation and subsequent decarbonylation of the acyl-silyl biradical **C** to yield the silabutane biradical **E**, which then collapses to silacyclobutane **F**, as illustrated in Scheme 4.1. Alternatively, decarbonylation of **A** could occur via the intermediacy of silacyclopentanone **D** (cf. Scheme 4.1). We will first consider the former decarbonylation pathway and then focus on the latter. The formation of both **C** and **D** was just discussed; this section addresses their decarbonylation. As shown in Scheme 4.1, decarbonylation of the acyl-silyl biradical **C** via $\mathbf{TS_{CE}}$ affords the silabutane biradical **E**, which then collapses via $\mathbf{TS_{EF}}$ to silacyclobutane **F**. The optimized geometric structures for $\mathbf{TS_{CE}}$, **E**, $\mathbf{TS_{EF}}$ and **F** are shown in Fig. 4.9, while some topological properties of the electronic density are listed in Table 4.8. For decarbonylation of **C**, considerable lengthening of the dissociating C1-C2 bond and shortening of the developing C2-O triple bond occur in $\mathbf{TS_{CE}}$ relative to **C** (cf. Fig. 4.5). This is accompanied by a significant decrease in $\rho_b(r)$ for the C1-C2 bond and a sizeable increase in $\rho_b(r)$ for the C2-O bond in $\mathbf{TS_{CE}}$ (cf. Table 8) relative to **C** (cf. Table 4.6). Also, the distance between the C2 and Si atoms increases significantly in $\mathbf{TS_{CE}}$ compared to **C** (cf. Fig. 4.5), consistent with the imminent loss of carbon monoxide. We note from the spin densities in Table 4.7 that there is a considerable shift of the α-spin density from the C2 and O atoms to the C1 atom while the β-spin density on the Si atom increases slightly in going from **C** to $\mathbf{TS_{CE}}$ (cf. Table 4.7), consistent with formation of the silabutane biradical **E** and loss of carbon monoxide.

Now turning to the ring closure of biradical **E**, we note that in going from **E** to $\mathbf{TS_{EF}}$, the distance between the C1 and Si atoms remains essentially unchanged while the

silyl group rotates significantly about the C6-Si bond, as evidenced by the ∠H8SiC6C5 dihedral angles listed in Fig. 4.9. From the plot of the Mulliken spin densities for **E** in Fig. 4.8, it can be seen that the β-spin density on Si is oriented away from the α-spin density on C1. Thus, it appears that rotation of the silyl group in $\mathbf{TS_{EF}}$ allows interaction between the β-spin density on Si and the α-spin density on C1 (cf. Fig. 4.8), resulting in C2-Si bond formation and hence ring closure. We also note that there is a slight decrease in the α- and β-spin densities on C1 and Si respectively in $\mathbf{TS_{EF}}$ relative to **E** (cf. Table 4.7), in accord with ring closure of **E** to afford the closed-shell silacyclobutane **F**.

We now consider the mechanism for decarbonylation of silacyclopentanone **D** (cf. Scheme 4.1). The computed transition-state structure $\mathbf{TS_{DF}}$ is shown in Fig. 4.9. Relative to **D** in Fig. 4.5, considerable lengthening of the dissociating C1-C2 bond and shortening of the developing C2-O triple bond is observed in $\mathbf{TS_{DF}}$, while the distance between the C1 and Si atoms decreases significantly. Surprisingly, though, modest contraction of the dissociating C2-Si bond occurs in $\mathbf{TS_{DF}}$. Topological properties of the electronic density at important BCPs for $\mathbf{TS_{DF}}$ can be found in Table 4.8. Compared with **D** (cf. Table 4.4), one finds a significant decrease in $\rho_b(r)$ for the dissociating C1-C2 bond, a sizeable increase in $\rho_b(r)$ for the developing C2-O triple bond and a slight decrease in $\rho_b(r)$ for the dissociating C2-Si bond in $\mathbf{TS_{DF}}$ (cf. Table 4.8). Thus, despite the slight C2-Si bond shortening in $\mathbf{TS_{DF}}$, the decrease in $\rho_b(r)$ for the C2-Si bond is clearly indicative of bond dissociation.

Figure 4.10 contains contour plots of the Laplacian of the electronic density overlaid by bond paths in the C1C2Si plane at selected points along the reaction path for decarbonylation of silacyclopentanone **D**. As mentioned earlier, negative IRC values

correspond to the reactant side of the reaction path, positive IRC values correspond to the product side of the reaction path and an IRC value of zero corresponds to the transition state. From the sequence of plots in the figure, it is apparent that the changes in molecular structure that accompany this reaction occur via a bifurcation mechanism. The plots for IRC = -0.19683 and 0.00000 are in the reactant region of structural stability, while those for IRC = 0.49649 and 0.59648 are in the ring-structure and product regions of structural stability respectively. The fact that C1-C2 bond cleavage and C1-Si bond formation occurs before complete C2-Si bond dissociation suggests that the density for C1-Si bond formation primarily results from C1-C2 bond dissociation (cf. Fig. 4.10). This is in keeping with the mechanism for decarbonylation of **D** involving nucleophilic attack by the C1-C2 bonding electrons at silicon (cf. Scheme 4.1).

ELF isosurfaces for **D** and $\mathbf{TS_{DF}}$ are shown in Fig. 4.7 and corresponding ELF basin properties are given in Table 4.5. The disappearance of the V(C1,C2) valence basin and appearance of the V(C1,Si) valence basin in going from **D** to $\mathbf{TS_{DF}}$, together with the fact that the V(C2,Si) basin remains intact, is also consistent with C1-C2 bond cleavage and C1-Si bond formation before complete C2-Si dissociation, and thus with the mechanism involving nucleophilic attack by the C1-C2 bonding electrons at silicon illustrated in Scheme 4.1. We note that the V_1(O) and V_2(O) lone-pair valence basins in **D** merge into a single V(O) lone-pair valence basin in $\mathbf{TS_{DF}}$, which is indicative of C2-O triple-bond formation,[21] a finding further supported by the fact that the population of the V(C2,O) valence basin increases in going from **D** to $\mathbf{TS_{DF}}$. We also note that there is a sizeable increase in the V(C2,Si) basin population in $\mathbf{TS_{DF}}$ relative to **D**, most likely as a result of additional cross-exchange contribution from the developing V(C1,Si) basin.

It is not immediately obvious from the thermochemical data in Table 4.3 and Fig. 4.4 if decarbonylation of 3-sila-2-oxacyclohexylidene **A** occurs preferentially through the pathway involving initial formation and subsequent decarbonylation of silacyclopentanone **D** via $\mathbf{TS_{AD}}$ and $\mathbf{TS_{DF}}$, respectively, or through the pathway involving initial formation and subsequent decarbonylation of the acyl-silyl biradical **C** via $\mathbf{TS_{AC}}$ and $\mathbf{TS_{CE}}$ respectively, followed by collapse of the silabutane biradical **E** via $\mathbf{TS_{EF}}$ (cf. Scheme 4.1). Inspection of the Gibbs free-energy profile in Fig. 4.4 clearly reveals that the initial formation of **D** via $\mathbf{TS_{AD}}$ is significantly more favorable kinetically than initial formation of **C** via $\mathbf{TS_{AC}}$, but the thermodynamic stability of **D** makes the barrier for decarbonylation of **D** via $\mathbf{TS_{DF}}$ considerably greater than that for decarbonylation of **C** via $\mathbf{TS_{CE}}$, **E** and $\mathbf{TS_{EF}}$. However, **C** would more readily revert back to **A** via $\mathbf{TS_{AC}}$ or collapse to **D** via $\mathbf{TS_{CD}}$, than fragment to **E** via $\mathbf{TS_{CE}}$. Thus, it seems most likely that decarbonylation of **A** would occur preferentially via initial formation and subsequent decarbonylation of silacyclopentanone **D** via $\mathbf{TS_{AD}}$ and $\mathbf{TS_{DF}}$, respectively.

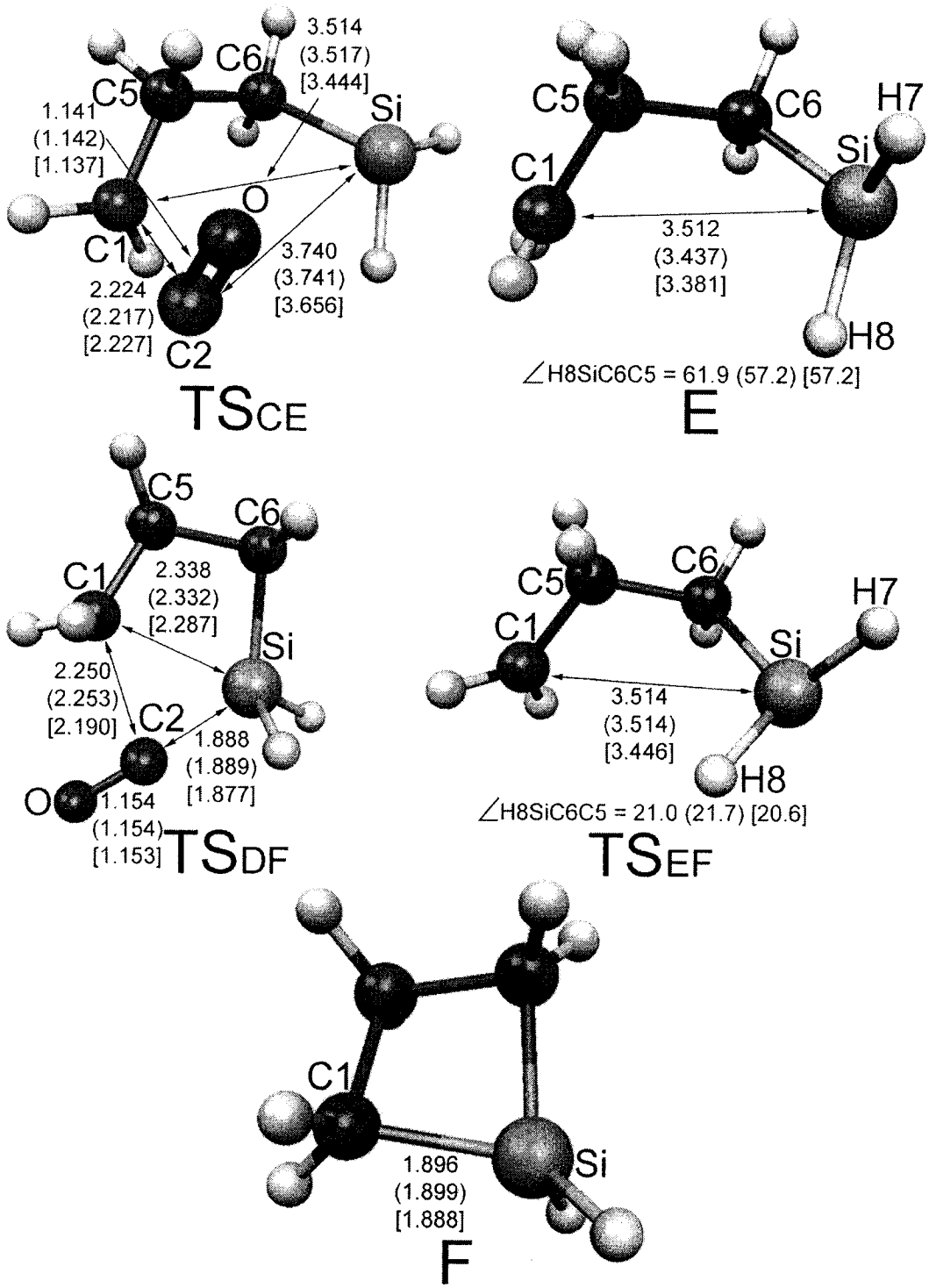

Figure 4.9 Optimized molecular geometries for TS_{CE}, **E**, TS_{DF}, TS_{EF} and **F**. Geometric parameters are given for B3LYP/6-311+G(2d,p), B3LYP/cc-pVTZ (parentheses) and PBE1PBE/6-311+G(2d,p) [brackets]. Interatomic distances are in Å and dihedral angles in degrees.

Table 4.8 Topological properties of the electronic density $\rho(r)$ at important bond critical points for $\mathbf{TS_{CE}}$ and $\mathbf{TS_{DF}}$.

	C1-C2	C2-O	C2-Si
		$\mathbf{TS_{CE}}$	
		B3LYP/6-311+G(2d,p)	
$\rho_b(r)$ (e/Å^3)	0.35	3.28	-
$\nabla^2\rho_b(r)$ (e/Å^5)	1.4	2.6	-
ε	0.03	0.00	-
		B3LYP/cc-pVTZ	
$\rho_b(r)$ (e/Å^3)	0.36	3.27	-
$\nabla^2\rho_b(r)$ (e/Å^5)	1.3	6.6	-
ε	0.04	0.00	-
		PBE1PBE/6-311+G(2d,p)	
$\rho_b(r)$ (e/Å^3)	0.32	3.31	-
$\nabla^2\rho_b(r)$ (e/Å^5)	1.5	5.4	-
ε	0.03	0.00	-
		$\mathbf{TS_{DF}}$	
		B3LYP/6-311+G(2d,p)	
$\rho_b(r)$ (e/Å^3)	0.44	3.16	0.63
$\nabla^2\rho_b(r)$ (e/Å^5)	1.1	1.3	6.2
ε	0.85	0.00	0.19
		B3LYP/cc-pVTZ	
$\rho_b(r)$ (e/Å^3)	0.45	3.18	0.63
$\nabla^2\rho_b(r)$ (e/Å^5)	1.0	5.4	7.7
ε	1.60	0.01	0.21
		PBE1PBE/6-311+G(2d,p)	
$\rho_b(r)$ (e/Å^3)	0.49	3.17	0.64
$\nabla^2\rho_b(r)$ (e/Å^5)	1.0	3.4	6.8
ε	0.81	0.01	0.19

[a] Obtained from AIM analysis.

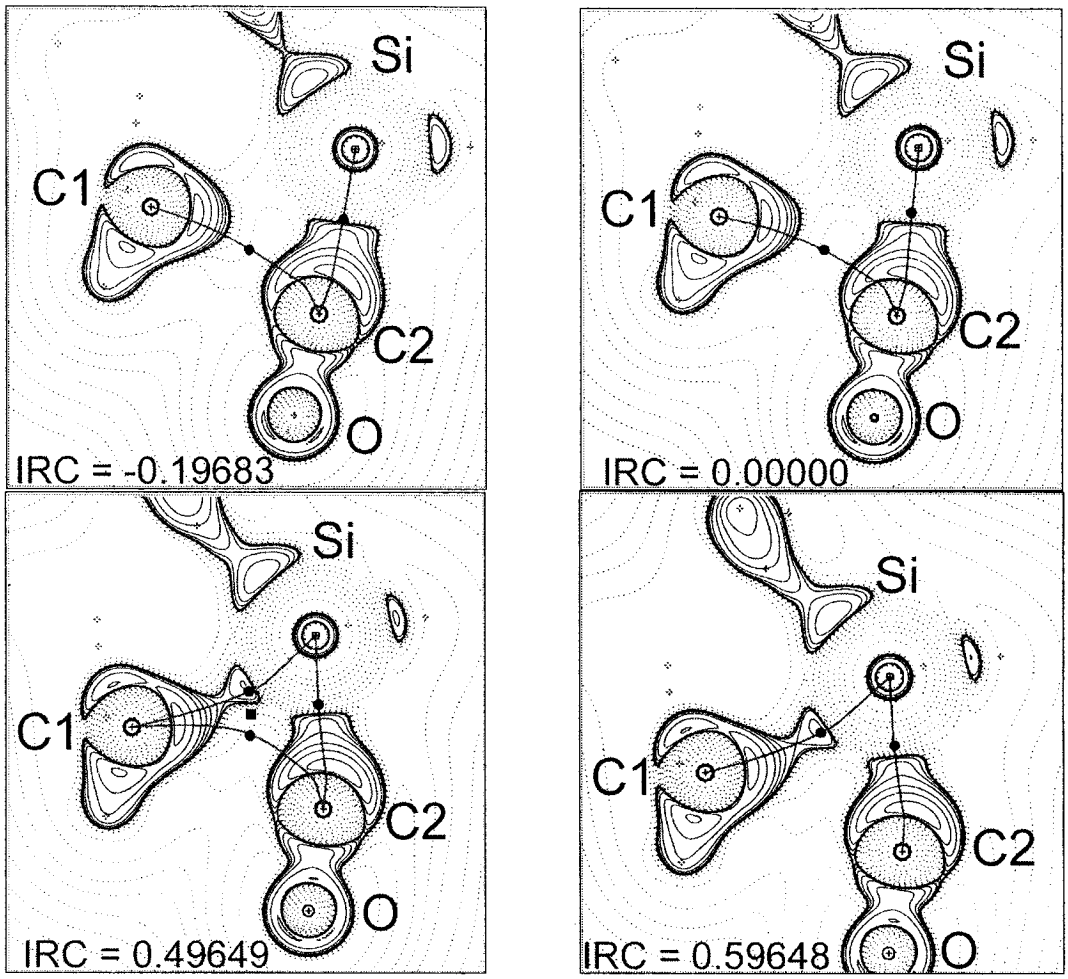

Figure 4.10 B3LYP/6-311+G(2d,p) contour plots of the Laplacian of the electronic density overlaid by bond paths at selected points along the IRC in the C1-C2-Si plane for decarbonylation of silacyclopentanone **D**. Plots for IRC = -0.19683 and 0.00000 are in the reactant region of structural stability, while those for IRC = 0.49649 and 0.59648 are in the ring-structure and product regions of structural stability. Positions of BCPs and RCPs are identified by round and square dots respectively. IRC values are in amu$^{1/2}$ bohr.

4.4 Conclusion

The mechanisms for 1,2-H migration, ring contraction and decarbonylation of 3-sila-2-oxacyclohexylidene have been investigated using hybrid density-functional theory calculations, the quantum theory of atoms in molecules and the electron localization function. The mechanism for 1,2-H migration was shown to involve a typical hydride-like shift from the migration origin to the "vacant" carbene *p* orbital, with axial 1,2-H migration being slightly more favorable than its equatorial counterpart. Ring contraction was found to occur via a concerted mechanism involving intramolecular front-side nucleophilic attack by the carbene lone pair at silicon as opposed to a stepwise mechanism involving an acyl-silyl biradical intermediate. As for decarbonylation, it is most likely a stepwise reaction that involves the intermediacy of silacyclopentanone rather than acyl-silyl and alkyl-silyl biradicals. Overall, 1,2-H migration and ring contraction turn out to be significantly more favorable energetically than decarbonylation.

Chapter 5
Conclusion

The mechanisms of the intramolecular rearrangements of siloxycarbenes were investigated using ab initio molecular orbital theory and density-functional theory calculations, together with the quantum theory of atoms in molecules (AIM), the electron localization function (ELF) and natural bond orbital (NBO) analysis. Unique approaches based on the aforementioned electronic structure methods for gaining insight into the mechanisms of these intramolecular rearrangements were described.

The first part of this research focused on the mechanisms of intramolecular rearrangements of methoxy(siloxy)carbene. Particular attention was paid to the mechanisms of 1,2-silyl migration, 1,2-methyl migration and decarbonylation. The 1,2-silyl migration and decarbonylation rearrangements were found to occur via symmetry-forbidden concerted mechanisms involving intramolecular front-side nucleophilic attack by the carbene lone pair at silicon and by the methoxy oxygen at silicon, respectively. In contrast, 1,2-methyl migration proceeds via a concerted rearrangement which involves an anion-like shift to the "vacant" carbene *p* orbital, a symmetry-allowed mechanism. In addition, AIM analysis revealed that the changes in molecular structure associated with 1,2-silyl migration occur via a bifurcation mechanism, whereas those that accompany 1,2-methyl migration occur via a conflict mechanism. Note also that the changes in molecular structure associated with decarbonylation of methoxy(siloxy)carbene involving intramolecular nucleophilic substitution proceed via a bifurcation mechanism.

The second part of this research examined the effects of substituents and the role of hyperconjugation in siloxycarbene rearrangements, building upon earlier findings. In

general, electron-withdrawing substituents were found to lower the activation barriers for 1,2-silyl migration and decarbonylation of methoxy(substituted-siloxy)carbenes, consistent with the proposed mechanisms. However, while good Hammett correlations were obtained for 1,2-silyl migration, those obtained for decarbonylation were poor. In addition, hyperconjugation was shown to play a role in determining the ease of intramolecular reactivity of siloxycarbenes: the finding that 1,2-silyl migration is more favorable energetically than decarbonylation seems to be related to stronger hyperconjugation in the ground-state siloxycarbene conformers.

The third and final part of this research dealt with the mechanisms of intramolecular rearrangements of 3-sila-2-oxacyclohexylidene, further building upon earlier observations. The rearrangements investigated were 1,2-H migration, ring contraction and decarbonylation. The 1,2-H migration rearrangement was shown to occur via a symmetry-allowed concerted mechanism involving a hydride-like shift to the "vacant" carbene *p* orbital, whereas ring contraction was found to proceed via a symmetry-forbidden concerted mechanism involving front-side nucleophilic attack by the carbene lone pair at silicon. AIM analysis revealed that the molecular-structure changes accompanying 1,2-H migration occurs via a conflict mechanism, while that associated with ring contraction proceeds via a bifurcation mechanism. Decarbonylation was found to occur via a stepwise pathway involving initial formation and subsequent decarbonylation of silacyclopentanone. The decarbonylation of silacyclopentanone was found to occur via intramolecular nucleophilic substitution, a symmetry-forbidden Brook-like rearrangement. The changes in molecular structure associated with the latter reaction also occurred via a bifurcation mechanism.

Use of the combination of AIM, ELF and NBO for probing reaction mechanism is quite possibly unique. Theoretical investigations of reaction mechanism usually tend to focus on reaction energetics and atomic charges. In this work, AIM, ELF and NBO were used to monitor the changes in electronic structure during the rearrangements and unambiguously infer reaction mechanisms.

AIM and ELF were instrumental in showing that the carbene lone pair remains intact in the transition states for 1,2-methyl and 1,2-H migrations in siloxycarbenes, while it develops into new carbon-silicon bonds in the transition states for 1,2-silyl migration and ring contraction. These observations led to the conclusion that 1,2-methyl and 1,2-H migrations proceed via an anion-like shift to the vacant carbene *p* orbital, while 1,2-silyl migration and ring contraction occur via nucleophilic attack by the carbene lone pair at silicon. AIM and ELF were also helpful for bond characterization (i.e. single, double or triple bond) and for monitoring bond dissociation and formation. In the case of ELF analysis, however, there were many instances where the bonding and lone-pair basin populations deviated significantly from those expected intuitively from idealized Lewis models.

NBO analysis was also instrumental in showing that 1,2-silyl migration and decarbonylation of methoxy(substituted-siloxy)carbenes occur via intramolecular front-side nucleophilic attack by the carbene lone pair at silicon and by the methoxy oxygen at silicon, respectively. This was achieved by monitoring the stabilization energies due to hyperconjugation between the carbene lone-pair n(σ) orbital and the $\sigma^*_{O\text{-}Si}$ orbital for 1,2-silyl migration, and between the methoxy oxygen lone-pair n(σ) orbital and the $\sigma^*_{O\text{-}Si}$ orbital for decarbonylation in going from the parent carbene conformers to the transition

states. In addition, NBO was helpful in establishing quantitative relationships between the extent of the pertinent hyperconjugative interactions in the siloxycarbene conformers and the barriers for intramolecular rearrangements. In fact, the results show that it may be possible to predict the relative magnitude of the barrier heights and hence, which of multiple rearrangements are most favorable, by simply examining the extent of the relative hyperconjugative interactions in the parent species.

It is conceivable that in the near future some of the approaches described in this thesis, or modified versions, will become routine when investigating the mechanisms of organic reactions. Monitoring the changes in electronic charge distribution along a reaction path using methods of wave function analysis such as AIM and ELF is immensely informative. In addition, since fairly good linear correlations were found between the activation enthalpies for some intramolecular rearrangements and the stabilization energies due to hyperconjugation in the parent siloxycarbenes according to NBO analysis, it may be possible to predict the relative magnitude of the barrier heights for intramolecular rearrangements based on the extent of hyperconjugation in the parent compounds.

References and Notes

(1) Page, P. C. B.; Klair, S. S.; Rosenthal, S. *Chem. Soc. Rev.* **1990**, *19*, 147.
(2) Patrocinio, A. F.; Moran, P. J. S. *J. Braz. Chem. Soc.* **2001**, *12*, 7.
(3) Wilson, S. R.; Hague, M. S.; Misra, R. N. *J. Org. Chem.* **1982**, *47*, 747.
(4) Bonini, B. F.; Comes-Franchini, M.; Fochi, M.; Mazzanti, G.; Nanni, C.; Ricci, A. *Tetrahedron Lett.* **1998**, *39*, 6737.
(5) Schinzer, D. *Synthesis* **1989**, 179.
(6) Brook, A. G. *Acc. Chem. Res.* **1974**, *7*, 77.
(7) Mi, Y.; Schreiber, J. V.; Corey, E. J. *J. Am. Chem. Soc.* **2002**, *124*, 11290.
(8) Fleming, I.; Barbero, A.; Walter, D. *Chem. Rev.* **1997**, *97*, 2063.
(9) Bourque, R. A.; Davis, P. A.; Dalton, J. C. *J. Am. Chem. Soc.* **1981**, *103*, 697.
(10) Brook, A. G.; Pearce, R.; Pierce, J. B. *Can. J. Chem.* **1971**, *49*, 1622.
(11) Duff, J. M.; Brook, A. G. *Can. J. Chem.* **1973**, *31*, 2869.
(12) Bassindale, A. R.; Brook, A. G.; Harris, J. *J. Organomet. Chem.* **1975**, *90*, C6.
(13) Brook, A. G.; Harris, J. W.; Bassindale, A. R. *J. Organomet. Chem.* **1975**, *99*, 379.
(14) Hassner, A.; Soderquist, J. A. *Tetrahedron Lett.* **1980**, *21*, 429.
(15) Watanabe, H.; Ohsawa, N.; Sawai, M.; Fukasawa, Y.; Matsumoto, H.; Nagai, Y. *J. Organomet. Chem.* **1975**, *93*, 173.
(16) Shih, C.; Swenton, J. S. *J. Org. Chem.* **1982**, *47*, 2668.
(17) Trommer, M.; Sander, W.; Ottosson, C.; Cremer, D. *Angew. Chem. Int. Ed. Engl.* **1995**, *34*, 929.
(18) Bader, R. F. W. *Atoms in Molecules. A Quantum Theory*; Clarendon Press: Oxford, 1990.
(19) Becke, A. D.; Edgecombe, K. E. *J. Chem. Phys.* **1990**, *92*, 539.
(20) Silvi, B.; Savin, A. *Nature* **1994**, *371*, 683.
(21) Savin, A.; Nesper, R.; Wengert, S.; Fassler, T. *Angew. Chem. Int. Ed. Engl.* **1997**, *36*, 1809.
(22) Savin, A.; Silvi, B.; Colonna, F. *Can. J. Chem.* **1996**, *74*, 1088.
(23) Noury, S.; Colonna, F.; Savin, A.; Silvi, B. *J. Mol. Struct.* **1998**, *450*, 59.
(24) Reed, A. E.; Curtiss, L. A.; Weinhold, F. *Chem. Rev.* **1988**, *88*, 899.
(25) Wentrup, C. *Reactive Molecules. The Neutral Reactive Intermediates in Organic Chemistry*; John Wiley & Sons, Inc.: New York, Chichester, Brisbane, Toronto, Singapore, 1984.
(26) Bettinger, H. F.; Schleyer, P. v. R.; Schreiner, P. R.; Schaefer, H. F. In *Modern Electronic Structure Theory and Applications in Organic Chemistry*; Davidson, E. R., Ed.; World Scientific Publishing Co. Pte. Ltd.: Singapore, New Jersey, London, Hong Kong, 1997, p 89.
(27) Bourissou, D.; Guerret, O.; Gabbai, F. P.; Bertrand, G. *Chem. Rev.* **2000**, *100*, 39.
(28) Moss, R. A. In *Advances in Carbene Chemistry*; Brinker, U. H., Ed.; JAI Press Inc.: Greenwich, CT, 1994; Vol. 1, p 59.
(29) Liu, M. T. H. *Acc. Chem. Res.* **1994**, *21*, 287.
(30) Schaefer, H. F. *Acc. Chem. Res.* **1979**, *12*, 288.
(31) Su, D. T.; Thornton, E. R. *J. Am. Chem. Soc.* **1978**, *100*, 1872.
(32) LaVilla, J. A.; Goodman, J. L. *J. Am. Chem. Soc.* **1989**, *111*, 6877.

(33) Bonneau, R.; Liu, M. T. H.; Rayez, M. T. *J. Am. Chem. Soc.* **1989**, *111*, 5973.
(34) Moss, R. A.; Ho, G.-J.; Liu, W. *J. Am. Chem. Soc.* **1992**, *114*, 959.
(35) Liu, M. T. H.; Bonneau, R. *J. Am. Chem. Soc.* **1992**, *114*, 3604.
(36) Liu, M. T. H.; Murray, S. K.; Zhu, J. H. *J. Chem. Soc., Chem. Commun.* **1990**, 1650.
(37) Hill, B. T.; Zhu, Z.; Boeder, A.; Hadad, C. M.; Platz, M. S. *J. Phys. Chem. A* **2002**, *106*, 4970.
(38) Evanseck, J. D.; Houk, K. N. *J. Phys. Chem.* **1990**, *94*, 5518.
(39) Evanseck, J. D.; Mareda, J.; Houk, K. N. *J. Am. Chem. Soc.* **1990**, *112*, 73.
(40) Evanseck, J. D.; Houk, K. N. *J. Am. Chem. Soc.* **1990**, *112*, 9148.
(41) Hoffmann, R.; Zeiss, G. D.; Dine, G. W. V. *J. Am. Chem. Soc.* **1968**, *90*, 1485.
(42) Keating, A. E.; Garcia-Garibay, M. A.; Houk, K. N. *J. Am. Chem. Soc.* **1997**, *117*, 10805.
(43) Keating, A. E.; Garcia-Garibay, M. A.; Houk, K. N. *J. Phys. Chem. A* **1998**, *102*, 8467.
(44) Sulzbach, H. M.; Platz, M. S.; Schaefer, H. F.; Hadad, C. M. *J. Am. Chem. Soc.* **1997**, *119*, 5682.
(45) LaVilla, J. A.; Goodman, J. L. *Tetrahedron Lett.* **1990**, *31*, 5109.
(46) Moss, R. A.; Zheng, F.; Krogh-Jespersen, K. *Org. Lett.* **2001**, *3*, 1439.
(47) Moss, R. A.; Liu, W.; Krogh-Jespersen, K. *J. Phys. Chem.* **1993**, *97*, 13413.
(48) Friedman, L.; Schecter, H. *J. Am. Chem. Soc.* **1960**, *82*, 1002.
(49) Liu, M. T. H. *J. Phys. Org. Chem.* **1993**, *6*, 696.
(50) Creary, X.; Wang, Y. *Tetrahedron Lett.* **1989**, *30*, 2493.
(51) Baird, M. S.; Dale, C. M.; Dulayymi, J. R. A. *J. Chem. Soc. Perkin Trans. 1* **1993**, 1373.
(52) Liu, M. T. H. *J. Org. Chem.* **1992**, *57*, 2483.
(53) Friedman, L.; Schechter, H. *J. Am. Chem. Soc.* **1961**, *93*, 3159.
(54) Freeman, P. K.; George, D. E.; Rao, V. N. M. *J. Org. Chem.* **1964**, *29*, 1682.
(55) Creary, X.; Wang, Y. *J. Org. Chem.* **1994**, *59*, 1604.
(56) Moss, R. A.; Wlostowski, M.; Shen, S.; Krogh-Jespersen, K.; Matro, A. *J. Am. Chem. Soc.* **1988**, *110*, 4443.
(57) Pole, D. L.; Sharma, P. K.; Warkentin, J. *Can. J. Chem.* **1996**, *74*, 1335.
(58) Lu, X.; Reid, D. L.; Warkentin, J. *Can. J. Chem.* **2001**, *79*, 319.
(59) Du, X.-M.; Fan, H.; Goodman, J. L.; Kesselmayer, M. A.; Krogh-Jespersen, K.; LaVilla, J. A.; Moss, R. A.; Shen, S.; Sheridan, R. S. *J. Am. Chem. Soc.* **1990**, *112*, 1920.
(60) El-Saidi, M.; Kassam, K.; Pole, D. L.; Tadey, T.; Warkentin, J. *J. Am. Chem. Soc.* **1992**, *114*, 8751.
(61) Moss, R. A.; Xue, S.; Liu, W.; Krogh-Jespersen, K. *J. Am. Chem. Soc.* **1996**, *118*, 12588.
(62) Venneri, P. C.; Warkentin, J. *J. Am. Chem. Soc.* **1998**, *120*, 11182.
(63) Reid, D. L.; Warkentin, J. *J. Chem. Soc., Perkin Trans. 2* **2000**, 1980.
(64) Merkley, N.; El-Saidi, M.; Warkentin, J. *Can. J. Chem.* **2000**, *78*, 356.
(65) Merkley, N.; Warkentin, J. *Can. J. Chem.* **2000**, *78*, 942.
(66) Foster, A. M.; Agosta, W. C. *J. Am. Chem. Soc.* **1972**, *94*, 5777.
(67) Foster, A. M.; Agosta, W. C. *J. Am. Chem. Soc.* **1973**, *95*, 608.
(68) Ayral-Kaloustian, S.; Agosta, W. C. *J. Org. Chem.* **1982**, *47*, 284.

(69) Miller, R. D.; Golitz, P.; Janssen, J.; Lemmens, J. *J. Am. Chem. Soc.* **1984**, *106*, 7277.
(70) Yates, P.; Loutfy, R. O. *Acc. Chem. Res.* **1975**, *8*, 209.
(71) Borden, W. T.; Hoo, L. H. *J. Am. Chem. Soc.* **1978**, *100*, 6274.
(72) Moss, R. A.; Balcerzak, P. *J. Am. Chem. Soc.* **1992**, *114*, 9386.
(73) Moss, R. A.; Ho, G. J.; Wilk, B. K. *Tetrahedron Lett.* **1989**, *30*, 2473.
(74) Moss, R. A.; Wilk, B. K.; Hadel, L. M. *Tetrahedron Lett.* **1987**, *28*, 1969.
(75) Moss, R. A.; Kim, H.-R. *Tetrahedron Lett.* **1990**, *31*, 4715.
(76) Moss, R. A.; Zdrojewski, T. *Tetrahedron Lett.* **1991**, *32*, 5667.
(77) Moss, R. A.; Zdrojewski, T.; Krogh-Jespersen, K.; Wlostowski, M.; Matro, A. *Tetrahedron Lett.* **1991**, *32*, 1925.
(78) Moss, R. A.; Johnson, L. A.; Merrer, D. C.; G.E. Lee, J. *J. Am. Chem. Soc.* **1999**, *121*, 5940.
(79) Yan, S.; Sauers, R. R.; Moss, R. A. *Org. Lett.* **1999**, *1*, 1603.
(80) Moss, R. A. *Acc. Chem. Res.* **1999**, *32*, 969.
(81) Moss, R. A.; Zheng, F.; Sauers, R. R.; Toscano, J. P. *J. Am. Chem. Soc.* **2001**, *123*, 8109.
(82) Likhotvorik, I. R.; M. Jones, J.; Yurchenko, A. G.; Krasutsky, P. A. *Tetrahedron Lett.* **1989**, *30*, 5089.
(83) Moss, R. A.; Zheng, F.; Johnson, L. A.; Sauers, R. R. *J. Phys. Org. Chem.* **2001**, *14*, 400.
(84) Crawford, R. J.; Raap, R. *Proc. Chem. Soc.* **1963**, 370.
(85) McDonald, R. M.; Krueger, R. A. *J. Org. Chem.* **1966**, *31*, 488.
(86) Pezacki, J. P.; Loncke, P. G.; Ross, J. P.; Warkentin, J.; Gadosy, T. A. *Org. Lett.* **2000**, *2*, 2733.
(87) Brook, A. G. *J. Am. Chem. Soc.* **1955**, *77*, 4827.
(88) Suh, D.; Pole, D. L.; Warkentin, J.; Terlouw, J. K. *Can. J. Chem.* **1996**, *74*, 546.
(89) Hoffmann, R.; Woodward, R. B. *Acc. Chem. Res.* **1968**, *1*, 17.
(90) Woodward, R. B.; Hoffmann, R. *Angew. Chem. Int. Ed. Engl.* **1969**, *8*, 781.
(91) Fleming, I. *Frontier Orbitals and Organic Chemical Reactions*; John Wiley & Sons, Ltd.: Chichester, 1976.
(92) Fukui, K. *Science* **1982**, *218*, 747.
(93) Rauk, A. *Orbital Interaction Theory of Organic Chemistry*; 2nd ed.; Wiley-Interscience: New York, 2001.
(94) Schreiner, P. R.; Schleyer, P.; Hill, R. K. *J. Org. Chem.* **1993**, *58*, 2822.
(95) Schreiner, P. R.; Schleyer, P.; Hill, R. K. *J. Org. Chem.* **1994**, *59*, 1849.
(96) Moss, R. A.; Ge, C. *J. Am. Chem. Soc.* **1996**, *118*, 9792.
(97) Loncke, P. G.; Peslherbe, G. H. *J. Phys. Chem. A*, (submitted 2003).
(98) Loncke, P. G.; Gadosy, T. A.; Peslherbe, G. H. *Can. J. Chem.* **2002**, *80*, 302.
(99) Loncke, P. G.; Gadosy, T. A.; Peslherbe, G. H. *Arkivok* **2001**, *2*, 179.
(100) Hehre, W. J.; Radom, L.; Schleyer, P. v. R.; Pople, J. A. *Ab Initio Molecular Orbital Theory*; John Wiley & Sons: New York, 1986.
(101) Jensen, F. *Introduction to Computational Chemistry*; John Wiley & Sons Ltd.: Baffins Lane, 1999.
(102) Becke, A. D. *J. Chem. Phys.* **1993**, *98*, 5648.
(103) Lee, C.; Yang, W.; Parr, R. G. *Phys. Rev. B* **1988**, *37*, 785.

(104) Feller, D.; Borden, W. T.; Davidson, E. R. *J. Chem. Phys.* **1979**, *71*, 4987.
(105) Sheridan, R. S.; Moss, R. A.; Wilk, B. K.; Shen, S.; Wlostowski, M.; Kesselmayer, M. A.; Subramanian, R.; Kmiecik-Lawrynowicz, G.; Krogh-Jespersen, K. *J. Am. Chem. Soc.* **1988**, *110*, 7563.
(106) Schlegel, H. B. *J. Comp. Chem.* **1982**, *3*, 214.
(107) Bannerjee, A.; Adams, N.; Simons, J.; Shepard, R. *J. Phys. Chem.* **1985**, *89*, 52.
(108) Simons, J.; Jorgensen, P.; Taylor, H.; Ozment, J. *J. Phys. Chem.* **1983**, *87*, 2745.
(109) Cerjan, C. J.; Miller, W. H. *J. Chem. Phys.* **1981**, *75*, 2800.
(110) Frisch, M. J.; Trucks, G. W.; Schlegel, H. B.; Scuseria, G. E.; Robb, M. A.; Cheeseman, J. R.; Zakrzewski, V. G.; J.A. Montgomery, J.; Stratmann, R. E.; Burant, J. C.; Dapprich, S.; Millam, J. M.; Daniels, A. D.; Kudin, K. N.; Strain, M. C.; Farkas, O.; Tomasi, J.; Barone, V.; Cossi, M.; Cammi, R.; Mennucci, B.; Pomelli, C.; Adamo, C.; Clifford, S.; Ochterski, J.; Petersson, G. A.; Ayala, P. Y.; Cui, Q.; Morokuma, K.; Malick, D. K.; Rabuck, A. D.; Raghavachari, K.; Foresman, J. B.; Cioslowski, J.; Ortiz, J. V.; Baboul, A. G.; Stefanov, B. B.; Liu, G.; Liashenko, A.; Piskorz, P.; Komaromi, I.; Gomperts, R.; Martin, R. L.; Fox, D. J.; Keith, T.; Al-Laham, M. A.; Peng, C. Y.; Nanayakkara, A.; Gonzalez, C.; M. Challacombe; Gill, P. M. W.; Johnson, B.; Chen, W.; Wong, M. W.; J. L. Andres; Gonzalez, C.; Head-Gordon, M.; Replogle, E. S.; Pople, J. A. *Gaussian 98, Revision A.11.4*; Gaussian, Inc.: Pittsburgh PA, 2002.
(111) Ochterski, J. W. *Thermochemistry in Gaussian*; Gaussian Inc.: Pittsburgh, PA, 2000.
(112) The AIMPAC suite of programs is available from Professor R.F.W. Bader, McMaster University, Canada, and from the AIMPAC website (www.chemistry.mcmaster.ca/aimpac).
(113) Biegler-Konig, F. W.; Bader, R. F. W.; Tang, T. *J. Comp. Chem.* **1982**, *3*, 317.
(114) Noury, S.; Krokidis, X.; Fuster, F.; Silvi, B. *TopMod Package*; Université Pierre et Marie Curie: Paris, 1997.
(115) SciAn is a free scientific visualization and animation program for high performance graphic workstations developed by E. Pepke, J. Murray, J. Lyons and Y. Hwu that can be obtained from the CCL website (www.ccl.net/cca/software/AIX/index.shtml).
(116) A bond critical point (BCP) is the point of minimum electronic density $\rho(r)$ along a bond or bond path (R.F.W. Bader, *Atoms in Molecules: A Quantum Theory*; Clarendon Press: Oxford, 1990).
(117) The bond ellipticity ε is a measure of the extent to which charge preferentially accumulates in a given plane along a bond or *bond path.* A value of zero reflects the cylindrical symmetry usually associated with single or triple bonds and a value larger than zero is indicative of the elliptical symmetry often associated with double bonds (R.F.W. Bader, *Atoms in Molecules: A Quantum Theory*; Clarendon Press: Oxford, 1990).
(118) The Laplacian of the electronic density allows identification of regions of local charge concentration ($\nabla^2\rho(r) < 0$) and local charge depletion ($\nabla^2\rho(r) > 0$) in the topology of the electronic density (R.F.W. Bader, *Atoms in Molecules: A Quantum Theory*; Clarendon Press: Oxford, 1990).
(119) The valence-shell charge concentration (VSCC) refers to the region of charge concentration corresponding to the outermost quantum shell of an atom where the

Laplacian of the electronic density is negative (R.F.W. Bader, *Atoms in Molecules: A Quantum Theory*; Clarendon Press: Oxford, 1990).
(120) Moss, R. A.; Wlostowski, M.; Terpinski, J.; Krogh-Jespersen, K. *J. Am. Chem. Soc.* **1987**, *109*, 3811.
(121) A low $\rho_b(r)$ and positive $\nabla^2\rho_b(r)$ are characteristic of a weak bond, while a large $\rho_b(r)$ and negative $\nabla^2\rho_b(r)$ are characteristics of a strong covalent bond (R.F.W. Bader, *Atoms in Molecules: A Quantum Theory*; Clarendon Press: Oxford, 1990).
(122) Large ε values for developing and dissociating bonds are usually a reflection of structural instability (R.F.W. Bader, *Atoms in Molecules: A Quantum Theory*; Clarendon Press: Oxford, 1990).
(123) A valence bonding basin usually migrates towards the more electronegative atom during bond dissociation (Savin *et al.* Angew. Chem. Int. Ed. Engl. **1997**, *36*, 1809).
(124) Hammond, G. S. *J. Am. Chem. Soc.* **1955**, *77*, 334.
(125) Nobes, R. H.; Radom, L.; Rodwell, W. R. *Chem. Phys. Lett.* **1980**, *74*, 269.
(126) Rondan, N. G.; Houk, K. N.; Moss, R. A. *J. Am. Chem. Soc.* **1980**, *102*, 1770.
(127) Moss, R. A. *Acc. Chem. Res.* **1980**, *13*, 58.
(128) We note that Moss et al. interpreted the negative ρ value as indicative of an anion-like shift of the acyl group to the "vacant" carbene *p* orbital (J. Am. Chem. Soc. **1996**, *118*, 12588), an interpretation that contradicted their ab initio findings.
(129) Ehrenson, S.; Brownlee, R. T. C.; Taft, R. W. In *Progress in Physical Organic Chemistry*; A.S. Streitwieser, J., Taft, R. W., Eds.; John Wiley & Sons: New York, 1973; Vol. 10, p 1.
(130) Nickon, A.; Huang, F.; Weglein, R.; Matsuo, K.; Yagi, H. *J. Am. Chem. Soc.* **1974**, *96*, 5264.
(131) Freeman, P. K.; Hardy, T. A.; Balyeat, J. R.; Wescott, L. D. *J. Org. Chem.* **1977**, *42*, 3356.
(132) Kyba, E. P.; Hudson, C. W. *J. Org. Chem.* **1977**, *42*, 1935.
(133) Press, L. S.; Shechter, H. *J. Am. Chem. Soc.* **1979**, *101*, 509.
(134) Kyba, E. P.; John, A. M. *J. Am. Chem. Soc.* **1977**, *99*, 8329.
(135) Kyba, E. P. *J. Am. Chem. Soc.* **1977**, *99*, 8330.
(136) Tomioka, H.; Sugiura, T.; Masumoto, Y.; Izawa, Y.; Inagaki, S.; Iwase, K. *J. Chem. Soc., Chem. Commun.* **1986**, 693.
(137) Tomioka, H.; Hayashi, N.; Inoue, N.; Izawa, Y. *Tetrahedron Lett.* **1985**, *26*, 1651.
(138) Pirrung, M. C.; Hwu, J. R. *Tetrahedron Lett.* **1983**, *24*, 565.
(139) Shustov, G. V.; Liu, M. T. H.; Rauk, A. *J. Phys. Chem. A* **1997**, *101*, 2509.
(140) Loncke, P. G.; Peslherbe, G. H. *Org. Biomol. Chem.*, (to be submitted).
(141) Glendening, E. D.; Reed, A. E.; Carpenter, J. E.; Weinhold, F. *NBO 3.0 Program Manual*; Theoretical Chemistry Institute and Department of Chemistry, University of Wisconsin: Madison, Wisconsin.
(142) Only carbene conformers with the Si-X bond antiperiplanar to the O2-C6 bond were considered in this work.
(143) Hansch, C.; Leo, A.; Taft, R. W. *Chem. Rev.* **1991**, *91*, 165.
(144) The substituent constants σ_I are measures of the electron-withdrawing and electron-donating ability of substituents through a combination of field and inductive effects. Generally, electron-withdrawing substituents have positive σ_I values while electron-donating substituents have negative σ_I values.

(145) Yates, P.; Tam, J. C. *J. Chem. Soc., Chem. Commun.* **1975**, 737.
(146) Umbricht, G.; Hellman, M. D.; Hegedus, L. S. *J. Org. Chem.* **1998**, *63*, 5173.
(147) Switlak, K.; He, D.; Yates, P. *J. Chem. Soc. Perkin Trans. 1* **1992**, 2579.
(148) Loncke, P. G.; Peslherbe, G. H. *J. Am. Chem. Soc.*, (Submitted 2003).
(149) Perdew, J. P.; Ernzerhof, M.; Burke, K. *J. Chem. Phys.* **1996**, *105*, 9982.
(150) Perdew, J. P.; Burke, K.; Ernzerhof, M. *Phys. Rev. Lett.* **1997**, *78*, 1396.
(151) Perdew, J. P.; Burke, K.; Ernzerhof, M. *Phys. Rev. Lett.* **1996**, *77*, 3865.
(152) Ernzerhof, M.; Scuseria, G. *J. Chem. Phys.* **1999**, *110*, 5029.
(153) Mixing the HOMO and LUMO results in a singlet wave function in which $\langle S^2 \rangle$ is greater than 0 due to contributions from triplet and higher-lying electronic states. While this is indicative of a spin-contaminated wave function in wave function-based theory, this is not necessarily the case in DFT (Cremer et al. *Int. J. Mol. Sci.* 2002, 3, 360). Since single-determinant DFT calculations on open-shell singlet biradicals often collapse to the closed-shell solutions (i.e. $\langle S^2 \rangle = 0$), we checked to make sure that $\langle S^2 \rangle$ is greater than 0 to ensure that we did indeed obtain the open-shell solutions.
(154) Grafenstein, J.; Kraka, E.; Filatov, M.; Cremer, D. *Int. J. Mol. Sci.* **2002**, *3*, 360.
(155) Biegler-König, F.; Schönbohm, J.; Bayles, D. *J. Comp. Chem.* **2001**, *22*, 545.
(156) Hohenberg, P.; Kohn, W. *Phys. Rev.* **1964**, *136*, B864.
(157) Kohn, W.; Sham, L. J. *Phys. Rev.* **1965**, *140*, A1133.

Appendix A

A.1 Electronic Structure Calculations

Electronic structure calculations refer to methods aimed at solving the electronic Schrödinger equation. Methods that generate solutions without reference to experimental data are referred to as *ab initio*. According to quantum mechanics, the energy and related properties of a molecule can be obtained by solving the time-independent Schrödinger equation, which in short-hand operator form is given by eq (A.1). In this equation, $\hat{H}_{tot}$ is the total Hamiltonian operator, E_{tot} is the total energy and Ψ_{tot} is the total wave function describing the system. Nuclear and electronic coordinates are denoted by R and r, respectively. Equation (A.1) can be simplified by application of the *Born-Oppenheimer* approximation, which allows separation of nuclear and electronic motions. In other words, a molecule may be viewed as electrons moving in a field of fixed nuclei. This means that $\hat{H}_{tot}$ can be expressed as a sum of operators representing the nuclear kinetic energy $\hat{T}_n$ and an electronic Hamiltonian operator $\hat{H}_e$ (cf. eq (A.2)), and the total wave function can be written as a product of nuclear and electronic wave functions (cf. eq (A.3)). As a consequence, one only needs to solve the electronic Schrödinger equation, which is given by eq (A.4), for fixed nuclear configurations.

$$\hat{H}_{tot}\Psi_{tot}(R,r) = E_{tot}\Psi_{tot}(R,r) \tag{A.1}$$

$$\hat{H}_{tot} = \hat{T}_n + \hat{H}_e \tag{A.2}$$

$$\Psi_{tot}(R,r) = \psi_n(R)\psi_e(r) \tag{A.3}$$

$$\hat{H}_e\psi_e(R,r) = E_e(R)\psi_e(R,r) \tag{A.4}$$

A.2 Hartree-Fock Theory

The simplest method for obtaining an approximate solution to the electronic Schrödinger equation is the *Hartree-Fock* (HF) method.[100,101] Since the *exact* electronic wave function ψ_e is unknown, use is made of a *trial* wave function written as a single *Slater determinant* Φ comprising *one-electron* molecular orbitals ϕ_i. The Slater determinant accounts for the anti-symmetry requirement (*Pauli principle*) of the wave function. Each molecular orbital (MO) is the product of a *spatial orbital* and a *spin function*. According to the *variational principle*, the best trial wave function can be obtained by finding the set of MOs which minimize the energy. In other words, the energy must remain stationary with respect to any orbital variation while simultaneously preserving orthonormality relationship between the MOs. These MOs are found by performing a *constrained minimization*, which leads to a set of *pseudo-eigenvalue equations* known as the Hartree-Fock equations (eq (A.5)), where $\hat{F}_i$ is the one-electron *Fock operator* and ε_i is the MO energy. The Fock operator $\hat{F}_i$ describes the motion of an electron i in a field of all nuclei and its repulsive interaction with all other electrons. Since each *Fock orbital* or *canonical* MO can only be found if all other occupied orbitals are known, an iterative procedure must be employed to find the orbitals. This is why the Hartree-Fock method is often referred to as the *Self-Consistent Field* (SCF) approach. Once the canonical MOs have been found, the Slater determinantal wave function is known, the electronic Schrödinger equation can be solved, and the energy and related properties can be obtained.

$$\hat{F}_i \phi_i = \varepsilon_i \phi_i \tag{A.5}$$

A.3 Møller-Plesset Perturbation Theory

The Hartree-Fock method, combined with an appropriately sized basis set, can account for about 99% of the total electronic energy. However, the remaining 1% is very important when describing chemical reactivity. The difference between the Hartree-Fock energy and the lowest possible energy that can be achieved with a given basis set is referred to as the *electron correlation energy*, and methods aimed at accounting for this energy are known as *electron-correlation methods*.[100,101]

Møller-Plesset (MP) perturbation theory accounts for electron correlation by adding higher excitations to the Hartree-Fock determinant using an approach known as *many-body perturbation theory* (MBPT).[100,101] The foundation of MBPT lies in the assumption that the solution to an unknown problem differs only slightly from one that has already been solved. This is expressed mathematically by defining the Hamiltonian operator $\hat{H}$ as a small perturbation $\hat{H}'$ to a known reference Hamiltonian $\hat{H}_0$ (eq (A.6)). The reference Hamiltonian used in Møller-Plesset perturbation theory is defined as a sum of Fock operators, as shown in eq (A.7). With this definition of the reference Hamiltonian, the *unperturbed* or *zero-order wave function* Ψ_0 is simply the HF determinant Φ_0, and the *unperturbed* or *zero-order energy* W_0 is the expectation value of the reference Hamiltonian over the HF determinant, which turns out to be the sum of MO energies (cf. eq (A.8)). From MBPT, the *first-order energy correction* W_1 is the expectation value of the perturbation Hamiltonian over the zero-order wave function (cf. eq (A.9)). This means that the total energy up to first order MP1 (i.e. the sum of the zero- and first-order energy corrections) is exactly the HF energy (eq (A.10)). Therefore, with the definition of the reference Hamiltonian in eq (A.7), corrections to the HF energy start

at second order. The second-order energy correction W_2 contains matrix elements of $\hat{H}'$ between the HF wave function and excited determinants (cf. eq (A.11)). However, only doubly excited determinants, where two electrons are promoted from occupied orbitals i and j to virtual orbitals a and b, can be considered, since matrix elements involving single excitations, as well as triple and higher excitations are zero. In other words, the MP2 contribution describes the interaction between pairs of electrons.

$$H = \hat{H}_0 + \hat{H}' \tag{A.6}$$

$$\hat{H}_0 = \sum_i \hat{F}_i \tag{A.7}$$

$$W_0 = \langle \Phi_0 | H_0 | \Phi_0 \rangle = \langle \Phi_0 | \sum_i F_i | \Phi_0 \rangle = \sum_i \varepsilon_0 \tag{A.8}$$

$$W_1 = \langle \Phi_0 | H' | \Phi_0 \rangle \tag{A.9}$$

$$MP1 = \langle \Phi_0 | H_0 + H' | \Phi_0 \rangle = \langle \Phi_0 | H | \Phi_0 \rangle = E(HF) \tag{A.10}$$

$$W_2 = \sum_{i \neq 0} \frac{\langle \Phi_0 | H' | \Phi_i \rangle \langle \Phi_i | H' | \Phi_0 \rangle}{(E_0 - E_i)} = \sum_{i<j}^{occ} \sum_{a<b}^{vir} \frac{\langle \Phi_0 | H' | \Phi_{ij}^{ab} \rangle \langle \Phi_{ij}^{ab} | H' | \Phi_0 \rangle}{(E_0 - E_{ij})} \tag{A.11}$$

A.4 Density-Functional Theory

Density-functional theory (DFT) is based on the theorem by Hohenberg and Kohn that the ground-state electronic energy E_0 is determined completely by the electronic density ρ.[156] In other words, the ground-state electronic energy is a functional of the electronic density. Unfortunately, the functional connecting E_0 and ρ is unknown. However, a number of functionals have been designed for calculating E_0 from ρ.

The ground-state electronic energy E_0 is usually partitioned into a kinetic energy term describing the motion of electrons $T[\rho]$, a nuclear-electron attraction term $E_{ne}[\rho]$ and an electron-electron repulsion term $E_{ee}[\rho]$ (cf. eq (A.12)). The $E_{ee}[\rho]$ term is further partitioned into coulomb $J[\rho]$ and exchange $K[\rho]$ terms, (cf. eq (A.13)), implicitly accounting for electron-correlation. The terms $E_{ne}[\rho]$ and $J[\rho]$ are given by the classical expressions in eqs (14) and (15). The kinetic energy functional $T[\rho]$ is calculated using the *Kohn-Sham* approach where it is divided into two parts; one that can be calculated exactly and a small correction factor.[157] The part that can be calculated exactly is based on a system of non-interacting electrons with a Slater determinantal wave function composed of one-electron orbitals ϕ_i, where the exact kinetic energy functional T_S is given by eq (A.16). An approximate ground-state electronic density ρ(r) can be found from the one-electron orbitals using eq (A.17). The small deviation from the *true* kinetic energy functional is accounted for by the exchange-correlation term $E_{XC}[\rho]$ in the general DFT expression given by eq (A.18). An expression for $E_{XC}[\rho]$, obtained by equating $E_{DFT}[\rho]$ to $E_0[\rho]$, is given by eq (A.19). The first parenthesis in eq (A19) represents the *kinetic correlation energy* while the second contains both *exchange* and *potential correlation energy*. The *exact* exchange-correlation functional $E_{XC}[\rho]$ is unknown but approximate functionals have been designed. If we assume for the moment that $E_{XC}[\rho]$ is known, then all that is needed is the set of orthogonal orbitals which minimizes the energy. This minimization leads to a set of *pseudo-eigenvalue* equations known as the *Kohn-Sham* equations (cf. eq (A.20)), where h_{KS} is the one-electron *Kohn-*

Sham operator and ϕ_i are the canonical *Kohn-Sham orbitals*. The Kohn-Sham orbitals can be found by solving the Kohn-Sham equations using an iterative procedure similar to that used to solve the Hartree-Fock equations.

The exchange-correlation functional $E_{XC}[\rho]$ is usually separated into a pure exchange functional $E_X[\rho]$ and a pure correlation functional $E_C[\rho]$ (cf. eq (A.21)), which correspond to *same spin* and *mixed spin* interactions, respectively. The E_X and E_C functionals are estimated using local density methods, referred to as *Local Density Approximation* (LDA) or *Local Spin-Density Approximation* (LSDA) methods, which depend on the electronic density ρ, where the density locally is treated as a uniform electron gas. Improvements to LDA methods can usually be achieved using *gradient-corrected* or *generalized gradient approximation* (GGA) methods which depend on the electronic density ρ and it gradient $\nabla\rho$. There are also *hybrid functionals* where $E_{XC}[\rho]$ is a mixture of HF and DFT exchange, along with DFT correlation. The *Becke-style 3-parameter hybrid functional* (B3) is summarized by the expression in eq (A.22). The parameter *a* allows a mixture of HF and LSDA exchange to be used, while the parameters *b* and *c* scale Becke's gradient correction to the LSDA exchange and the gradient correction to the LSDA correlation, respectively. The parameters *a*, *b* and *c* are determined by fitting to experimental data and depend on the form of E_C^{GGA} chosen. The Perdew-Burke-Ernzerhof one-parameter hybrid functional is summarized by eq (A.23).[149-152]

$$E_0[\rho] = T[\rho] + E_{ne}[\rho] + E_{ee}[\rho] \tag{A.12}$$

$$E_{ee}[\rho] = J[\rho] + K[\rho] \tag{A.13}$$

$$E_{ne}[\rho] = \sum_a \int \frac{Z_a \rho(r)}{|R_a - r|} dr \tag{A.14}$$

$$J[\rho] = \frac{1}{2} \iint \frac{\rho(r)\rho(r')}{|r - r'|} dr dr' \tag{A.15}$$

$$T_S = \sum_{i=1}^{N} \langle \phi_i | -\frac{1}{2} \nabla^2 | \phi_i \rangle \tag{A.16}$$

$$\rho(r) = \sum_{i=1}^{N} |\phi_i(r)|^2 \tag{A.17}$$

$$E_{DFT}[\rho] = T_S[\rho] + E_{ne}[\rho] + J[\rho] + E_{XC}[\rho] \tag{A.18}$$

$$E_{XC}[\rho] = (T[\rho] - T_S[\rho]) + (E_{ee}[\rho] - J[\rho]) \tag{A.19}$$

$$h_{KS}\phi_i = \varepsilon_i \phi_i \tag{A.20}$$

$$E_{XC}[\rho] = E_X[\rho] + E_C[\rho] \tag{A.21}$$

$$E_{XC}^{B3} = a\left(E_X^{HF} - E_X^{LSDA}\right) + E_X^{LSDA} + b\Delta E_X^{B88} + E_C^{LSDA} + c\Delta E_C^{GGA} \tag{A.22}$$

$$E_{XC}^{PBE\backslash PBE} = a\left(E_X^{HF} - E_X^{PBE}\right) + E_{XC}^{PBE} \tag{A.23}$$

A.5 Quantum Theory of Atoms in Molecules

The quantum theory of atoms in molecules (AIM) is a means of mapping topological properties of the electronic density ρ(r) to Lewis-structure and valence-shell electron-pair repulsion representations of molecules.[18] Gradient vector field analysis partitions the molecular electronic density into regions or *basins*, each belonging to a specific nucleus. The basins can then be integrated to afford properties usually ascribed to atoms. For example, atomic charges can be determined by integration of the electronic density over the basin volume and subtracting the integrated value from the atomic number. *Critical points* correspond to maxima, minima and saddle points in the topology

of $\rho(r)$, i.e. points where the density gradient $\nabla\rho(r)$ is zero. These critical points are classified according to their rank ω and signature σ as (ω, σ), where the rank ω is the number of non-zero curvatures in $\rho(r)$ and the signature σ is the sum of the signs of the curvatures at the critical point. More explicitly, a (3, -3) critical point or an *attractor* (nucleus) has three negative curvatures, a (3, -1) or *bond critical point* (BCP) has two negative curvatures and one positive curvature, and a (3, +1) or *ring critical point* has one negative curvature and two positive curvatures. The Laplacian of the electronic density $\nabla^2\rho(r)$ identifies regions of local charge concentration ($\nabla^2\rho(r) < 0$) and local charge depletion ($\nabla^2\rho(r) > 0$) in the topology of the electronic density. The outermost quantum shell of an atom where $\nabla^2\rho(r) < 0$ is commonly referred to as the valence-shell charge concentration (VSCC).[18] The nature of bonding between atoms can be characterized by the value of the electronic density $\rho_b(r)$ and the sign of the Laplacian of the electronic density $\nabla^2\rho_b(r)$ at the BCP. A large value of $\rho_b(r)$ together with a large negative value of $\nabla^2\rho_b(r)$ are indicative of a sharing of electronic density between atoms and represents a *shared interaction*, characteristic of covalent bonding. On the contrary, a low value of $\rho_b(r)$ along with a positive value of $\nabla^2\rho_b(r)$ indicates that electronic density accumulates in the separate atomic basins away from the BCP. The latter features are representative of *closed-shell* interactions typically found in ionic bonding, hydrogen bonding, and Van der Waals interactions. The *bond ellipticity*, given by $\varepsilon = \lambda_1/\lambda_2 - 1$, where the parameters λ_1 and λ_2 are the two negative curvatures at the BCP perpendicular to the bond path, is a measure of the extent to which charge preferentially accumulates in a given plane along an atomic interaction line or *bond path*. For example, an ε value of zero reflects the *cylindrical symmetry* of the charge density at the BCP of a single or triple bond and a

value greater than zero is indicative of the *elliptical symmetry* of the BCP charge density of a typical double bond.[18]

A.6 Natural Bond Orbital Analysis

Natural bond orbital analysis is another means of extracting Lewis-structure information from electronic wave functions.[24,101] The procedure involves a sequence of transformations from the input basis set to natural atomic orbitals (NAOs), natural hybrid orbitals (NHOs) and eventually natural bond orbitals (NBOs). The sequence may also be extended to other types of localized orbitals.

Assuming that the basis functions are arranged in such a way that those on atom **A** are before those on atom **B**, which are before those on atom **C**, and so on, the density matrix D can be expressed as localized blocks of basis functions corresponding to each atomic centre (cf. eq (A.24)). Diagonalization of these localized blocks defines a set of *natural atomic orbitals* (NAOs) for each atom in the molecule. The NAOs are divided into a *natural minimal basis* (NMB) set (corresponding to the occupied atomic orbitals of the isolated atom) and a remaining set of *natural Rydberg orbitals*, based on the magnitudes of the occupation numbers. NAOs corresponding to the NMB set are densely occupied whereas the occupancy of the Rydberg orbitals is close to zero.

$$D = \begin{pmatrix} D^{AA} & D^{AB} & D^{AC} & \cdots \\ D^{AB} & D^{BB} & D^{BC} & \cdots \\ D^{AC} & D^{BC} & D^{CC} & \cdots \\ \cdots & \cdots & \cdots & \cdots \end{pmatrix} \tag{A.24}$$

Although NAOs within individual atomic blocks are orthogonal to each other, they are not orthogonal to NAOs from other atomic blocks, and therefore they are actually referred to as *pre-NAOs*. The final set of orthogonal NAOs are obtained by

applying an *occupancy-weighted symmetric orthogonalization* (OWSO) procedure, which removes the inter-atomic overlap while preserving the form of the high occupancy orbitals. The population on a given atom is obtained from the diagonal elements of the density matrix in the NAO basis and the atomic populations can be obtained by summing the contributions of these orbital occupancies.

Once the density matrix has been transformed to the NAO basis, the high occupancy (>1.999*e*) NAOs in each atomic block are identified and removed as *core orbitals*. As well, NAOs in each atomic block with occupancies of about 1.90*e* are identified and removed as *lone-pair orbitals*. The remaining off-diagonal blocks of the density matrix in the NAO basis are then diagonalized and the resulting *eigenvectors* with large *eigenvalues* (corresponding to occupation numbers) are identified as *natural bond orbitals* (NBOs). Once the NBOs have been identified, they can be decomposed into their constituent *natural hybrid orbitals* (NHOs), which in turn are composed of NAOs. The *core*, *lone-pair* and *natural bond* orbitals make up the *natural Lewis structure* of a molecule.

The natural Lewis structure accounts for about 99% of the total electronic density. The remaining valence-shell electronic density leads to low occupancies of anti-bonding NBOs, which account for small deviations from the idealized Lewis structure. In other words, occupation of anti-bonding NBOs is attributed to non-covalent hyperconjugative interactions between filled (donor) and unfilled (acceptor) NBOs. The energy associated with these anti-bonding NBOs can be evaluated by deleting them from the basis set and recalculating the total energy to determine the associated variational energy lowering. In this way, the total energy E_{tot} is decomposed into covalent E_{Lewis} and non-covalent

$E_{non-Lewis}$ terms (cf. eq (A.25)). Moreover, the energy lowering that results from individual interactions between filled (donor) σ and unfilled (acceptor) σ^* NBOs is so small that it can be estimated from the second-order perturbation-energy expression given in eq (A.26), where ε_σ and ε_{σ^*} correspond to the NBO orbital energies and $\hat{F}$ is the *Fock* operator. The energy lowering associated with these individual interactions can also be determined by deletion of the appropriate Fock matrix elements.

$$E_{tot} = E_{Lewis} + E_{non-Lewis} \tag{A.25}$$

$$\Delta E^2_{\sigma\sigma^*} = -2\frac{\langle \sigma | F | \sigma^* \rangle}{\varepsilon_{\sigma^*} - \varepsilon_\sigma} \tag{A.26}$$

A.7 Electron-Localization Function

The electron-localization function (ELF) originally derived by Becke and Edgecombe[19] provides a means of identifying localized electron pairs in atomic and molecular systems.[19-23] This function, denoted by η(r), is given by eq (A.27) for a single determinant wave function built from Hartree-Fock or Kohn-Sham orbitals, where $D(r)$ is the excess local kinetic energy density due to *Pauli repulsion* and $D_h(r)$ is the kinetic energy density of a homogeneous electron gas with the same electronic density.

$$\eta(r) = \frac{1}{1 + \left(\frac{D(r)}{D_h(r)} \right)^2} \tag{A.27}$$

Gradient vector analysis of ELF partitions the molecular electronic density into regions or *basins* of localized electron pairs or *attractors.*[19-23] These basins are classified as *core basins* which surround nuclei with atomic number greater than 2 and *valence basins* in the remaining space. Each valence basin is classified according to its *synaptic*

order, which is the number of core basins to which it is attached. Thus, valence basins attached to one, two, three and more core basins are classified as *monosynaptic* (non-bonding), *disynaptic* (bonding), *trisynaptic* and *polysynaptic* valence basins respectively. A "disynaptic" basin containing a proton is referred to as a *protonated valence basin.* Core and valence basins are usually denoted by $C(X_i)$ and $V(X_i,X_j,...)$ respectively, where X_i and X_j are the atom labels. ELF values fall in the range $0 \leq \eta(r) \leq 1$. An ELF value of 1.0 corresponds to perfect localization and a value of 0.5 is equivalent to localization in a homogeneous electron gas (i.e. essentially perfect delocalization).

The average basin population $N(\Omega_i)$ can be obtained by integration of the one-electronic density over the basin volume Ω_i as shown by eq (A.28).[22,23] The population variance, $\sigma^2(N,\Omega_i)$s, which is a measure of basin population delocalization, is given by eq (A.29). It can be shown that the population variance of a given basin is the sum of the contributions of all other basins (cf. eq (A.30)), where $N(\Omega_i)N(\Omega_j)$ is the number of electron pairs in the isolated non-interacting basins and $N(\Omega_i,\Omega_j)$ is the actual number of electron pairs obtained by integration of the quantum mechanical pair density over the basins Ω_i and Ω_j, taking into account their interactions.[22,23] In actual calculations, $B(\Omega_i,\Omega_j)$ is assessed from eq (31), where $\phi_\mu(r)$ and $\phi_\nu(r)$ are the molecular or natural orbitals, and n_μ^α, n_μ^β, n_ν^α and n_ν^β are the occupation numbers.[22,23] The relative fluctuation $\lambda(\Omega_i)$ given by eq (A.32), is often used as a more general measure of basin delocalization. Its values usually lie within the range $0 \leq \lambda(\Omega_i) \leq .1$.

$$N(\Omega_i) = \int_{\Omega_i} \rho(r)dr \qquad \text{(A.28)}$$

$$\sigma^2(N,\Omega_i) = \left\langle N^2 \right\rangle_{\Omega_i} - \left\langle N \right\rangle_{\Omega_i}^2 \tag{A.29}$$

$$\sigma^2(N,\Omega_i) = \sum_{i\neq j}[N(\Omega_i)N(\Omega_j) - N(\Omega_i,\Omega_j)] = \sum_{i\neq j} B(\Omega_i,\Omega_j) \tag{A.30}$$

$$B(\Omega_i,\Omega_j) = \sum_{\mu}\sum_{\nu}\left(n_\mu^\alpha n_\nu^\alpha + n_\mu^\beta n_\nu^\beta\right)\left\langle \phi_\mu \middle| \phi_\nu \right\rangle_{\Omega_i} \left\langle \phi_\nu \middle| \phi_\mu \right\rangle_{\Omega_j} \tag{A.31}$$

$$\lambda(\Omega_i) = \frac{\sigma^2\left(N_i,\Omega_i\right)}{\bar{N}_i\left(\Omega_i\right)} \tag{A.32}$$

Appendix B

B.1 Contour plots of the Laplacian of the electronic density of the ground-state conformers of methoxy(siloxy)carbene

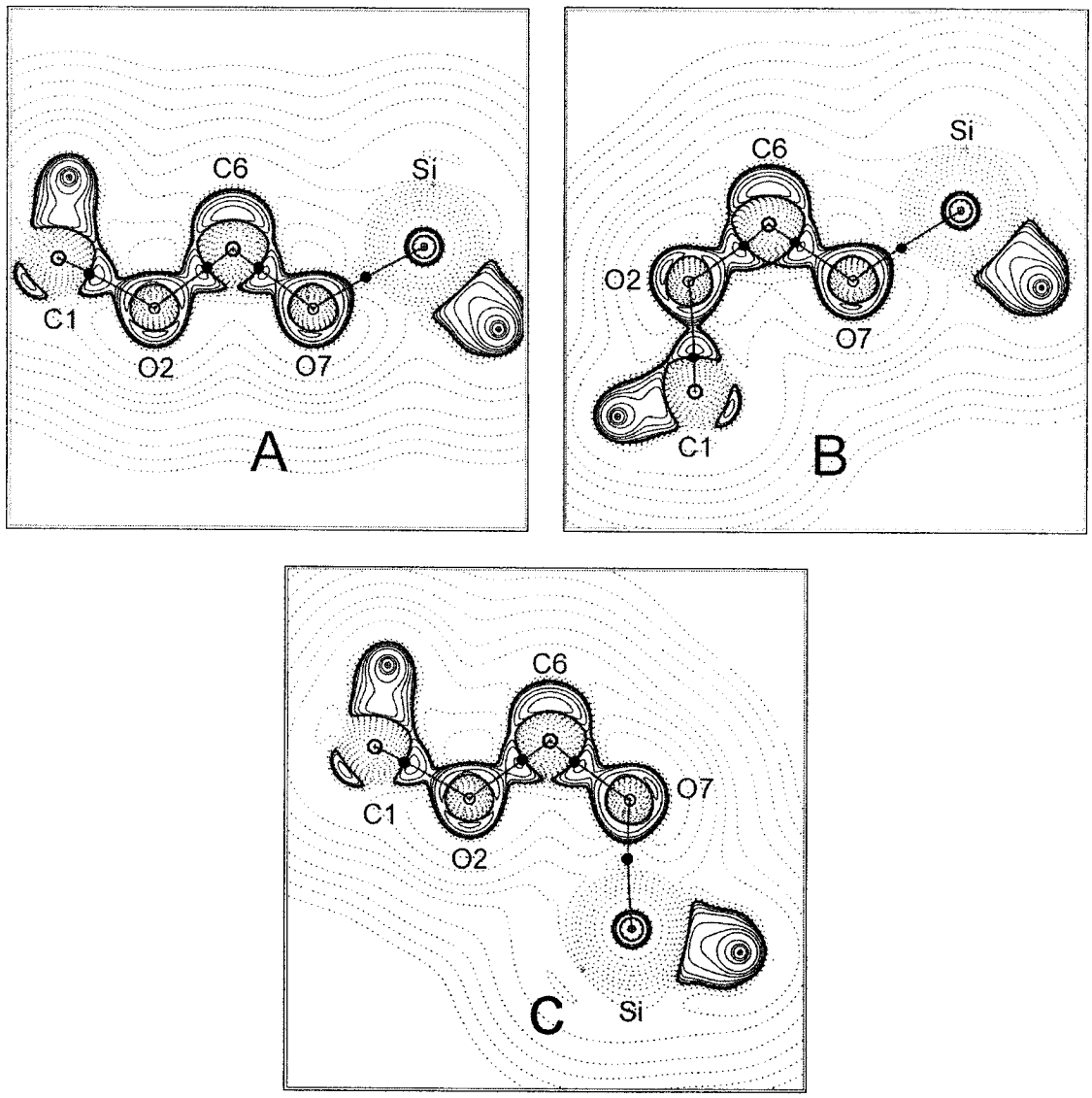

Figure B1 B3LYP/6-311+G(2d,p) contour plots of the Laplacian of the electronic density for the methoxy(siloxy)carbene conformers in the O2C6O7 plane. Solid and broken contours depict regions of charge concentration and charge depletion, respectively. Solid dots identify the positions of the BCPs.

B.2 Plots of bond distances and BCP electronic densities versus reaction coordinate for decarbonylation of *syn*-methyl silylformate

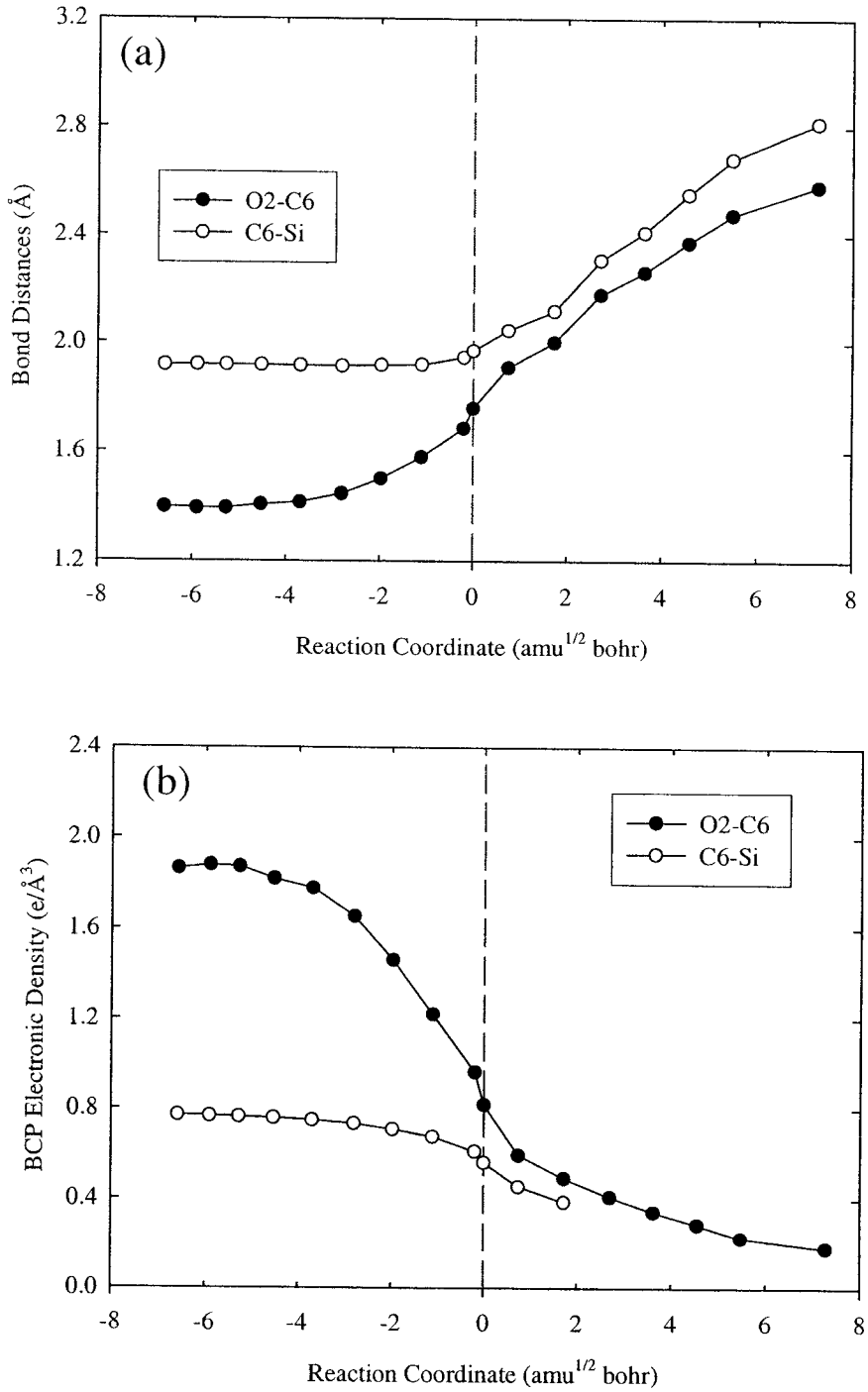

Figure B2 Plots of (a) bond distance and (b) BCP electronic density versus intrinsic reaction coordinate for decarbonylation of *syn*-methyl silylformate.

Appendix C

C.1 Tables of BCP electronic densities for methoxy(substituted-siloxy)carbenes and the transition states for 1,2-silyl migration and decarbonylation

Table C1 HF/6-311+G(2d,p) BCP electronic densities of the ground-state conformers of methoxy(substituted-siloxy)carbenes.[a]

X	C1-O2	O2-C6	C6-O7	O7-Si
		A(X)		
H	1.677	2.297	2.187	0.885
NH_2	1.686	2.272	2.220	0.865
CCH	1.671	2.306	2.180	0.906
SH	1.668	2.309	2.174	0.902
OH	1.674	2.294	2.193	0.893
Cl	1.659	2.329	2.156	0.930
F	1.662	2.324	2.165	0.934
CN	1.645	2.352	2.128	0.942
		B(X)		
H	1.640	2.282	2.125	0.874
NH_2	1.655	2.256	2.159	0.853
CCH	1.632	2.293	2.116	0.897
SH	1.627	2.305	2.095	0.903
OH	1.635	2.287	2.127	0.910
Cl	1.619	2.316	2.094	0.920
F	1.623	2.311	2.104	0.922
CN	1.605	2.339	2.067	0.932
		C(X)		
H	1.659	2.194	2.188	0.856
NH_2	1.672	2.174	2.212	0.839
CCH	1.654	2.195	2.178	0.878
SH	1.651	2.198	2.168	0.875
OH	1.659	2.190	2.188	0.866
Cl	1.641	2.203	2.152	0.902
F	1.645	2.196	2.164	0.907
CN	1.626	2.216	2.134	0.912

[a] BCP electronic densities are in $e/Å^3$ and were obtained from AIM analysis.

Table C2 B3LYP/6-311+G(2d,p) BCP electronic densities of the ground-state conformers of methoxy(substituted-siloxy)carbenes.[a]

X	C1-O2	O2-C6	C6-O7	O7-Si
		A(X)		
H	1.663	2.194	2.114	0.839
NH_2	1.636	2.163	2.144	0.817
CCH	1.593	2.159	2.066	0.827
SH	1.621	2.196	2.109	0.847
OH	1.626	2.186	2.122	0.846
Cl	1.612	2.218	2.102	0.871
F	1.613	2.217	2.110	0.877
CN	1.600	2.241	2.070	0.885
		B(X)		
H	1.545	2.216	2.052	0.830
NH_2	1.562	2.183	2.085	0.808
CCH	1.545	2.218	2.046	0.847
SH	1.538	2.229	2.038	0.850
OH	1.553	2.207	2.066	0.836
Cl	1.534	2.241	2.051	0.858
F	1.535	2.240	2.064	0.862
CN	1.523	2.262	2.015	0.874
		C(X)		
H	1.610	2.091	2.135	0.800
NH_2	1.626	2.066	2.153	0.787
CCH	1.610	2.089	2.131	0.815
SH	1.608	2.089	2.119	0.814
OH	1.615	2.081	2.131	0.815
Cl	1.600	2.095	2.105	0.841
F	1.602	2.096	2.114	0.851
CN	1.585	2.109	2.096	0.843

[a] BCP electronic densities are in $e/Å^3$ and were obtained from AIM analysis.

Table C3 HF/6-311+G(2d,p) BCP electronic densities of the transition states for 1,2-silyl migration and decarbonylation of methoxy(substituted-siloxy)carbenes.[a]

X	C1-O2	O2-C6	C6-O7	O7-Si	C6-Si
			TS_{AD}		
H	1.638	2.325	2.657	0.493	0.514
NH_2	1.645	2.313	2.626	0.547	na
CCH	1.629	2.332	2.682	na	0.551
SH	1.620	2.350	2.648	0.523	0.532
OH	1.637	2.332	2.666	0.483	0.527
Cl	1.621	2.353	2.729	na	0.624
F	1.631	2.338	2.743	na	0.630
CN	1.602	2.373	2.693	na	0.611
			TS_{BE}		
H	1.601	2.344	2.591	0.488	0.514
NH_2	1.612	2.328	2.552	0.556	na
CCH	1.590	2.354	2.620	na	0.555
SH	1.585	2.369	2.580	0.527	0.528
OH	1.602	2.343	2.597	0.486	0.523
Cl	1.578	2.371	2.669	na	0.633
F	1.588	2.356	2.683	na	0.638
CN	1.561	2.397	2.632	na	0.617
			TS_{CH}		
	C1-O2	O2-C6	C6-O7	O7-Si	O2-Si
H	1.592	1.535	2.727	0.496	0.418
NH_2	1.601	1.559	2.703	0.511	0.409
CCH	1.581	1.504	2.734	0.510	0.450
SH	1.571	1.492	2.728	0.502	0.468
OH	1.587	1.505	2.731	0.477	0.444
Cl	1.525	1.657	2.628	0.613	0.415
F	1.555	1.650	2.637	0.591	0.412
CN	1.550	1.379	2.774	0.504	0.527

[a] BCP electronic densities are in $e/Å^3$ and were obtained from AIM analysis.

Table C4 B3LYP/6-311+G(2d,p) BCP electronic densities of the transition states for 1,2-silyl migration and decarbonylation of methoxy(substituted-siloxy)carbenes.[a]

X	C1-O2	O2-C6	C6-O7	O7-Si	C6-Si
			TS_{AD}		
H	1.594	2.207	2.480	0.516	0.522
NH_2	1.607	2.191	2.449	0.569	na
CCH	1.591	2.209	2.503	na	0.560
SH	1.586	2.226	2.468	0.544	0.533
OH	1.595	2.207	2.488	0.514	0.535
Cl	1.583	2.221	2.560	na	0.644
F	1.590	2.210	2.573	na	0.649
CN	1.569	2.248	2.507	na	0.611
			TS_{BE}		
H	1.532	2.248	2.411	0.519	0.516
NH_2	1.545	2.228	2.374	0.583	na
CCH	1.531	2.250	2.441	na	0.563
SH	1.527	2.264	2.394	0.557	0.521
OH	1.539	2.245	2.413	0.530	0.519
Cl	1.525	2.267	2.485	na	0.635
F	1.530	2.261	2.485	na	0.622
CN	1.511	2.289	2.445	na	0.616
			TS_{CH}		
	C1-O2	O2-C6	C6-O7	O7-Si	O2-Si
H	1.498	1.630	1.796	0.332	0.434
NH_2	1.586	1.521	2.581	0.504	0.389
CCH	1.572	1.471	2.619	0.491	0.427
SH	1.563	1.488	2.596	0.498	0.426
OH	1.574	1.461	2.609	0.478	0.425
Cl	1.530	1.580	2.541	0.564	0.420
F	1.547	1.589	2.532	0.566	0.412
CN	1.546	1.360	2.649	0.492	0.490

[a] BCP electronic densities are in $e/Å^3$ and were obtained from AIM analysis.

C.2 Tables of the changes in NPA atomic charges in the transition states for 1,2-silyl migration and decarbonylation of methoxy(substituted-siloxy)carbenes

Table C5 Changes in HF/6-311+G(2d,p) NPA atomic charges in the transition states relative to the parent carbene conformers.

X	C1	O2	C6	O7	Si
			$\mathbf{TS_{AD}(X)}$ relative to **A(X)**		
H	-0.0009	0.0298	0.0060	0.1769	-0.2165
CCH	-0.0010	0.0317	0.0123	0.1887	-0.2386
Cl	-0.0038	0.0253	0.0067	0.2261	-0.2659
CN	-0.0009	0.0321	0.0165	0.2077	-0.2627
F	-0.0039	0.0236	-0.0047	0.2294	-0.2778
NH_2	-0.0007	0.0321	0.0098	0.1607	-0.1914
OH	-0.0026	0.0267	0.0062	0.1833	-0.2416
SH	-0.0007	0.0327	0.0130	0.1847	-0.2242
			$\mathbf{TS_{BE}(X)}$ relative to **B(X)**		
H	0.0021	0.0329	-0.0107	0.1672	-0.1981
CCH	0.0028	0.0348	-0.0067	0.1807	-0.2219
Cl	0.0038	0.0337	-0.0196	0.2138	-0.2453
CN	0.0040	0.0347	-0.0054	0.1986	-0.2406
F	0.0040	0.0317	-0.0294	0.2148	-0.2615
NH_2	0.0011	0.0341	-0.0037	0.1492	-0.1755
OH	0.0027	0.0342	-0.0129	0.1624	-0.2342
SH	0.0026	0.0354	-0.0096	0.1786	-0.2261
			$\mathbf{TS_{CH}(X)}$ relative to **C(X)**		
H	0.0053	-0.1084	0.0170	0.1213	-0.0447
CCH	0.0057	-0.1115	0.0249	0.1239	-0.0429
Cl	0.0062	-0.0941	0.0240	0.1055	-0.0397
CN	0.0053	-0.1336	0.0383	0.1374	-0.0456
F	0.0062	-0.0908	0.0190	0.1090	-0.0844
NH_2	0.0067	-0.1027	0.0249	0.1149	-0.0372
OH	0.0057	-0.1172	0.0247	0.1206	-0.0553
SH	0.0058	-0.1189	0.0280	0.1273	-0.0499

Table C6 Changes in B3LYP/6-311+G(2d,p) NPA atomic charges in the transition states relative to the parent carbene conformers.

X	C1	O2	C6	O7	Si
			TS_{AD}(X) relative to **A(X)**		
H	-0.0016	0.0232	0.0236	0.1611	-0.2092
CCH	-0.0005	0.0281	0.0210	0.1767	-0.2286
Cl	-0.0009	0.0241	0.0109	0.2123	-0.2536
CN	-0.0006	0.0279	0.0230	0.1915	-0.2423
F	-0.0009	0.0216	0.0044	0.2144	-0.2740
NH_2	0.0001	0.0283	0.0197	0.1474	-0.1821
OH	-0.0002	0.0277	0.0143	0.1686	-0.2373
SH	-0.0002	0.0293	0.0209	0.1718	-0.2068
			TS_{BE}(X) relative to **B(X)**		
H	0.0067	0.0272	-0.0041	0.1527	-0.1849
CCH	0.0077	0.0301	-0.0053	0.1691	-0.2088
Cl	0.0093	0.0269	-0.0180	0.1965	-0.2223
CN	0.0085	0.0289	-0.0062	0.1815	-0.2150
F	0.0094	0.0249	-0.0190	0.1899	-0.2403
NH_2	0.0059	0.0289	0.0023	0.1356	-0.1639
OH	0.0074	0.0294	-0.0063	0.1542	-0.2145
SH	0.0069	0.0296	-0.0081	0.1607	-0.2082
			TS_{CH}(X) relative to **C(X)**		
H	0.0051	-0.1153	0.0311	0.1260	-0.0633
CCH	0.1143	-0.1173	0.0334	0.1338	-0.0578
Cl	0.0054	-0.1019	0.0327	0.1188	-0.0591
CN	0.0047	-0.1376	0.0433	0.1429	-0.0534
F	0.0079	-0.0972	0.0282	0.1161	-0.0921
NH_2	0.0070	-0.1065	0.0328	0.1194	-0.0496
OH	0.0060	-0.1233	0.0341	0.1248	-0.0689
SH	0.0060	-0.1179	0.0336	0.1313	-0.0641

C.3 Tables of absolute Gibbs free energies and absolute enthalpies for the methoxy(substituted-siloxy)carbenes

Table C7 Absolute Gibbs free energies and enthalpies of the ground-state conformers of methoxy(substituted-siloxy)carbenes in hartrees at 298.15 K and 1.0 atm.

	HF/6-311+G(2d,p)		B3LYP/6-311+G(2d,p)		MP2/6-311+G(2d,p)	
	G	H	G	H	G	H
			A(X)			
H	-517.88774	-517.84874	-519.78287	-519.74347	-518.70966	-518.67069
CCH	-593.59152	-593.54711	-595.95759	-595.91254	-594.68116	-594.63631
Cl	-976.88539	-976.84281	-979.47358	-979.43081	-977.85388	-977.81136
CN	-609.66258	-609.61855	-612.06619	-612.02167	-610.78370	-610.73943
F	-616.85919	-616.81799	-619.13619	-619.09471	-617.90185	-617.86069
NH_2	-572.96329	-572.92044	-575.18316	-575.13997	-573.97827	-573.93539
OH	-592.83172	-592.78932	-595.08608	-595.04354	-593.86794	-593.82569
SH	-915.46787	-915.42390	-918.04123	-917.99690	-916.43157	-916.38752
			B(X)			
H	-517.88211	-517.84406	-519.77944	-519.74065	-518.70664	-518.66840
CCH	-593.58633	-593.54291	-595.95463	-595.91014	-594.67866	-594.63455
Cl	-976.88022	-976.83857	-979.47084	-979.42847	-977.85155	-977.80971
CN	-609.65735	-609.61423	-612.06340	-612.01935	-610.78137	-610.73776
F	-616.85387	-616.81362	-619.13324	-619.09228	-617.89935	-617.85889
NH_2	-572.95760	-572.91575	-575.17976	-575.13705	-573.97522	-573.93309
OH	-592.82667	-592.78294	-595.08262	-595.04055	-593.86477	-593.82331
SH	-915.46133	-915.41794	-918.03730	-917.99249	-916.42870	-916.38343
			C(X)			
H	-517.88211	-517.84406	-519.77944	-519.74065	-518.70664	-518.66840
CCH	-593.58700	-593.54308	-595.95387	-595.90934	-594.67704	-594.63266
Cl	-976.88084	-976.83869	-979.46966	-979.42706	-977.84922	-977.80701
CN	-609.65818	-609.61459	-612.06236	-612.01826	-610.77924	-610.73540
F	-616.85469	-616.81388	-619.13204	-619.09082	-617.89711	-617.85626
NH_2	-572.95861	-572.91633	-575.17931	-575.13661	-573.97409	-573.93171
OH	-592.82725	-592.78531	-595.08241	-595.04011	-593.86370	-593.82183
SH	-915.46332	-915.41983	-918.03747	-917.99355	-916.42723	-916.38364

C.4 Table of the stabilization energies due to hyperconjugation in the ground-state conformers of methoxy(substituted-siloxy)carbenes

Table C8 Computed HF/6-311+G(2d,p) stabilization energies that result from hyperconjugation in the ground-state conformers of methoxy(substituted-siloxy)carbenes.[a]

X	$n(\sigma)_{C6}\rightarrow\sigma^*_{O7\text{-}Si}$	$n(\sigma)_{C6}\rightarrow\sigma^*_{Si\text{-}X}$	$n(\sigma)_{C6}\rightarrow RY^*_{Si}$	$E^{(tot)}_{stab}$
		A(X)		
H	4.52	1.13	1.70	7.35
NH_2	3.31	1.12	2.62	7.05
CCH	4.42	1.45	5.14	11.00
SH	4.64	1.59	4.64	10.87
OH	3.17	0.91	2.82	6.90
Cl	4.61	1.67	4.54	10.82
F	3.30	1.03	4.13	8.46
CN	5.08	1.54	3.66	10.28
		B(X)		
H	4.41	1.36	1.69	7.47
NH_2	3.20	1.45	4.76	9.42
CCH	4.34	1.75	2.23	8.32
SH	4.85	1.72	4.52	11.09
OH	3.28	1.31	3.87	8.46
Cl	4.64	2.07	6.28	12.99
F	3.31	1.39	2.74	7.44
CN	5.22	2.03	2.67	9.92
		C(X)		
	$n(\sigma)_{O2}\rightarrow\sigma^*_{O7\text{-}Si}$	$n(\sigma)_{O2}\rightarrow\sigma^*_{Si\text{-}X}$	$n_{O2}\rightarrow RY^*_{Si}$	$E^{(tot)}_{stab}$
H	2.59	1.63	0.00	4.22
NH_2	1.89	1.60	0.00	3.49
CCH	2.61	1.85	0.00	4.46
SH	1.89	1.47	0.00	3.36
OH	2.60	1.92	0.00	4.52
Cl	2.64	2.00	0.00	4.64
F	1.99	1.56	0.00	3.55
CN	3.10	2.13	0.00	5.23

[a] Stabilization energies are in kcal/mol and were obtained from NBO analysis by deletion of specific Fock matrix elements. $E^{(tot)}_{stab}$ is the sum of the stabilization energies that arises from $n_{C6}\rightarrow\sigma^*_{O7\text{-}Si}$, $n_{C6}\rightarrow\sigma^*_{Si\text{-}X}$ and all $n_{C6}\rightarrow RY^*_{Si}$ interactions in conformers **A(X)** and **B(X)**, and from $n_{O2}\rightarrow\sigma^*_{O7\text{-}Si}$ and $n_{O2}\rightarrow\sigma^*_{Si\text{-}X}$ interactions in conformers **C(X)**.

Table C9 Computed B3LYP/6-311+G(2d,p) stabilization energies due to hyperconjugation in the ground-state conformers of methoxy(substituted-siloxy)carbenes.

X	$n(\sigma)_{C6}\rightarrow\sigma^{*}_{O7\text{-}Si}$	$n(\sigma)_{C6}\rightarrow\sigma^{*}_{Si\text{-}X}$	$n(\sigma)_{C6}\rightarrow RY^{*}_{Si}$	$E^{(tot)}_{stab}$
		A(X)		
H	5.71	1.78	1.94	9.43
NH_2	4.05	1.84	2.37	8.26
CCH	5.60	2.29	1.54	9.44
SH	4.22	1.82	2.07	8.11
OH	5.87	2.80	3.30	11.98
Cl	6.57	3.66	4.29	14.52
F	5.22	2.76	4.47	12.45
CN	7.08	2.99	2.50	12.57
		B(X)		
H	5.50	2.14	1.97	9.61
NH_2	3.81	2.37	3.09	9.26
CCH	5.43	2.78	3.65	11.85
SH	6.40	3.21	7.50	17.11
OH	4.12	2.56	4.38	11.07
Cl	5.82	5.53	11.76	23.11
F	5.73	4.15	3.65	13.54
CN	4.90	4.31	2.84	12.06
		C(X)		
	$n(\sigma)_{O2}\rightarrow\sigma^{*}_{O7\text{-}Si}$	$n(\sigma)_{O2}\rightarrow\sigma^{*}_{Si\text{-}X}$	$n_{O2}\rightarrow RY^{*}_{Si}$	$E^{(tot)}_{stab}$
H	2.49	1.79	0.00	4.28
NH_2	1.72	1.77	0.00	3.49
CCH	2.49	2.03	0.00	4.51
SH	2.40	2.12	0.00	4.52
OH	1.75	1.65	0.00	3.40
Cl	2.48	2.23	0.00	4.71
F	1.93	1.81	0.00	3.74
CN	3.03	2.39	0.00	5.42

[a] Stabilization energies are in kcal/mol and were obtained from NBO analysis by deletion of specific Fock matrix elements. $E^{(tot)}_{stab}$ is the sum of the stabilization energies that arises from $n_{C6}\rightarrow\sigma^{*}_{O7\text{-}Si}$, $n_{C6}\rightarrow\sigma^{*}_{Si\text{-}X}$ and all $n_{C6}\rightarrow RY^{*}_{Si}$ interactions in conformers **A(X)** and **B(X)**, and from $n_{O2}\rightarrow\sigma^{*}_{O7\text{-}Si}$ and $n_{O2}\rightarrow\sigma^{*}_{Si\text{-}X}$ interactions in conformers **C(X)**.

C.5 Tables of the NBO energies and polarization coefficients for the ground-state conformers of methoxy(substituted-siloxy)carbenes

Table C10 HF/6-311+G(2d,p) NBO energies and polarization coefficients for the ground-state conformers of methoxy(substituted-siloxy)carbenes.[a]

X	$n(\sigma)_{C6}$	$\sigma^*_{O7\text{-}Si}$	$c_{(O7)}$[b]	$c_{(Si)}$[b]	$\sigma^*_{Si\text{-}X}$	$c_{(Si)}$[c]	$c_{(X)}$[c]
				A(X)			
H	-0.5003	0.3888	0.3684	-0.9297	0.3982	0.7895	-0.6137
NH_2	-0.4932	0.4171	0.3621	-0.9321	0.4857	0.9038	-0.4280
CCH	-0.5016	0.4070	0.3702	-0.9289	0.4811	0.8620	-0.5069
SH	-0.5044	0.3753	0.3675	-0.9300	0.3050	0.8329	-0.5535
OH	-0.5021	0.4290	0.3600	-0.9330	0.4751	0.9266	-0.3761
Cl	-0.5114	0.3833	0.3677	-0.9299	0.3148	0.8717	-0.4900
F	-0.5121	0.4330	0.3600	-0.9329	0.4461	0.9401	-0.3409
CN	-0.5212	0.3838	0.3737	-0.9276	0.4221	0.8599	-0.5104
				B(X)			
H	-0.4825	0.3768	0.3650	-0.9310	0.3943	0.7906	-0.6124
NH_2	-0.4747	0.4066	0.3586	-0.9335	0.4834	0.9045	-0.4265
CCH	-0.4837	0.3969	0.3667	-0.9304	0.4765	0.8627	-0.5058
SH	-0.4879	0.3688	0.3642	-0.9313	0.2975	0.8340	-0.5517
OH	-0.4825	0.4280	0.3601	-0.9329	0.4618	0.9263	-0.3767
Cl	-0.4935	0.3717	0.3641	-0.9313	0.3101	0.8725	-0.4886
F	-0.4943	0.4229	0.3562	-0.9344	0.4412	0.9404	-0.3399
CN	-0.5033	0.3730	0.3700	-0.9290	0.4174	0.8607	-0.5090
				C(X)			
X	$n(\sigma)_{O2}$	$\sigma^*_{O7\text{-}Si}$	$c_{(O7)}$[b]	$c_{(Si)}$[b]	$\sigma^*_{Si\text{-}X}$	$c_{(Si)}$[c]	$c_{(X)}$[c]
H	-0.7973	0.3688	0.3768	-0.9263	0.4012	0.7884	-0.6152
NH_2	-0.7907	0.4006	0.3693	-0.9293	0.4862	0.9030	-0.4296
CCH	-0.8004	0.3882	0.3790	-0.9254	0.4827	0.8610	-0.5086
SH	-0.7993	0.4107	0.3754	-0.9269	0.4752	0.8319	-0.5550
OH	-0.8028	0.3579	0.3672	-0.9302	0.3056	0.9260	-0.3776
Cl	-0.8103	0.3639	0.3757	-0.9267	0.3148	0.8707	-0.4917
F	-0.8102	0.4141	0.3675	-0.9300	0.4446	0.9395	-0.3425
CN	-0.8210	0.3645	0.3829	-0.9238	0.4229	0.8588	-0.5123

[a] NBO energies are in atomic units. [b] Polarization coefficients $c_{(O7)}$ and $c_{(Si)}$ are for $\sigma^*_{O7\text{-}Si}$. [c] Polarization coefficients $c_{(Si)}$ and $c_{(X)}$ are for $\sigma^*_{Si\text{-}X}$.

Table C11 B3LYP/6-311+G(2d,p) NBO energies and polarization coefficients for the ground-state conformers of methoxy(substituted-siloxy)carbenes.[a]

X	$n(\sigma)_{C6}$	$\sigma^*_{O7\text{-}Si}$	$c_{(O7)}$[b]	$c_{(Si)}$[b]	$\sigma^*_{Si\text{-}X}$	$c_{(Si)}$[c]	$c_{(X)}$[c]
				A(X)			
H	-0.3477	0.1552	0.3875	-0.9219	0.1985	0.7716	-0.6361
NH_2	-0.3391	0.1823	0.3809	-0.9246	0.2507	0.8953	-0.4454
CCH	-0.3484	0.1727	0.3887	-0.9214	0.2627	0.8506	-0.5258
SH	-0.3477	0.1854	0.3868	-0.9222	0.2295	0.8259	-0.5638
OH	-0.3497	0.1477	0.3785	-0.9256	0.1083	0.9193	-0.3936
Cl	-0.3567	0.1478	0.3865	-0.9223	0.1107	0.8648	-0.5022
F	-0.3576	0.1803	0.3778	-0.9259	0.1977	0.9345	-0.3560
CN	-0.3673	0.1506	0.3919	-0.9200	0.2126	0.8486	-0.5290
				B(X)			
H	-0.3318	0.1464	0.3839	-0.9234	0.1957	0.7728	-0.6347
NH_2	-0.3225	0.1741	0.3773	-0.9261	0.2492	0.8961	-0.4439
CCH	-0.3325	0.1647	0.3850	-0.9229	0.2591	0.8512	-0.5248
SH	-0.3357	0.1397	0.3822	-0.9241	0.1013	0.8269	-0.5623
OH	-0.3312	0.1771	0.3748	-0.9271	0.2260	0.9197	-0.3927
Cl	-0.3208	0.1376	0.3821	-0.9241	0.1076	0.8657	-0.5005
F	-0.3415	0.1704	0.3729	-0.9279	0.1959	0.9350	-0.3547
CN	-0.3256	0.1421	0.3876	-0.9218	0.2093	0.8495	-0.5277
				C(X)			
X	$n(\sigma)_{O2}$	$\sigma^*_{O7\text{-}Si}$	$c_{(O7)}$[b]	$c_{(Si)}$[b]	$\sigma^*_{Si\text{-}X}$	$c_{(Si)}$[c]	$c_{(X)}$[c]
H	-0.5952	0.1346	0.3991	-0.9169	0.1994	0.7693	-0.6388
NH_2	-0.3329	0.1662	0.3898	-0.9209	0.2470	0.8940	-0.4482
CCH	-0.5972	0.1517	0.4009	-0.9161	0.2616	0.8488	-0.5287
SH	-0.5986	0.1308	0.3971	-0.9178	0.1053	0.8240	-0.5665
OH	-0.5959	0.1681	0.3877	-0.9218	0.2261	0.9181	-0.3964
Cl	-0.6066	0.1316	0.3974	-0.9176	0.1064	0.8628	-0.5056
F	-0.6073	0.1642	0.3882	-0.9216	0.1926	0.9332	-0.3594
CN	-0.6177	0.1288	0.4056	-0.9141	0.2104	0.8466	-0.5323

[a] NBO energies are in atomic units. [b] Polarization coefficients $c_{(O7)}$ and $c_{(Si)}$ are for $\sigma^*_{O7\text{-}Si}$. [c] Polarization coefficients $c_{(Si)}$ and $c_{(X)}$ are for $\sigma^*_{Si\text{-}X}$.

C.6 Plots of bond angles and bond distances versus Swain-Lupton modified Hammett substituent constants for methoxy(substituted-siloxy)carbenes

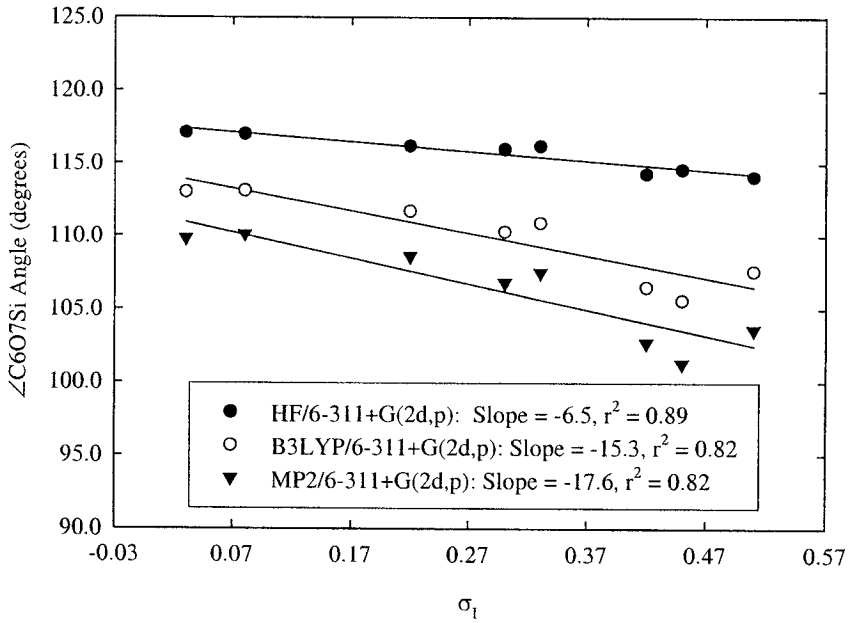

Figure C1 Dependence of the ∠C6O7Si bond angle of conformers **B(X)** of methoxy(substituted-siloxy)carbenes on the Swain-Lupton substituent constants σ_I.

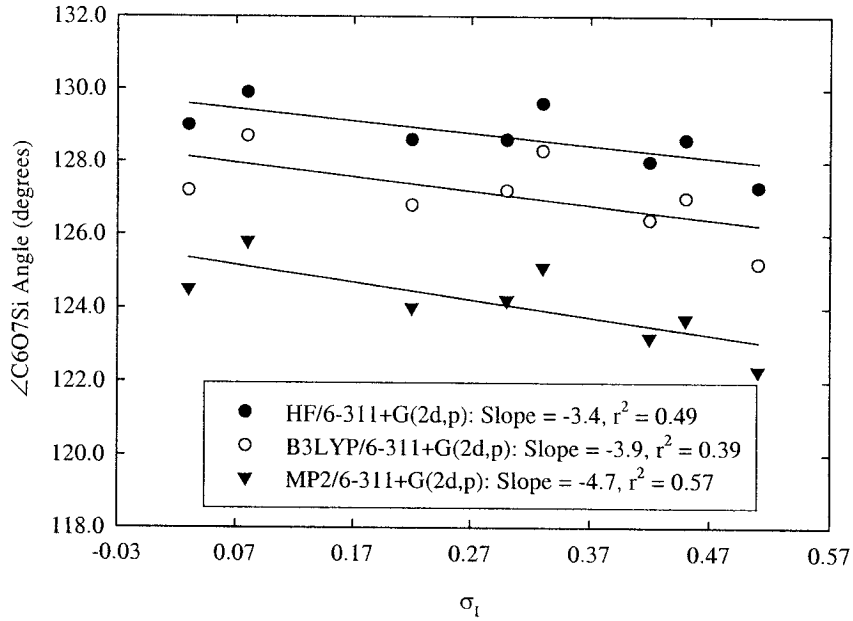

Figure C2 Dependence of the ∠C6O7Si bond angle of conformers C(X) of methoxy(substituted-siloxy)carbenes on the Swain-Lupton modified Hammett substituent constants σ_I.

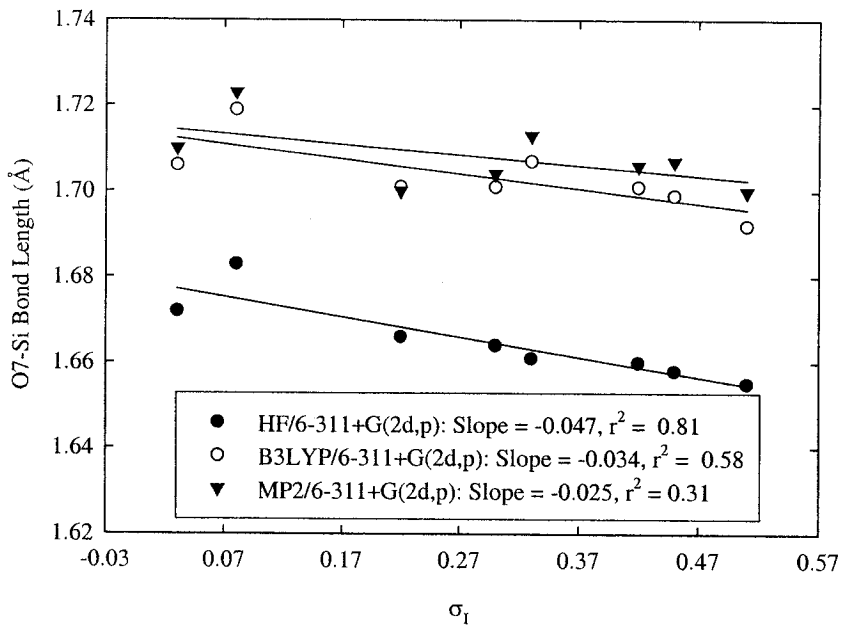

Figure C3 Dependence of the O7-Si bond length of conformers **B(X)** of methoxy(substituted-siloxy)carbenes on Swain-Lupton modified Hammett substituent constant σ_I.

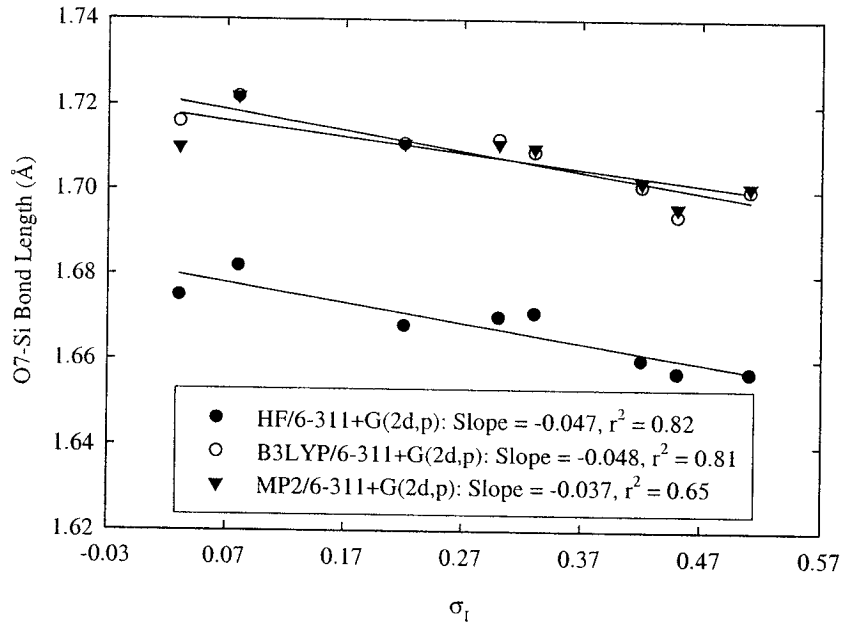

Figure C4 Dependence of the O7-Si bond length of conformers **C(X)** of methoxy(substituted-siloxy)carbenes on Swain-Lupton modified Hammett substituent constants σ_I.

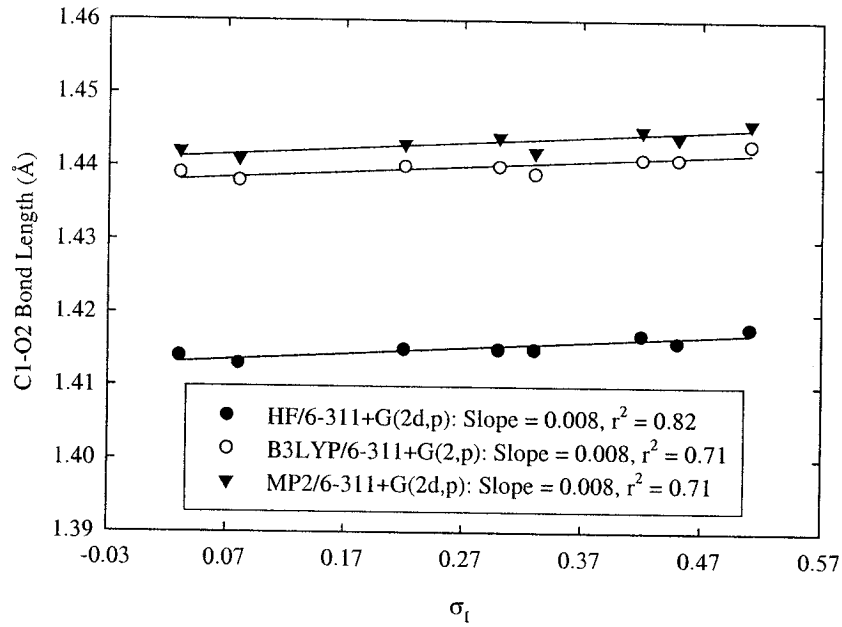

Figure C5 Dependence of the C1-O2 bond length of conformers **A(X)** of methoxy(substituted-siloxy)carbenes on Swain-Lupton modified Hammett substituent constants σ_I.

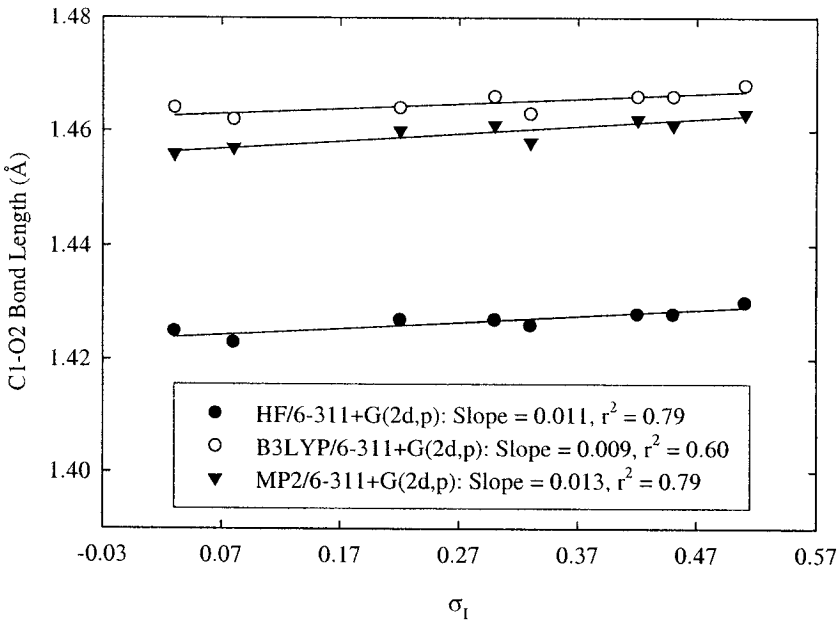

Figure C6 Dependence of the C1-O2 bond length of conformers **B(X)** of methoxy(substituted-siloxy)carbenes on Swain-Lupton modified Hammett substituent constants σ_I.

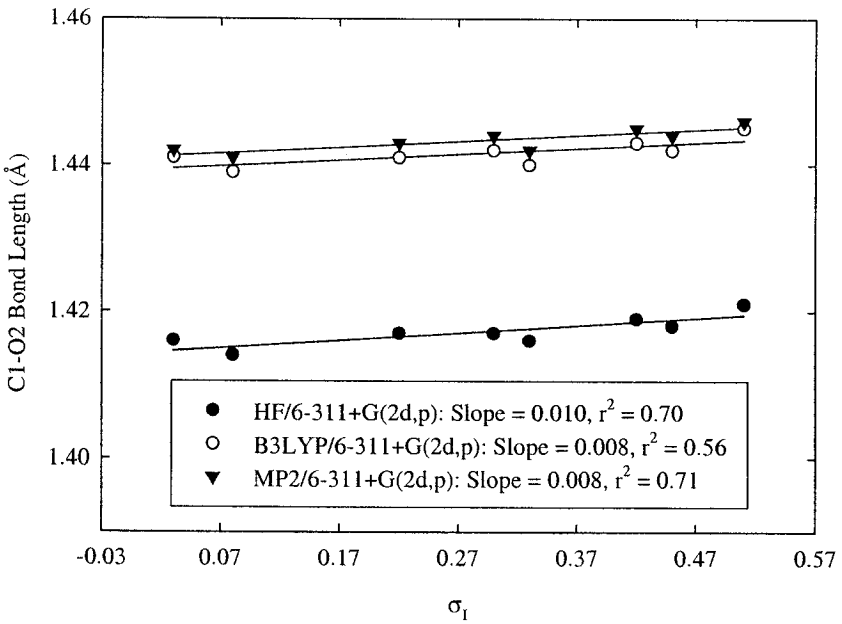

Figure C7 Dependence of the C1-O2 bond length of conformers **C(X)** of methoxy(substituted-siloxy)carbenes on Swain-Lupton modified Hammett substituent constants σ_I.

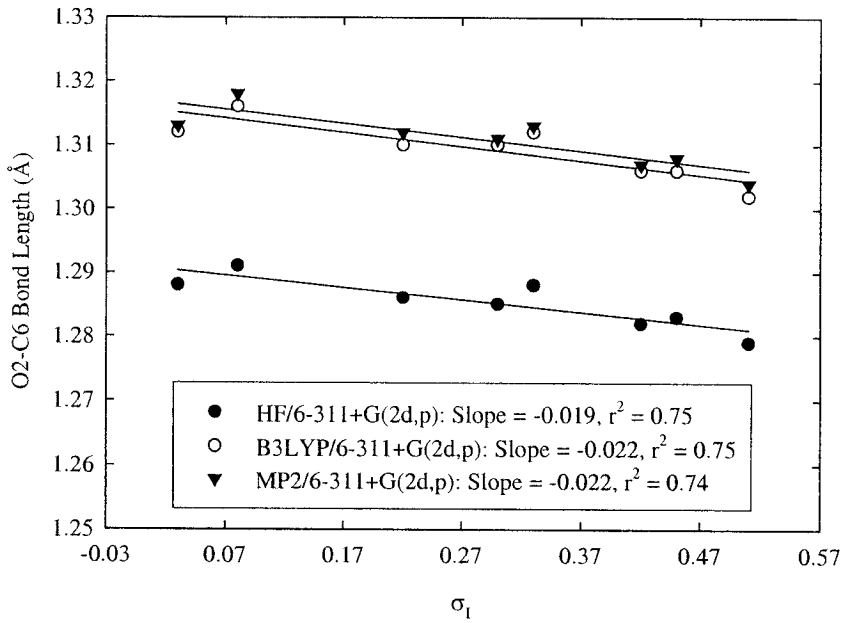

Figure C8 Dependence of the O2-C6 bond length of conformers **A(X)** of methoxy(substituted-siloxy)carbenes on Swain-Lupton modified Hammett substituent constants σ_I.

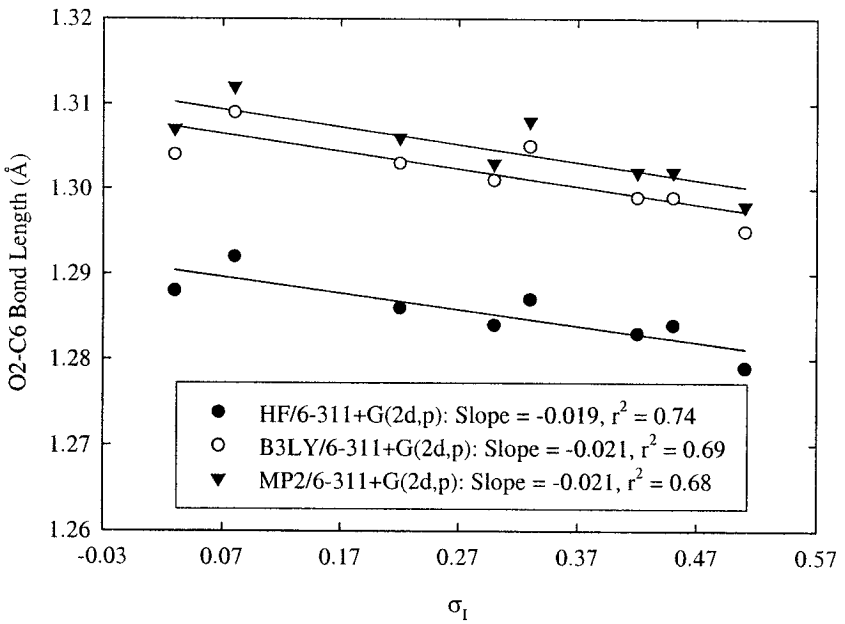

Figure C9 Dependence of the O2-C6 bond length of conformers **B(X)** of methoxy(substituted-siloxy)carbenes on Swain-Lupton modified Hammett substituent constants σ_I.

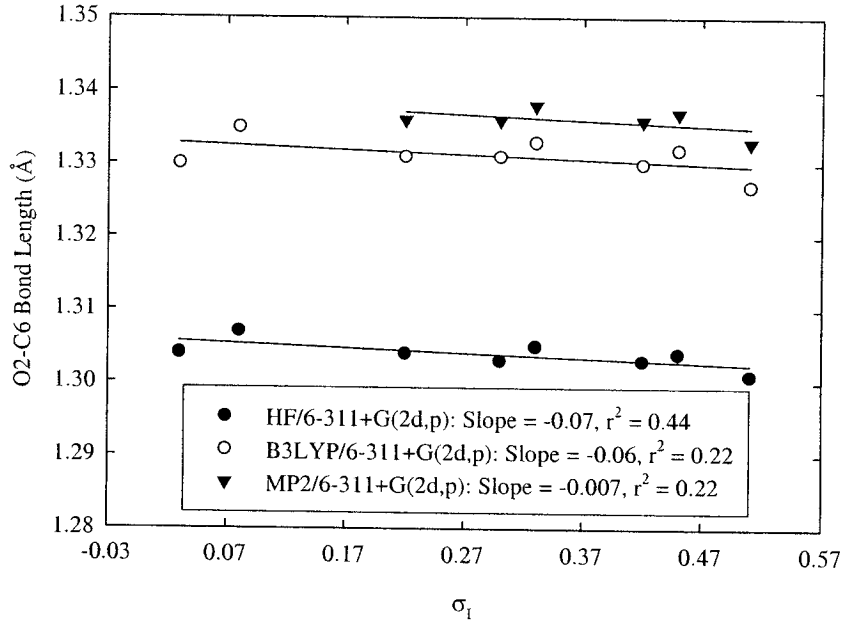

Figure C10 Dependence of the O2-C6 bond length of conformers **C(X)** of methoxy(substituted-siloxy)carbenes on Swain-Lupton modified Hammett substituent constants σ_I.

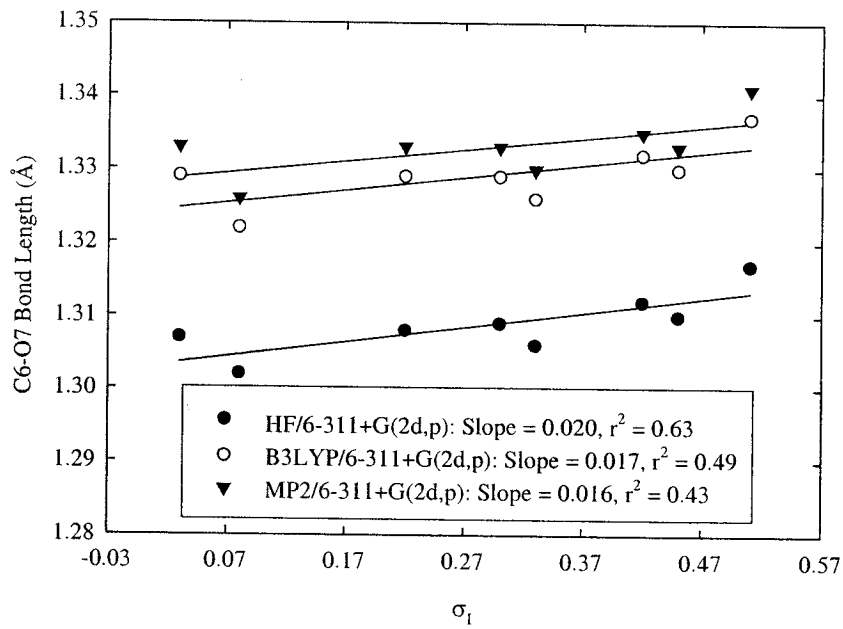

Figure C11 Dependence of the C6-O7 bond length of conformers **A(X)** of methoxy(substituted-siloxy)carbenes on Swain-Lupton modified Hammett substituent constant σ_I.

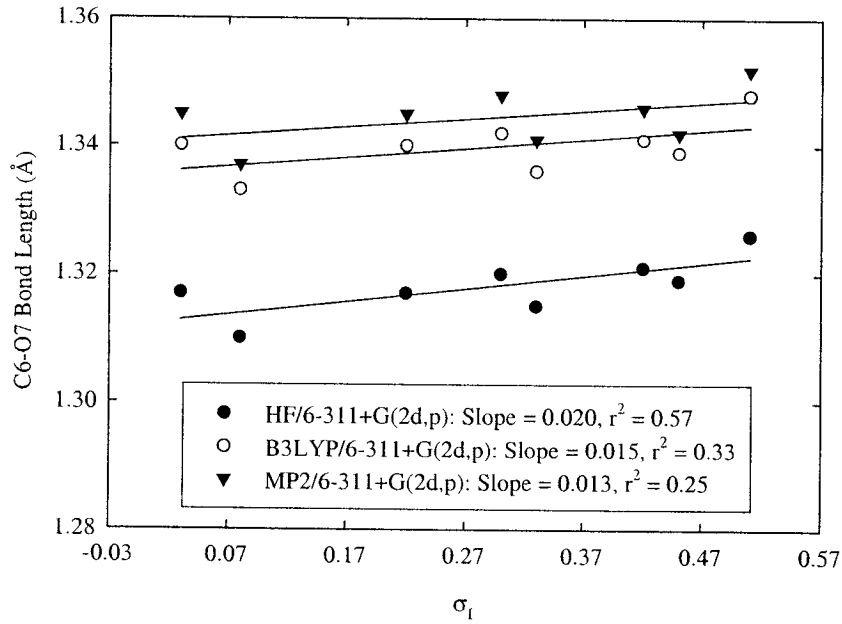

Figure C12 Dependence of the C6-O7 bond length of conformers **B(X)** of methoxy(substituted-siloxy)carbenes on Swain-Lupton modified Hammett substituent constants σ_I.

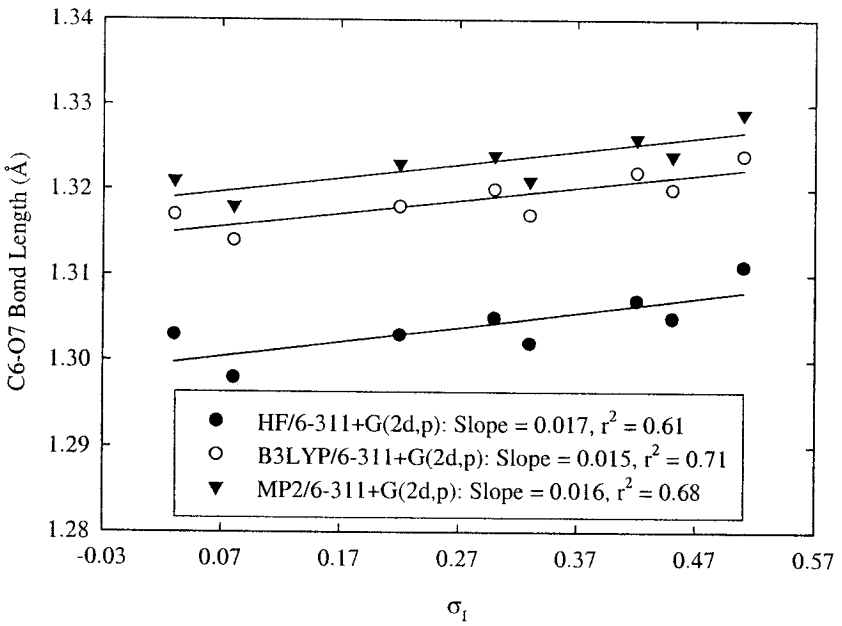

Figure C13 Dependence of the C6-O7 bond length of conformers **C(X)** of methoxy(substituted-siloxy)carbenes on Swain-Lupton modified Hammett substituent constants σ_I.

C.7 Plots of BCP electronic densities versus Swain-Lupton modified Hammett substituents constants for methoxy(substituted-siloxy)carbenes

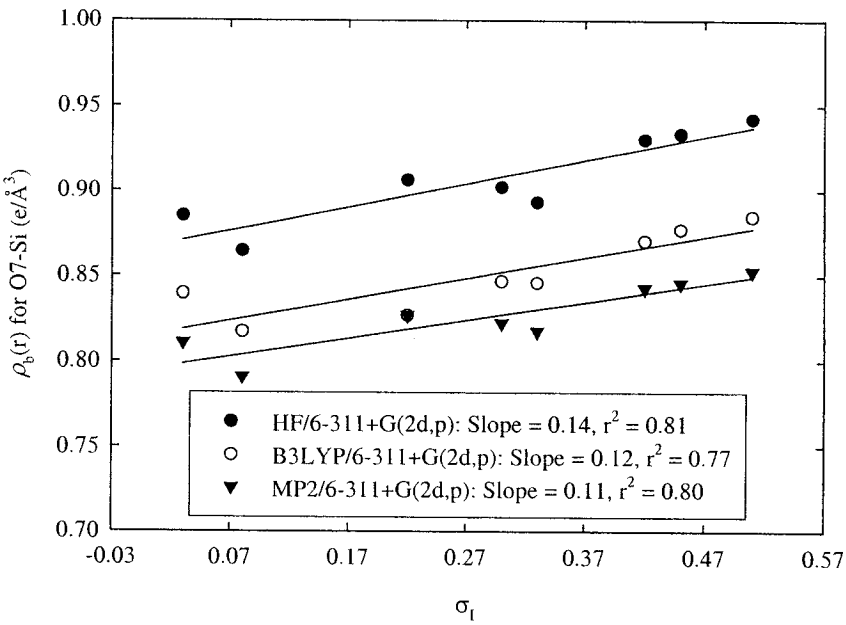

Figure C14 Dependence of the O7-Si BCP electronic density on Swain-Lupton modified Hammett substituent constants σ_I for conformers **A(X)** of methoxy(substituted-siloxy)carbenes.

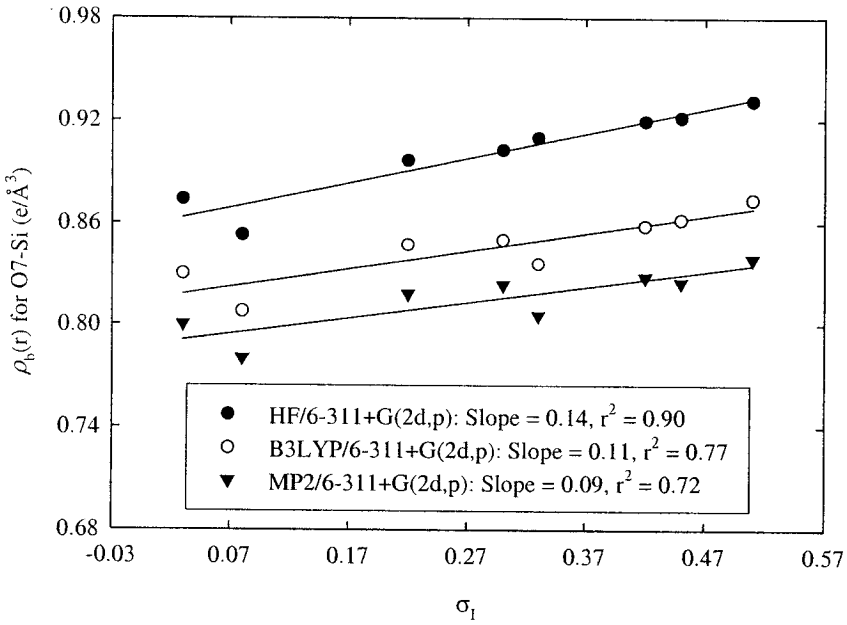

Figure C15 Dependence of the O7-Si BCP electronic density on Swain-Lupton modified Hammett substituent constants σ_I for conformers **B(X)** of methoxy(substituted-siloxy)carbenes.

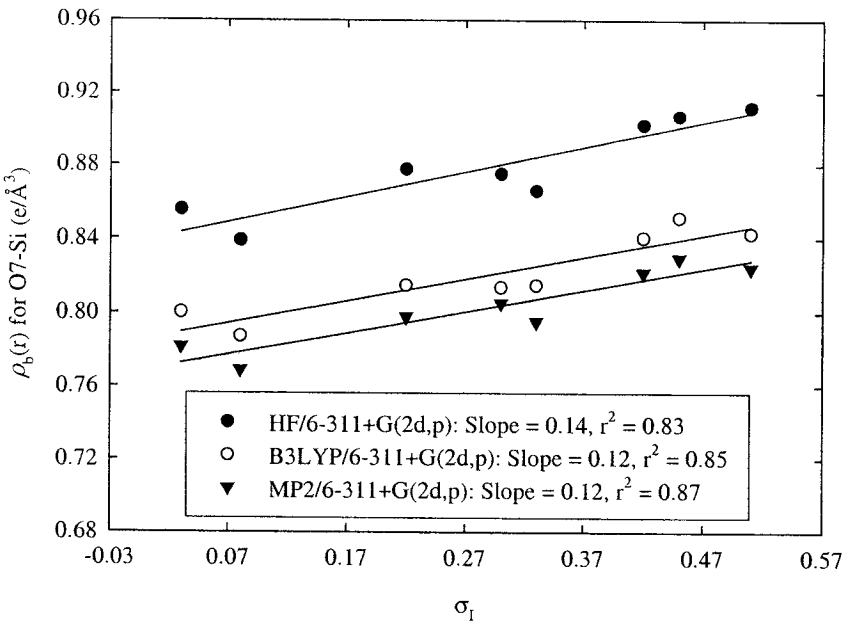

Figure C16 Dependence of the O7-Si BCP electronic density on Swain-Lupton modified Hammett substituent constants σ_I for conformers **C(X)** of methoxy(substituted-siloxy)carbenes.

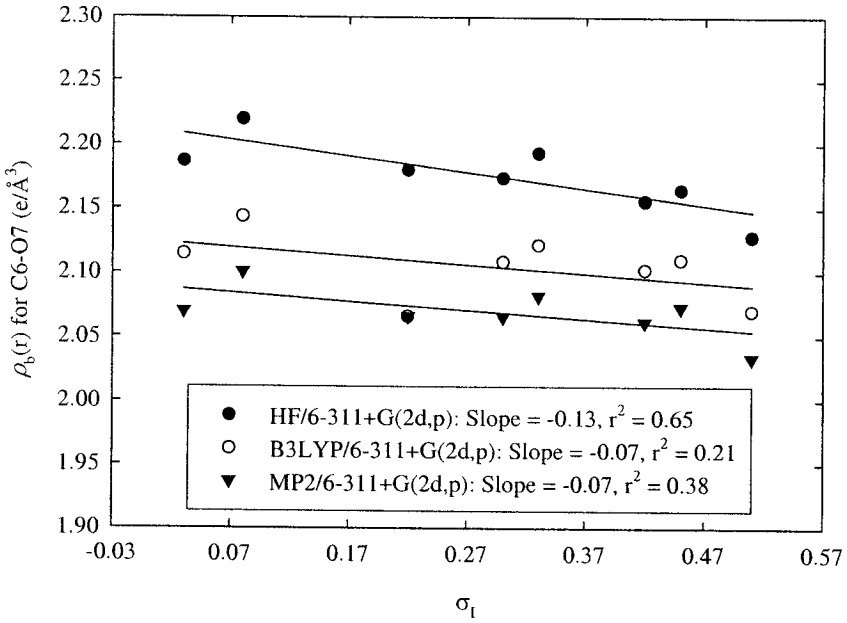

Figure C17 Dependence of the C6-O7 BCP electronic density on Swain-Lupton modified Hammett substituent constants σ_I for conformers **A(X)** of methoxy(substituted-siloxy)carbenes.

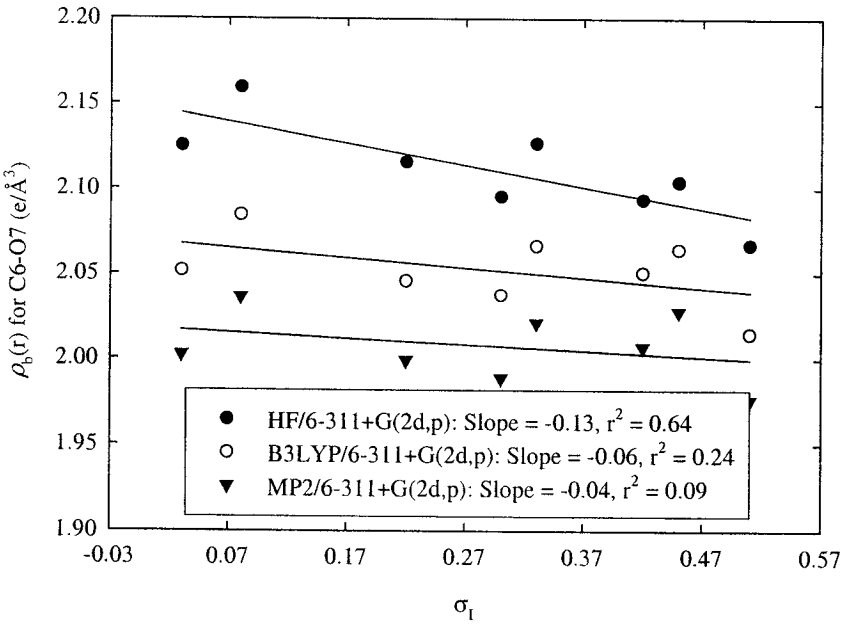

Figure C18 Dependence of the C6-O7 BCP electronic density on Swain-Lupton modified Hammett substituent constants σ_I for conformers **B(X)** of methoxy(substituted-siloxy)carbenes.

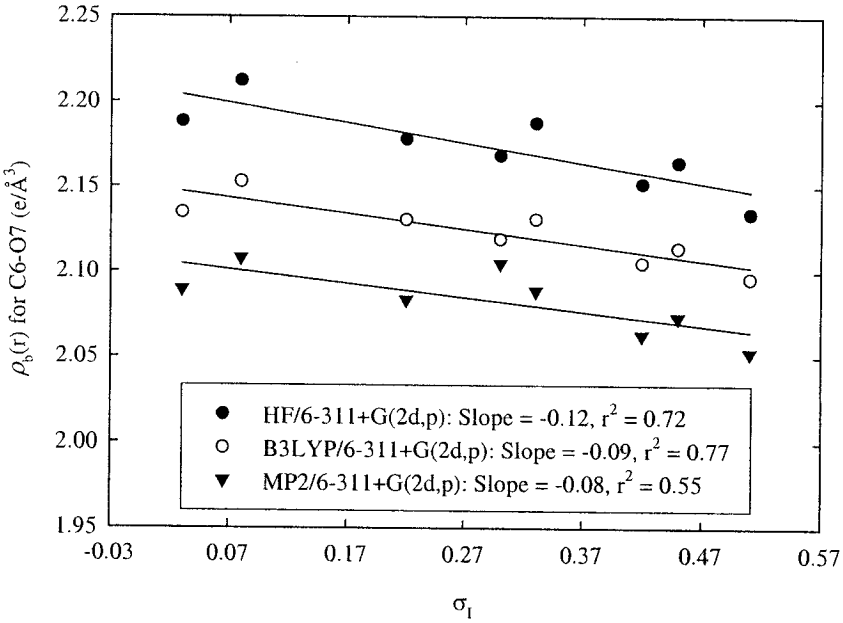

Figure C19 Dependence of the C6-O7 BCP electronic density on Swain-Lupton modified Hammett substituent constants σ_I for conformers **C(X)** of methoxy(substituted-siloxy)carbenes.

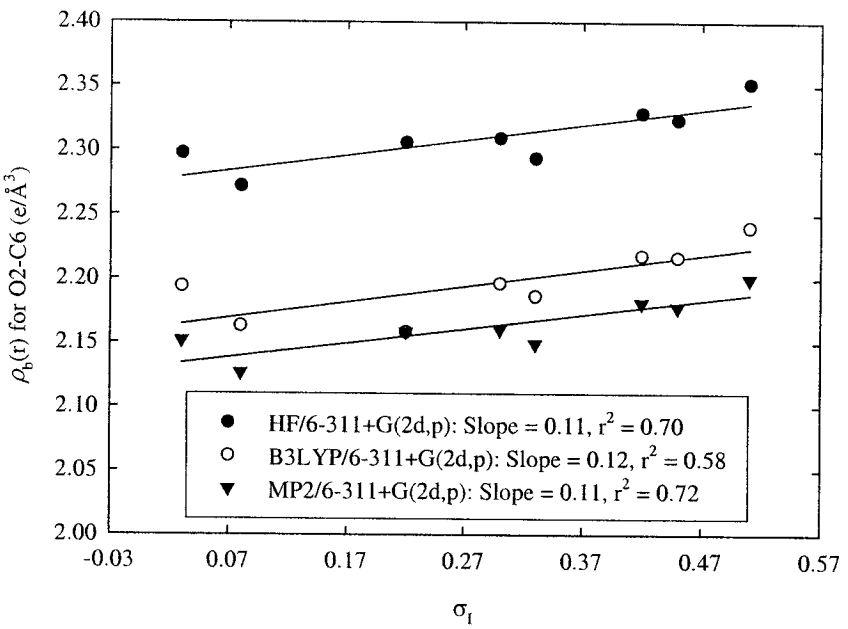

Figure C20 Dependence of the O2-C6 BCP electronic density on Swain-Lupton modified Hammett substituent constants σ_I for conformers **A(X)** of methoxy(substituted-siloxy)carbenes.

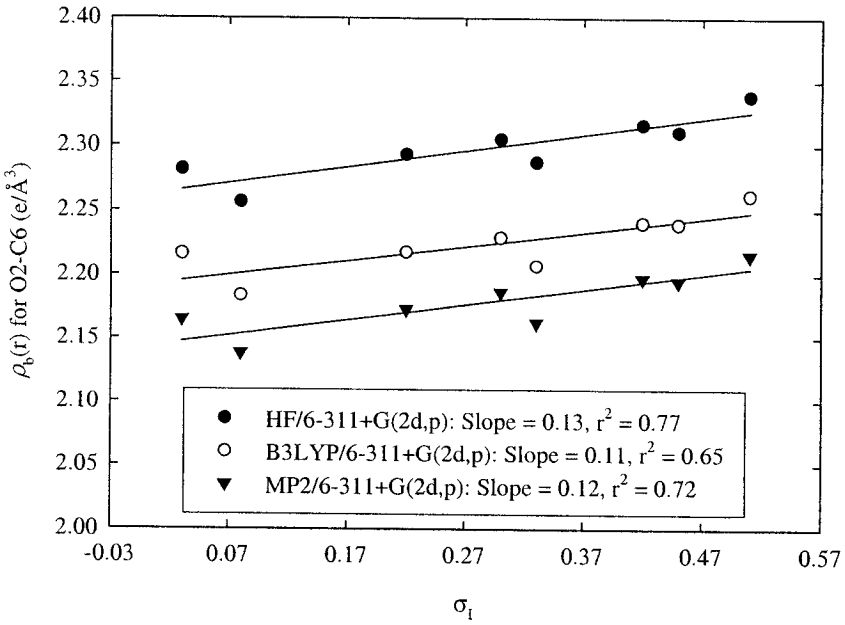

Figure C21 Dependence of the O2-C6 BCP electronic density on Swain-Lupton modified Hammett substituent constants σ_I for conformers **B(X)** of methoxy(substituted-siloxy)carbenes.

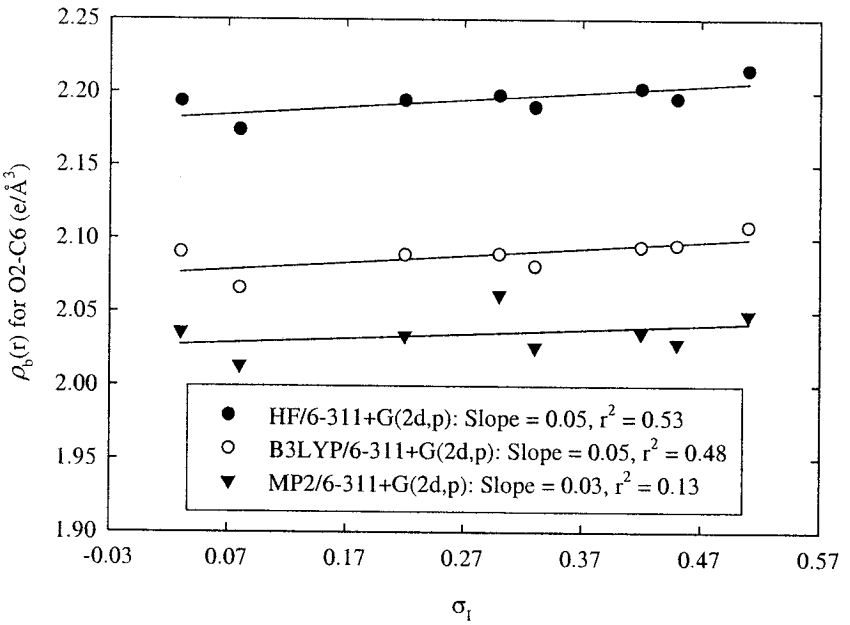

Figure C22 Dependence of the O2-C6 BCP electronic density on Swain-Lupton modified Hammett substituent constants σ_I for conformers **C(X)** of methoxy(substituted-siloxy)carbenes.

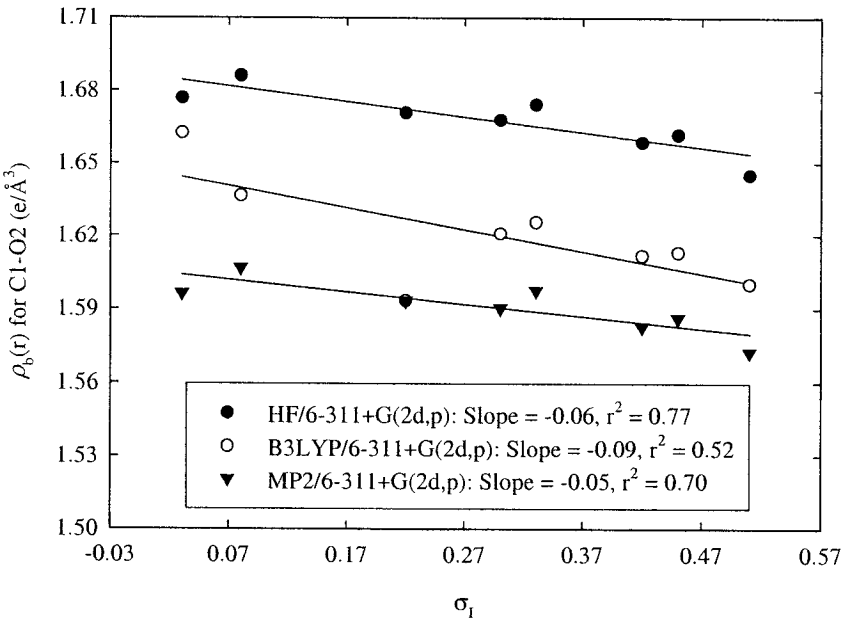

Figure C23 Dependence of the C1-O2 BCP electronic density on Swain-Lupton modified Hammett substituent constants σ_I for conformers **A(X)** of methoxy(substituted-siloxy)carbenes.

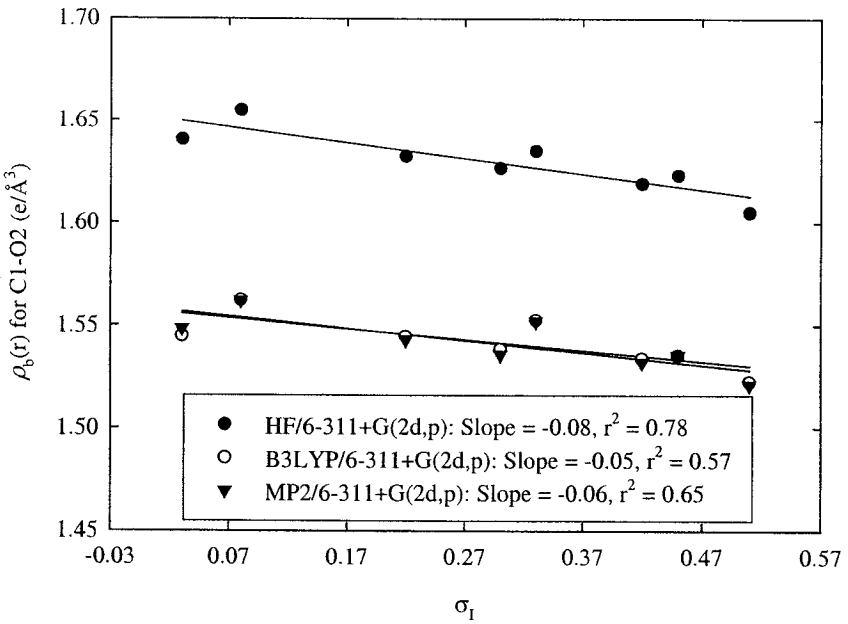

Figure C24 Dependence of the C1-O2 BCP electronic density on Swain-Lupton modified Hammett substituent constants σ_I for conformers **B(X)** of methoxy(substituted-siloxy)carbenes.

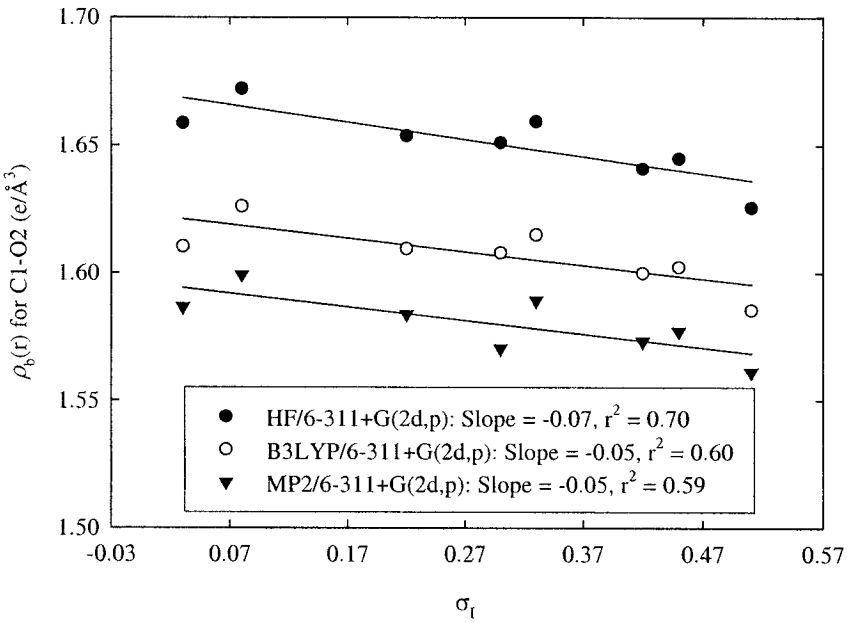

Figure C25 Dependence of the C1-O2 BCP electronic density on Swain-Lupton modified Hammett substituent constants σ_I for conformers **C(X)** of methoxy(substituted-siloxy)carbenes.

C.8 Plots of bond angles and bond distance versus stabilization energies due to hyperconjugation

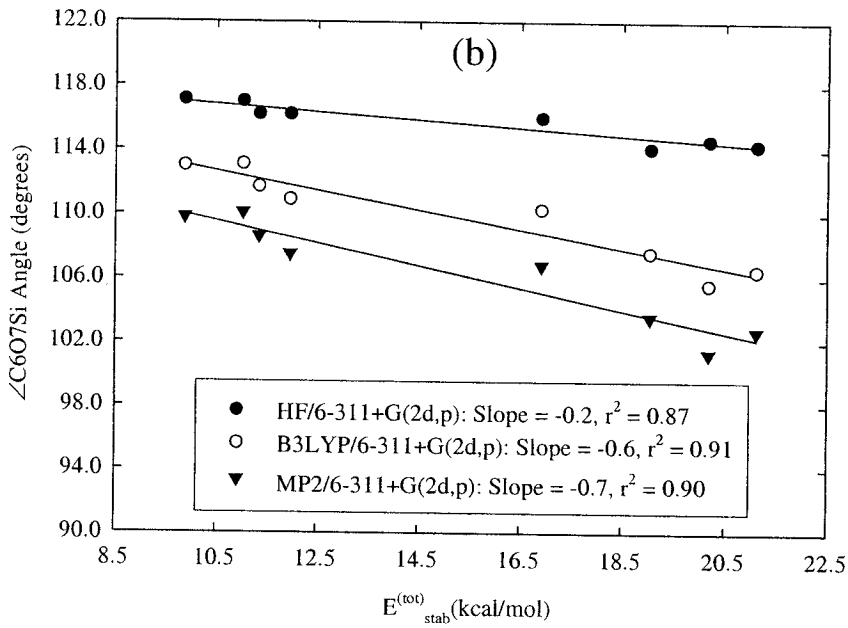

Figure C26 Plots of the ∠C6O7Si angles of conformers **B(X)** of methoxy(substituted-siloxy)carbenes versus stabilization energies $E^{(tot)}_{stab}$ due to hyperconjugation.

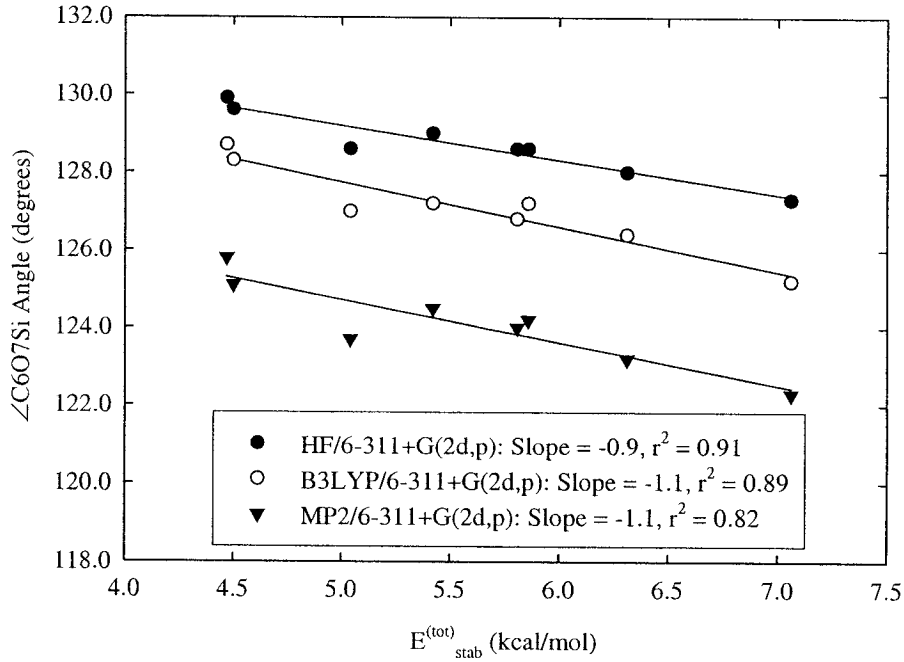

Figure C27 Plots of the ∠C6O7Si angles of conformers **C(X)** of methoxy(substituted-siloxy)carbenes versus stabilization energies $E^{(tot)}_{stab}$ due to hyperconjugation.

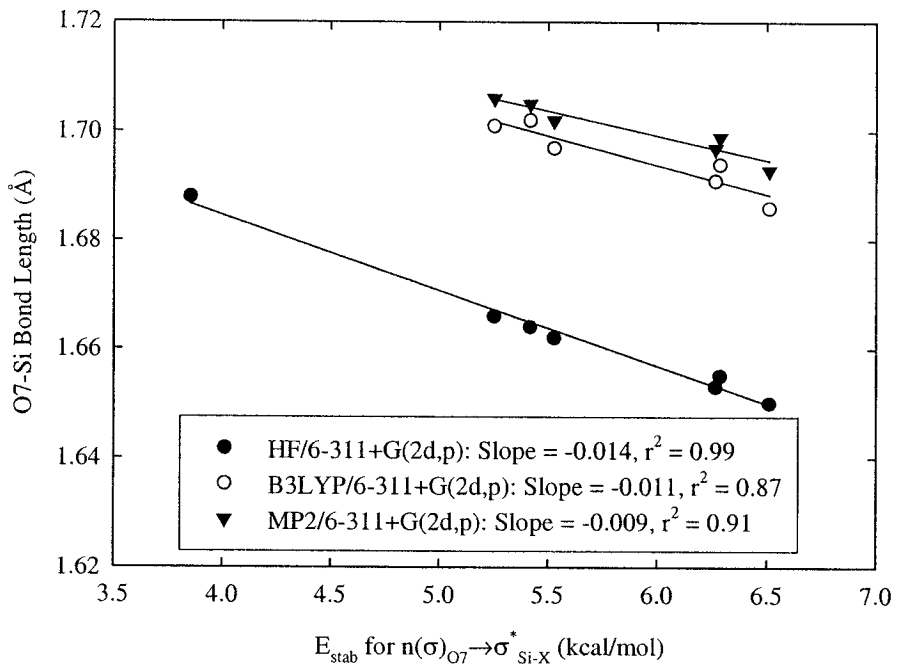

Figure C28 Plots of the O7-Si bond length versus stabilization energies E_{stab} due to $n(\sigma)_{O7} \rightarrow \sigma^*_{Si\text{-}X}$ hyperconjugation in the methoxy(substituted-siloxy)carbene conformers **A(X)**. Note that E_{stab} also includes $n(\sigma)_{O7} \rightarrow RY^*_{Si}$ interactions.

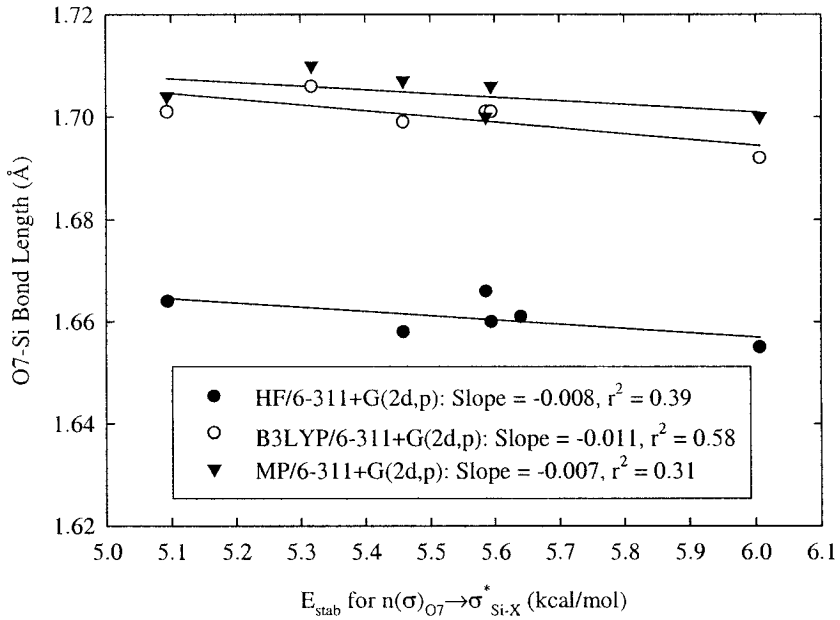

Figure C29 Plots of the O7-Si bond length versus stabilization energies E_{stab} due to $n(\sigma)_{O7} \rightarrow \sigma^*_{Si\text{-}X}$ hyperconjugation in the methoxy(substituted-siloxy)carbene conformers **B(X)**. Note that E_{stab} also includes $n(\sigma)_{O7} \rightarrow RY^*_{Si}$ interactions.

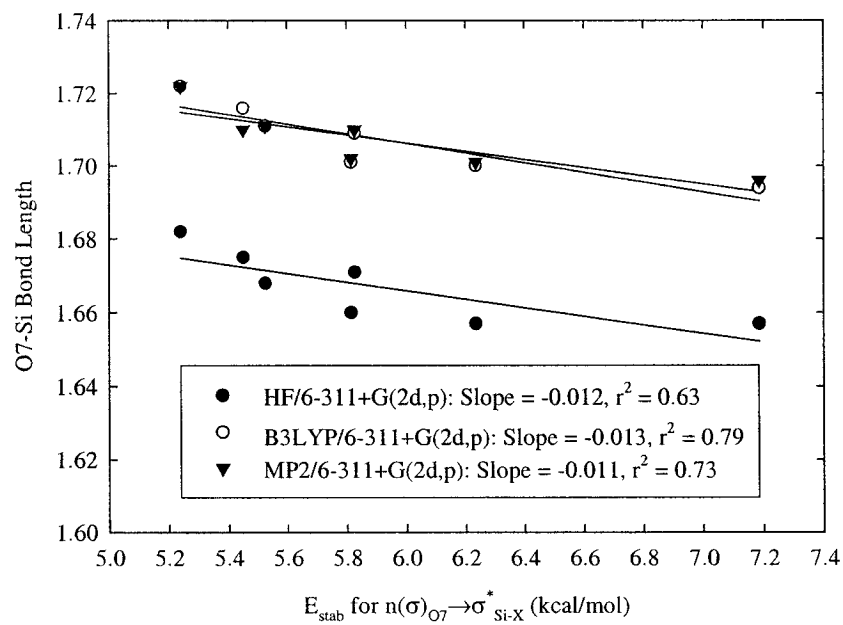

Figure C30 Plots of the O7-Si bond length versus stabilization energies E_{stab} due to $n(\sigma)_{O7} \rightarrow \sigma^*_{Si\text{-}X}$ hyperconjugation in the methoxy(substituted-siloxy)carbene conformers **C(X)**. Note that E_{stab} also includes $n(\sigma)_{O7} \rightarrow RY^*_{Si}$ interactions.

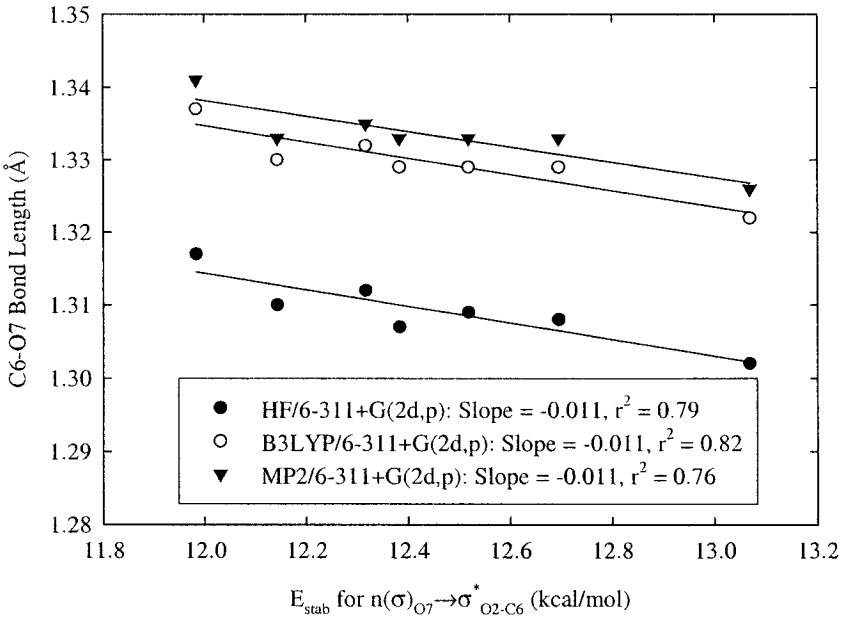

Figure C31 Plots of the C6-O7 bond length versus stabilization energies E_{stab} due to $n(\sigma)_{O7} \rightarrow \sigma^*_{O2\text{-}C6}$ hyperconjugation in the methoxy(substituted-siloxy)carbene conformers **A(X)**. Note that E_{stab} also includes $n(\sigma)_{O7} \rightarrow RY^*_{C6}$ interactions.

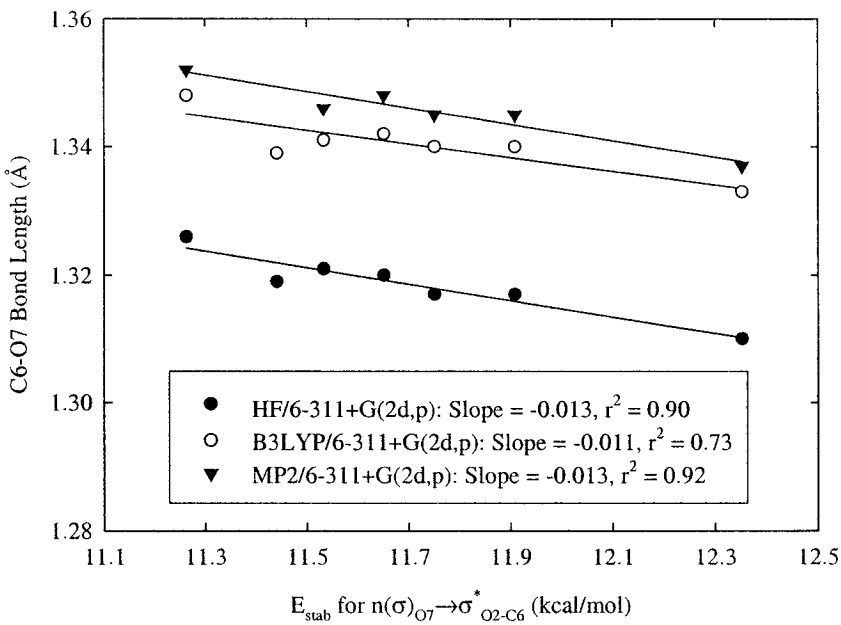

Figure C32 Plots of the C6-O7 bond length versus stabilization energies E_{stab} due to $n(\sigma)_{O7} \rightarrow \sigma^*_{O2\text{-}C6}$ hyperconjugation in the methoxy(substituted-siloxy)carbene conformers **B(X)**. Note that E_{stab} also includes $n(\sigma)_{O7} \rightarrow RY^*_{C6}$ interactions.

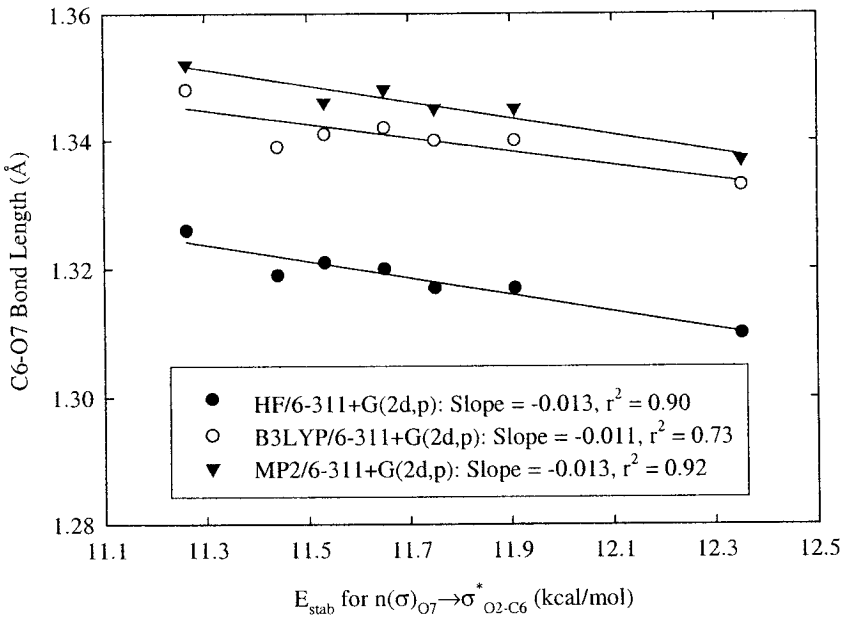

Figure C33 Plots of the C6-O7 bond length versus stabilization energies E_{stab} due to $n(\sigma)_{O7} \rightarrow \sigma^*_{O2\text{-}C6}$ hyperconjugation in the methoxy(substituted-siloxy)carbene conformers **C(X)**. Note that E_{stab} also includes $n(\sigma)_{O7} \rightarrow RY^*_{C6}$ interactions.

C.9 Plots of activation enthalpies for 1,2-silyl migration and decarbonylation versus stabilization energies due to hyperconjugation

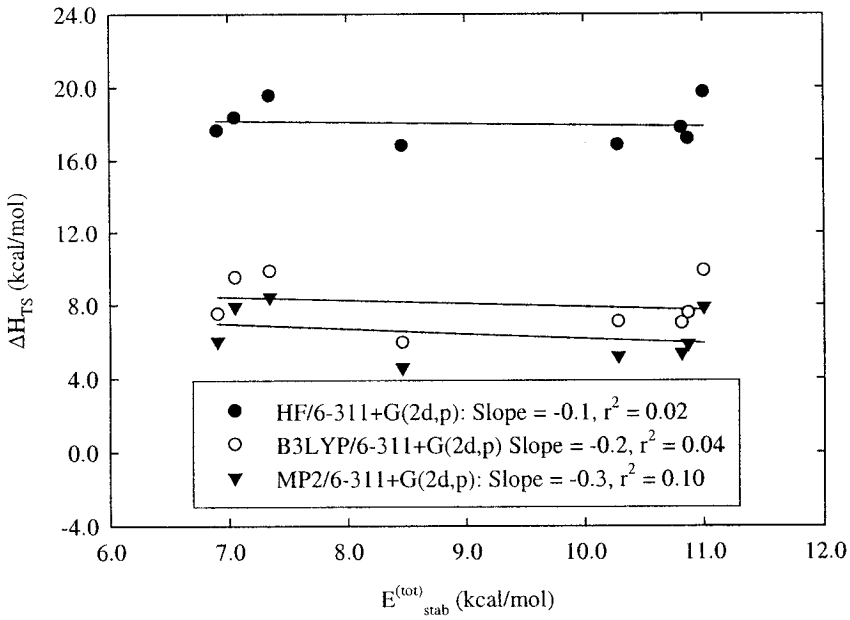

Figure C34 Plots of activation enthalpies for 1,2-silyl migration versus computed HF/6-311+G(2d,p) stabilization energies due to hyperconjugation in conformers **A(X)** of methoxy(substituted-siloxy)carbenes.

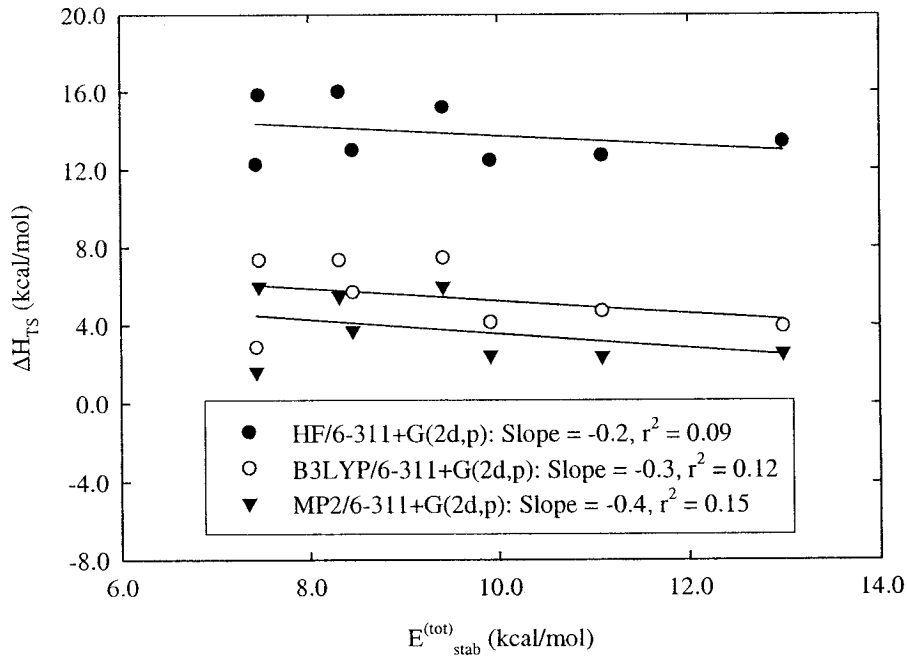

Figure C35 Plots of activation enthalpies for 1,2-silyl migration versus computed HF/6-311+G(2d,p) stabilization energies due to hyperconjugation in conformers **B(X)** of methoxy(substituted-siloxy)carbenes.

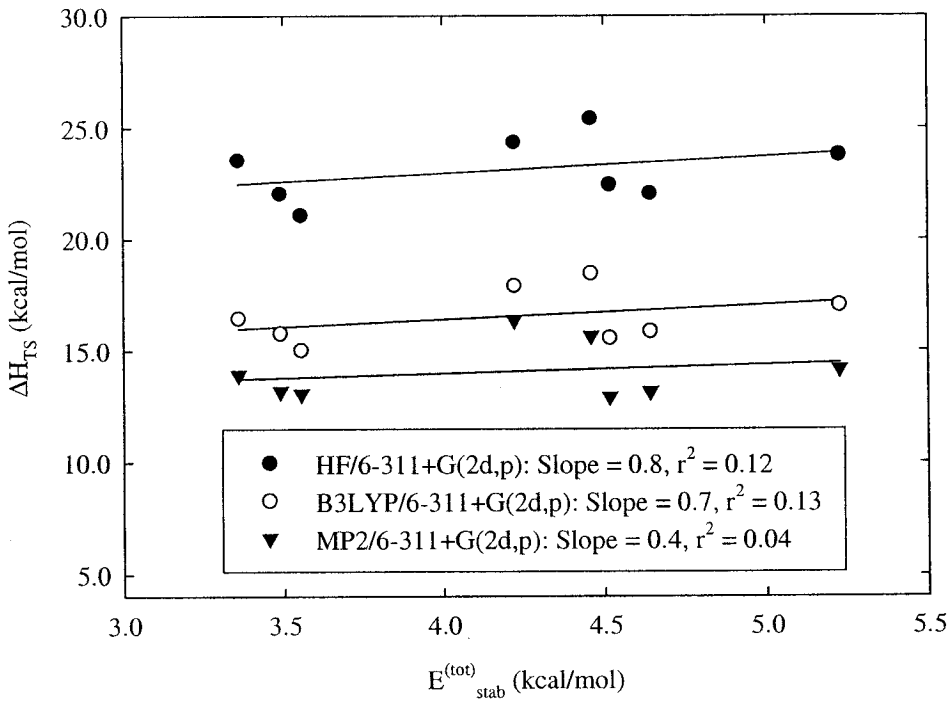

Figure C36 Plots of activation enthalpies for decarbonylation versus computed HF/6-311+G(2d,p) stabilization energies due to hyperconjugation in conformers **C(X)** of methoxy(substituted-siloxy)carbenes.

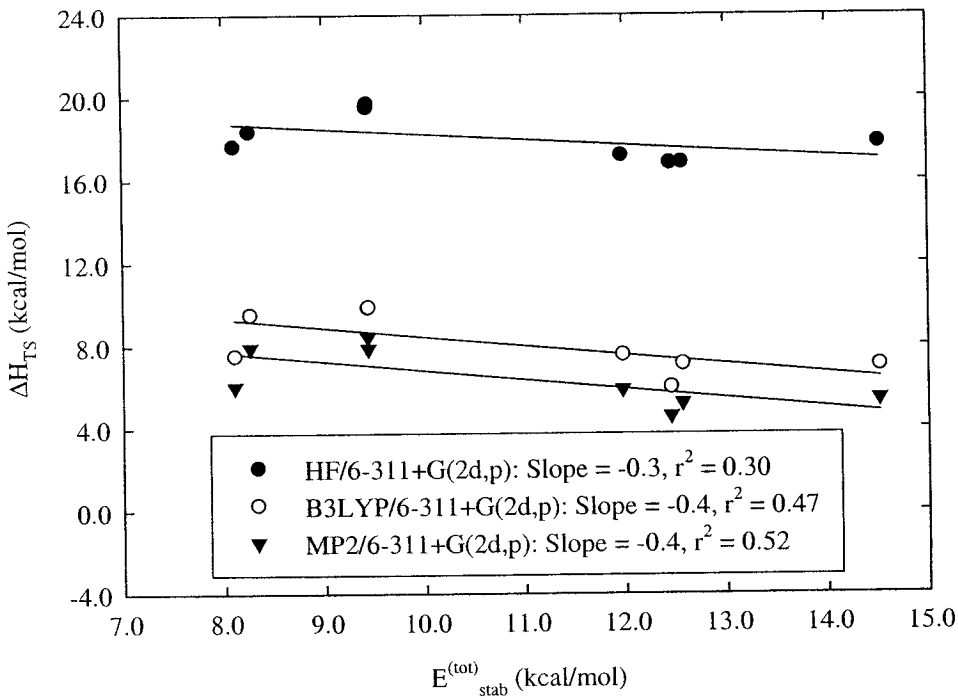

Figure C37 Plots of activation enthalpies for 1,2-silyl migration versus computed B3LYP/6-311+G(2d,p) stabilization energies due to hyperconjugation in conformers **A(X)** of methoxy(substituted-siloxy)carbenes.

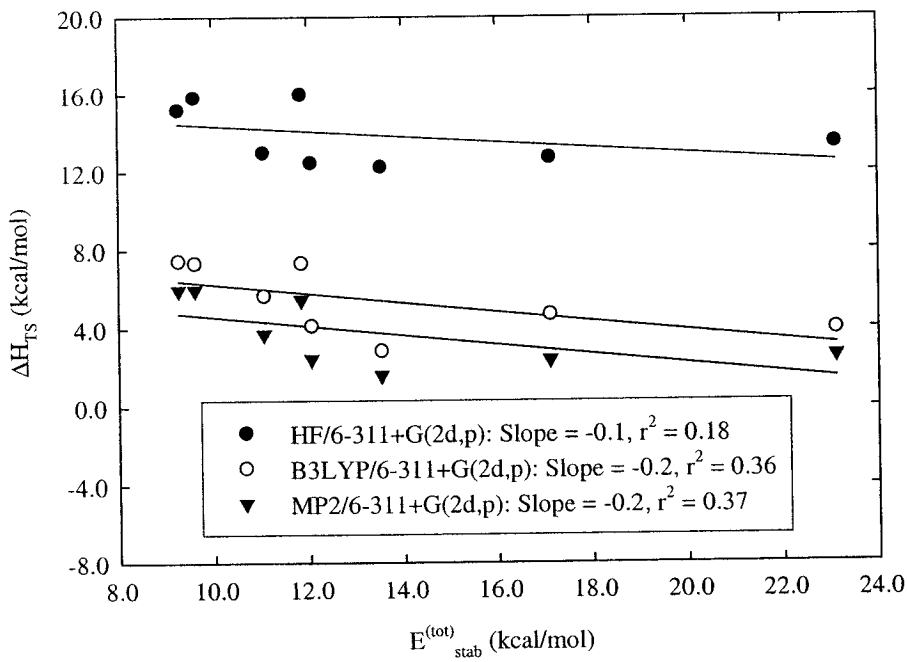

Figure C38 Plots of activation enthalpies for 1,2-silyl migration versus computed B3LYP/6-311+G(2d,p) stabilization energies due to hyperconjugation in conformers **B(X)** of methoxy(substituted-siloxy)carbenes.

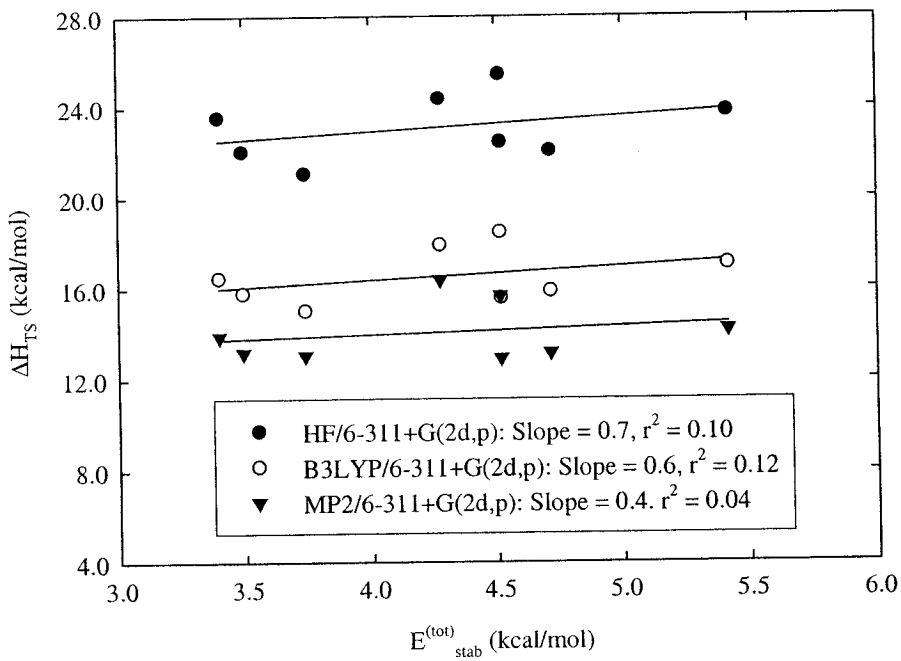

Figure C39 Plots of activation enthalpies for decarbonylation versus computed B3LYP/6-311+G(2d,p) stabilization energies due to hyperconjugation in conformers **C(X)** of methoxy(substituted-siloxy)carbenes.

Appendix D

D.1 Contour plots of the Laplacian of the electronic density for 3-sila-2-oxacyclohexylidene and 4-sila-3-oxacyclohexene

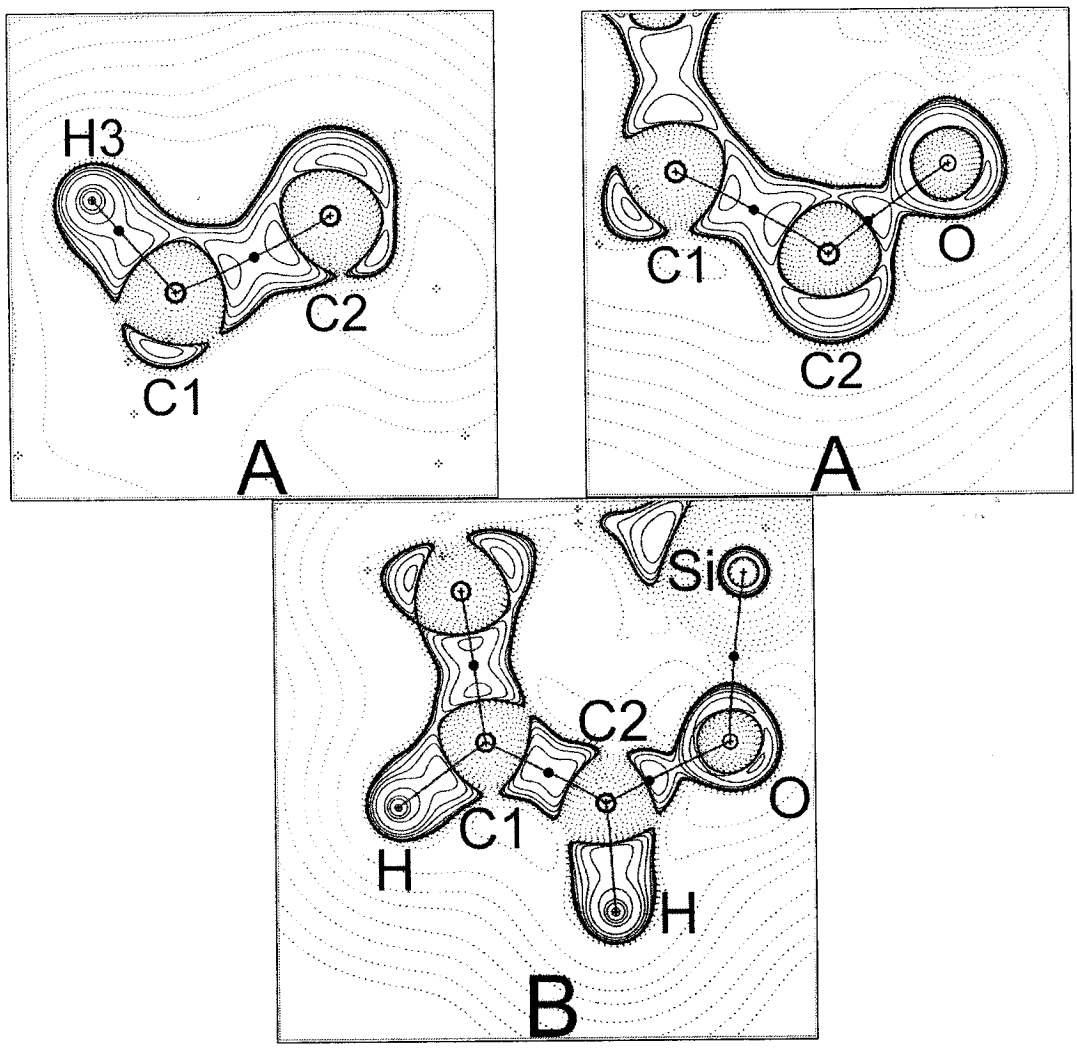

Figure D1 Contour plots of the Laplacian of the electronic density overlaid by bond paths in the H3C1C2 and C1C2O planes for 3-sila-2-oxacyclohexylidene **A**, and the C1C2O plane for 4-sila-3-oxacyclohexene **B**.